UNIVERSITY OF COPENHAGEN

PhD Thesis

Modelling oxygen evolution for electrochemical water splitting

Adrian Malthe Frandsen

Supervisor:
Prof. Ph.D. Jan Rossmeisl
Center for High Entropy Alloy Catalysis (CHEAC)
Department of Chemistry, University of Copenhagen
30/09/2024

This thesis has been submitted to the PhD School of The Faculty of Science, University of Copenhagen

Acknowledgements

No researcher stands alone, and all work is in some way or form derivative. I appreciate the atmosphere of openness and collaboration that exists within this field. As such I would like to thank my collaborators:

From the Center of High Entropy Alloy Catalysis (CHEAC):
Jan Rossmeisl, Katrine Louise Svane, Georgios Stavroglou, Henrik Høgh Kristoffersen, Rebecca Pittkowski, Søren Scott, Spyridon Divanis, Tugce Kutlosoy.

From international collaboration (in no particular order):
Petr Krtil, Kateřina Minhová Macounová, Catalina Astudillo, Roman Nebel, Caiwu Liang, Reshma Rao, Joseph Hadden, Benjamin Moss, Michael Sachs, James Murawski, Jason Riley, Mary Ryan, James Durrant, Ifan Stephens, Riccardo Marina, Dongni Zhao, Stijn Mertens, Harry Hoster.

Additionally I would like to thank:

Katrine Louise Svane and Amanda Schramm Petersen for proofreading this thesis.

My officemates: Christian, Martin, Mailde, Amanda, Zacharias.

Everyone at CHEAC that I have not directly worked with, but who have made the center the nice place it is.

My lovely fiancé Linda Ruohua Feng ♡
Family and friends for keeping me sane.

The open software I have been using for visualization: Inkscape, ASE, Matplotlib.

And of course the funding agencies:
The Danish National Research Foundation and the Villum Foundation

I declare no conflicts of interest.

Abstract

Electrocatalysis promises to detach society from fossil fuels, by allowing production of energy-rich molecules from abundant energy-poor molecules and renewable energy. A major roadblock towards this vision is the lack of efficient and stable catalyst materials made from readily available materials. Of particular importance is the oxygen evolution reaction (OER), which kinetically limits the electrolytic production of hydrogen for purposes such as energy storage, and chemical reduction. This thesis aims to expand our oxygen evolution reaction modelling approaches and increase our understanding of the catalytic mechanisms on highly active platinum group metal-oxides RuO_2 and IrO_2 in acid. Additionally, it aims to investigate and understand activation of the stable but inactive semi-conducting TiO_2.

The dissertation includes five articles, the first of which seeks to explain the gap between Density Functional Theory (DFT) calculated and experimental activity of RuO_2. The proposed solution is that RuO_2 employs a different reaction pathway than most other oxides, with protons in key intermediates migrating to an active site-adjacent proton-acceptor site. The second and third articles aim to introduce a screening method for the determination of lattice oxygen exchange tendency in rutile structures. The screening approach is a general method that can easily be extended to other oxide systems. The method is applied to $Ru_{1-x}Ni_xO_2$, $Ru_{1-x}Ti_xO_2$ and $Ru_{1-x}Mn_xO_2$ systems to good agreement with experimental results. The fourth article discusses catalytic activation of TiO_2 by simultaneous n- and p-type doping. The study finds that TiO_2 can indeed be activated, and the activation tuned, by co-substitution doping approaches. The finding is corroborated by experiments. As follow up studies to this article, unpublished DFT data is presented for the Ru-Ti conductor-semi-conductor transition as well as Ti in a high entropy oxide (HEO) system. The investigation of the conductor-semi-conductor transition finds that binding energies on Ti are mainly determined by whether there is Ru in the structure or not. Ti binding energies in the deep semi-conducting regime are found to be highly variable, and while this is possibly due to computational artefacts, it is replicated in conducting HEO structures. It is shown that the binding energy of oxygen on Ti is highly correlated with the Fermi level of the structure relative to stable oxygen 2s orbitals. Additionally, it is shown that the Fermi level of structures can be modelled as a simple weighted average of the constituent oxides. These results indicate that it is possible to optimize the binding of OER intermediates on Ti in HEOs. Finally, the fifth article discusses the role of redox-active site density in the OER on amorphous and rutile iridium oxide. The redox-active sites are quantified by operando time-resolved ultraviolet-visible spectroscopy, and it is found that oxygen intermediates at OER relevant potentials interact, contributing to O-O bond formation. This leads to a modified Sabatier volcano plot, dependent on the size of this adsorbate-adsorbate interaction.

These results are seen as significant steps towards the rational design of abundant catalyst materials for the OER reaction in acid.

Resumé

Elektrokatalyse lover at afkoble samfundet fra fossile brændsler gennem produktion af energi-holdige molekyler fra lettilgængelige energi-fattige molekyler. Denne vision er primært tilbageholdt af manglen på effektive og stabile katalysatormaterialer, der selv er lavet af lettilgængelige materialer. Især vigtig er oxygen udviklings reaktionen (OER), som kinetisk begrænser den elektrolytiske produktion af hydrogen til formål som energi opbevaring og kemisk reduktion. Denne afhandling søger at udvide vores modellerings tilgang til oxygen udvikling, samt at øge vores forståelse af de katalytiske reaktionsveje på de højt-aktive platinmetaloxider RuO_2 og IrO_2 i syre. Yderligere søges der en forståelse af tilgange til aktivering af den stabile, men inaktive, halvleder TiO_2 som OER katalysator.

Afhandlingen inkluderer fem artikler, hvoriblandt den første sigter efter at forklare forskellen på den forventede aktivitet af RuO_2 som beregnet med tæthedsfunktional teori (DFT) og eksperimentel litteratur. Som løsning foreslås at RuO_2 benytter en anden reaktionsvej sammenlignet med de fleste andre oxider. Den foreslåede reaktionsvej kendetegnes ved at protoner fra nøgleintermediater er migreret til en proton acceptor nær reaktionsstedet. Den anden og tredje artikel introducerer en screeningsmetode til at identificere udvikling af gitterilt fra rutile strukturer. Screeningsmetoden er en generel metode, der nemt kan udvides til nye systemer. Metoden bliver anvendt på $Ru_{1-x}Ni_xO_2$, $Ru_{1-x}Ti_xO_2$ og $Ru_{1-x}Mn_xO_2$, og finder god overensstemmelse med eksperimentelle resultater. Den fjerde artikel diskuterer katalytisk aktivering af TiO_2 ved samtidig n- og p-type dopning. Studiet finder at det er muligt at aktivere titandioxid med co-substituering, samt at tune aktiviteten. Disse resultater bliver korroboreret af eksperimentelle resultater. Som opfølgning på dette studie, præsenteres ikke-udgivet DFT data for leder-halv-leder overgangen i ruthen-titan dioxid, samt data for Ti i højentropiske oxider (HEO). Undersøgelsen af Ru-Ti leder-halv-leder overgangen finder at bindingsenergien for intermediater på Ti er mest af alt bestemt af hvorvidt der er ruthen i strukturen eller ej. Bindings energier på Ti i det dybe halvledende domæne er fundet til at være højt varierende. Dette kan være på grund af komputationelle artefakter, men en bred spredning for bindingsenergier på Ti er også set i de højentropiske oxid systemer. Det vises at bindings energien af oxygen på Ti er højt korreleret med Fermi niveauet af strukturen, beregnet som relativ til dybe stabile oxygen 2s orbitaler. Fermi niveauet findes at kunne modelleres som et simpelt vægtet gennemsnit af komponent-oxiderne i et HEO system. Disse resultater indikerer at det er muligt at optimere bindingen af OER intermediater på TI i høj-entropiske oxider. Endelig, den femte artikel diskuterer rollen af redox-aktive centre i OER på amorf og rutil iridium oxid. De redox aktive centre bliver kvantificeret med ultraviolet-synlig spektroskopi, og det findes at oxygen intermediater ved OER relevante potentialer interagerer. Dette bidrager til dannelsen af O-O bindinger, og leder til et alternative vulkan plot afhængigt af styrken på denne interaktion.

Disse resultater ses som signifikante skridt mod rationelt design af lettilgængelige katalysator materialer for oxygen udvikling i syre.

Contents

1 Introducing the Grand Vision

Writing introductions in this field can easily become (somewhat justified) doom and gloom. I included an introduction of such character in my master's thesis, and would like to do something else this time around. Therefore, I will focus on the hopeful promise of electrocatalysis. Because electrocatalysis truly is hopeful. It tells the tale of a world powered entirely by renewable sources [1]. Where our fuels and chemicals are derived from air and sea. Air provides abundant amounts of carbon dioxide, nitrogen and oxygen as building blocks, and the sea provides water and salt. The wonderful thing about this vision, is that it is not a fantasy. These technologies exist, and are working. In this regards, we are simply figuring out the kinks to allow for industrial upscaling.

Due to the enormous energy consumption of the modern world, any technology that is to have noticeable impact on global energy demand and infrastructure has to operate on the terawatt scale. The challenge of meeting this criteria has been dubbed the "*terawatt challenge*", and solutions require finding alternative energy carriers to compete with oil [2]. Coupling the intermittent nature of renewable energy sources with electrocatalysis could provide this "*oil*" of the future by converting electric energy from the grid to a chemical of choice. A significant candidate for this "*power-to-X*" is green electrolytic hydrogen [3], as it is simultaneously pollutant free, readily available, an important reducing agent in chemical industry and has *the highest* energy per mass metric [4]. The green production of hydrogen thus holds a key role in defossilization of energy infrastructure *and* chemical industry.

While hydrogen is the desired product in water electrolysis, the major technological challenges are related to the slow kinetics of the oxygen evolution reaction (OER) at the anode [5], making the process largely inefficient. The most commercially mature water electrolyzers are for OER in alkaline conditions, it would however be ideal to have efficient electrolyzers for acidic conditions. Acidic electrolyzer technology allows for higher current densities, smaller electrolyzer modules, purer gas output and pressurized working conditions [6]. The harsh working conditions of acidic water electrolyzers put significant stability limitations on the types of catalyst materials that can be employed. The currently best known catalysts for such conditions are oxides of rare platinum group metals like ruthenium and iridium [7, 8, 6]. This makes industrial upscaling to meet the terawatt challenge straight up impossible [9], and calls for alternative materials. This thesis provides a step towards new materials, by providing a deeper understanding of Ru and Ir as OER catalysts. Additionally, it explores ways to activate the otherwise inactive titanium oxide.

This dissertation primarily concerns OER for acidic working conditions, and as such these reaction conditions will be implicitly assumed throughout.

2 Surface modelling approaches

With the motivation laid out, what tools and techniques do we use to address the subject of electrocatalysis? The main tool of choice employed in this thesis is Density Functional Theory (DFT). DFT is based upon the idea that the energy of a system is given by the electronic density, and that it is therefore a functional of the electron density [10]. DFT provides multiple types of output that can be beneficial to understanding the electrocatalytic surface; examples being the total energy of a system, the forces within the system, the electronic density of states (DOS) or the work function. In my Master's thesis I have previously written a chapter on the basic theory and algorithmic design of DFT [11]. In this thesis, I will therefore refrain from going into too much detail about the inner workings of DFT, and instead refer back in case of interest (made available at link `https://curis.ku.dk/ws/files/403981637/Adrian_Master_s_Thesis.pdf` or QR code: section 10).

In practise you construct a structure of interest in a simulation environment like the Atomic Simulation Environment (ASE) [12], and then employ a DFT calculator such as Grid-based Projector Augmented-Wave (GPAW) [13, 14, 15]. The calculator attempts to converge the electron density to determine energy and forces. Once converged, the output is rarely useful, as the system is generally not in a relaxed state. Thus the calculator comes equipped with a geometry optimizer that translates atoms in the system according to their forces. The DFT calculator then runs again to see whether the total forces in the system are smaller than the user-defined convergence criteria. A DFT relaxation thus requires the convergence of the electronic wave functions many times over as well as the convergence of the geometry. Issues related to convergence of DFT calculations can therefore be related to either converging the wave functions or finding the relaxed state of a system.

DFT is not perfect, and approximations are a part of the approach. Of practical importance are the approximations introduced to describe the electronic interaction energies [16]. The Kohn-Sham equations used to extract the electron density describe this interaction as a Coulombic repulsion between the individual electron and the entire electron cloud [17]. This is of course unphysical, as it would imply electron self-interaction. The Kohn-Sham equations attempt to rectify this with an additional additive term in the single-electron Hamiltonian, namely the exchange-correlation (xc) functional [16]. Setting up a DFT calculator thus requires the choice of an xc functional, and the descriptive accuracy of the method is directly dependent on this choice. This approach leads to errors of electron over-delocalization, and brings with it computational artefacts like underestimation of band-gaps in semi-conductors.

Throughout this thesis I have mainly been using the RPBE xc functional due to its focus on strong chemical interactions [18], making it a good choice for describing oxygen binding on surfaces. Depending on the system, DFT can however still have issues due to strong electron correlation effects. Relevant to this thesis in particular are oxides. It might therefore be necessary to include extra corrections to better describe the system. An example of such an approach is DFT+U [19], which allows the adjustment of the electron localization via a user-defined parameter Hubbard's U. This correction comes with the added challenge of determining a suitable value for U without over-engineering the output. Corrections approaches are relevant to keep in mind when working on highly correlated oxide systems, as the output is particularly prone to computational artefacts like band-gap underestimation and electron over-delocalization.

2.1 Modelling surface reactions

DFT is an incredible tool to understand (small) nanoscale systems. With such a tool in hand the question becomes how to employ it for useful and telling output. Many electrochemical surface reactions, and especially those of interest in this thesis, are proton-electron coupled reactions. This type of reaction is defined by a concerted proton electron transfer during the reaction step [20]. A generic example of a coupled proton-electron oxidation reaction could be:

$$2\mathrm{AH} \rightarrow \mathrm{A}_2 + 2(\mathrm{H}^+ + e^-) \tag{1}$$

Here, AH is a molecule consisting of arbitrary element A and hydrogen, H. This reaction in reverse on the other hand constitutes an example of a generic reduction reaction:

$$\mathrm{A}_2 + 2(\mathrm{H}^+ + e^-) \rightarrow 2\mathrm{AH} \tag{2}$$

Imagine now the electrocatalysis of the oxidation reaction eq. (1). During catalysis, the anodic catalyst surface facilitates intermediate reaction steps, lowering the activation barrier of the reaction as a whole. We might model this catalyzed reaction pathway as an adsorption step:

$$\mathrm{AH} + * \rightarrow \mathrm{A}^* + (\mathrm{H}^+ + e^-) \tag{3}$$

Followed by a desorption step:

$$\mathrm{A}^* + \mathrm{AH} \rightarrow \mathrm{A}_2 + * + (\mathrm{H}^+ + e^-) \tag{4}$$

As is common in this field, the surface is denoted with an asterisk (*), and when written in superscript implies a surface bound intermediate. The above reaction pathway thus adsorbs A onto the surface (A^*), releasing an electron and a proton in the process. This is followed by the surface intermediate reacting with AH, causing the desorption of A_2 as the final product, leaving the catalyst surface unchanged and open for another catalytic cycle.

Let us explore the energetics associated with this reaction pathway. Employing DFT for the determination of energies, we can calculate the adsorbate binding energy for our example eq. (3):

$$\Delta E_{\mathrm{A}^*} = E_{\mathrm{A}^*} + E_{(\mathrm{H}^+ + e^-)} - E_* - E_{\mathrm{AH}(g)} \tag{5}$$

The energy of the proton-electron pair $E_{(\mathrm{H}^+ + e^-)}$ is highlighted in red, as determining this energy cannot be done directly with DFT calculations. For now, assume that we have a fitting model for treating this term. This will be the topic of the next section 2.2.

Useful as it is, the DFT binding energy does not reflect the spontaneity of the reaction. For this we need the Gibbs free energy of reaction. We can go from the DFT binding energy to Gibbs free energy of reaction by the addition of zero-point energy (C_{ZPE}), enthalpic ($C_{Enthalpic}$) and entropic corrections ($C_{Entropic}$) [20, 21]:

$$\Delta G_{bind} = \Delta E_{DFT} + C_{ZPE} + C_{Enthalpic} + C_{Entropic} \tag{6}$$

The change in zero-point energy is approximated by the quantum mechanic harmonic oscillator and can be calculated using DFT. The enthalpic correction can be calculated as the integral of the change in specific heat (Δc_p):

$$C_{Enthalpic} = \int_0^T \Delta c_p dT \tag{7}$$

In practice, this enthalpic correction is often disregarded [20]. The entropic correction can be calculated from the temperature and change in entropy as [22]:

$$C_{Entropic} = -T\Delta S \tag{8}$$

In real systems, the electric field from the electrode also has an influence on the binding energy of intermediates [23]. This effect is generally negligible for small intermediates, but can become relevant for larger intermediates protruding the interface [20], or special cases like solvated ions in the interface [24]. These field effects are discounted throughout this thesis, as they have been shown to be negligible for the OER intermediates [21]. Additionally, the energy corrections used in this thesis mirror those from [21] and are presented in section 9.

To determine the Gibbs free energy of reaction thus requires a DFT calculation of the gas AH, the surface $*$, the surface with adsorbate A* and a model for the chemical potential of the electron proton pair (all in addition to the above corrections). Of course the Gibbs free energy of reaction should change according to the conditions i.e. applied potential and the pH. A good model for the proton-electron pair thus allows us to determine the conditions that thermodynamically favor surface intermediates of interest.

2.2 Computational Hydrogen Electrode

The famous computational hydrogen electrode (CHE). The absolute cornerstone of all that I have done during my PhD years. It has been the source of quite the confusion for me, and I know it has been for others as well. This is particularly odd due to the simplicity of the model. In my case, I suspect that I simply didn't understand exactly what it was attempting to model, and by extension when it was applied. The CHE is a model for the chemical potential of the electron-proton pair, such that the Gibbs free energy of binding described in the preceding section becomes computable [21]. It serves the purpose of a computational reference electrode. A reference electrode is used in real (experimental) systems to allow comparison between different catalyst performances. In computational systems, the CHE allows for "asking" a system how it would look at a specific electrode potential as determined by the reference. The CHE is based on the

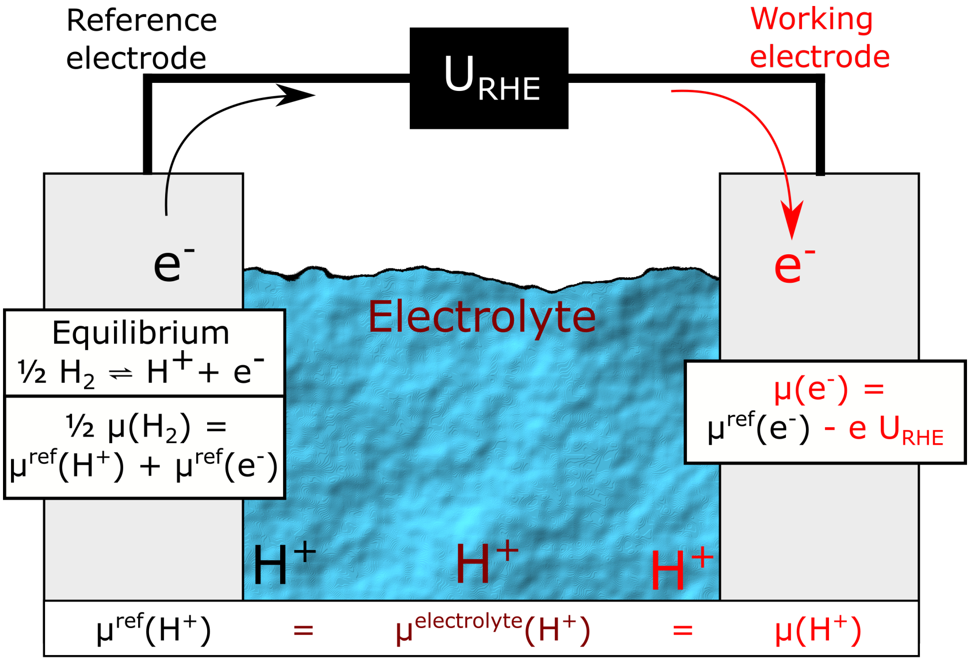

Figure 1: The computational hydrogen electrode. The reference electrode is a hydrogen electrode, meaning it is in equilibrium with the hydrogen oxidation/reduction reaction. The chemical potential of electrons at the working electrode is determined relative to the reference by the applied potential. Due to the assumption of being in quasi-equilibrium, the chemical potential of the protons is the same at the reference, as in the electrolyte, as at the working electrode. This allows for modelling the chemical potential of electron and proton at the working electrode by using the chemical potential of hydrogen gas.

standard hydrogen electrode (SHE), which defines the equilibrium potential of

$$\frac{1}{2}\mathrm{H}_2(g) \rightleftharpoons (\mathrm{H}^+ + e^-) \tag{9}$$

as 0 V at pH 0. It additionally models the reversible hydrogen electrode (RHE), which is normalized by the activity of protons [20]. This allows for both varying the electrode potential as well as the pH in the CHE. The RHE is linearly connected to the SHE through the Nernst equation as follows:

$$U_{RHE} = U_{SHE} - 0.059\mathrm{V} \cdot pH \tag{10}$$

So, how is the CHE model set up? A schematic representation of the CHE is produced in fig. 1. At the reference electrode we have the equilibrium reaction of the hydrogen electrode eq. (9). This equilibrium establishes a relation between the chemical potentials of hydrogen gas, electrons and protons at the reference:

$$\frac{1}{2}\mu(\mathrm{H}_2) = \mu^{ref}(\mathrm{H}^+) + \mu^{ref}(e^-) \tag{11}$$

The model is made for concerted proton-electron transfers and builds on three assumptions as laid out by Bagger et al. [20]:

1. The electrolyte bulk is in equilibrium.
2. The electrodes are in equilibrium with the catalytic surfaces, which are in turn in equilibrium with the electrolyte.
3. The binding energy of intermediates is unaffected by the electrostatic field.

It follows from the first and second assumption that the chemical potential of protons at the reference electrode ($\mu^{ref}(\mathrm{H}^+)$) is the same as in the electrolyte ($\mu^{electrolyte}(\mathrm{H}^+)$), is the same as at the working electrode ($\mu(\mathrm{H}^+)$):

$$\mu^{ref}(\mathrm{H}^+) = \mu^{electrolyte}(\mathrm{H}^+) = \mu(\mathrm{H}^+) \tag{12}$$

The chemical potential of electrons at the working electrode are accelerated by the applied electrode potential compared to the reference:

$$\mu(e^-) = \mu^{ref}(e^-) - eU_{RHE} \tag{13}$$

We are now in a position where we can calculate the proton-electron pair from eq. (5) for the sake of calculating the Gibbs free energy of binding for eq. (6). Combining eq. (11), eq. (12) and eq. (13):

$$\mu(\mathrm{H}^+) + \mu(e^-) = [\mu^{ref}(\mathrm{H}^+) + \mu^{ref}(e^-)] - eU_{RHE} = \frac{1}{2}\mu(\mathrm{H}_2) - eU_{RHE} \tag{14}$$

Thus it is possible to determine the chemical potential of the proton-electron pair at the working electrode by simply calculating the energy of a gas-phase hydrogen molecule in DFT and then adding the applied potential. We can now return to our generic example adsorption eq. (5) and determine the Gibbs free energy of binding:

$$\Delta G_{\mathrm{A}^*} = E_{\mathrm{A}^*} + (\frac{1}{2}\mu(\mathrm{H}_2(g)) - eU_{RHE}) - E_* - E_{\mathrm{AH}} + C \tag{15}$$

where C is the sum of the corrections mentioned in eq. (6). We can further generalize this to any number of proton-electron transfers (n):

$$\Delta G_n = E_n + n(\frac{1}{2}\mu(\mathrm{H}_2(g)) - eU_{RHE}) - E_{n=0} + C \tag{16}$$

Here ΔG_n is the Gibbs free energy of binding for an adsorption reaction with n oxidations, E_n is the total ground state energy of reaction products (excluding proton-electron couple) as calculated by DFT after n concerted proton-electron oxidative transfers, and $E_{n=0}$ is the DFT energy of reactants before any transfers have happened. In this case, n being positive designates an oxidation whereas n being negative designates reduction.

2.3 Free energy diagrams

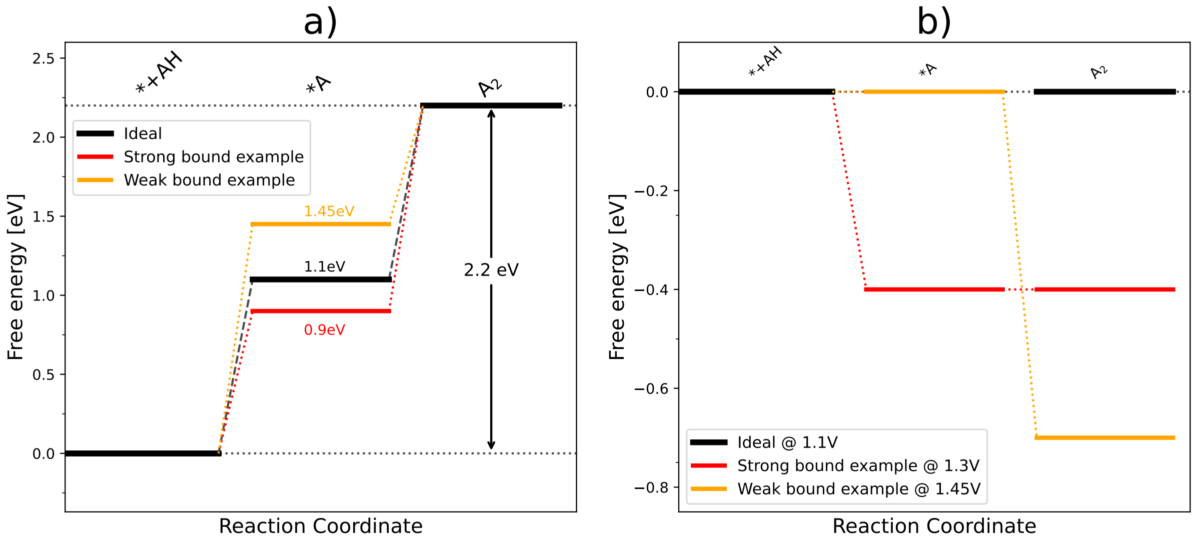

Figure 2: Free energy diagrams for a generic example of an electrochemical oxidation reaction (eq. (1)). The binding energy of the intermediate A^* determines the potential determining reaction step. Orange represents a weak binding surface and red represents a strong binding surface. **a)** The free energy diagram in the case of 0V vs RHE. **b)** Free energy diagram of the case of $U_{RHE} = U_{PDS}$.

Once the reaction free energies of surface configurations have been determined, a free energy diagram can be constructed to visualize the energy landscape established by those surface states. If the energy landscape is a reaction pathway of interest, the potential determining step (PDS) can be determined. As an example let us return to our generic oxidation reaction eq. (1). Assume that the free energy change of this reaction is 2.2 eV. If that is the case, it would ideally cost 1.1 eV of energy per concerted proton-electron transfer to drive this reaction (2.2 eV divided by the number of transfers). This is illustrated in fig. 2a as the ideal reaction energetics with each step being the same size. Real catalyst surfaces rarely conform to the ideal case. Therefore the intermediate binding energy rarely equalizes all the reaction steps. In some cases the intermediate might be "weakly" bound, such that the largest energy reaction step is that of getting onto the surface. An example of this could be the orange line, where $\Delta G_{\mathrm{A}^*} = 1.45\ e\mathrm{V}$. In other cases the surface might bind the intermediate too strongly, such that the most difficult step is to desorb from the surface (example in red, $\Delta G_{\mathrm{A}^*} = 0.9 e\mathrm{V}$). The size of the potential determining step (U_{PDS} can thus be determined with the knowledge of the binding energy:

$$U_{PDS} = \mathbf{max}(\Delta G_{\mathrm{A}^*}, 2.2\ e\mathrm{V} - \Delta G_{\mathrm{A}^*}) \tag{17}$$

The PDS determines the potential needed for every reaction step to be downhill in Gibbs free energy, thus allowing the reaction to run (illustrated in fig. 2b). When the binding energy is not at the ideal value, the reaction requires an elevated electrode potential to run. This potential elevation is named the overpotential, η, and signifies the energy loss associated with each reaction step [25]. It can be calculated as the difference between the PDS and the equilibrium potential for the reaction. In this case:

$$\eta = U_{PDS} - 1.1\ \mathrm{V} \tag{18}$$

2.4 Volcano plots

The free energy diagrams of fig. 2 illustrates that the bond strength of an intermediate should be just right. Neither too strong, as to be limited by desorption, nor too weak, as to be limited by adsorption. This principle is named the Sabatier principle, after Paul Sabatier [26], and is illustrated in fig. 3a. The principle is qualitative in nature, as it holds no indication of what to be considered the appropriate descriptor for bond strength. The free energy diagrams show that the binding energy of reaction intermediates can be used as bond strength descriptor. This holds true for single-intermediate reactions like the fictional AH oxidation. In case of multi-step reaction pathways, caution must however be applied. This will be discussed in detail during treatment of the four-step OER in the next chapter, section 3. As for the y-axis, this thesis will use the overpotential as activity descriptor. This choice is in no way perfect, as it does not take into account reaction barriers or kinetics. It is however easily identifiable from calculation, and has been shown to relate directly to reaction barriers of surface reactions [27]. As such it is ultimately connected to reaction rate through the Arrhenius equation [28]. The main draw from this approach is to avoid difficult reaction barrier calculations, and even though the approach constitutes a purely thermodynamic view, the trends are expected to hold when including barriers [29].

To construct a volcano plot we need relations between the chosen bond strength descriptor and the energy change associated with the reaction steps of the reaction. This is effectively what we did in eq. (17), where the size of the two reaction steps were found to be:

$$\Delta G_1(\Delta G_{\mathrm{A}^*}) = \Delta G_{\mathrm{A}^*} \tag{19}$$

$$\Delta G_2(\Delta G_{\mathrm{A}^*}) = 2.2\ e\mathrm{V} - \Delta G_{\mathrm{A}^*} \tag{20}$$

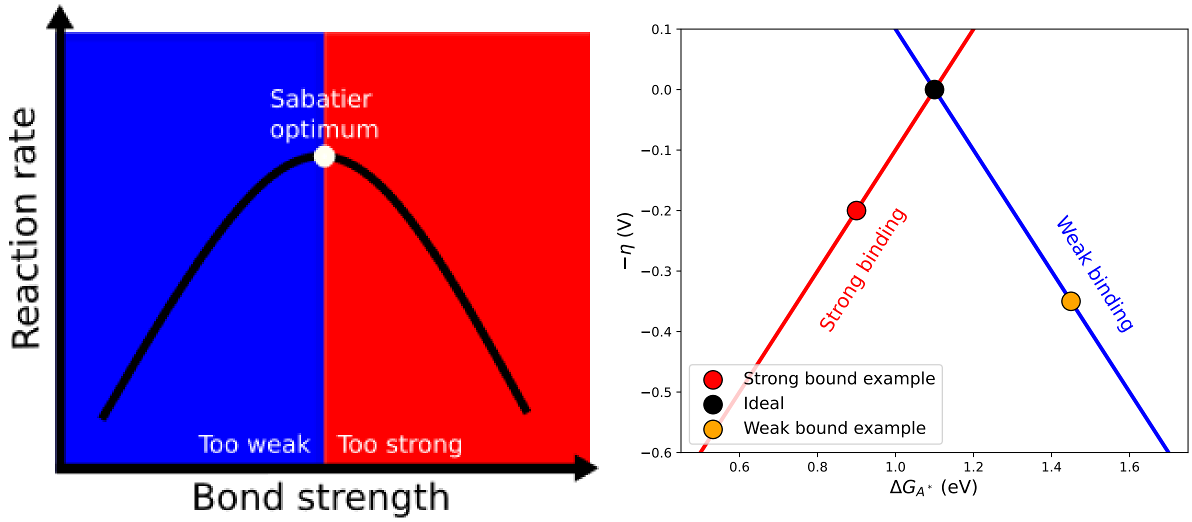

(a)

(b)

Figure 3: **a)** Graphical illustration of the Sabatier principle. The bond strength of the reaction intermediate on the surface determines the reaction rate, with the optimum being neither too strong nor too weak. Reproduced from [11]. **b)** Example of a volcano plot for the fictional AH oxidation reaction. The binding energy of A^* is used as descriptor for bond strength, and $-\eta$ as activity descriptor. Three points are plotted on the volcano; the ideal case, the strong binding example and the weak binding example from fig. 2.

Here ΔG_1 is the size of the adsorption step, and ΔG_2 is the size of the desorption step. When $\Delta G_1 > \Delta G_2$, we have the case of a weak binding surface. As such the function $\Delta G_1(\Delta G_{\mathrm{A}^*})$ corresponds to what is coined the weak binding side of the volcano. The opposite is true for ΔG_2, which thus corresponds to the strong binding side. Together these two functions make up the volcano as illustrated in fig. 3b. Additionally, the three examples from fig. 2 have been plotted along the volcano. The volcano plot graphically represents how close a given surface reaction is to being ideally catalyzed, as well as whether the surface overshoots or undershoots the ideal value of the bond strength descriptor.

2.5 Phase diagrams and surface Pourbaix diagrams

Take now the strong binding example from fig. 2, that is a surface that binds A^* with a binding energy of 0.9 eV. During working conditions the electrocatalyst material making up this surface will probably be in contact with an electrolyte. Assume the electrolyte is nothing but water and AH molecules ready for oxidation. Even from this simple perspective the surface quickly becomes a messy place. What is on the surface? Is it water? Oxygen? Hydrogen? Hydroxides? Using the CHE we can establish a simplified model to get an idea of the dominant surface intermediate at different electrode potentials. Say that we have identified the following adsorption reactions that we suspect are occurring

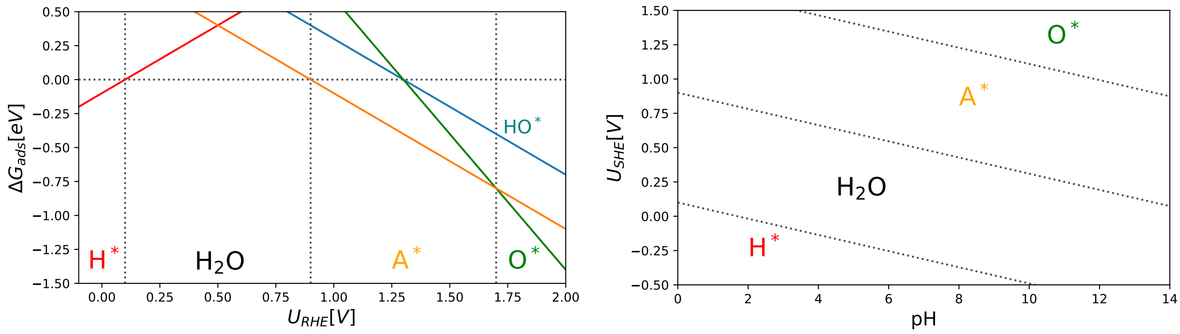

(a) **(b)**

Figure 4: **a)** Example of a phase diagram using fictional data points. The lowest line determines the most stable surface intermediate at a given electrode potential. Vertical lines signify the points of change for the surface. The slope of each intermediate is, as dictated by the CHE, equal to the number of oxidations required to reach that surface intermediate. **b)** Example of a surface Pourbaix diagram using fictional data points. The dotted lines signify a change in surface configuration. Additionally they represent lines of constant potential versus RHE.

in our system in addition to AH oxidation:

Hydrogen adsorption

$$* + \mathrm{H}^+ + e^- \rightleftharpoons \mathrm{H}^* \tag{21}$$

$$\Delta G_{\mathrm{H}^*} = -0.1\ e\mathrm{V} \tag{22}$$

Hydroxide adsorption:

$$* + \mathrm{H}_2 O \rightleftharpoons \mathrm{HO}^* + \mathrm{H}^+ + e^- \tag{23}$$

$$\Delta G_{\mathrm{HO}^*} = 1.3\ e\mathrm{V} \tag{24}$$

Oxygen adsorption:

$$* + \mathrm{H}_2\mathrm{O} \rightleftharpoons \mathrm{O}^* + 2(\mathrm{H}^+ + e^-) \tag{25}$$

$$\Delta G_{\mathrm{O}^*} = 2.6\ e\mathrm{V} \tag{26}$$

We can now plot a phase diagram of the free energy of reaction for the above intermediates (fig. 4a). The phase diagram shows which surface intermediate is the most stable at a given electrode potential, as well as when the most stable intermediate changes. The plot tells us that below 0.1 V versus the RHE hydrogen is stable on the surface. Between 0.1 V and 0.9 V none of the above intermediates are stable. From 0.9 V to 1.7 V A^* is the most stable intermediate and anywhere above that oxygen takes the cake. A purely thermodynamic view would expect the most stable intermediate to dominate the surface at a given potential.

If we are only interested in the most stable surface intermediate, we can exclude plotting the free energy lines, and simply plot the points of change. We can also split up the U$_{RHE}$ into an SHE term and a pH term. This way we can construct a surface Pourbaix diagram that has demarcated areas of stability for the surface intermediates modelled [29][30]. For example, to find the border between no intermediate and adsorbed hydrogen you equate the energy terms for these two surface states to determine where they cross:

$$\Delta G_{\mathrm{H}^*} = 0 \tag{27}$$

$$-0.1\ e\mathrm{V} + eU_{RHE} = 0 \tag{28}$$

$$-0.1\ e\mathrm{V} + e(U_{SHE} + 0.059\mathrm{pH}/e) = 0 \tag{29}$$

$$U_{SHE} = 0.1\mathrm{V} - 0.059V\mathrm{pH} \tag{30}$$

If you do this for all neighbouring surface states you get the Pourbaix diagram presented in fig. 4b. This tool allows the prediction of surface structure from pH and electrode potential. Since neighbouring surface configurations differ by single counts of concerted proton-electron transfers, the lines of the plot also represent lines of constant RHE potential.

In many ways every tool I have presented in this chapter is a variation of the phase diagram; the drawing of a straight line to determine what potential makes a surface structure stable. The phase diagram can thus be seen as the embodiment of the CHE, the clockwork behind the scenes. It therefore also illustrates the issues with this computational approach. The CHE can only calculate the stability of the structures you feed it. What we would really like is a mapping that takes a potential, a surface and an electrolyte and spits out the surface. This is effectively the opposite of what we actually do, which is (educated) guessing of surface structures, followed by calculating when they could appear. We are therefore severely limited by our intuition and idea generation, and might miss the most stable surface configurations.

3 Mechanistic complexity of the Oxygen Evolution Reaction

When it comes to modelling a catalyzed reaction like the OER, the very first challenge is how to model the reaction pathway, as this directly informs the types of surface states that we calculate. This is a very important step of the modelling process, as it directly correlates to the activity of the catalyst. In this way the catalyst is not mechanism agnostic. Modelling a catalyst using a mismatched reaction pathway can lead to discrepancies between theory and experimental work. Throughout this chapter the importance of this decision will be illustrated, ending with the specific and relevant case of RuO_2.

3.1 Overview of reaction mechanisms

The exact OER reaction mechanism is a topic of much debate, with quite the list of proposed mechanisms [31]. Despite the sheer amount of reaction mechanisms that could be expected to occur on the surface, a 4-step single site concerted proton electron transfer reaction has been widely successful in reproducing the experimental trends of oxides [21, 22]:

$$* + \mathrm{H_2O} \rightleftharpoons \mathrm{HO}^* + \mathrm{H}^+ + e^- \tag{31}$$

$$\mathrm{HO}^* \rightleftharpoons \mathrm{O}^* + \mathrm{H}^+ + e^- \tag{32}$$

$$\mathrm{O}^* + \mathrm{H_2O} \rightleftharpoons \mathrm{HOO}^* + \mathrm{H}^+ + e^- \tag{33}$$

$$\mathrm{HOO}^* \rightleftharpoons \mathrm{O_2} + * + \mathrm{H}^+ + e^- \tag{34}$$

This reaction type with surface adsorption, followed by reaction between liquid and surface intermediate, followed by product desorption, is sometimes called an Eley-Rideal mechanism due to the similarities [32]. Sometimes it is also denoted a Volmer-Heyrovsky mechanism, due to the electrochemical surface adsorption step (Volmer step) followed by the liquid-intermediate reaction step (Heyrovsky step).

A second proposed reaction mechanism is a so-called Langmuir-Hinshelwood reaction, with multiple surface adsorptions, surface recombination and desorption:

$$2\mathrm{O}^* \rightarrow \mathrm{O_2} + * \tag{35}$$

This reaction is sometimes also denoted a Volmer-Tafel reaction pathway, with surface recombination and desorption being the Tafel step. It is often discounted due to expectations of a large activation barrier in OER [27].

A third reaction mechanism mirrors that of the above Eley-Rideal mechanism, except that a lattice oxygen near the active site serves as a proton acceptor in the water-splitting steps (eqs. (31) and (33)) [33, 34]. When this was first proposed it was specifically for the case of ruthenium dioxide with Co or Ni dopants near the acceptor oxygen.

$$H_2O + * + O^*_A \rightarrow O^* + HO^*_A + H^+ + e^- \tag{36}$$

Here O^*_A designates the proton acceptor oxygen.

The final reaction mechanism that I will introduce now is the Mars-van Krevelen (MvK) mechanism, also called lattice oxygen exchange or lattice oxygen evolution reaction (LOER). This is less of a well-defined reaction pathway, and instead more of an experimental observation that you can have oxygen in the product stemming from the oxide catalyst [35, 36]. This is not to be confused with the chemical dissolution of the lattice, even though the two can be seen as connected [37]. In Mars-van Krevelen, reactant water interacts with oxygen in the lattice, evolving oxygen molecules that are a combination of lattice and electrolyte oxygen atoms. Water from the electrolyte then reacts with the vacant oxygen lattice site left behind to resaturate the surface.

3.2 OER energetics and volcano plots

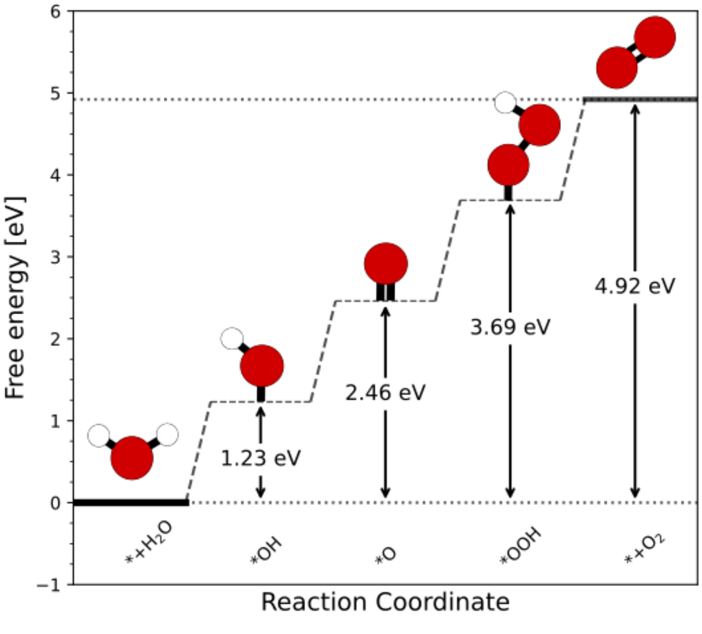

Figure 5: Free energy diagram for ideal case of the oxygen evolution reaction. A schematic ball-and-stick representation is used for the OER intermediates along the reaction pathway eqs. (31) to (34). With each coupled proton-electron step requiring 1.23 eV, no reaction step becomes the sole PDS. Reproduced from [11].

Define the energy steps along the single site Eley-Rideal style reaction pathway (eqs. (31) to (34)) as ΔG_1 through ΔG_4:

$$\Delta G_1 = \Delta G_{HO^*} \tag{37}$$

$$\Delta G_2 = \Delta G_{\mathrm{O}^*} - \Delta G_{\mathrm{HO}^*} \tag{38}$$

$$\Delta G_3 = \Delta G_{\mathrm{HOO}^*} - \Delta G_{\mathrm{O}^*} \tag{39}$$

$$\Delta G_4 = 4.92\ e\mathrm{V} - \Delta G_{\mathrm{HOO}^*} \tag{40}$$

The sum of these reaction steps has to be the 4.92 eV required for oxygen evolution:

$$\Delta G_1 + \Delta G_2 + \Delta G_3 + \Delta G_4 = 4.92\ e\mathrm{V} \tag{41}$$

A perfect catalyst is one where every reaction step is of size $4.92\ e\mathrm{V}/4 = 1.23\ e\mathrm{V}$. This would be a catalyst that catalyzes the OER as well as the reverse, the oxygen reduction reaction (ORR), at no overpotential. In an ideal world we would be able to independently tune the energy of individual reaction steps to obtain this ideal catalyst. Unfortunately the energy steps are interconnected through the aptly named scaling relations [38], that is, relationships that seem to hold across any surface. For the OER these scaling relations put two additional constraints on the reaction step sizes. The first constraint is that the size of the first reaction step is approximately equal to the size of the second reaction step:

$$\Delta G_{\mathrm{O}^*} = 2\Delta G_{\mathrm{HO}^*} \tag{42}$$

$$\Delta G_1 = \Delta G_2 \tag{43}$$

This can be rationalized by the idea that the oxygen bond strength should be twice that of the bound hydroxide species due to having two surface bonds, rather than one. The second scaling relation is that the energy gap between the HO* intermediate and the HOO* intermediate is 3.2 eV.

$$\Delta G_{\mathrm{HOO}^*} = \Delta G_{\mathrm{HO}^*} + 3.2\ e\mathrm{V} \tag{44}$$

This constraint constitutes a deal-breaker regarding finding an ideal catalyst, as it forces the optimal PDS to be $3.2\ e\mathrm{V}/2 = 1.6\ e\mathrm{V}$. The perfect catalyst following this reaction mechanism would therefore have an overpotential of $\eta_{OER} = 1.6\mathrm{V} - 1.23\mathrm{V} = 0.37$ V. The scaling relations are the primary reason that technological development in this field is slow. They have proven to be present and robust in computational results across wide varieties of surfaces and methods [39]. Breaking them have been the target for much research since they were first discovered. Yet a decade later, no breakthrough has been made. Coupled with the lack of standardization in electrochemical experimental work [40], the field is forced to consider new approaches to OER catalyst design. The scaling relations make it unlikely that any two-dimensional surface following the conventional Eley-Rideal single site mechanism will be efficient. Thus a scaling-relation breaking catalyst would either employ a different pathway, or in some way include the third dimension to stabilize specific intermediates [41]. Additionally, it has to be noted that breaking the scaling relations for the sake of breaking them does not guarantee an enhanced catalyst [42, 43]. Rather, the break is only beneficial if it pushes the OER reaction steps towards equal size.

Rutile RuO_2 as an OER catalyst

Take now the rutile $RuO_2(110)$ surface as presented in fig. 6. The rutile (110) surface is usually split into two different types of exposed sites. The first is the so called coordinatively unsaturated sites (CUS), which represents sites of undercoordination compared to the rest of the bulk. This type of site is generally believed to be an OER active site [22]. The second site is the bridge site, where metal atoms are fully coordinated, connected by "bridging" oxygen atoms.

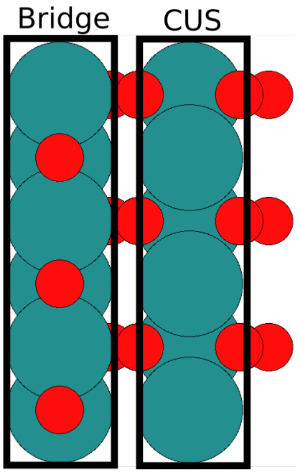

Figure 6: Rutile (110) surface with CUS and bridge sites indicated. Reproduced from [11]).

RuO_2 is long known for being a great OER catalyst [7], and is of central importance to this thesis. If DFT is employed to calculate the energetics of the OER on a single CUS site, you produce a free energy diagram like the one in fig. 7. Notice how fig. 7a illustrates the scaling relations, with the first reaction step ($* \rightarrow HO^*$) being approximately the size of the second, as well as the sum of the second and third step being approximately 3.2 eV. An observant reader might notice that the PDS is 2.16 eV as shown in fig. 7b. This result does not match the experimental reality of RuO_2 being an active catalyst.

Even though the scaling relations guarantee an overpotential for the reaction, the good news is that they solve our struggles with the descriptor based approach to a Sabatier-style analysis. With three equations (eq. (41), eq. (43), eq. (44)) for four variables (ΔG_1, ΔG_2, ΔG_3, ΔG_4) we can choose one as a descriptor. Theoretically the decision seems arbitrary. But since reality never plays nice, the choice should incorporate what we deem

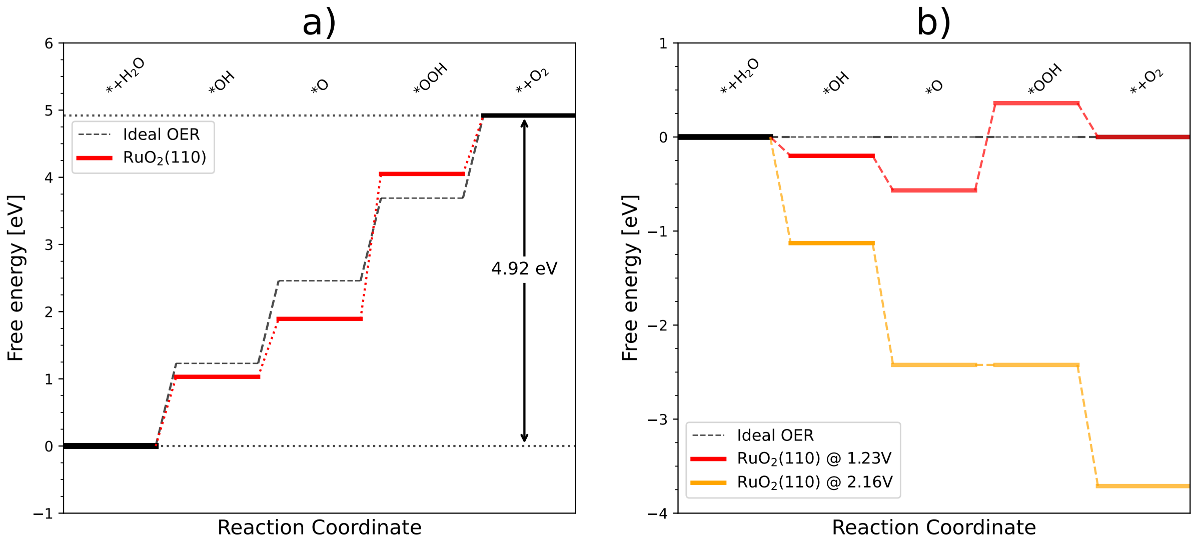

Figure 7: Free energy diagram for the Eley-Rideal single site mechanism of OER on RuO_2. **a)** The case of no applied potential. **b)** At electrode potentials equal to the equilibrium potential as well as the PDS of 2.16 V. Reproduced with minor modifications from [11].

the most important intermediates. For this reason, ΔG_2 is a good choice, as it requires calculating the binding energy of both HO^* as well as O^*. These two intermediates provide the strong double bond of the oxygen, as well as including, indirectly, scaling relation eq. (44). This descriptor thus provides the most important aspects of being a good OER descriptor for metal oxide catalysts [44]. We can now write up the reaction steps ΔG_1, ΔG_3, ΔG_4 as functions of ΔG_2. We already have the first of such functions from eq. (43). As for ΔG_3:

$$\begin{aligned}\Delta G_3(\Delta G_2) &= \Delta G_{\mathrm{HOO}^*} - \Delta G_{\mathrm{O}^*} \\ &= (\Delta G_{\mathrm{HO}^*} + 3.2\ e\mathrm{V}) - (2\Delta G_{\mathrm{HO}^*}) \\ &= 3.2\ e\mathrm{V} - \Delta G_{\mathrm{HO}^*} \\ &= 3.2\ e\mathrm{V} - \Delta G_2 \end{aligned} \tag{45}$$

And finally ΔG_4:

$$\begin{aligned}\Delta G_4(\Delta G_2) &= 4.92\ e\mathrm{V} - (3.2\ e\mathrm{V} + \Delta G_1) \\ &= 1.72\ e\mathrm{V} - \Delta G_2 \end{aligned} \tag{46}$$

The resulting volcano plot, using only a single descriptor for bond strength, is presented in fig. 8. This plot showcases why the ideal catalyst for the OER and ORR is currently but

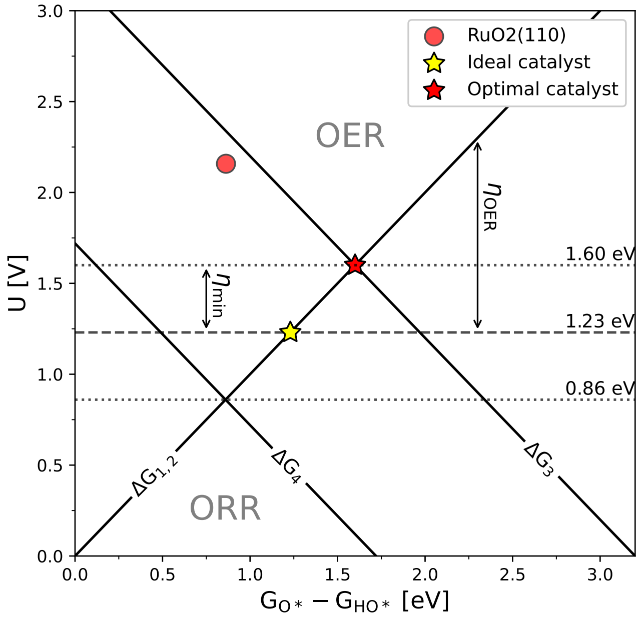

Figure 8: The OER and ORR activity volcanoes. A point is plotted for the ideal and optimal OER catalysts, as well as $RuO_2(110)$ as computed by DFT. OER follows the top line at any point, whereas ORR follows the bottom line. The overpotential for the OER, η_{OER}, is visualized as the distance from the volcano to the ideal electrode potential of 1.23V. This distance is the smallest at the apex of the volcano (η_{min}). The figure is reproduced with minor modifications from [44].

a ghost. The OER volcano is created by the top line at any point, i.e. a combination of ΔG_1 and ΔG_3. This can be understood as either being on the weak binding side, limited by the formation of bonds or being on the strong binding side, limited by breaking the double bond of O^*. This volcano does not allow a catalyst to reach the ideal state, and visually illustrates where the minimum overpotential is derived from. Again the RuO_2 point is far out on the strong binding side of the volcano, in no way representing the real catalyst. Were it not for experimental work we wouldn't even know that it is quite the good catalyst. So what exactly is the issue?

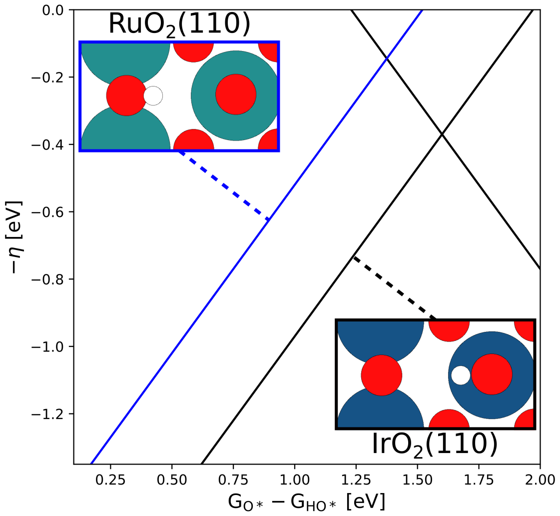

Reproduced from [45] with permission from the PCCP Owner Societies.

3.3 Article 1: Lifting the discrepancy between experimental results and the theoretical predictions for the catalytic activity of RuO$_2$(110) towards Oxygen Evolution Reaction

This work was motivated by the aforementioned apparent inability of calculation to predict the high activity of RuO$_2$ as an OER catalyst. Before this work, the main perspective was that the discrepancy was due to computational artefacts. For example, Kiejna et al. argue that DFT specifically has issues with oxygen binding on ruthenium [46]. A study by Briquet et al. further concluded that the issue seems to persist across DFT implementations, and that oxygen binding is consistently too strong compared to the other matching OER intermediates [47]. In the present work, we argue that it is not a computational artefact of DFT, but rather due to erroneous modelling. That is, the predominant OER reaction pathway employed by ruthenia differs from most other oxides by preferring the pathway of eq. (36) [33]. This reaction pathway changes the OH-OOH scaling relation and creates a new activity volcano, allowing better catalysts [44]. The idea is cooperated by experimental evidence from Rao et al. [48], who have observed an OO* species on the surface, as well as Kuo et al. [49][50], who showed that RuO$_2$ systematically binds O* stronger than IrO$_2$ when compared to the matching HO* binding energy. Finally, we show that employing the new pathway moves RuO$_2$(110) away from the theoretical ΔG_{HO^*} vs ΔG_{O^*} trendline produced by Briquet et al. by varying DFT implementation [47], and towards the experimental trendline, produced by Kuo et al. by varying pH [50].

Lifting the discrepancy between experimental results and the theoretical predictions for the catalytic activity of $RuO_2(110)$ towards Oxygen Evolution Reaction

Spyridon Divanis, Adrian Malthe Frandsen, Tugce Kutlusoy, Jan Rossmeisl

Article reproduced from [45] with permission from the PCCP Owner Societies.

Article available at DOI:

https://doi.org/10.1039/D1CP02999A

PCCP

ROYAL SOCIETY OF CHEMISTRY

COMMUNICATION

View Article Online
View Journal | View Issue

Check for updates

Cite this: *Phys. Chem. Chem. Phys.*, 2021, **23**, 19141

Received 1st July 2021,
Accepted 19th August 2021

DOI: 10.1039/d1cp02999a

rsc.li/pccp

Lifting the discrepancy between experimental results and the theoretical predictions for the catalytic activity of RuO_2(110) towards oxygen evolution reaction

Spyridon Divanis, Adrian Malthe Frandsen,* Tugce Kutlusoy and Jan Rossmeisl

Developing new efficient catalyst materials for the oxygen evolution reaction (OER) is essential for widespread proton exchange membrane water electrolyzer use. Both RuO_2(110) and IrO_2(110) have been shown to be highly active OER catalysts, however DFT predictions have been unable to explain the high activity of RuO_2. We propose that this discrepancy is due to RuO_2 utilizing a different reaction pathway, as compared to the conventional IrO_2 pathway. This hypothesis is supported by comparisons between experimental data, DFT data and the proposed reaction model.

Introduction

As part of a transition to a future sustainable economy, there is a need for sustainable fuel and energy storage. Hydrogen gas is an ideal candidate for such a fuel and storage compound, as it can be readily produced by the electrolysis of water.[1] Furthermore, the hydrogen is completely sustainable if the source of electricity is renewable.[2] Currently, the major challenge facing widespread electrolyzer use is the sluggish kinetics of the Oxygen Evolution Reaction (OER) at the anode,[3] fundamentally limited by the universal scaling relations.[4,5] Further development of the water electrolyzer thus requires finding efficient and practical catalysts to facilitate the OER. There are three types of water electrolyzers: alkaline water electrolyzers, proton exchange membrane (PEM) water electrolyzers and solid oxide water electrolyzers.[6] Of these three the alkaline water electrolyzer is the most mature and commercialized. Yet PEM technology has many advantages compared to the alkaline electrolyzer. Some examples include a much higher current density, purer gas, a smaller size for the same power and even the ability to operate at high pressure.[6,7] Currently the best candidates for PEM electrolyzer anode material are IrO_2 and RuO_2, as these are both stable and active.[8–13] Both iridium and ruthenium are however scarce materials and thus expensive.[14] It is therefore unrealistic to expect that these catalysts can be used on an industrial scale that would have an impact on society.[1,15] Due to the high catalytic performance of IrO_2 and RuO_2,[9] a deeper understanding of how these catalysts interact with water could greatly improve the search for and development of new efficient OER catalysts.[16] Current theory and computational DFT models form a relatively accurate description of the experimental behaviour of IrO_2.[9,17,18] However, for the case of RuO_2 there is a glaring discrepancy between theoretical predictions and experimental results.[18–20] This suggests that either the current reaction model is wrong in the case of RuO_2 or the under-evaluation is due to a computational artefact. In this work we propose that the discrepancy is due to RuO_2 utilizing an alternate reaction pathway for oxygen evolution as compared to IrO_2. We therefore argue that it is not due to a computational artefact.

Results-discussion

The conventional pathway describing the interaction between water molecules and the surface of an electrocatalyst was suggested in 2004.[21] During this reaction pathway three intermediates are produced *via* four electron–proton pair exchanges between the anode and the electrolyte, presented in the following reactions:

$$H_2O + * \rightarrow HO* + H^+ + e^- \quad (1)$$

$$HO* \rightarrow O* + H^+ + e^- \quad (2)$$

$$H_2O + O* \rightarrow HOO* + H^+ + e^- \quad (3)$$

$$HOO* \rightarrow * + O_2 + H^+ + e^- \quad (4)$$

where * indicates an active site of the surface and HO*, O*, HOO* the adsorbed intermediates on that particular site. The above reaction path describes the oxygen evolution reaction taking place in an acidic environment but it can also be used

---

Center for High Entropy Alloy Catalysis, Department of Chemistry, University of Copenhagen, Denmark. E-mail: amf@chem.ku.dk

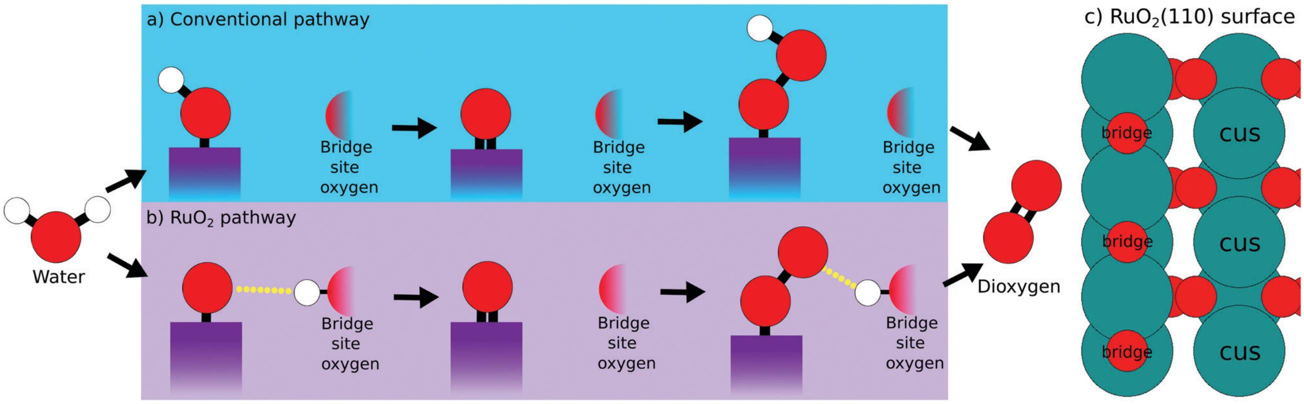

Fig. 1 Illustration of two oxygen evolution reaction pathways. Each step is accompanied with the exchange of a proton–electron pair between the electrolyte and the catalyst surface. (a) The conventional OER path. (b) The proposed reaction mechanism for OER on RuO_2 surfaces. (c) Illustration of the relevant $RuO_2(110)$ surface sites.

for the thermodynamic description of the procedure happening in alkaline environment.[21,22]

A schematic representation of the conventional OER reaction path is depicted in Fig. 1a, while the RuO_2 surface sites are illustrated in Fig. 1c. First, water approaches the surface and the first intermediate HO* is created. Second, the oxygen forms another bond to the surface losing the remaining proton as shown in eqn (2). Third, a water molecule binds to the surface-bound oxygen, dropping a proton in the process. Simultaneously the double bond of O* breaks, creating the third intermediate HOO*. The fourth and last step, happens while the oxygen atoms bond with each other, breaking their bonds with the surface and the hydrogen respectively. This reaction mechanism succeeds to accurately describe the trends of catalytic activity for the majority of the metal oxides. For example the per site DFT activity of IrO_2 places IrO_2 among the best catalysts, in agreement with the experimental observations concerning the performance of the material either in the nanoparticle or the single crystal form.[4,9,17,23]

DFT calculations following this model have however been unable to explain the high experimental activity of RuO2.[18–20] Previous studies have shown that the usage of a dopant at the bridge site of RuO_2 makes the bridge oxygen more eager to interact with the proton of the intermediates.[24,25] We propose that RuO_2 follows such a mechanism without the usage of a dopant, as illustrated in the schematic representation Fig. 1b. This RuO_2 pathway is very reminiscent of the conventional pathway, differing only in steps one and three. Here, instead of the proton being directly bound to the adsorbed intermediate, the proton has migrated to the bridge site oxygen. This complex is stabilized by a weak interaction between this bridge-bound proton and the intermediate (indicated by a yellow dotted line). This hypothesis is supported by the experimental works of Rao *et al.*, who identified a –OO species at high potentials.[17,26] This –OO species is the experimental equivalent of the third intermediate of the RuO_2 pathway depicted in Fig. 1b.

The different way that the first and third intermediates are adsorbed on the surface, has an effect on their binding energy and thereby on the overall activity. The energy interdependency of the HO* and HOO* intermediates thus changes from $\approx$3.2 eV, as dictated by the universal scaling relations,[4,5] to $\approx$2.7 eV, a value that is closer to the ideal value of 2.46 eV. This relation is depicted in the activity volcano of Fig. 2 by the blue trend line. The activity volcano supports our hypothesis, as the DFT data point corresponding to RuO_2 following pathway Fig. 1b (blue pentagon), holds a lower overpotential compared to the data point corresponding to the conventional pathway (blue circle). This places it right on top of the blue trend line. An observation that is strengthening our analysis, is that the blue trend line is followed by experimental data produced in the work of Suntivich *et al.*[27] In their experiments, $RuO_2(110)$ surfaces were synthesized and their electrochemical response in different pH is recorded. Furthermore, they assign the first and second pre-oxidation peaks observed at the cyclic voltammetries, as the HO* and O* intermediates respectively. The experimental HO* energies serve the role of the descriptor for the experimental data at the activity volcano in the diagram (Fig. 2). The red triangles corresponding to IrO_2, reproduced from another work of Suntivich *et al.*,[28] tend as an ensemble to be placed closer towards the strong binding side of the conventional activity volcano. This is an indication that IrO_2 follows the conventional reaction pathway. The RuO_2 experimental data points are however spread. The two most active data points, corresponding to pH 13 (the left-most point) and pH 1 (the right-most point), are placed right on top of the blue trend-line together with the theoretical prediction for pathway Fig. 1b. In contrast, those corresponding to neutral, weakly acidic and weakly alkaline electrolytes are placed closer to the conventional activity volcano. This V-shaped activity trend has been attributed to a dependence of the HOO* formation energy on pH in tandem with the fact that there is a clear pathway to HOO* formation (from O*) in both high and low pH.[27] Furthermore, recent studies have suggested that the activity at high pH is mediated by cations.[29]

In Fig. 3 the scaling relations between HO* and O* intermediates on the cus site are depicted for both experimental and

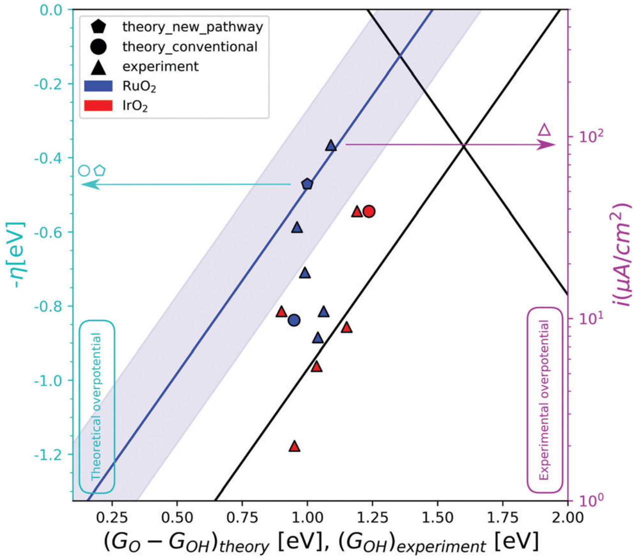

Fig. 2 The OER activity volcano. The red data points correspond to IrO_2 and the blue ones to RuO_2. The triangles represent the experimental data in varying pH conditions,[27,28] while the circle and the pentagon are theoretical data for the conventional and the RuO_2 pathway respectively. The blue trend line corresponds to the strong binding side of the volcano if the RuO_2 pathway is followed. The blue shaded area around the blue trend line, is the DFT error of ±0.2 eV. The left y-axis (cyan) presents the theoretical overpotential and the right y-axis (magenta) presents the experimental overpotential, as the logarithm on the current is what you would expect from the Butler–Volmer equation to compare with potential. As we can only hope to compare trends, and not absolute numbers, the theoretical and experimental overpotentials are calibrated by overlapping the theoretical and experimental overpotential for IrO_2(110). We cannot expect the scale of changes to be the same for calculations and experiments as the predicted differences are often larger than the measured. This figure is therefore two different figures overlapped for the comparison of trends. This also means that the two y-axes can be scaled and translated relative to each other. Two different descriptors with the same scale are used on the x-axis. G_O–G_{HO} and G_{HO} for the theoretical and the experimental data respectively.

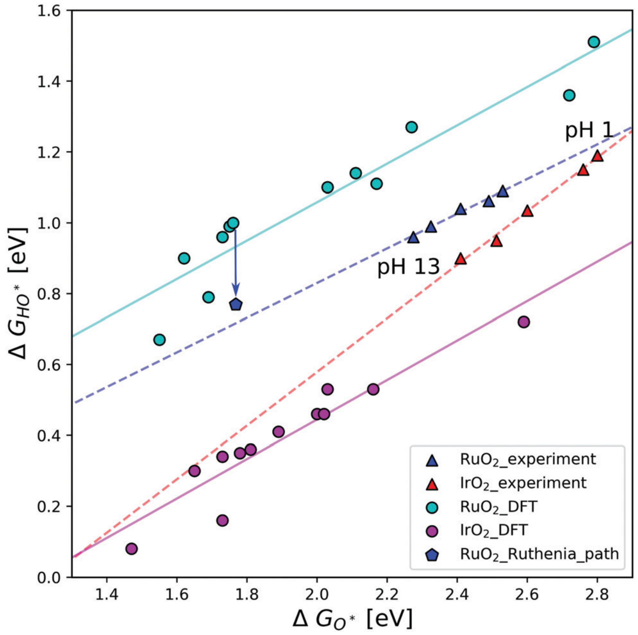

Fig. 3 Scaling relation of HO* binding energies against O* on the cus site for IrO_2 and RuO_2(110) surfaces. The circles correspond to DFT data following different DFT implementations as reproduced from Federico Calle-Vallejo *et al.*[19] In contrast, the triangles correspond to experimental data in varying electrolyte conditions.[27,28] Each of these data sets have their own corresponding trend-line. The blue pentagon represents RuO_2 DFT data following pathway Fig. 1b, and the blue arrow represents the difference in ΔG_{HO^*} as a result of following this pathway. This indicated difference is the same size as the difference between the experimental and DFT trend-lines for RuO_2.

theoretical results. The calculated data subtracted from the work of Federico Calle-Vallejo *et al.*,[19] were produced by DFT calculations on (110) surfaces of IrO_2 and RuO_2, using different implementations of DFT. In this figure, the experimental points relating to the aforementioned V-shaped activity pattern constitute a clear trend-line. This hints at them following the same pathway, even though their activity dips at neutral pH, and suggests that the activity dip might be mechanistic in nature.

It is the relative strong binding of the oxygen intermediate, which makes the calculated activity of RuO_2 smaller than IrO_2. Whereas the binding of HO* and HOO* on the RuO_2 cus site is similar, the O* binding is much stronger than that on IrO_2. This could be an artefact of the DFT calculations, however, it is seen to hold across DFT implementations. The binding energies vary between the different methods, but the difference between HO* and O* binding is close to constant. Previous experimental studies also show that RuO_2 binds oxygen stronger than IrO_2 for the same HO* binding,[27] even if the difference is smaller than that found in the DFT data. In contrast to the DFT data, differences in experimental data is due to varying electrolyte pH. As previously mentioned, the experiments measure the potentials for the first and second oxidation peaks, those are normally assumed to be related to the HO* and O* intermediates on the cus site. However, it could just as well be related to the reaction path Fig. 1b. The stronger the relative O* binding on the cus site, the more likely reaction (1) becomes, as the then relatively unstable HO* intermediate is avoided. Doing a DFT calculation following the RuO_2 pathway creates the point represented by a blue pentagon. This point is placed towards a stronger binding of HO*, and thus comes very close to the experimental trend-line. As points corresponding to different DFT implementations could lie anywhere on the teal trend-line, it is fair to assume that the calculated pentagon could lie anywhere on the experimental trend-line, as dependent on the specific DFT implementation. It therefore seems that pathway Fig. 1b accurately describes the experimental trend.

Computational methods

Density functional theory calculations were done using Grid-based Projector Augment Wave (GPAW),[30,31] assisted by the Atomic Simulation Environment (ASE)[32] interface. Using the generalized gradient approximation (GGA), the BEEF-vdW functional[33] expressed exchange and correlation. This functional was chosen specifically, as it gives a better description of the long range interactions, compared to the initially chosen RPBE.[34] RPBE provides trustworthy results for strong interacting chemical complexes (chemi-adsorption of a molecule on a surface), but it is not as efficient as BEEF-vdW in describing long range interactions. In this particular case the usage of RPBE, placed the blue trend-line of Fig. 2 much closer to the strong side of the conventional volcano. This result differentiates the interpretation of the phenomena and thus the conclusions of the study. The IrO_2 and $RuO_2(110)$ surfaces consist of four atomic layers where the two bottom layers were fixed in their initial position, as to mimic the bulk of the corresponding material. The top layers were free to converge to their minimum electronic energy positions. In the x and y directions the structures were replicated by 1 and 3 times respectively. The sampling of the Brillouin zone was done with a k-point mesh of (3, 2, 1) and the calculations were conducted with a grid spacing of 0.18 Å. Above and below the structures a vacuum of 15 Å was introduced to avoid unintended interactions between the slab and itself. The structures were relaxed until the total forces in the system were below 0.05 eV $Å^{-1}$.

Conclusion

In this work we are studying the discrepancy between DFT and experimental results, regarding the oxygen evolving reactivity of RuO_2. We propose that the reaction pathway for electrochemical water oxidation on $RuO_2(110)$ surfaces, at least in acidic conditions, is slightly different from the reaction path on IrO_2. In particular, the differences are located at the first and third intermediates, where the protons of HO* and HOO* are migrating towards the bridge oxygen surface. The energy interdependency of HO* and HOO* is 2.7 eV for the RuO_2 pathway, and is much closer to the ideal difference of 2.46 eV. As a consequence the DFT activity is much higher than the one produced by the conventional mechanism and thus the structure is placed closer to the apex of the activity volcano. Furthermore the new placement of $RuO_2(110)$ on the activity volcano, is at the same region of the RuO_2 experimental results for highly acidic and highly alkaline electrolytes. By using the conventional pathway we have a very weak interaction of HO* with the surface's cus site. On the other hand, using the RuO_2 pathway widens the energy difference between HO* and O*, placing this DFT calculation closer to experimental trend-lines. This theoretical–experimental agreement, indicates that the RuO_2 mechanism is generally followed. It is to be expected that this trend extends to other active RuO_2 facets, as it is the strong binding of the O* intermediate that makes the conventional path too difficult. Given that other facets share this strong oxygen binding, the alternate mechanism would likely apply.

Conflicts of interest

There are no conflicts to declare.

Acknowledgements

This project was supported by European Union's Horizon 2020 research and innovation programme under the Marie Skłodowska–Curie Innovative Training Network (ITN-ELCOREL-722614), the Villum Foundation to the Villum Center for the Science of Sustainable Fuels and Chemicals (#9455) and The Center of Excellence program. The Center of Excellence is funded by the Danish National Research Foundation DNRF 149.

References

1 H. B. Gray, *Nat. Chem.*, 2009, **1**, 7.
2 Z. Yan, J. L. Hitt, J. A. Turner and T. E. Mallouk, *Proc. Natl. Acad. Sci. U. S. A.*, 2020, **117**, 12558–12563.
3 J. Durst, C. Simon, F. Hasché and H. A. Gasteiger, *J. Electrochem. Soc.*, 2014, **162**, F190–F203.
4 I. C. Man, H.-Y. Su, F. Calle-Vallejo, H. A. Hansen, J. I. Martínez, N. G. Inoglu, J. Kitchin, T. F. Jaramillo, J. K. Nørskov and J. Rossmeisl, *ChemCatChem*, 2011, **3**, 1159–1165.
5 S. Divanis, T. Kutlusoy, I. M. Ingmer Boye, I. C. Man and J. Rossmeisl, *Chem. Sci.*, 2020, **11**, 2943–2950.
6 Q. Feng, X. Yuan, G. Liu, B. Wei, Z. Zhang, H. Li and H. Wang, *J. Power Sources*, 2017, **366**, 33–55.
7 G. Matute, J. Yusta and L. Correas, *Int. J. Hydrogen Energy*, 2019, **44**, 17431–17442.
8 S. Trasatti, *J. Electroanal. Chem. Interfacial Electrochem.*, 1980, **111**, 125–131.
9 Y. Lee, J. Suntivich, K. J. May, E. E. Perry and Y. Shao-Horn, *J. Phys. Chem. Lett.*, 2012, **3**, 399–404.
10 R. Frydendal, E. A. Paoli, B. P. Knudsen, B. Wickman, P. Malacrida, I. E. L. Stephens and I. Chorkendorff, *ChemElectroChem*, 2014, **1**, 2075–2081.
11 O. Kasian, S. Geiger, T. Li, J.-P. Grote, K. Schweinar, S. Zhang, C. Scheu, D. Raabe, S. Cherevko, B. Gault and K. J. J. Mayrhofer, *Energy Environ. Sci.*, 2019, **12**, 3548–3555.
12 M. Escudero-Escribano, A. F. Pedersen, E. A. Paoli, R. Frydendal, D. Friebel, P. Malacrida, J. Rossmeisl, I. E. L. Stephens and I. Chorkendorff, *J. Phys. Chem. B*, 2018, **122**, 947–955.
13 M. Bernt, A. Siebel and H. A. Gasteiger, *J. Electrochem. Soc.*, 2018, **165**, F305–F314.
14 D. Hageluken and V. den Broeck, *Precious Materials Handbook*, 2012, pp. 10–35.
15 P. C. K. Vesborg and T. F. Jaramillo, *RSC Adv.*, 2012, **2**, 7933–7947.
16 A. Grimaud, A. Demortière, M. Saubanère, W. Dachraoui, M. Duchamp, M.-L. Doublet and J.-M. Tarascon, *Nat. Energy*, 2016, **2**, 16189.
17 R. Rao, M. Kolb and L. E. A. Giordano, *Nat Catal.*, 2020, **3**, 516–525.
18 J. Rossmeisl, Z.-W. Qu, H. Zhu, G.-J. Kroes and J. Nørskov, *J. Electroanal. Chem.*, 2007, **607**, 83–89.
19 L. G. V. Briquet, M. Sarwar, J. Mugo, G. Jones and F. Calle-Vallejo, *ChemCatChem*, 2017, **9**, 1261–1268.
20 Y. Lee, J. Suntivich, K. J. May, E. E. Perry and Y. Shao-Horn, *J. Phys. Chem. Lett.*, 2012, **3**, 399–404.

21 J. K. Nørskov, J. Rossmeisl, A. Logadottir, L. Lindqvist, J. R. Kitchin, T. Bligaard and H. Jónsson, *J. Phys. Chem. B*, 2004, **108**, 17886–17892.

22 J. Rossmeisl, A. Logadottir and J. Nørskov, *Chem. Phys.*, 2005, **319**, 178–184.

23 K. A. Stoerzinger, O. Diaz-Morales, M. Kolb, R. R. Rao, R. Frydendal, L. Qiao, X. R. Wang, N. B. Halck, J. Rossmeisl, H. A. Hansen, T. Vegge, I. E. L. Stephens, M. T. M. Koper and Y. Shao-Horn, *ACS Energy Lett.*, 2017, **2**, 876–881.

24 N. B. Halck, V. Petrykin, P. Krtil and J. Rossmeisl, *Phys. Chem. Chem. Phys.*, 2014, **16**, 13682–13688.

25 M. Busch, N. Halck, U. Kramm, S. Siahrostami, P. Krtil and J. Rossmeisl, *Nano Energy*, 2016, **29**, 126–135.

26 R. R. Rao, M. J. Kolb, N. B. Halck, A. F. Pedersen, A. Mehta, H. You, K. A. Stoerzinger, Z. Feng, H. A. Hansen, H. Zhou, L. Giordano, J. Rossmeisl, T. Vegge, I. Chorkendorff, I. E. L. Stephens and Y. Shao-Horn, *Energy Environ. Sci.*, 2017, **10**, 2626–2637.

27 D.-Y. Kuo, H. Paik, J. Kloppenburg, B. Faeth, K. M. Shen, D. G. Schlom, G. Hautier and J. Suntivich, *J. Am. Chem. Soc.*, 2018, **140**, 17597–17605.

28 D.-Y. Kuo, J. K. Kawasaki, J. N. Nelson, J. Kloppenburg, G. Hautier, K. M. Shen, D. G. Schlom and J. Suntivich, *J. Am. Chem. Soc.*, 2017, **139**, 3473–3479.

29 R. R. Rao, B. Huang, Y. Katayama, J. Hwang, T. Kawaguchi, J. R. Lunger, J. Peng, Y. Zhang, A. Morinaga, H. Zhou, H. You and Y. Shao-Horn, *J. Phys. Chem. C*, 2021, **125**, 8195–8207.

30 J. Enkovaara, C. Rostgaard, J. J. Mortensen, J. Chen, M. Dułak, L. Ferrighi, J. Gavnholt, C. Glinsvad, V. Haikola and H. A. Hansen, *J. Phys.: Condens. Matter*, 2010, **22**, 253202.

31 J. J. Mortensen, L. B. Hansen and K. W. Jacobsen, *Phys. Rev. B: Condens. Matter Mater. Phys.*, 2005, **71**, 035109.

32 A. H. Larsen, J. J. Mortensen, J. Blomqvist, I. E. Castelli, R. Christensen, M. Dułak, J. Friis, M. N. Groves, B. Hammer and C. Hargus, *J. Phys.: Condens. Matter*, 2017, **29**, 273002.

33 J. Wellendorff, K. T. Lundgaard, A. Møgelhøj, V. Petzold, D. D. Landis, J. K. Nørskov, T. Bligaard and K. W. Jacobsen, *Phys. Rev. B: Condens. Matter Mater. Phys.*, 2012, **85**, 235149.

34 B. Hammer, L. B. Hansen and J. K. Nørskov, *Phys. Rev. B: Condens. Matter Mater. Phys.*, 1999, **59**, 7413–7421.

3.4 Is the matter settled?

Since the time of writing the above article, I have been made aware of a third pespective on the origin of the RuO_2 activity discrepancy. Commonly during modelling rutile RuO_2, the system is assumed non-magnetic. However, in 2017 Berlijn et al. found rutile RuO_2 to be anti-ferromagnetic [51]. A recent computational study has shown that employing an anti-ferromagnetic slab and DFT+U reduces the predicted overpotential [52]. This perspective points towards the discrepancy being a mix of modelling errors (due to the anti-ferromagneticity) and computational artefacts (due to the need for DFT+U).

Where does this leave us now? A new perspective on reaction pathway modelling is a solid and simple solution, especially given how well it fits the experimental evidence. Di Liberto et al. did a computational follow-up study to our work using molecular dynamics to look at the role of water on OER intermediates, including the new pathway. One of their results was that water molecules can shuttle the proton to the bridge [53]. Interestingly, this was found to be a one way trip, as the proton did not shuttle back. Once again this illustrates the preference RuO_2 has for this surface configuration.

In theory there are often many ways to arrive at similar results. This is where experimental evidence and results become important, as without such results we cannot distinguish. In this case, it is a perfectly reasonable solution that RuO_2 is both anti-ferromagnetic and employing a different pathway than other oxides. One could attempt to model the system as anti-ferromagnetic, using DFT+U, and employing the new pathway. Only if the new pathway is found to be less stable than the conventional is there then a conflict between the two perspectives.

4 Selectivity Control in Sea-Water Electrolysis

Large scale implementation of water electrolysis plants to fuel a hydrogen economy could put a strain on fresh-water resources. The water source of choice would ideally be the sea, as it provides a practically infinite supply of readily available water, on all currently realistic conceivable scales. The large chloride content in sea-water introduces an issue with the parasitic chlorine evolution reaction (ClER) at the oxygen evolving anode:

$$\mathrm{Cl}^-(aq) \rightleftharpoons \frac{1}{2}\mathrm{Cl}_2 + e^- \tag{47}$$

With the equilibrium potential U_{eq} for this reaction being:

$$U_{eq}(\frac{1}{2}\mathrm{Cl}_2 + e^- \rightleftharpoons \mathrm{Cl}^-(aq))@U_{SHE} = 1.36\mathrm{V} \tag{48}$$

This reaction can be approached computationally in much the same way as the CHE to describe the chemical potential of the electron in reactions involving chloride [29]:

$$\mu(\mathrm{Cl}^-(aq)) - \mu(e^-) = \frac{1}{2}\mu(\mathrm{Cl}_2(g)) - e(U_{SHE} - 1.36V) + k_B T \ln(a_{\mathrm{Cl}^-}) \tag{49}$$

where k_B is the Boltzmann constant and a_{Cl^-} is the activity of the chlorine ions in solution. The equilibrium potential of 1.36 V lies close to the ideal OER potential of 1.23 V. Thus the reactions are largely activated in the same potential range, leading to unwanted gas by-products.

The chlor-alkali industry is interested in the chlorine gas as the primary product, and towards this end the dimensionally stable anode (DSA) has been developed, mostly solving the issue [54]. On the other hand, oxygen evolving catalysts still have issues with the corrosive and toxic chlorine gas. This renders OER in sea-water largely unfeasible. Selectivity between the two gas products has been found to be dependent on factors such as surface stress/strain [55], as well as chemical composition and local structure [56, 57, 58]. Importantly chlorine-selectivity has been found to be positively correlated with LOER tendency in Ru-Ti-O systems [59]. LOER is in turn related to the morphology of the catalyst [60], the chemical composition of the catalyst [61] and electrode potential [59]. Understanding the mechanisms of LOER tendency would therefore provide another lever for the rational design of selective catalysts.

LOER is generally seen in systems that form and stabilize oxygen surface vacancies [62]. On the one hand this can be rationalized as due to the lattice becoming unstable under reaction conditions [37], yet the MvK is conventionally not seen as dissolution of the lattice, even though the two might be linked. The formation of surface vacancies is something that should be screenable in DFT studies. Yet computational studies focused on identifying LOER activity and reaction pathways are mainly isolated to perovskite materials [62].

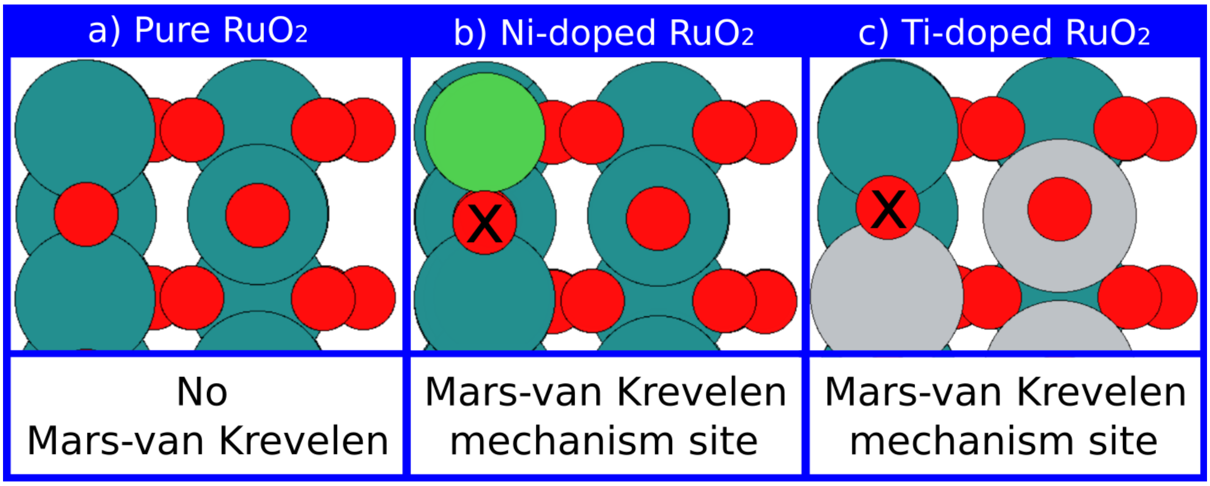

4.1 Article 2: Lattice oxygen evolution in rutile $Ru_{1-x}Ni_xO_2$ electrocatalysts

Motivated by a perceived lack of theoretical MvK/LOER studies, this work aims to introduce a simple screening approach to determining the intrinsic LOER tendency of oxides. Using the example systems of rutile (110) $Ru_{1-x}Ni_xO_2$ and $Ru_{1-x}Ti_xO_2$, the binding energy of top-layer oxygen species is determined while systematically varying local configuration. This allows for identifying oxygen species that significantly weaken their binding energy in the presence of dopants. A full Sabatier-style OER pathway analysis like the one presented in section 3.2 can then be performed for the identified oxygen sites, yielding their activities.

In the case of the Ru-Ni system, it is determined that oxygen bridging between a ruthenium and a nickel atom are evolvable at elevated electrode potentials. To test the validity of the finding, comparison to experimental data is needed. This requires a mapping from nickel content to LOER activity. Towards this end two different surface models are set up as corresponding to the clustering tendency of nickel in this system at low and high nickel content [63]. The first model has nickel clustering together in threes, but never along bridge/cus lines. A small algorithm for this model is developed to construct surfaces with nickel clusters, and then count the number of Ru-Ni bridge sites as a LOER tendency descriptor. The second model for high Ni content clusters nickel along [121] shear planes in the structure. This is modelled as simply setting atoms along such a shear plane to be Ni, ignoring the actual rock-salt motif for simplicity. The concentration is then determined by the distance between two shear planes. The result is compared to presented Differential Electrochemical Mass Spectrometry (DEMS) data for the Ru-Ni-O system finding decent agreement.

As for the Ru-Ti system, the predictable LOER becomes apparent in structures with 3 Ti in the top layer. At 20% Ti content such surface structures would be expected to produce minor lattice oxygen exchange due to the probability of the surface structure forming. Yet experimental evidence from the literature shows high tendency for LOER at this regime [59]. This can likely be attributed to characterized defects in the experimental system, as defects are generally correlated with LOER tendency [60].

Lattice oxygen evolution in rutile $Ru_{1-x}Ni_xO_2$ electrocatalysts

Adrian Malthe Frandsen, Kateřina Minhová Macounová, Jan Rossmeisl, Petr Krtil

Article and supplementary material available at DOI:

https://doi.org/10.1016/j.electacta.2024.144567

Electrochimica Acta 497 (2024) 144567

Contents lists available at ScienceDirect

Electrochimica Acta

journal homepage: www.journals.elsevier.com/electrochimica-acta

Lattice oxygen evolution in rutile $Ru_{1-x}Ni_xO_2$ electrocatalysts

Adrian Malthe Frandsen [a,*], Kateřina Minhová Macounová [b], Jan Rossmeisl [a], Petr Krtil [b]

[a] *Center for High Entropy Alloy Catalysis, Department of Chemistry, University of Copenhagen, Universitetsparken 5, Copenhagen, 2100, Denmark*
[b] *J. Heyrovsky Institute of Physical Chemistry, Dolejškova 2155/3, Prague 8, 182 23, Czech Republic*

ARTICLE INFO

Dataset link: https://nano.ku.dk/english/research/theoretical-electrocatalysis/katladb/loer-runio2/

Keywords:
Lattice oxygen evolution
$Ru_{1-x}Ni_xO_2$
$Ru_{1-x}Ti_xO_2$ theoretical catalysis
Electrolysis
DFT
Surface modeling

ABSTRACT

Efficient predictive tools for oxygen evolution reaction (OER) activity assessment are vital for rational design of anodes for green hydrogen production. Reaction mechanism prediction represents an important pre-requisite for such catalyst design. Even then, lattice oxygen evolution remains understudied and without reliable prediction methods. We propose a computational screening approach using density functional theory to evaluate the lattice oxygen evolution tendency in candidate surfaces. The method is based on a systematic assessment of the adsorption energies of oxygen evolution intermediates on model active sites with varying local structure. The power of the model is shown on model rutile (110) oriented surfaces of (a) RuO_2, (b) $Ru_{1-x}Ni_xO_2$ and (c) $Ru_{1-x}Ti_xO_2$. The model predicts (a) no lattice exchange, (b) lattice exchange at elevated electrode potentials and (c) minor lattice exchange at elevated electrode potentials and high titanium content. While in the case of (a) and (b) the predictions provide sufficiently accurate agreement with experimental data, (c) experimentally deviates from the above prediction by expressing a high tendency to evolve lattice oxygen at high titanium content ($x = 0.20$). This discrepancy can likely be attributed to the presence of structural defects in the prepared material, which are hard to accurately model with the applied methodology.

1. Introduction

The oxygen evolution reaction (OER) belongs to one of the most studied electrochemical reactions in the last decade. This is in large part due to the OER kinetically controlling electrochemical water splitting [1]. Facilitating efficient and scalable electrochemical water splitting would enable accelerated replacement of fossil fuel with green fuel sources generated by renewable electricity.

The OER is confined to oxide-like surfaces, which often re-structure under operando conditions. Experimental development of oxygen evolving catalysts is done separately for acidic water electrolysis [2–4] and alkaline media electrolysis [5–7]. State of the art OER catalysts for acidic electrolysis are based on noble metal oxides such as RuO_2 and IrO_2, the scarcity of which adversely affects large scale deployment of this technology. Alkaline electrolyzers employ more abundant (and affordable) catalysts based on oxides of transition metals such as Ni [8,9].

The catalyst development process is based on so called rational design in which one synthesizes only materials showing prospective activity in theoretical and computational prescreening. This prescreening can be done by computational assessment of the binding energies of OER surface intermediates on candidate surfaces. Such analysis allows for determination of the potential limiting reaction step, and thereby the theoretical overpotential [1,10]. The method is however crucially dependent on the reaction mechanism embedded into the calculation. Reaction mechanism modeling is therefore a central part of the computational approach.

The oxygen evolving process is generally perceived as four one-electron oxidation steps each accompanied by a concomitant proton transfer. Yet the exact mechanism is a complex topic of much debate. A simplified view is that the reaction mechanism in large part follows one of three reaction types [11]. The most common one, which is generally used as a foundation for the computational screening of prospective oxygen evolving catalysts conforms to a Volmer–Heyrovsky type of mechanism and can be described as a sequence of four consecutive concerted one electron/proton transfer reactions as outlined in Eqs. (1)–(4):

$$H_2O + * \rightleftharpoons HO^* + H^+ + e^- \tag{1}$$

$$HO^* \rightleftharpoons O^* + H^+ + e^- \tag{2}$$

$$O^* + H_2O \rightleftharpoons HOO^* + H^+ + e^- \tag{3}$$

$$HOO^* \rightleftharpoons * + O_2(g) + H^+ + e^- \tag{4}$$

---

[*] Corresponding author.
E-mail address: amf@chem.ku.dk (A.M. Frandsen).

https://doi.org/10.1016/j.electacta.2024.144567
Received 20 November 2023; Received in revised form 3 June 2024; Accepted 7 June 2024

This reaction mechanism is analogous to the Eley–Rideal reaction sequence known from heterogeneous catalysis. This single site mechanism evolves oxygen derived solely from water and the model assumes no active involvement of the catalyst's anionic sublattice.

A modification of the conventional Volmer–Heyrovsky sequence yields the Volmer–Tafel mechanism, involving surface recombination of oxo species generated in Eq. (2):

$$2O^* \rightleftharpoons O_2(g) + 2* \tag{5}$$

The occurrence of the Volmer-Tafel sequence is frequently discounted due to the anticipation of a large activation barrier for this type of reaction [12].

An alternative oxygen evolving mechanism which features active involvement of lattice oxygen has been known since the 1980s. The experimental evidence conclusively shows that in many cases (regardless of pH) the produced oxygen molecule may contain at least one oxygen atom originating from the catalysts lattice [13,14]. The nature of this behavior has been most systematically studied in materials intended for alkaline water electrolysis (such as Ni based perovskites) [15]. These materials show an enhancement of the overall oxygen evolving activity if the lattice oxygen activation contributed to the overall oxygen evolution process. This behavior of the Ni-based perovskites was attributed to a stabilization of oxygen surface vacancies which in turn can be affected by the chemical element at the A site of the perovskite structure [14].

A similar type of behavior was also reported for oxides intended as anode materials for water electrolysis in acidic media, i.e. RuO_2 and IrO_2 based catalysts. In this case the literature data show a certain controversy regarding the extent of the lattice oxygen activation to the overall evolution reaction. While the original data on sputtered ruthenium dioxide electrodes indicate a significant contribution of lattice oxygen evolution reaction (LOER) to the overall oxygen evolution [13], more recent data presented on well characterized or even oriented nanocrystalline RuO_2 electrodes reflect low to negligible contribution of LOER for RuO_2 based materials [16,17]. Differential electrochemical mass spectroscopy (DEMS) studies of RuO_2 substitutionally doped with transition metal cations find that LOER tendency is generally increased in such systems compared to the pure system [18]. Additionally, the extent of the lattice oxygen activation increases with electrode potential [19].

While the enhanced lattice oxygen activation for the transition metal substituted ruthenia could be attributed to particular local structure formations triggered by transition metal substitution, the extent of the LOER is usually related to the material's morphology [20]. Low-dimensional sites like crystal edges/vertices may be disproportionally represented at the surface of nanocrystalline electrodes, thereby decreasing the intrinsic stability of the catalyst material.

While the nature of the lattice oxygen activation is not fully understood its occurrence is generally aligned with the ability of the system to form and stabilize surface oxygen vacancies [14,21]. This rationalization of the LOER mechanism should be universal and its occurrence can be tested computationally e.g. by DFT calculations of surface stabilities and construction of Sabatier-type volcano plots [1,22]. Surprisingly, the computational approach towards LOER has, to our knowledge, not yet been extended beyond Ni based perovskites. This paper aims at extending this fundamental computational approach to modeling the behavior of OER catalysts in acidic media — namely of the ruthenium dioxide and substitutionally doped ruthenium dioxide.

The DFT approach is employed as a systematic screening method to identify possible active sites for LOER on rutile $Ru_{1-x}Ni_xO_2(110)$ and $Ru_{1-x}Ti_xO_2(110)$ surfaces. The results are then compared to experimental evidence of local structure arrangements and LOER activity in these materials.

2. Computational methods

The DFT calculations were performed using Grid-based Projector Augment Wave (GPAW) [23,24], assisted by the Atomic Simulation Environment (ASE) [25]. The employed functional was RPBE as it describes strong chemical interactions very well [26]. This makes it a decent choice for the study of oxygen binding energies in and on the rutile surface. The rutile RuO_2 slab was made up of four atomic layers with the bottom two emulating bulk by being positionally constrained. The structure was replicated two times in the y direction to produce the structure shown in Fig. 1. To avoid unwanted self-interaction, a vacuum was introduced above and below the structure. All other structures were created by substitution of atoms in this slab and removal/addition of surface adsorbates. Due to the magnetic properties of nickel, the calculations including nickel were spin polarized. For Brillouin zone sampling, a k-point mesh of (3,2,1) was used. The grid-spacing used for the calculations was 0.20 Å and the relaxation was terminated when the sum of forces in the system went below 0.05 eV $Å^{-1}$. No solvation layer is used for the adsorbates in this work as the solvation energy for OER intermediates on RuO_2 has previously been found to be small [1]. Structures and scripts are available in the electronic supplementary material at link:
https://nano.ku.dk/english/research/theoretical-electrocatalysis/katladb/loer-runio2/

3. Experimental methods

The ruthenium dioxide and Ru–Ni–O samples were prepared by a co-precipitation approach which was in detail described in [27,28]. The synthetic procedures were carried out in solutions with normal isotope composition oxygen suggesting that the prepared materials almost entirely contained ^{16}O isotope.

The electrodes for DEMS were deposited from a water base suspension containing approximately 2 g of the catalyst per liter on a Ti mesh (open area 20%, Goodfellow). The deposition aimed at obtaining the surface coverage of about 1–2 mg/cm^2. The deposited layers were later stabilized by annealing the electrodes for 4 h at 400 °C in air. All electrochemical experiments were carried out in 0.1 M $HClO_4$ dissolved in H218O (98%, Medical Isotopes Inc., USA) in a home-made Kel-F single compartment cells described previously in [29]. The residual ^{16}O fractions before and after electrochemical experiments coincided within the margin of the experimental error and ranged between 0.02 and 0.06. The experiments were done in a three electrode arrangement with Pt auxiliary and an Ag/AgCl (sat. KCl) reference electrode placed outside the cell. All potentials in the paper are quoted in RHE scale. The potential control in the experiments was achieved using PAR 263 A potentiostat. The DEMS measurements were done on an experimental station composed of Prisma TM QMS200 quadrupole mass spectrometer (Balzers) connected to TSU071E turbomolecular drag pumping station (Balzers).

4. Results and discussion

To assess the intrinsic ability of a rutile (110) surface to evolve lattice oxygen, it is useful to calculate oxygen binding energies at the surface. The system is modeled by a computational slab such as the one shown in Fig. 1. Employing DFT one can determine the binding energy of oxygen bound in positions 1 through 9 while varying the local structure by substituting metal cations in positions A through L. Positions 1, 3 and 5 are commonly referred to as the bridge sites in the rutile structure. Oxygen bound here is singly undercoordinated compared to that of the lattice, but is usually considered inactive. Positions 2, 4, 6 are the coordinatively unsaturated sites (CUS). Oxygen bound here are doubly undercoordinated compared to the lattice and considered active. This surface site is generally considered to be an

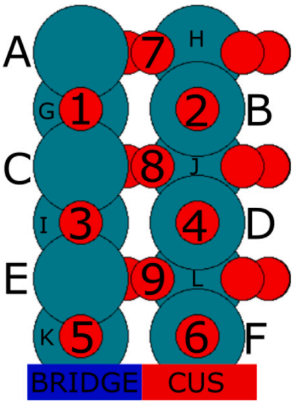

Fig. 1. The rutile $RuO_2(110)$ surface with Ru atoms labeled and oxygen atoms numbered. Oxygens 1, 3, 5 are bound to bridge sites and part of the lattice, whereas oxygens 2, 4 and 6 are CUS site adsorbates. Binding energy of oxygen on the CUS and bridge sites of the pure rutile RuO_2 (110) surface. Teal atoms are ruthenium and red atoms are oxygen.

active site for Volmer–Heyrovsky type single site oxygen evolution on rutile (110) surfaces [1].

The oxygen binding energy (ΔE_O) is calculated as the energy change associated with going from a water molecule and a surface to a hydrogen molecule and a surface with the adsorbed oxygen:

$$\Delta E_O = E_{O*} + E_{H_2} - E_* - E_{H_2O} \tag{6}$$

Here E_{O*}, E_{H_2}, E_*, E_{H_2O} are the DFT energies of the surface slab with the oxygen species, a hydrogen molecule, the surface slab without the oxygen species and a water molecule respectively. The oxygen binding energy can indicate the stability of the bound oxygen, and is thereby a useful indicator of whether it may be expected to be active. In and of itself, screening oxygen binding energies in a surface can only serve as a pointer towards identifying active sites of interest. In this manner, it serves to narrow the scope of the succeeding analysis. Once surface sites of interest have been identified, a thermodynamic analysis of the full catalytic reaction cycle at such sites can be performed, leading to an OER volcano plot of the prospective active sites. This requires calculation of the binding energy of every intermediate along the reaction path. In similar fashion as for oxygen binding in Eq. (6), the DFT binding energies of OH and OOH can be calculated as:

$$\Delta E_{OH} = E_{HO*} + \frac{1}{2}E_{H_2} - E_* - E_{H_2O} \tag{7}$$

$$\Delta E_{OOH} = E_{HOO*} + \frac{3}{2}E_{H_2} - E_* - 2E_{H_2O} \tag{8}$$

The Gibbs free energy of binding can be obtained by the addition of zero-point energy and entropic corrections. In this work, the corrections used mirror those of [30]. Once binding energies have been determined, the potential determining step can be identified from among the reaction steps (1–4). The overpotential η for the reaction is then the size of the potential determining step minus the ideal reaction potential 1.23 V.

This approach does not and cannot predict stability, or any surface restructuring that might occur, under prolonged electrochemical conditions. Additionally, it makes no judgment about the rarity of the active sites investigated. For information regarding the DFT calculations, as well as access to the electronic supplementary material (scripts, data and structures), see the **Computational Methods** section.

Initial analysis of the *pure* (i.e. non-doped) RuO_2 surface is presented in Fig. 2. Since an oxygen intermediate is the second step of conventional four step single site OER mechanism, the ideal catalyst would have the oxygen intermediate binding energy being 4.92 eV/2 = 2.46 eV [31]. With this in mind, the bridge site oxygen binding energy being 0.56 eV indicates that it is strongly bound, and would not be expected to evolve oxygen. Experimentally RuO_2 is a highly active catalyst, with the CUS site being the commonly anticipated active site. Therefore, at first glance you would expect active oxygen in/on the lattice to be bound with a similar binding energy as the CUS-bound oxygen (≈1.89 eV). However, compared to the oxygen binding energy of the ideal catalyst, 1.89 eV is too strongly bound for it to be an efficient catalyst if it is to follow the conventional single site mechanism (similar to iridium oxide).

In the literature there are multiple perspectives on the origin of this activity gap. One perspective is that DFT struggles to accurately represent *O adsorbate binding on ruthenium. This has been discussed by Kiejna et al. [32] and then later echoed by Briquet et al. in the case of the OER intermediates specifically [33]. Briquet et al. determined that the error was specifically related to the adsorption of oxygen and not the other OER intermediates. A second perspective is that the discrepancy is mostly due to the choice of reaction pathway during modeling. Consider the alternate reaction pathway on the surface in which the proton in intermediates *OH and *OOH migrates to the bridge position. This reaction mechanism was first proposed for systems including dopants in the bridge [34,35], but it has since been found by Divanis et al. to alleviate the aforementioned activity gap for pure RuO_2 [36]. A third perspective is that the discrepancy arises due to the common assumption of a non-magnetic system during modeling. Experiments have found RuO_2 to be anti-ferromagnetic [37], and it has since been shown by Liang et al. that by employing an anti-ferromagnetic RuO_2 model system the predicted overpotential decreases [38]. This idea, as with the second perspective, points to modeling errors and not computational artefacts as the main source of the discrepancy. In fact, Divanis et al. argued against it being a computational artefact for two primary reasons [36]: First, the overevaluation of the oxygen binding energy as compared to that of OH seems to be present across DFT implementations (as shown by Briquet et al. [33]). Second, the strong oxygen binding is also observed in experiments, such as those performed by Kuo et al. [39]. For these reasons, this paper includes the above mentioned alternative ruthenium reaction pathway as a possibility during modeling. The anti-ferromagneticity of the RuO_2 is not something that manifested itself in the spin polarized calculations of the Ru–Ni oxides performed in this work. The Ru atoms were found to have mostly negligible magnetic moments after relaxation.

The *pure* rutile surface serves as a reference for binding energies of the oxygen intermediates when one exchanges metal atoms in the lattice. It would generally be expected that active lattice oxygen following a single-site mechanism would be at least somewhat weaker bound than the 1.89 eV presented by the CUS site. It needs to be noted that only this CUS site oxygen is bound weakly enough to be evolvable on the *pure* surface. It is therefore to be expected that this surface does not evolve lattice oxygen. This is in line with the more recent experimental findings in the literature [16,17].

By substituting a single surface ruthenium atom with a nickel atom we get two possible local structures *A* and *B*. Comparing the binding energies of oxygen in these surfaces to those of the pure structure, it is clear that the biggest change is present in structure *A* at position 1. The binding energy of this oxygen has been severely weakened due to the introduction of the neighboring Ni in the bridge. The binding energy of 1.48 eV is still strongly bound compared to the ideal catalyst, however one could imagine this oxygen site becoming an active site for the OER at elevated electrode potentials. Structure *B* is, however, similar to the pure surface, except for the deactivated nickel CUS site.

If one substitutes in two nickel atoms instead, one gets the three structures *AC*, *BC* and *BD*. *AC* and *BD* both present cases in which the nickel has clustered along the bridge/CUS lines, whereas *BC* presents the case where it clusters across from bridge to CUS. Again the structures with nickel in the bridge positions become interesting when looking for active lattice oxygen. Compared to the pure structure *AC* presents two bridge site oxygen that are weakly bound (compared to

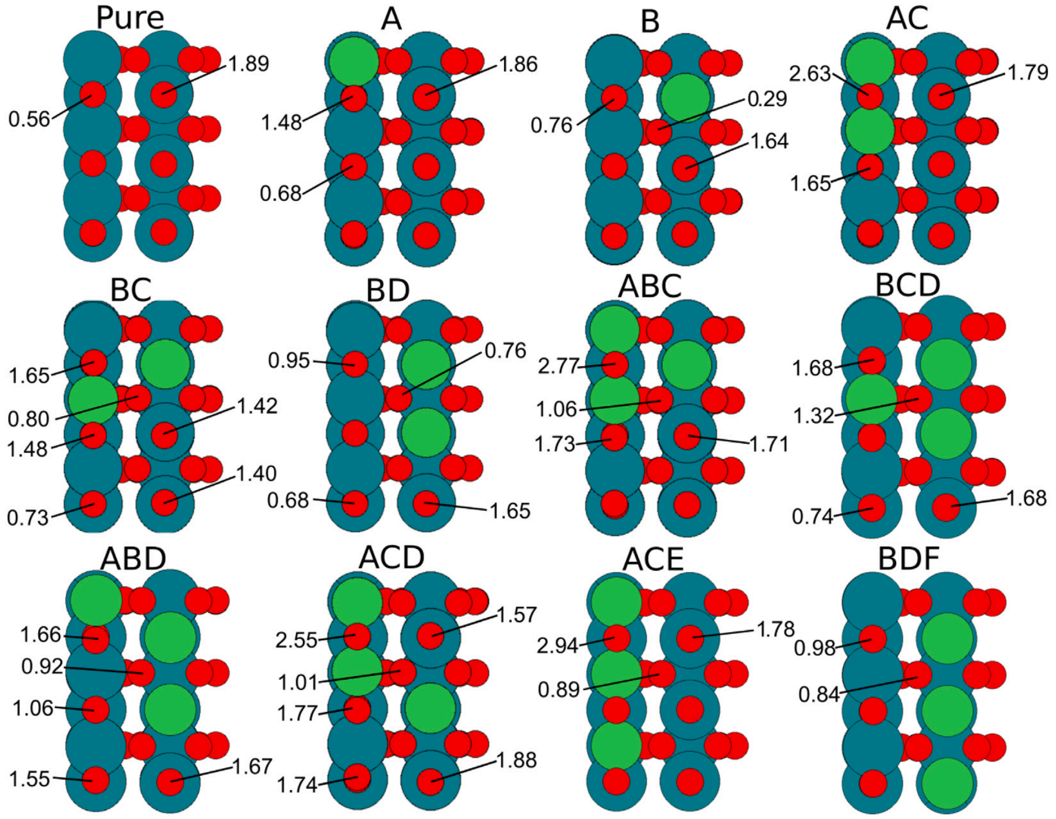

Fig. 2. Binding energy (in eV) of oxygen on an array of different local surface arrangements for rutile $Ru_{1-X}Ni_XO_2$ (110). These structures comprise the exhaustive list of local arrangements with zero to three nickel atoms in the surface layer. The structures are named according to the lattice positions occupied by nickel, conforming to the labeling scheme presented in Fig. 1. Green atoms are nickel, teal are ruthenium and red are oxygen.

the *pure* case). Position 1 is weakened to the point that it is slightly weaker than the ideal case. Position 3 presents an oxygen bound at a strength comparable to the position 1 oxygen of structure *A*. In the case of structure *BC* positions 1 and 3, the bridge sites neighboring nickel, are also severely weakened. In fact it is a common trend throughout all the structures presented that a Ru–Ni bridge site weakens the bridge site oxygen enough to be potentially active at higher potentials. Additionally, a Ni–Ni bridge site oxygen is bound even weaker, to the point that it might be expected to be an ordinary active site of the surface. These trends can also be observed in the structures with three nickel substitutions: *ABC*, *BCD*, *ABD*, *ACD*, *ACE*, *BDF*. Finally, it is worth it to note that surrounding a subsurface oxygen with Ni (position 8 of structure *BCD*) destabilizes it enough that a high potential could perhaps make it reactive.

To be confident in our assessment of the reactivities of the active sites of interest, it is necessary to model the full OER pathway at these active sites. The above screening has identified a set of theoretically prospective active sites. The following is an outline of the reaction mechanisms deemed relevant to these active sites (see Fig. 3).

Bridge site mechanism: The first type of mechanism investigated is the bridge site mechanism. This is the mechanism one might expect for evolving oxygen from a bridge site. The steps are essentially the same as the conventional Volmer–Heyrovsky type mechanism, however the adsorbates are bound to multiple bridge metals instead of a single CUS metal. This pathway has been illustrated in Fig. 3(a).

Popout mechanism: The second mechanism investigated is the “popout” mechanism. This mechanism is what could be expected if sublattice oxygen was to be evolved, as could be the case for the BCD surface structure. This mechanism is illustrated in Fig. 3(b).

Conventional and ruthenium mechanisms: The last two mechanisms are the conventional single site mechanism as discussed earlier and the ruthenium pathway with protons migrating to the bridge [36]. These mechanisms are illustrated in Figs. 3(c) and 3(d) and are mainly included as references to allow for better evaluation of the potential LOER active sites. Recent theoretical studies on high entropy oxides showcase the impact of local configuration on the reaction mechanism and highlight that a combination of two reaction mechanisms is also a possibility that should be accounted for during screening [40].

The OER activity volcano including active sites from this system is presented in Fig. 4. Note that the benchmark catalyst IrO_2 has been marked as a pointer for what should be considered highly active. Together with the IrO_2 on the strong binding side of the volcano lies the AC4 (Ni in positions A and C, active site at position 4) point following the ruthenium pathway. This point serves to illustrate the high catalytic activity of the ruthenium CUS sites in the system. At a similar overpotential, but on the opposite side of the volcano, lie three points: The two Ni–Ni bridge sites and the AC2 point following the ruthenium pathway. These should all be considered efficient active sites of the surface, without the expectation of them being occupied before the reaction starts (due to them being on the weak side of the volcano). Take note of the large change in activity associated with a change of mechanism for AC2. The conventional pathway places this point in the bottom left of the volcano where it is not expected to be very efficient, whereas the ruthenium pathway places it at the top with IrO_2 as is also seen experimentally. Based on these results it is expected that the first sites to activate are the Ni–Ni site and the ruthenium CUS sites of the system. By increasing the electrode potential a point can be reached where a lot of Ru–Ni sites become active. This echoes the sentiment from the initial rough analysis of surface oxygen binding energies. In the bottom of the plot is found the BCD8 site associated with the “popout” mechanism. This placement implies that the mechanism is not particularly relevant and that this subsurface oxygen is therefore not expected to evolve under normal working conditions. These findings paint a picture of LOER being dependent on Ru–Ni bridge sites in this

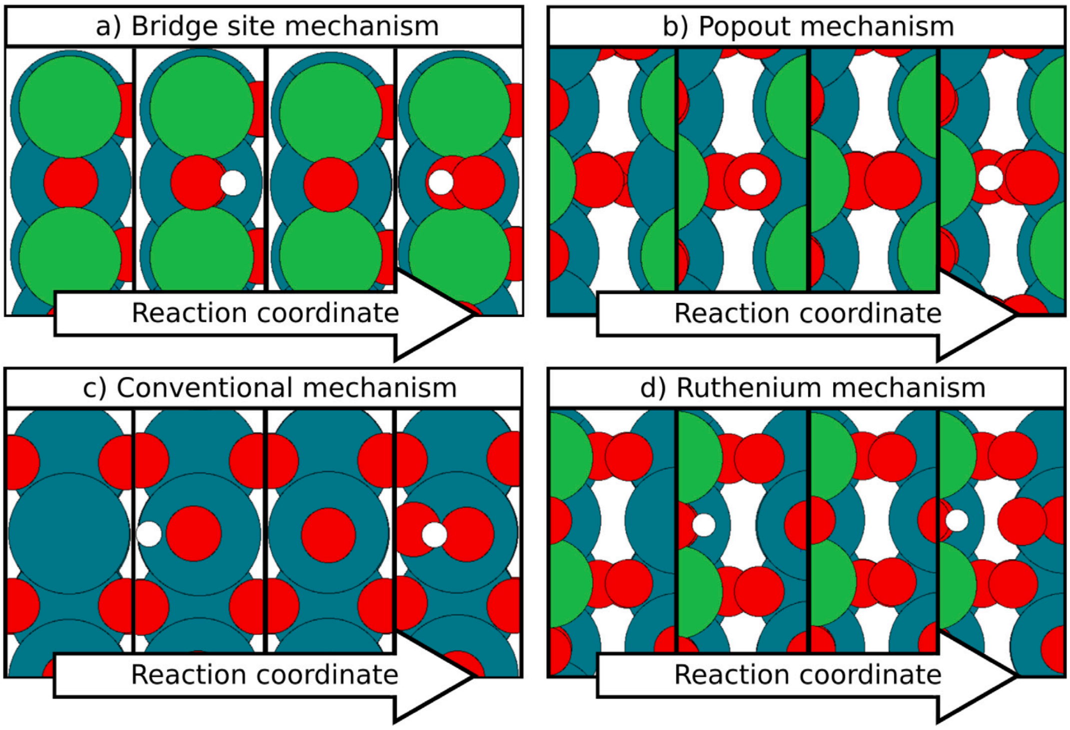

Fig. 3. Schematic representation of the investigated OER surface mechanisms. a: The bridge site mechanism. b: The "popout" mechanism. c: The conventional mechanism. d: The ruthenium mechanism. Green atoms are nickel, teal are ruthenium and red are oxygen.

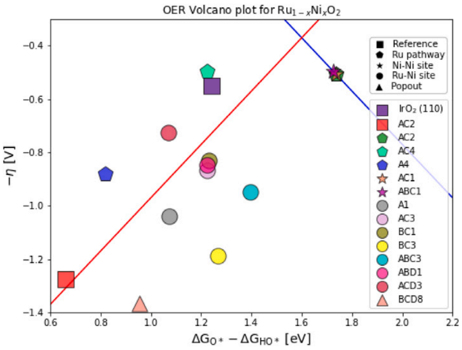

Fig. 4. The OER activity volcano plot. Squares represent reference values calculated following the conventional OER pathway whereas pentagons are calculated following the alternative ruthenium pathway. Stars are Ni–Ni bridge sites, whereas circles are the Ru–Ni sites of interest. Finally the triangle represents the "popout" mechanism as presented in Fig. 3(b). The square AC2 point is included for clarity to show the major difference in predicted activity depending on pathway employed.

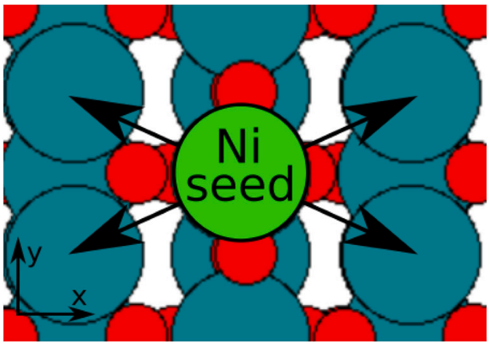

Fig. 5. Nickel clustering directions for $Ru_{1-x}Ni_xO_2$ for $x < 0.05$. The nickel tends to cluster as neighbors, excluding the closest neighbor. This includes clustering diagonally along the z-direction (into the surface).

system. It can therefore be expected that an occurrence of Ru–Ni bridge sites is associated with the extent of LOER. It can also be expected that this LOER tendency is activatable by elevated electrode potentials.

From this surface analysis we can predict the composition at which we would expect to see the most LOER, as that would be the composition which maximizes the number of Ru–Ni bridge sites. This task requires the construction of a model for the prediction of surface Ru–Ni bridge site density as a function of nickel content. In order for the model to be as true to the real system as possible, we choose to base it on experimental characterization. The $Ru_{1-x}Ni_xO_2$ system has previously been experimentally characterized by Petrykin et al. [41]. They found that the nickel atoms tend to cluster together, and the exact method of clustering depends on x. For $x < 5\%$ nickel atoms tend to cluster in groups of three, in zig-zag patterns excluding the shortest metal–metal distance for neighbors. Thus the nickel clusters across the surface from bridge site to CUS site (or into the surface), however it does not cluster along the CUS or bridge lines. This type of clustering has been illustrated in Fig. 5. On the other hand, for $x > 10\%$, nickel begins clustering as shear planes along the [121] direction.

With this in mind, two simple models for the prediction of LOER active site density as a function of nickel concentration can be set up. One for low nickel content ($x < 5\%$) and one for high nickel content ($x > 10\%$).

Surface model for $x < 5\%$: At low concentration the nickel clusters in groups of three, but never along CUS or bridge sites.

1. Set up a rutile RuO_2 (110) surface slab.
2. For each ruthenium atom in the structure, change it to nickel with probability x (*where* x *is the nickel concentration*). Denote the number of nickel atoms introduced to the structure this way N_{init}. It represents the initial number of seeds for the following clustering algorithm.

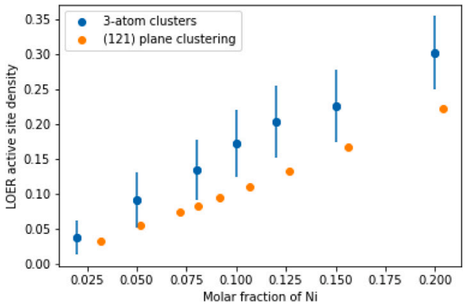

Fig. 6. Modeled relation between x and the LOER active site density for $Ru_{1-x}Ni_xO_2$. Two different types of nickel clustering have been modeled: clusters of three nickel atoms and planes along the (121) direction.

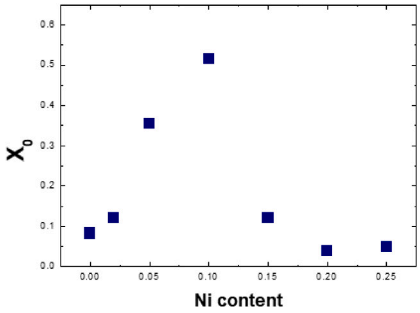

Fig. 7. Dependence of lattice oxygen evolution ($\mathbf{X}_0$) on nickel content in $Ru_{1-x}Ni_xO_2$ samples as measured by DEMS. Here, $\mathbf{X}_0$ is the fraction of LOER to the total measured OER.

3. Calculate the allowed number of seeds in the structure, $N_{allowed}$. With the size of the clusters (in this case 3), the nickel concentration x and the total number of metal atoms in the structure N, this is given as $N_{allowed} = \frac{N \cdot x}{3}$ (rounded to the nearest integer).
4. Remove seeds from the structure until the number of seeds is equal to $N_{allowed}$. This is done by changing Ni atoms back into Ru atoms.
5. For each cluster seed, choose at random two neighboring ruthenium atoms from among neighboring metal atoms, excluding neighbors along the CUS/bridge direction, and exchange these with nickel atoms. The clustering process is now completed.
6. Count the number of RuNi bridge sites in the surface. The number of RuNi sites in the surface divided by the total number of bridge sites provides an estimate of LOER active site density for the surface.

This process can be repeated as many times as necessary to be statistically confident in the results.

Surface model for $x > 10\%$: In the case of higher nickel concentration, the nickel clusters as shear planes along the [121] orientation in the crystal [41]. A simple way to model this behavior is to lay out a [121] plane of height 2 Å in the unit cell, converting all ruthenium atoms within the volume to nickel. It is then possible to count LOER sites on the surface. The nickel concentration of the structure can then be controlled by the distance between any two of these planes. For the case of one nickel plane per three cells the surface saturation of nickel is 20%. It is then possible to count the number of Ru–Ni bridge sites in the surface.

The results of these surface models have been presented in Fig. 6. Notice that the three-Ni cluster mechanism expects the LOER active site density to increase with the nickel concentration throughout the entirety of the probed domain. On the other hand, the shear plane clustering shows a lower tendency for LOER than would be expected for purely 3-atom clustering. Since 20% nickel content is within the bounds of shear plane clustering [41], it is reasonable to assume that the orange points more closely represents the actual system in this end of the domain. When considering only these two methods of clustering, it would therefore be expected that peak LOER tendency is found at a point between $x \approx 12.5\%$ and $x \approx 20\%$, as this is the region where shear plane clustering becomes dominant while the predicted LOER tendency of three-Ni clustering is high.

Compare this to the experimental data presented in Fig. 7. Here, the lattice oxygen evolution ($\mathbf{X}_0$) is reported for the rutile $Ru_{1-x}Ni_xO_2$ as measured by DEMS in labeled water $H_2{}^{18}O$. The parameter $\mathbf{X}_0$ is defined as the fraction of oxygen evolved by Mars van Krevelen mechanism (m/z 34 as a combination of ^{16}O from the surface and ^{18}O from the solvent) to the total amount of evolved oxygen directly after potential application [18]. Notice how the LOER tendency has a steep increase up until the peak LOER activity at around $x = 10\%$, whereafter it has a relatively steep decline. Due to the limited number of data points, it is difficult to assess where the exact optimum lies, it would however be expected that it lies close to the 10% mark. This is in general agreement with the theoretical analysis shown above which predicts a presence of a LOER maximum between 12.5% and 20%. Some of this discrepancy between experiments and theory could be explained by nickel enrichment of the surface in the real systems [41]. As such there should be more LOER at low nickel content than modeled due to the few nickel present having a high probability of being near or in the surface. At high nickel content the opposite would be expected due to nickel over-saturation in the surface, reducing the likelihood of the Ru–Ni bridge site.

The computational methodology has also been applied to rutile $Ru_{1-x}Ti_xO_2$. The surface screening is presented in Fig. 8. Notice how the greatest destabilization of bridge site oxygen occurs for the surface configurations featuring three titanium atoms with examples being ABC positions 1 and 3, BCD position 1 and ACD positions 1 and 3. A volcano plot including such active sites of interest is presented in Fig. 9. Specifically Ru–Ti surface bridge sites including three-titanium clusters tend towards being destabilized enough where activation is expected at elevated electrode potentials. Due to requiring three titanium atoms at the surface, these sites are expected to be very rare at low Ti content. By extension, low to negligible LOER activity would be expected at low titanium content. As the Ti content increases, the probability of these three-titanium clusters being in the top layer also rises. Their contribution to LOER is therefore mostly expected at higher Ti content. This is in somewhat agreement with experiments where LOER is not observed at low titanium content but is observed at higher Ti content ($x = 0.20$) [19]. However, due to the rarity of the identified surface sites, it would be unexpected that these sites are major contributors to LOER at $x = 0.20$. Such a discrepancy could be the result of structural defects, as they are known to correlate positively with LOER tendency [20]. To conceptualize why this would be the case consider that lattice defects would expose a variety of oxygen species in the surface. No longer protected by the lattice motif, these oxygen atoms would be prone to be evolved. The $Ru_{1-x}Ti_xO_2$ system has previously been characterized by means of X-ray diffraction, X-ray absorption spectroscopy, Extended X-ray absorption fine structure, as well as X-ray absorption near edge structure [19]. It was found that defects such as oxygen deficiencies are present around the titanium in the structure, especially at x > 15%.

Structural defects like these present a challenge for this computational method that hinges on knowledge of the structure. The method is therefore not expected to accurately represent LOER tendency in structures with major lattice defects. With basis in the computational analysis, it seems probable that the observed LOER is promoted by the defects in the structure.

The LOER tendency of these systems seems to be closely correlated to the amount and types dopants introduced. This opens up

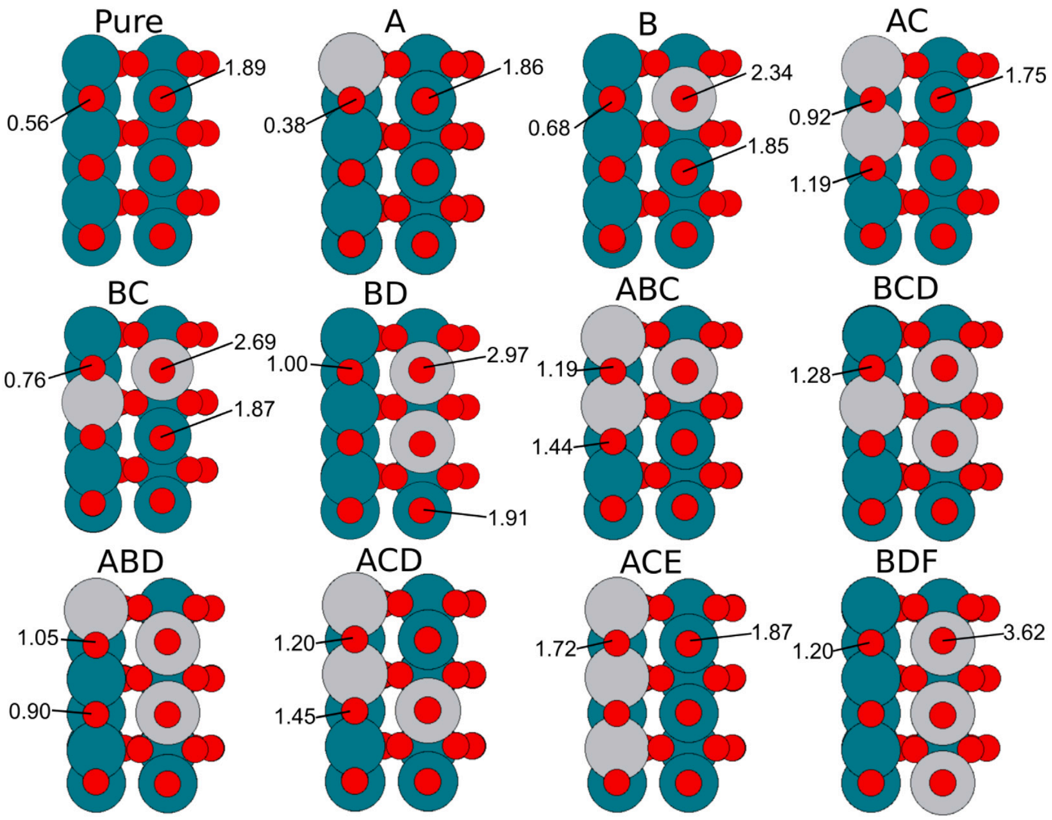

Fig. 8. DFT binding energy (in eV) of oxygen on an array of local surface arrangements for rutile $Ru_{1-x}Ti_xO_2$ (110) (as likewise done for $Ru_{1-x}Ni_xO_2$ in Fig. 2). The structures are named according to the lattice positions occupied by titanium (Fig. 1). Gray atoms are titanium, teal are ruthenium and red are oxygen.

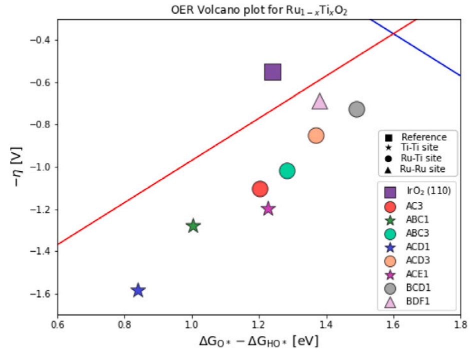

Fig. 9. The OER activity volcano. Squares represents the reference value for IrO_2 as calculated following the conventional OER pathway. Stars are Ti–Ti bridge sites, circles are Ru–Ti bridge sites and triangles are Ru–Ru bridge sites.

the potential avenue of tuning LOER tendency by carefully selecting dopants and codopants. This approach has proven to be fruitful for other catalytically relevant properties such as OER activity on stable materials [4].

5. Conclusion

This article presents a methodology for computational prediction of LOER on well-ordered oxide structures, exemplified by a case study of the rutile $Ru_{1-x}Ni_xO_2$ (110) and $Ru_{1-x}Ti_xO_2$ (110) surfaces. This is done by calculating the binding energies of the oxygen atoms in the surface for all different local configurations including one to three metal atom substitutions in the surface layer. This allows for identification of weakly bound oxygen atoms that could potentially be evolvable. A volcano plot for such active sites is then established, and allows for prediction of LOER activity and active sites. For the case of $Ru_{1-x}Ni_xO_2$ it is found that LOER should be active at elevated electrode potentials, matching experimental findings in the literature. The LOER active sites are found to be mainly Ru–Ni bridge sites. This result forms a direct link between surface structure and LOER activity, assuming that more LOER active sites result in higher LOER activity. By applying experimental knowledge of the clustering mechanisms of nickel in this system it is possible to construct a model of LOER activity as a function of nickel content in the catalyst. The resulting model predicts that the maximum LOER activity should be found between $x = 12.5\%$ and $x = 20\%$.

Experimental DEMS data are presented for this system, unveiling how LOER varies with nickel content in a real system. It is found that the LOER activity peaks at around 10% nickel content, which is in relative good agreement with the theoretical prediction.

For the case of $Ru_{1-x}Ti_xO_2$, the calculations predict no LOER activity at low Ti content, and small contributions at higher Ti content ($x = 0.20$). This is in contrast to the literature which observes LOER at $x = 0.20$. This region does, however, feature major lattice defects like oxygen deficiencies near titanium in the structure. The discrepancy is therefore unsurprising since the computational method hinges on a perfect lattice structure. It is expected that the observed LOER tendency for this system is derived primarily from lattice defects rather than being intrinsic to the $Ru_{1-x}Ti_xO_2$ rutile structure.

CRediT authorship contribution statement

Adrian Malthe Frandsen: Writing – review & editing, Writing – original draft, Visualization, Validation, Software, Project administration, Methodology, Investigation, Formal analysis, Data curation, Conceptualization. **Kateřina Minhová Macounová:** Writing – review & editing, Visualization, Validation, Resources, Investigation, Funding acquisition, Formal analysis, Data curation. **Jan Rossmeisl:** Writing

– review & editing, Supervision, Resources, Methodology, Funding acquisition, Conceptualization. **Petr Krtil:** Writing – review & editing, Writing – original draft, Supervision, Resources, Funding acquisition, Conceptualization.

Declaration of competing interest

The authors declare that they have no known competing financial interests or personal relationships that could have appeared to influence the work reported in this paper.

Data availability

Structures, scripts and data are available in the electronic supplementary material: https://nano.ku.dk/english/research/theoretical-electrocatalysis/katladb/loer-runio2/.

Acknowledgments

The work was supported by the Center of Excellence program by the Danish National Research Foundation DNRF 149, the Grant Agency of the Czech Republic under contract 21-03037S and the Villum Foundation to the Villum Center for the Science of Sustainable Fuels and Chemicals (#9455).

References

[1] J. Rossmeisl, Z.-W. Qu, H. Zhu, G.-J. Kroes, J. Nørskov, Electrolysis of water on oxide surfaces, J. Electroanal. Chem. 607 (2007) 83–89.

[2] I.A. Moreno-Hernandez, C.A. MacFarland, C.G. Read, K.M. Papadantonakis, B.S. Brunschwig, N.S. Lewis, Crystalline nickel manganese antimonate as a stable water-oxidation catalyst in aqueous 1.0 M H_2SO_4, Energy Environ. Sci. 10 (2017) 2103–2108.

[3] A. Weiß, A. Siebel, M. Bernt, T.-H. Shen, V. Tileli, H.A. Gasteiger, Impact of intermittent operation on lifetime and performance of a PEM water electrolyzer, J. Electrochem. Soc. 166 (2019) F487.

[4] T. Kutlusoy, S. Divanis, R. Pittkowski, R. Marina, A.M. Frandsen, K. Minhova-Macounova, R. Nebel, D. Zhao, S.F.L. Mertens, H. Hoster, P. Krtil, J. Rossmeisl, Synergistic effect of p-type and n-type dopants in semiconductors for efficient electrocatalytic water splitting, Chem. Sci. 13 (2022) 13879–13892.

[5] S. Dresp, F. Dionigi, M. Klingenhof, T. Merzdorf, H. Schmies, J. Drnec, A. Poulain, P. Strasser, Molecular understanding of the impact of saline contaminants and alkaline pH on NiFe layered double hydroxide oxygen evolution catalysts, ACS Catal. 11 (2021) 6800–6809.

[6] J. Villalobos, D.M. Morales, D. Antipin, G. Schuck, R. Golnak, J. Xiao, M. Risch, Stabilization of a Mn-Co oxide during oxygen evolution in alkaline media, ChemElectroChem 9 (2022) e202200482.

[7] F. Gonell, G. Rousse, M. Odziomek, W. Baaziz, O. Ersen, A. Grimaud, C. Sanchez, Nanostructured layered lithium iridates as electrocatalysts for improved oxygen evolution reaction, ACS Appl. Nano Mater. 6 (2023) 2577–2584.

[8] N. Hales, T.J. Schmidt, E. Fabbri, Reversible and irreversible transformations of Ni-based electrocatalysts during the oxygen evolution reaction, Curr. Opin. Electrochem. 38 (2023) 101231.

[9] D.J. Zheng, M. Görlin, K. McCormack, J. Kim, J. Peng, H. Xu, X. Ma, J.M. LeBeau, R.A. Fischer, Y. Román-Leshkov, Y. Shao-Horn, Linker-dependent stability of metal-hydroxide organic frameworks for oxygen evolution, Chem. Mater. 35 (2023) 5017–5031.

[10] E. Romeo, F. Illas, F. Calle-Vallejo, A general but still unknown characteristic of active oxygen evolution electrocatalysts, Chem. Sci. 14 (2023) 3622–3629.

[11] T. Binninger, R. Mohamed, K. Waltar, E. Fabbri, P. Levecque, R. Kötz, T.J. Schmidt, Thermodynamic explanation of the universal correlation between oxygen evolution activity and corrosion of oxide catalysts, Sci. Rep. 5 (2015) 12167.

[12] J. Nørskov, T. Bligaard, A. Logadottir, S. Bahn, L. Hansen, M. Bollinger, H. Bengaard, B. Hammer, Z. Sljivancanin, M. Mavrikakis, Y. Xu, S. Dahl, C. Jacobsen, Universality in heterogeneous catalysis, J. Catalysis 209 (2002) 275–278.

[13] M. Wohlfahrt-Mehrens, J. Heitbaum, Oxygen evolution on Ru and RuO_2 electrodes studied using isotope labelling and on-line mass spectrometry, J. Electroanal. Chem. Interfacial Electrochem. 237 (1987) 251–260.

[14] J.O. Bockris, T. Otagawa, The electrocatalysis of oxygen evolution on perovskites, J. Electrochem. Soc. 131 (1984) 290–302.

[15] Z. Shi, X. Wang, J. Ge, C. Liu, W. Xing, Fundamental understanding of the acidic oxygen evolution reaction: mechanism study and state-of-the-art catalysts, Nanoscale 12 (2020) 13249–13275.

[16] K.A. Stoerzinger, O. Diaz-Morales, M. Kolb, R.R. Rao, R. Frydendal, L. Qiao, X.R. Wang, N.B. Halck, J. Rossmeisl, H.A. Hansen, T. Vegge, I.E.L. Stephens, M.T.M. Koper, Y. Shao-Horn, Orientation-dependent oxygen evolution on RuO_2 without lattice exchange, ACS Energy Lett. 2 (2017) 876–881.

[17] R.R. Rao, M.J. Kolb, N.B. Halck, A.F. Pedersen, A. Mehta, H. You, K.A. Stoerzinger, Z. Feng, H.A. Hansen, H. Zhou, L. Giordano, J. Rossmeisl, T. Vegge, I. Chorkendorff, I.E.L. Stephens, Y. Shao-Horn, Towards identifying the active sites on RuO_2(110) in catalyzing oxygen evolution, Energy Environ. Sci. 10 (2017) 2626–2637.

[18] K. Macounova, M. Makarova, P. Krtil, Oxygen evolution on nanocrystalline RuO_2 and $Ru_{0.9}Ni_{0.1}O_{2-\delta}$ electrodes – DEMS approach to reaction mechanism determination, Electrochem. Commun. 11 (2009) 1865–1868.

[19] K.M. Macounová, R.K. Pittkowski, R. Nebel, A. Zitolo, P. Krtil, Selectivity of Ru-rich Ru-Ti-O oxide surfaces in parallel oxygen and chlorine evolution reactions, Electrochim. Acta 427 (2022) 140878.

[20] L.-A. Näslund, C.M. Sánchez-Sánchez, Á.S. Ingason, J. Bäckström, E. Herrero, J. Rosen, S. Holmin, The role of TiO_2 doping on RuO_2-coated electrodes for the water oxidation reaction, J. Phys. Chem. C 117 (2013) 6126–6135.

[21] J.T. Mefford, X. Rong, A.M. Abakumov, W.G. Hardin, S. Dai, A.M. Kolpak, K.P. Johnston, K.J. Stevenson, Water electrolysis on $La_{1-x}Sr_xCoO_{3-\delta}$ perovskite electrocatalysts, Nature Commun. 7 (2016) 11053.

[22] I.C. Man, H.-Y. Su, F. Calle-Vallejo, H.A. Hansen, J.I. Martínez, N.G. Inoglu, J. Kitchin, T.F. Jaramillo, J.K. Nørskov, J. Rossmeisl, Universality in oxygen evolution electrocatalysis on oxide surfaces, ChemCatChem 3 (2011) 1159–1165.

[23] J. Enkovaara, C. Rostgaard, J.J. Mortensen, J. Chen, M. Dułak, L. Ferrighi, J. Gavnholt, C. Glinsvad, V. Haikola, H.A. Hansen, Electronic structure calculations with GPAW: a real-space implementation of the projector augmented-wave method, J. Phys.: Condens. Matter. 22 (2010) 253202.

[24] J.J. Mortensen, L.B. Hansen, K.W. Jacobsen, Real-space grid implementation of the projector augmented wave method, Phys. Rev. B 71 (2005) 035109.

[25] A.H. Larsen, J.J. Mortensen, J. Blomqvist, I.E. Castelli, R. Christensen, M. Dułak, J. Friis, M.N. Groves, B. Hammer, C. Hargus, The atomic simulation environment—a Python library for working with atoms, J. Phys.: Condens. Matter. 29 (2017) 273002.

[26] B. Hammer, L.B. Hansen, J.K. Nørskov, Improved adsorption energetics within density-functional theory using revised Perdew-Burke-Ernzerhof functionals, Phys. Rev. B 59 (1999) 7413–7421.

[27] J. Jirkovský, M. Makarova, P. Krtil, The effect of coherent domain size on the insertion activity of nanocrystalline RuO_2, J. Electrochem. Soc. 152 (2005) A1613.

[28] K. Macounová, M. Makarova, J. Jirkovský, J. Franc, P. Krtil, Parallel oxygen and chlorine evolution on $Ru_{1-x}Ni_xO_{2-y}$ nanostructured electrodes, Electrochim. Acta 53 (2008) 6126–6134.

[29] J. Jirkovský, H. Hoffmannová, M. Klementová, P. Krtil, Particle size dependence of the electrocatalytic activity of nanocrystalline RuO_2 electrodes, J. Electrochem. Soc. 153 (2006) E111.

[30] J. Rossmeisl, A. Logadottir, J. Nørskov, Electrolysis of water on (oxidized) metal surfaces, Chem. Phys. 319 (1) (2005) 178–184.

[31] J.K. Nørskov, J. Rossmeisl, A. Logadottir, L. Lindqvist, J.R. Kitchin, T. Bligaard, H. Jónsson, Origin of the overpotential for oxygen reduction at a fuel-cell cathode, J. Phys. Chem. B 108 (2004) 17886–17892.

[32] A. Kiejna, G. Kresse, J. Rogal, A. De Sarkar, K. Reuter, M. Scheffler, Comparison of the full-potential and frozen-core approximation approaches to density-functional calculations of surfaces, Phys. Rev. B 73 (2006) 035404.

[33] L.G.V. Briquet, M. Sarwar, J. Mugo, G. Jones, F. Calle-Vallejo, A new type of scaling relations to assess the accuracy of computational predictions of catalytic activities applied to the oxygen evolution reaction, ChemCatChem 9 (7) (2017) 1261–1268.

[34] N.B. Halck, V. Petrykin, P. Krtil, J. Rossmeisl, Beyond the volcano limitations in electrocatalysis – oxygen evolution reaction, Phys. Chem. Chem. Phys. 16 (2014) 13682–13688.

[35] M. Busch, N.B. Halck, U.I. Kramm, S. Siahrostami, P. Krtil, J. Rossmeisl, Beyond the top of the volcano? – A unified approach to electrocatalytic oxygen reduction and oxygen evolution, Nano Energy 29 (2016) 126–135.

[36] S. Divanis, A.M. Frandsen, T. Kutlusoy, J. Rossmeisl, Lifting the discrepancy between experimental results and the theoretical predictions for the catalytic activity of RuO_2(110) towards oxygen evolution reaction, Phys. Chem. Chem. Phys. 23 (2021) 19141–19145.

[37] T. Berlijn, P.C. Snijders, O. Delaire, H.-D. Zhou, T.A. Maier, H.-B. Cao, S.-X. Chi, M. Matsuda, Y. Wang, M.R. Koehler, P.R.C. Kent, H.H. Weitering, Itinerant antiferromagnetism in RuO_2, Phys. Rev. Lett. 118 (2017) 077201.

[38] Q. Liang, A. Bieberle-Hütter, G. Brocks, Anti-ferromagnetic RuO2: A stable and robust OER catalyst over a large range of surface terminations, J. Phys. Chem. C 126 (3) (2022) 1337–1345.

[39] D.-Y. Kuo, H. Paik, J. Kloppenburg, B. Faeth, K.M. Shen, D.G. Schlom, G. Hautier, J. Suntivich, Measurements of oxygen electroadsorption energies and oxygen evolution reaction on RuO2(110): A discussion of the sabatier principle and its role in electrocatalysis, J. Am. Chem. Soc. 140 (50) (2018) 17597–17605.

[40] K.L. Svane, J. Rossmeisl, Theoretical optimization of compositions of high-entropy oxides for the oxygen evolution reaction, Angew. Chem. Int. Ed. 61 (2022) e202201146.

[41] V. Petrykin, Z. Bastl, J. Franc, K. Macounova, M. Makarova, S. Mukerjee, N. Ramaswamy, I. Spirovova, P. Krtil, Local structure of nanocrystalline $Ru_{1-x}Ni_xO_{2-\delta}$ dioxide and its implications for electrocatalytic behavior—An XPS and XAS study, J. Phys. Chem. C 113 (2009) 21657–21666.

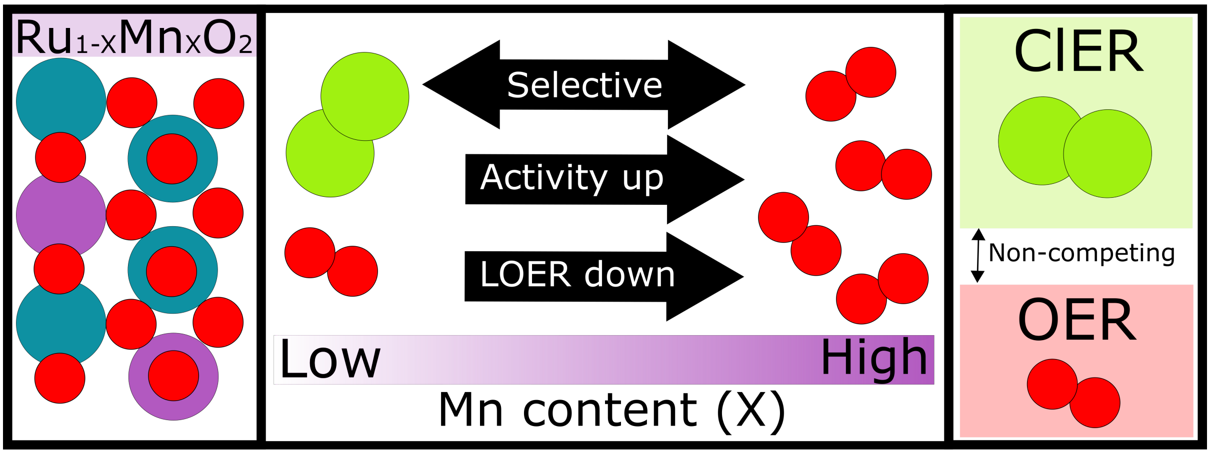

4.2 Article 3: Ru rich Ru-Mn-O phases for selective suppression of chlorine evolution in sea water electrolysis

This article studies the control chemical composition of $Ru_{1-x}Mn_xO_2$ exhibits over the selectivity between OER and ClER in saltwater electrolysis. The materials were synthesized by spray-freeze-freeze-drying approach, their rutile nature and size was characterized by X-ray diffraction (XRD) and scanning electron microscopy (SEM). Structurally, it was found that lattice parameter a does not change much with increasing Mn content, whereas lattice parameter c, as well as structural parameter c/a, changes but without a clear trend. This is in contrast to other similarly substitutionally doped systems [63], and could be due to the lack of a clear tendency for Mn to cluster.

The electrocatalytic activity of the samples increases with increasing Mn, topping at $x = 0.15$, and subsequently decreasing. Another clear trend is the sensitivity to chlorides, with increasing Mn content leading to less sensitivity for the anodic current. Rotating Ring-Disc Electrode (RRDE) measurements find that oxygen evolution tendency is largely unaffected by changing salt concentrations. Thus any increase in anodic current from the addition of salt is mainly ClER, and the two reactions are generally not competing. Manganese content thus constitutes a lever for the control of the ClER selectivity, with 15% cationic manganese constituting only 30% ClER at 300 mM. This compares to 55% for the case of $x = 0.05$.

To gain understanding of the reaction mechanism at play, and since LOER has been known to correlate with ClER [59], the samples are screened for LOER using DEMS. The trend from literature is replicated, with samples exhibiting LOER also evolving the most chlorine. Despite this, the overall LOER tendency is quite low.

Finally, a computational screening like the one presented in section 4.1 is done in an attempt to identify LOER active sites. On the rutile (110) surface only CUS site oxygen are found to be active, and thus the model does not expect significant LOER tendency. The analysis additionally predicts Mn CUS sites to be highly active in the structure, potentially explaining the increase in OER activity observed.

Ru rich Ru-Mn-O phases for selective suppression of chlorine evolution in sea water electrolysis

Catalina Astudillo, Kateřina Minhová Macounová, Adrian Malthe Frandsen, Roman Nebel, Jan Rossmeisl, Petr Krtil

Article and supplementary material available at DOI:

https://doi.org/10.1016/j.electacta.2023.143295

Electrochimica Acta 470 (2023) 143295

Contents lists available at ScienceDirect

Electrochimica Acta

journal homepage: www.journals.elsevier.com/electrochimica-acta

Ru rich Ru-Mn-O phases for selective suppression of chlorine evolution in sea water electrolysis

Catalina Astudillo [a], Kateřina Minhová Macounová [a], Adrian Malthe Frandsen [b], Roman Nebel [a], Jan Rossmeisl [b], Petr Krtil [a,*]

[a] J. Heyrovský Institute of Physical Chemistry, Czech Academy of Sciences, Dolejškova 3, Prague 18223, Czech Republic
[b] Center of High Entropy Alloy Catalysis, Department of Chemistry, University of Copenhagen, Universitetsparken 5, 2100 København Ø, Copenhagen, Denmark

ARTICLE INFO

Keywords:
Oxygen evolution reaction
Chlorine evolution reaction
Selectivity
Electrolysis
Oxide anode

ABSTRACT

Limits of steering selectively gas evolving reaction on Ru rich oxide phases in Ru-Mn-O system were investigated by combined theoretical and experimental approach. $Ru_{1-x}Mn_xO_2$ materials of single phase nature conforming to the rutile structure were prepared by the spray freeze - freeze drying approach and tested for activity in oxygen and chlorine evolution reactions. The overall electrocatalytic activity of the prepared materials increases with increasing Mn content. In this manner also increases the selectivity towards oxygen evolution in acidic chloride containing solutions. Closer analysis shows that the amount of evolved oxygen (for a given electrode material) is practically independent of the chloride concentration. This is illustrated by the order of the oxygen evolution reaction with respect to chloride concentration being close to 0 in the whole range of the prepared Ru-Mn-O phases. The high selectivity towards oxygen evolution reaction coincides with low tendency of Ru-Mn-O phases to evolve oxygen via lattice oxygen activation (LOER). The experimental behavior is further confirmed by DFT analysis of the reactivity of the Ru-Mn-O surfaces.

1. Introduction

Anodic gas evolving reactions gain an importance in connection with growing role of water electrolysis as the main process producing green hydrogen. It is known, that kinetically hindered four electron oxygen evolution is effectively limiting possible deployment of water electrolyzers in replacement of fossil fuels powering the society. It needs to be noted that the mass utilization of electrolytic hydrogen generation may put a strain on availability of fresh water which is requested in the water electrolyzers. An alternative to energy consuming desalination may be a sea water electrolysis [1–4] which is mainly impeded by a parallel anodic chlorine evolution.

A production of chlorine in water electrolysis, in contrast to, e.g., chlor-alkali industry, is undesirable due to a high toxicity and corrosiveness of the evolved gas. A selectivity of the parallel anodic gas evolution reactions was treated previously in chlorine production as well chlorate electrolysis. The aim of selectivity control in these applications is at suppression of oxygen evolution which either decreases the yield and/or causes safety problems (e.g. chlorate electrolysis). It needs to be reflected that each of the considered gas evolving reactions shows a different pH sensitivity. As a result of this the thermodynamic preference of OER (at a constant potential) increases with increasing pH. This pH dependent thermodynamic preference can be in principle used to control the practical selectivity of the anodes in parallel chlorine and oxygen evolution. One needs to note, however, that the electrode selectivity is difficult to assess at pH higher than 4 due to rather facile chemical hydrolysis of the originally produced chlorine to hypochlorite which severely complicates the experimental selectivity evaluations. To avoid possible confusion we will restrict further consideration to the acid media ($pH<4$) and we will understand the selectivity as intrinsic kinetic preference of the electrode surface for OER or CER, respectively. An alternative approach towards selectivity control can be associated with engineering the surface to control nature and abundance of the active sites supporting corresponding electrode reaction [5–8].

While the first approach is rather convenient for practical optimization, the later one requires a detailed understanding of both electrode processes and can, therefore, contribute fundamentally to rational design of electrode materials [9]. In fact, the second approach has been dictated by the chlor-alkali industry when the pH cannot be freely manipulated. The chlorine as well as oxygen evolution in relevant pH

---

* Corresponding author.
E-mail address: Petr.Krtil@jh-inst.cas.cz (P. Krtil).

https://doi.org/10.1016/j.electacta.2023.143295
Received 29 May 2023; Received in revised form 1 October 2023; Accepted 2 October 2023

range proceed under rather harsh conditions which restrict the selection of suitable electrode materials to noble metal oxides mostly based on Ru and Ir. The anodic gas evolving behavior of both Ru and Ir based oxides has been treated theoretically as well as experimentally. The theoretical analysis was based on practical application of Bronsted-Polanyi relations which allow to assess thermodynamic limits of kinetic behavior by comparing the driving forces of given reactions at different electrode surfaces. Such DFT based thermodynamic analysis clearly points towards a kinetic preference of chlorine evolution for most of the conceivable surfaces [9,10]. This theoretical prediction is in fact reflecting the behavior empirically observed on so-called dimension stable anodes (DSA), which represent an industrial standard for selective anodes for chlorine evolution in acid media. The industry grade DSAs are based on phases existing in the ternary system Ru-Ti-O where conventionally Ru rich oxides are associated with the activity while the Ti rich phases are traditionally linked with stability of the DSAs [11]. This conventional description has been challenged recently [9,12] identifying the Ti sites as actively binding in gas evolving reaction on Ru-Ti-O catalysts. Similar conclusion was reached also by Over's group [13]. Regarding the practical steering of the selectivity in parallel oxygen and chlorine evolution it was shown that preference for a particular gas evolving reaction can be altered by controlling surface stress and strain of the catalytically active layer [12,14]. The selectivity of the Ru based catalysts is also affected by chemical composition and of the role of local structure as has been outlined for ternary systems Ru-Me-O (Me = Ni, Co, Zn, Mg) [4,15–16] as well for well-defined single phase catalysts in Ru-Ti-O system [5,17]. In a similar manner, the behavior of Ir based systems, despite less favourable cost of Ir based catalysts compared with Ru based systems, was in detail treated for Ir based double perovskites [18] or for phases in Ir-Mn-O system [19].

For all studied complex catalytic systems the change of the chemical composition affects the selectivity of the surfaces in parallel oxygen and chlorine evolution. [13] An increase in selectivity towards chlorine evolution was observed for Ni [16] and Mg [17] substituted materials while, on the other hand, Zn [4] substitution leads to oxygen evolution promotion. The role of the local structure was exemplified on the single-phase Ru rich phases in the Ru-Ti-O system which clearly indicated that a specific clustering of Ti on the catalysts' structure is needed to promote chlorine evolution while suppressing oxygen evolution [5]. In fact the experimental behavior reported for Ru-Ti-O phases outlines limitations of the generalized computational screening of the selectivity in parallel OER and CER which disregards the local structure effects [9]. The generalized model of Ru-Ti-O oxides predicts a competition of both conceived electrode reactions for the same surface-active sites for all involved surfaces. The Ru-Ti-O based data clearly identify that the theory predicted behavior indeed can be observed in the given system. It, however, requires that the Ti in the active phase needs to occupy at least 20 % cationic positions [5]. On the other hand, the data obtained for materials with low Ti content suggest that both considered electrode reactions proceed at the surface independently without actual competition for the same surface sites. This observed behavior was tentatively assigned to the applicability of different oxygen evolving mechanisms when the tendency of the surface to evolve chlorine (at the expense of oxygen) was stronger on materials showing substantial contribution of lattice oxygen (LOER) to the OER [5]. Similar level of characterization of parallel OER and CER for other systems is, unfortunately, so far missing and the nature of the selectivity of oxide catalysts still needs to be conclusively explained.

This paper aims at bridging the gap in fundamental knowledge of the selectivity control in parallel OER and CER on the phases in Ru-Mn-O systems which have been studied in anodic gas evolutions previously [20–22]. We put together a detailed electrochemical and DEMS based characterization of the selectivity of the single phase Ru rich Ru-Mn-O phases and combine it with DFT analysis of the intermediate binding tendencies to rationalize observed selectivity behavior.

2. Experimental

2.1. Synthesis

The $Ru_{1-x}Mn_xO_2$ samples were prepared by spray-freezing/ freeze-drying method [5]. Stock solutions of ruthenium (III) nitrosyl nitrate (Alpha Aesar, 31.3% Ru), potassium permanganate (Aldrich, >99 %) and manganese (II) sulfate in MilliQ quality deionized water were mixed to reach Ru to Mn ratio of 19, 9, 5.6 and 4. The ratio between manganese permanganate and sulfate was kept at 2.5:1 in all syntheses. The concentration of the starting solution containing sources of Ru and Mn was adjusted to reach 8 mM of total metal content. 100 mL of the starting solution was stirred for 30 min and sprayed into 1 L of liquid nitrogen to form the ice precursor. The ice-precursor was immediately transferred into the pre-cooled lyofilizer (FreeZone Triad Freeze-Dry System 7,400, 030, (Labconco)) and freeze dried at 0.5 mBar according to the following temperature program: −30 °C (1 h), −25 °C (3 h), −20 °C (4 h), −15 °C (6 h), and 30 °C (5 h). The dried foam-like precursor was then annealed at 400 °C in air for 4 h.

2.2. Solid state characterizations

The phase purity of all samples was analyzed using Rigaku Miniflex 600 powder X-ray diffractometer with $Cu_{K\alpha}$ radiation operating at 30 kV and 10 mA. Structural parameters of the prepared materials were assessed by Rietveld analysis of the measured powder diffraction patterns using Profex 4.3 software package. The morphology and average chemical composition of the Ru-Mn-O materials were determined using scanning electron microscopy (SEM, Hitachi S-4800) equipped with EDX detector (Noran System Six, Thermo Fisher). The SEM micrographs were also used to determine the parameters of the particle size distribution based on 200 randomly selected particles.

The porosity and BET surface area of studied samples were determined by nitrogen adsorption at the boiling temperature of liquid nitrogen (77 K). Before adsorption experiments, samples were degassed in two steps: at 80 °C for 1 h and finally at 300 °C for 6 hrs. The experiments were performed using an 3Flex instrument (Micromeritics). The BET (Brunauer-Emmett-Teller) theory was used to evaluate the total surface areas. The porosity distribution was evaluated by Original Density Functional Theory using N_2 - DFT Model with non-negative regularization.

2.3. Electrochemical characterization

Activity and selectivity of synthesized Ru-Mn-O materials in anodic gas evolution reactions was studied in acid media in 0.1 M $HClO_4$ (p.a., Sigma Aldrich) containing variable amount of chlorides in the concentration range 0.01 – 0.3 M. The selectivity in parallel oxygen and chlorine evolution was assessed by two principal approaches exploring rotating ring disk electrode (RRDE) (Pine Research MSR) with graphite disk (diameter 5 mm) and Pt ring (inner diameter 6.5 mm; outer diameter 7.5 mm) and on-line mass spectroscopic detection of reaction products. The RRDE experiments outlining selectivity of the Ru-Mn-O phases followed procedure described in [23] and [24] using a bi-potentiostatic control of the experiment with an AUTOLAB (PGSTAT 30, Metrohm) potentiostat in a single-compartment glass cell with Ru-Mn-O working electrode, Pt auxiliary and saturated calomel (SCE) reference electrode. The Pt ring electrode was kept at constant potential (0.9 V with respect to reference electrode) throughout the experiment. The Ru-Mn-O working electrodes were prepared from water-based suspension containing 2 g of the prepared Ru-Mn-O materials per liter of suspension. The suspension was freshly sonicated before deposition of 20 μL on the graphite disk. The overall surface coverage of the Ru-Mn-O oxide at the working electrode was about 200 $\mu g cm^{-2}$. Both disk and ring were polished with alumina suspensions (0.5, 0.3 and 0.05 μm, Allie, High Technology Products, Inc, USA) between experiments.

Mechanical polishing was followed by electrochemical cleaning by cycling in 0.1 M $HClO_4$ solution between −0.3 and 1.5 V (vs. SCE) until characteristic and stable voltammograms of glassy carbon and platinum materials were observed.

The collection factor of the RRDE setup was determined in 0.1 M K_2SO_4 (150 mL) containing 1 mM of potassium ferrocyanide (K_4[*Fe* $(CN)_6$], (both p.a. Sigma Aldrich) keeping the ring potential at +0,01 V (vs. SCE) while sweeping the disk potential between −0,05 V and +0,50 V (vs. SCE) at a scan rate of 50 mV/s and different rotating speeds ranging between 200 and 1600 RPM. The collection factor was evaluated as a ratio of limiting disk and ring currents, yielding the collection factor equal to 0.2390.

The DEMS experiments were carried out in a home made Kel-F single compartment cell in a three electrode arrangement with Ru-Mn-O working electrode, Ag/AgCl reference electrode and Pt auxiliary electrode. The working Ru-Mn-O electrode was prepared by a repetitive deposition of 50 μL of the water based Ru-Mn-O suspension on Ti mesh (open area 20%, Goodfellow) until a surface coverage of about 1 mg/cm^2 of active oxide was achieved. The deposited layers were stabilized by annealing the electrodes at 400 °C for 4 h. Potential control in DEMS experiments was achieved by PAR 263A potentiostat. Mass spectroscopic part of the DEMS apparatus consisted of a PrismaPlusTM QMQ220 quadrupole mass spectrometer (Pfeiffer) connected to a HiPace80 (PMP03941) turbomolecular drag pumping station (Pfeiffer). The extent of the lattice oxygen evolution was determined from experiments carried out in isotopically labeled water (Oxygen-18 water, Medical Isotopes, Inc., Pelham, USA).

2.4. DFT modeling

All DFT calculations are performed using Grid-based Projector Augmented Wave (GPAW)[25–26] in unison with the Atomic Simulation Environment (ASE) [25]. The functional of choice is the revised Perdew-Burke-Ernzerhof functional (RPBE) as this functional describes strong chemical interactions well [9,26–28]. The computational slab of rutile RuO_2 was made of four atomic layers with the bottom two being constrained in position as to emulate bulk material. The structure is further replicated twice along the y-axis such that the surface provides three *cus* sites and three *bridge* sites. A 10 Å vacuum is introduced above and below the structure to avoid unwanted self-interaction due to the periodic boundary conditions. All discussed structures were created by modification of this RuO_2 slab by the removal/addition of adsorbates and by replacement of metal atoms in the lattice (exchanging Ru for Mn). Due to the magnetic properties of manganese, the calculations were set to be spin polarized. A k-point mesh of (2,2,1) was used for Brillouin zone sampling and the plane wave energy cutoff was set to 500 eV. Each structure was then relaxed until the total forces went below 0.05 eV A^{-1}.

3. Results and discussion

3.1. Material characterization

Spray freeze freeze drying approach in Ru-Mn-O system yields single phase materials conforming to formula $Ru_{1-x}Mn_xO_2$ with x ranging between 0.0 and 0.2. All prepared materials were of black color apparently of nanocrystalline nature (see Fig. 1).

The X-ray diffraction patterns shown in Fig. 1 conform to tetragonal rutile type structure ($P4_2/mnm$). Although the oxides of both components (Ru and Mn) can form rutile type oxides (see patterns marked in Fig. 1) the actual position of the observed diffraction maxima corresponds rather to those of the RuO_2. Such a behavior can be expected given the chemical composition of the prepared phases which is dominated by Ru.

The analysis of the experimental diffraction pattern allows to elucidate the structural parameters which are listed in Table 1.

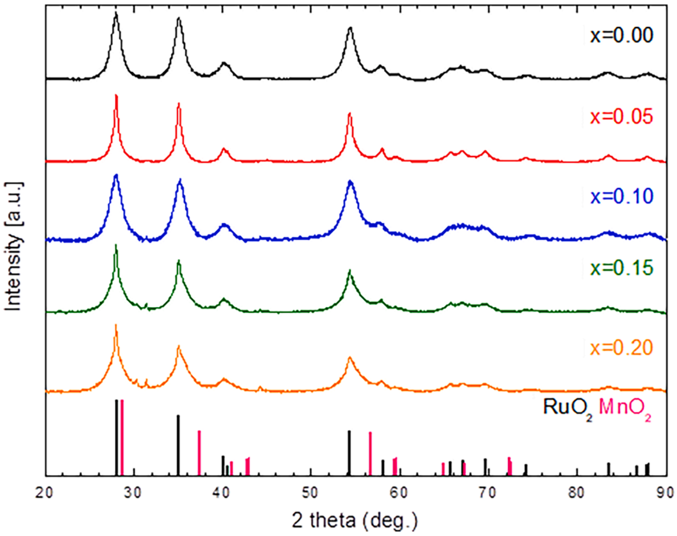

Fig. 1. XRD diffraction patterns of $Ru_{1-x}Mn_xO_2$ catalyst prepared by spray-freezing/ freeze-drying approach. The actual Mn content is indicated in the Figure legend. The diffraction patterns for reference compounds RuO_2 (blue) and MnO_2 (violet) are depicted as vertical bars.

Table 1
The parameters of the Retvield analysis of the diffraction patterns of $Ru_{1-x}Mn_xO$ catalysts.

X	*a* (Å)	c(Å)	*V* (Å^3)
0.00	4.498±0.001	3.096±0.001	62.661±0.019
0.05	4.496±0.001	3.108±0.001	62.836±0.021
0.10	4.505±0.003	3.088±0.002	62.676±0.070
0.15	4.501±0.001	3.099±0.001	62.788±0.028
0.20	4.498±0.001	3.081±0.001	62.330±0.028

As follows from Table 1 the change of the chemical composition has no clear projection into the structural parameters *a* and *c*. While the substitution of the Ru in the structure has apparently no effect on the lattice parameter in the x and y direction (parameter *a*), the incorporation of Mn, on the other hand, affects the arrangement of the structure along the z axis. This variation of the *c* parameter, however, does not show any clear correlation with the Mn content (see Fig. 2). At the same time the c/a ratio – a structural descriptor proposed for rutile type oxides in the literature [16] is composition independent (see Fig. 3). This

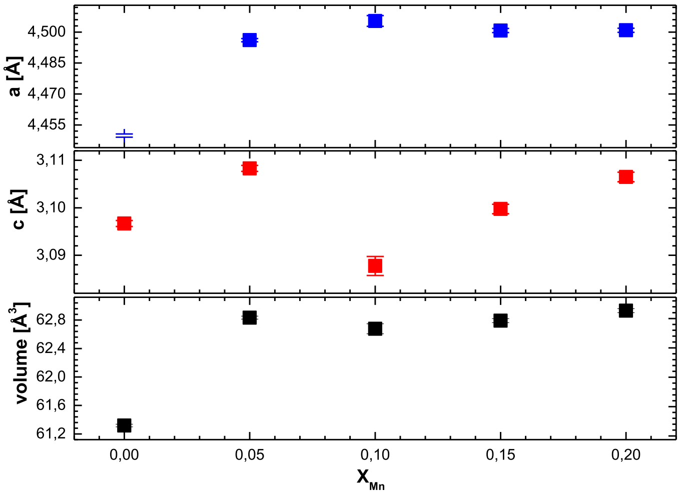

Fig. 2. Unit cell parameters and corresponding unit cell volume extracted fom XRD diffraction patterns of $Ru_{1-x}Mn_xO_2$ materials.

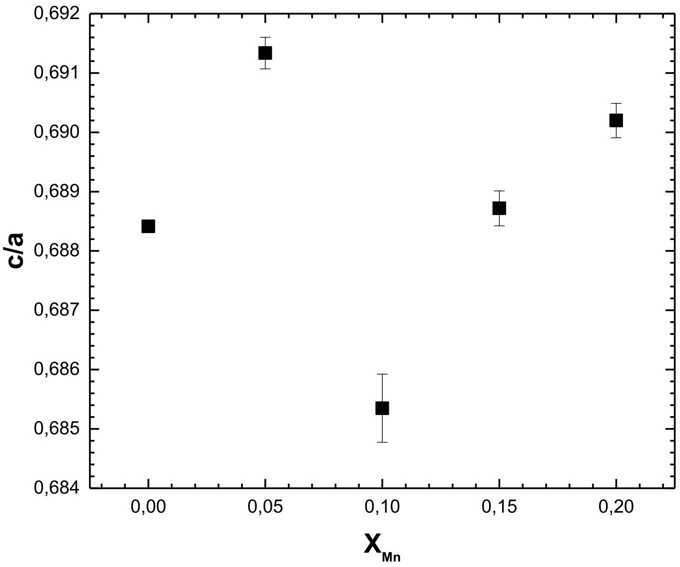

Fig. 3. c/a structural descriptor as a function of the chemical composition of $Ru_{1-x}Mn_xO_2$ materials.

contrasts with the behavior reported on similar systems conforming to $Ru_{1-x}Ni_xO_2$ composition. The absence of a clear trend in the c/a dependence on the chemical composition can be taken as an indication that Mn, in contrast to Ni, shows a decreased tendency to form clusters in the structure on sub-nanometer level and that the $Ru_{1-x}Mn_xO_2$ materials have a stronger tendency to retain the mixing of the cations present in the ice precursor in the spray freeze- freeze drying synthesis.

The character of the observed diffraction patterns suggests nanocrystalline nature of the prepared materials. More precise information regarding the actual particle size distribution can be extracted from the widths of the diffraction peaks (see Fig. 4) as well as by analysis of SEM micrographs (see Fig. 5). A closer analysis of the diffraction peaks, namely of the materials characterized by x higher than 0.1 reveals a complex nature of the prepared materials. The shape of the observed diffraction peaks clearly deviates from that expected for simple single phase indicating a coexistence of two phases differing primarily in coherent domain size. These two peaks coincide with their positions but significantly differ in their width (see Fig. 4). This type of behavior is observed for all diffraction maxima observed in diffraction patterns of $Ru_{1-x}Mn_xO_2$ with x higher than 0.1.

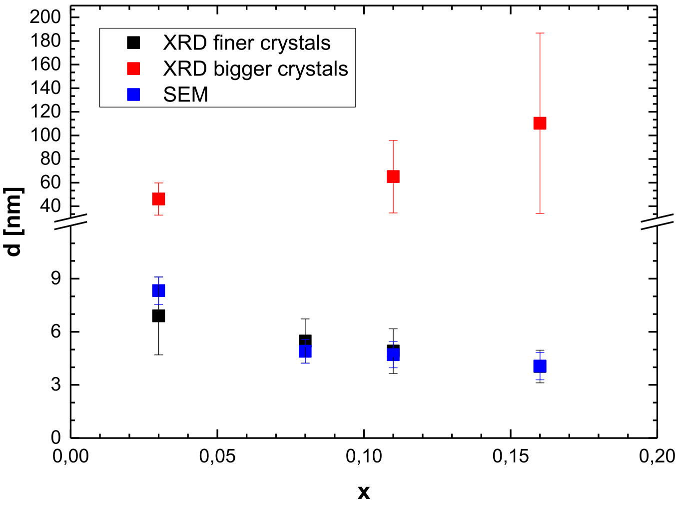

Fig. 4. Particle size (left) and coherent domain (right) size of the $Ru_{1-x}Mn_xO_2$ materials. Particle size values were extracted from SEM micrographs while the coherent domain sizes were extracted from diffraction patterns using a Scherrer formula.

In fact, a presence of two characteristic crystal shapes and sizes can be tracked also in the SEM micrographs (see Fig. 5). The prepared materials are mainly composed of rather small nanocrystals with characteristic particle size below 20 nm. This fine crystal fraction is, however complemented by relatively minor fraction of coarser bipyramidal nanocrystals the size of which increases from ca. 40 nm (in the case of $x = 0.05$) to 120 nm (in the case of $x = 0.20$). This increase of the large crystal size is also accompanied by a change of their characteristic shape which develops from bipyramidal one to an elongated one when a large prismatic part is capped with two rather insignificant pyramids. It needs to be noted that although the large nanocrystals are disproportionally underrepresented in all materials with x higher than 0.05, their coherent domain is significantly bigger than that of the small nanocrystals (responsible for most of the electrocatalytic behavior - see below) and they dominate the diffraction pattern namely for materials with x higher than 0.1. It needs to be noted that the characteristic coherent domain sizes obtained using the Scherrer formula for finer phases agree well with the characteristic particle size obtained by analysis of the SEM micrographs (see Fig. 5).

Comparing the characteristic particle sizes (based on SEM with coherent domain sizes) based on diffraction data one finds that the phases in Ru-Mn-O system tend to form nanocrystals smaller than pure RuO_2 prepared using the same synthetic procedure. The characteristic particle size decreases with increasing Mn content (from 7 nm for material with $x = 0.05$ to about 4 nm for material with x equal to 0.20) which seems to suggest a metastable nature of the Ru-Mn-O oxides which need to be stabilized by surface energy. The formation of large crystals in this context cannot be easily explained since, unfortunately, even in the case of the largest crystals it is rather difficult to investigate independently the chemical composition of this minority phase. Nevertheless, given the large disparity in the particle size of small and large nanocrystals, one may assume that the contribution of the large nanocrystals to the electrocatalytic behavior is negligible. The presence of the coarse nanocrystal fractions is also reflected in the BET based specific surface area values of the prepared materials which range between 35 and 52 m^2/g when the highest specific surface area is observed for materials with x equal to 0.1 which is apparently free of large nanocrystals.

3.2. *Electrochemical behavior*

All prepared Ru-Mn-O phases are active in electrocatalytic oxygen as well as chlorine evolution. The electrocatalytic activity of all prepared materials (complemented with that of pure RuO_2) in oxygen evolution is summarized in Fig. 6. As follows from the data shown in Fig. 6 the anodic activity of the Ru-Mn-O phases increases with increasing Mn content. The observed activity increase is linear in the range $0 < x < 0.15$ and starts to decrease for materials with higher Mn content. The observed trend reflects two possible effects which can be difficult to distinguish. The actual activity trend suggests that Mn substituting the Ru in the rutile structure is likely active in the oxygen evolution process or that it facilitates a formation of structural motifs enhancing the oxygen evolution with respect to that of pure ruthenium dioxide. In this respect one might assume that Mn, in contrast to, e.g. Ni or Co [16] can actively bind oxygen if present in *cus* sites. Alternatively, one cannot discount the possible effect of the low dimensionality sites – crystal edges and vertices, which are more frequently present at the surface of materials with higher x due to their smaller particle size.

The trend observed for electrocatalytic oxygen evolution is apparently replicated also for parallel oxygen and chlorine evolution in acid media (see Fig. 7). The presence of chlorides increases observed anodic activity in a linear way, the sensitivity of anodic activity of the Ru-Mn-O phases towards presence of chlorides, however, becomes less evident with increasing Mn content. The effect of the chloride presence is

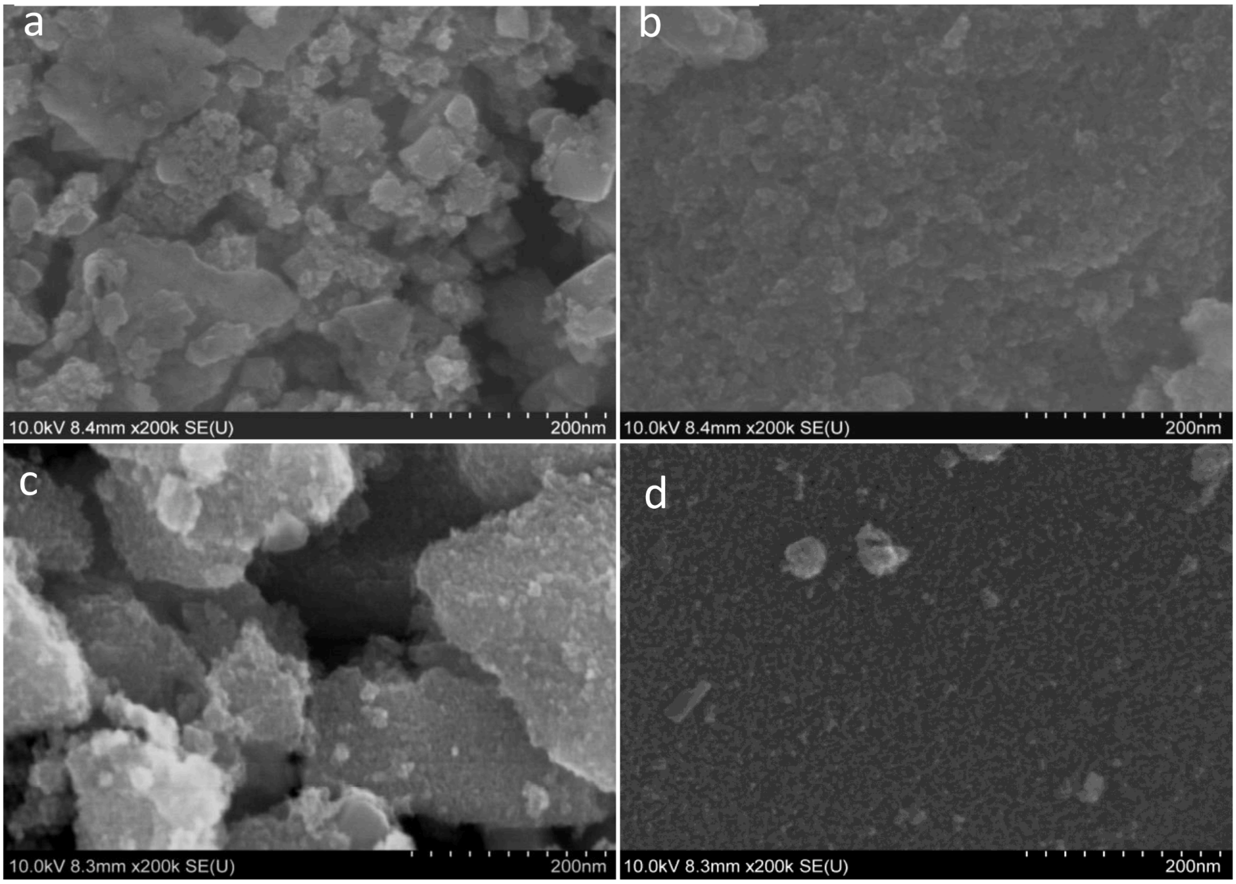

Fig. 5. SEM micrographs of the $Ru_{1-x}Mn_xO_2$ catalysts prepared by spray freeze - freeze drying approach with changing Mn content a) $x = 0.05$, b) $x = 0.1$, c) $x = 0.15$, d) $x = 0.2$.

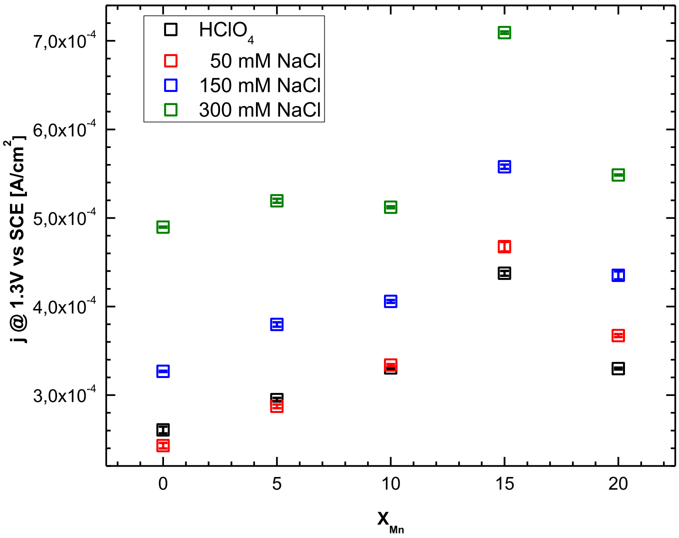

Fig. 6. Electrocatalytic activity $Ru_{1-x}Mn_xO_2$ materials in anodic gas evolution reactions. The activity is represented as a current density measured at 1.3 V vs. SCE in 0.1 M $HClO_4$ containing variable amount of chlorides. Actual chloride concentration is indicated in the Figure legend.

notable namely for materials featuring low Mn content ($x<0.1$). The pure RuO_2 shows a doubling of the observed anodic current upon introduction of chlorides in concentration of ca. 0.3 M. The incorporation of Mn into the RuO_2 structure suppresses chloride induced current increase to ca. 1.5.

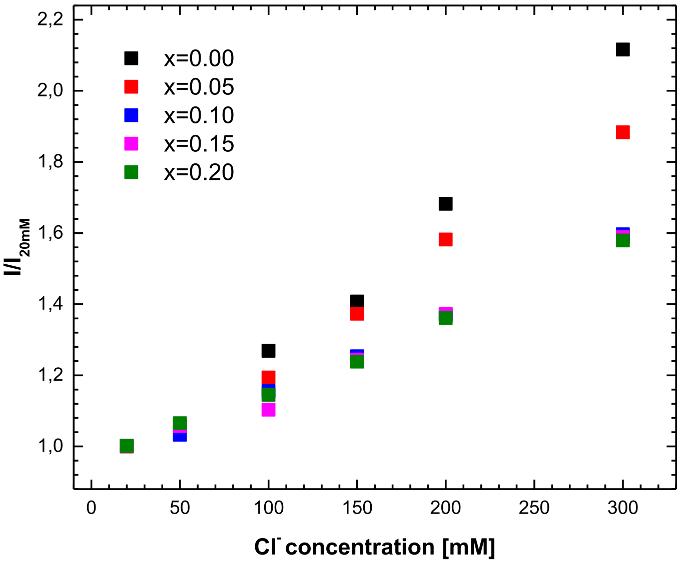

Fig. 7. Chloride concentration dependence of the anodic current on $Ru_{1-x}Mn_xO_2$ materials during cyclic voltammetry in 0.1 M $HClO_4$ containing variable concentration of NaCl. Actual measured currents are normalized by the current measured at the lowest chloride concentration (0.02 M).

This activity trend transcribes into selectivity data extracted from RRDE as well as DEMS experiments. In the case of the RRDE experiments the selectivity can be directly assessed from comparison of ring and disk currents as long as the ring potential is kept at a potential when one can reduce the produced chlorine while simultaneously preventing the oxygen reduction due to its kinetic hindrance (ORR does not proceed at potentials positive to 0.8 V vs. RHE).

Typical course of the disk and ring currents in the RRDE experiments following the selectivity of the Ru-Mn-O materials in parallel oxygen and chlorine evolution is depicted in Fig. 8.

It needs to be noted that disk current as well as ring current show in principle analogous course. Both the disk and ring current increase exponentially with potential at anodic potentials higher than 1.1 V vs. SCE. The recorded disk currents are 2 orders of magnitude higher than the corresponding ring currents. The ring to disk current ratio of ca. 0.01 is about 10 times lower than the collection factor of the RRDE setup (see above) suggesting that the anodic process is dominated rather by oxygen evolution than by chlorine evolution. Also the exponential increase of the ring current with electrode potential even at the lowest chloride concentrations suggests that the chlorine evolution process at the electrode is not transport limited and, therefore, reflects the intrinsic selectivity of the Ru-Mn-O surfaces. A typical anodic behavior of Ru-Mn-O materials for different chloride concentrations at pH 1, i.e., a comparison of the measured currents and of its oxygen and chlorine related contributions, for $Ru_{0.9}Mn_{0.1}O_{2-y}$ is shown in Fig. 9.

A comparison of the measured currents and contributions oxygen and chlorine partial currents for different catalysts compositions is summarized in Fig. 10.

As follows from Fig. 10 the observed increase of the measured current after addition of chlorides is practically attributable to chlorine evolution. The current corresponding to oxygen evolution remains practically unaffected by the presence of chlorides. This behavior is somewhat surprising since it essentially suggests that the thermodynamically allowed anodic processes – OER and CER – are in fact not competing and apparently proceed exclusively exploring different active sites present at the material's surface. This type of behavior is observed for all $Ru_{1-x}Mn_xO_2$ phases with $x>0.05$. Pure RuO_2 and Ru-Mn-O phases featuring low Mn content ($x \leq 0.05$), on the other hand, show a decrease of the OER related current at chloride concentrations higher than 0.1 M (see Fig. 10).

The data presented in Fig. 10 may be recalculated into selectivity parameter which shows the fraction of the charge being transferred into a particular gas evolving reaction. The selectivity towards CER is presented in Fig. 11. The selectivity data clearly show that although the selectivity towards chlorine evolution generally decreases with increasing Mn content there seems to be a weak minimum indicating the highest attained selectivity for oxygen evolution for material featuring 15% of cationic position occupied by Mn. It needs to be noted that this material pushes the chlorine evolution extent down to 30% even at significant chloride concentration of 0.3 M which makes it a prospective material for further optimization for selective OER in chloride containing media.

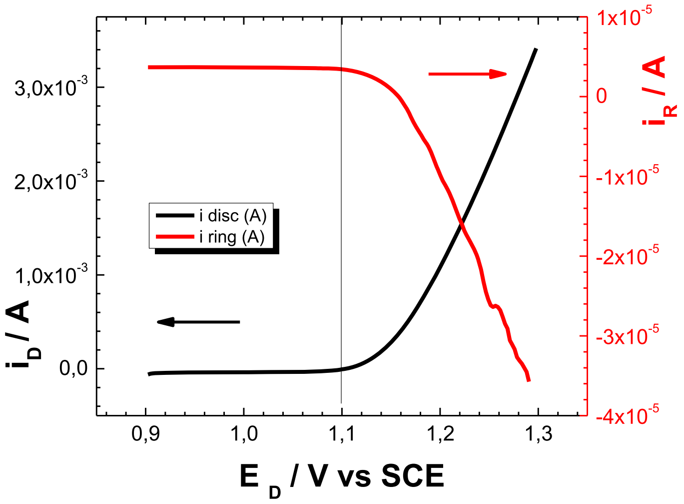

Fig. 8. Characteristic course of the disk current (left) and of the ring current (right) recorded during linear scan polarization of a $Ru_{0.9}Mn_{0.1}O_2$ catalysts deposited on a glassy carbon disk electrode in RRDE arrangement utilizing a Pt ring polarized at 0.9 V vs. SCE. The experiments were carried out in 0.1 M $HClO_4$ containing 0.1 M NaCl. The disk electrode was polarized at scan rate of 10 mV/s. The applied rotation rate was 1600 rpm.

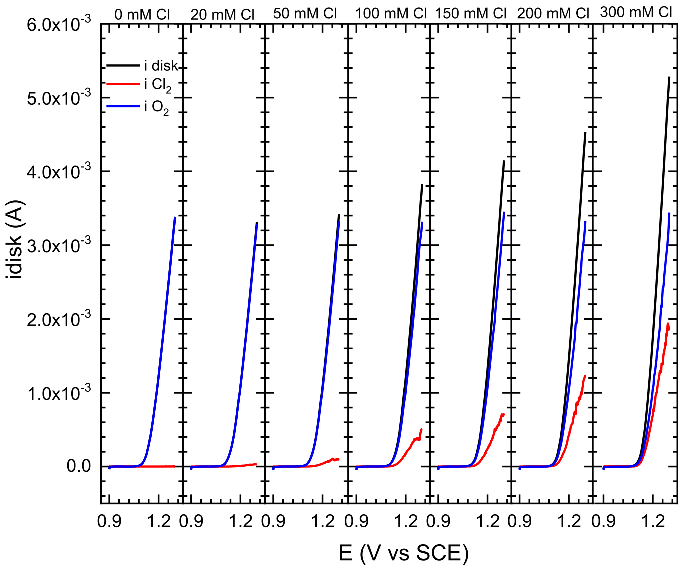

Fig. 9. Measured anodic disk current and its oxygen (blue) and chlorine (red) evolution related contributions for $Ru_{0.9}Mn_{0.1}O_2$ catalyst in 0.1 M $HClO_4$ containing variable amount of sodium chloride. The actual chloride concentration is indicated in the Figure legend. Actual experimental conditions were identical as shown for Fig. 8.

Qualitative difference in the selectivity behavior of pure RuO_2 and Ru-Mn-O phases can be further demonstrated comparing the order of chlorine evolution and oxygen evolution reactions for variable chloride concentration (see Fig. 12). The order of reaction for chlorine evolution clearly shows no significant difference between the behavior of the pure RuO_2 and Mn substituted materials. Regardless of the catalysts composition the order of chlorine evolution ranges between 1.4 and 1.8. The coincidence of the order of reaction of CER may suggest that the chlorine evolving mechanism is most likely the same on all studied materials. The order of oxygen evolution reaction on the other hand achieves negative value of -0.224 for pure RuO_2 while in the case of all Ru-Mn-O phases it attains a value close to 0. The observed trend in the order of OER with respect to chloride concentration suggests that the actual selectivity behavior is primarily affected by the oxygen evolution reaction, namely by its mechanism.

Even though the complexity of the OER mechanism cannot be understated (please refer to the dedicated reviews on the subject [29] for more detailed information), a simplified approach applicable for the purposes of this paper can be based on an assumption that OER may proceed by one of three reaction mechanisms which could be combined from the following elementary steps [30]:

$$\mathrm{S}+H_2O \rightarrow \mathrm{S}\text{–}OH + H^+ + e^- \tag{1}$$

$$\mathrm{S}\text{–}OH \rightarrow \mathrm{S}\text{–}O + H^+ + e^- \tag{2}$$

$$\mathrm{S}\text{–}O \rightarrow 2S + O_2 \tag{3}$$

$$\mathrm{S}\text{–}O + H_2O \rightarrow \mathrm{S}\text{–}OOH + H^+ + e^- \tag{4}$$

$$\mathrm{S}\text{–}OOH + H_2O \rightarrow \mathrm{S} + O_2 + H^+ + e^- \tag{5}$$

Where S marks an active site at the surface.

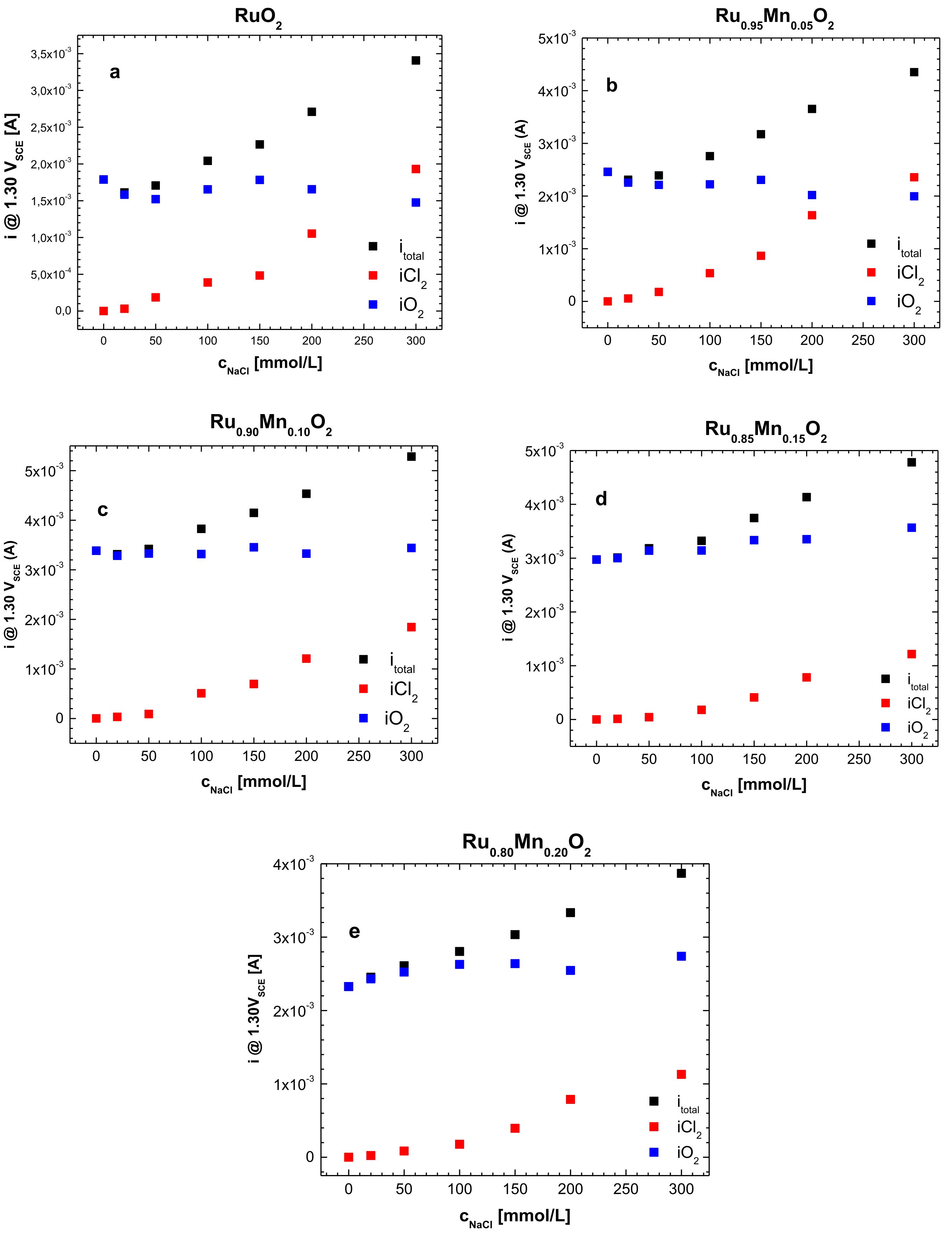

Fig. 10. Concentration dependence of the measured anodic disk current and its OER (blue) and CER (red) contributions for $Ru_{1-x}Mn_xO_2$ phases measured in 0.1 M $HClO_4$ containing variable amount of sodium chloride. The presented activity data were extracted from voltammetric experiments.

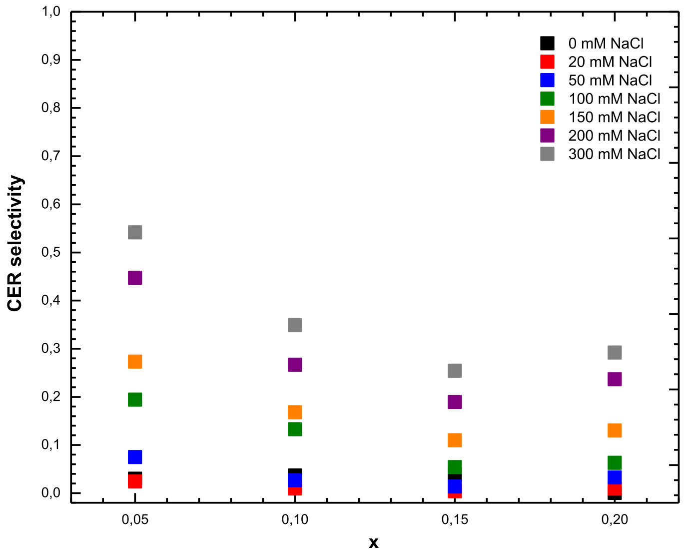

Fig. 11. Selectivity towards CER of the $Ru_{1-x}Mn_xO_2$ catalyst in acid media as a function of the chemical composition and chloride concentration. The selectivity data were extracted from voltammetric experiments illustrated in Figs 8 and 9. The experimental details were identical to those described for Fig. 8.

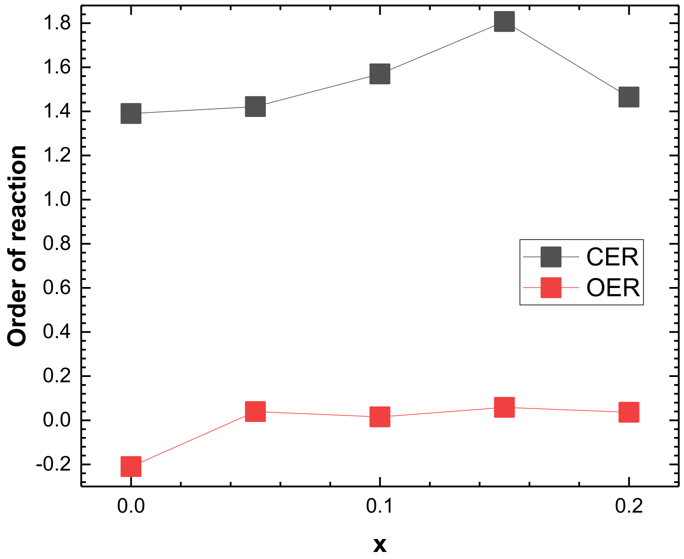

Fig. 12. Order of chlorine evolution (black) and oxygen evolution (red) reaction at 1.3 V vs Ag/AgCl with respect to chloride concentration extracted from voltammetric experiments on $Ru_{1-x}Mn_xO_2$ catalysts at pH 1. Actual experimental conditions were identical as shown for Fig. 7.

The reaction sequence (1)–(3) is conventionally denoted as Langmuir Hinshelwood mechanism. In the same manner we may take the reaction sequence (1), (2), (4), (5) as Elye Rideal mechanism of OER. It needs to be noted that in both these reaction mechanisms the evolved oxygen molecule contains only oxygen atoms originating from water. Both reaction mechanisms are also difficult to distinguish experimentally. An alternative reaction mechanism, which could be experimentally quantified is in the literature denoted as the Mars – Van Krevelen when the process of oxygen evolution involves an exchange of an oxygen atom between the electrolyte solution and catalysts' lattice resulting in the situation when evolved oxygen molecule contains at least one oxygen atom originally present in the catalysts lattice. This reaction mechanism is frequently denoted as a lattice oxygen activation (LOER) [31,32] and – aside of the experimentally proven involvement of the lattice oxygen – the theory assumes that formally proceeds via single site pathway outlined in the Elye Rideal mechanism.

The presence of the LOER mechanism can be quantified from OER experiments carried in isotopically labelled water when one follows the isotopic distribution in the produced oxygen. Given the natural isotopic distribution of oxygen one should expect that oxygen evolution in ^{18}O labelled water yields primarily $^{18}O_2$ molecules, which can be identified (and quantified) in differential electrochemical mass spectroscopy (DEMS) as a signal with characteristic *m/z* of 36. In the case when the LOER mechanism plays a significant role in oxygen evolution one should expect that the produced oxygen contains a significant fraction of $^{16}O^{18}O$ molecules which is characterized in produced oxygen by a signal with *m/z* of 34. It also needs to be noted that the fraction of the signal with *m/z* of 34 should decrease with time as the surface of the catalyst involved in LOER gets enriched and eventually dominated by ^{18}O.

A presence of the LOER for ruthenium dioxide-based materials has been reported previously and it was found to be dependent on the electrode potential as well as on the catalyst's morphology [33,34]. More relevant in the context of the above presented selectivity data of the Ru-Mn-O is a comparison of the behavior of Ru-Mn-O oxides featuring different amounts of Mn. A comparison of the isotopic distribution of the electrochemically produced oxygen is shown in Fig. 13. It needs to be stressed that in the case of potentiostatic oxygen evolution on $Ru_{0.95}Mn_{0.05}O_2$ the DEMS identifies a measurable fraction of $^{16}O^{18}O$ in the produced oxygen. The total extent of the LOER does not exceed 10 % of the produced oxygen. In the case of the Ru-Mn-O oxides featuring more than 10 % of Mn, on the other hand, one does not detect any measurable amounts of $^{16}O^{18}O$ suggesting that LOER does not contribute appreciably to the oxygen evolution. One may stress that the presence of the LOER coincides with enhanced selectivity of the Ru-Mn-O oxide towards chlorine evolution. In fact, a similar trend was tracked for Ru rich Ru-Ti-O phases [5].

The observed LOER tendency is difficult to rationalize since the Ru-Mn-O phases have never been systematically explored neither spectroscopically nor theoretically. A certain lead on the observed selectivity can be deduced from a simple computational analysis investigating the reactivity of theoretically conceivable oxygen intermediates on Ru-Mn-O surfaces and linking them with a probability of the LOER mechanism in Ru-Mn-O materials. Such an analysis can be done using (110) oriented surface of a rutile type oxide mimicking possible Mn arrangements characteristic for Ru-Mn-O phases. Generally, employing DFT one can determine the binding energy of oxygen species on the surface as

$$\Delta E_{0*} = E_{0*} + E_{H_2} - E_* - E_{H_2O} \tag{6}$$

where ΔE_{O^*} is the oxygen binding energy of interest, E_* is the DFT energy of the relaxed surface without the oxygen adsorbed, E_{O^*} is the energy of the surface with the adsorbate and E_{H_2} and E_{H_2O} are DFT reference values of hydrogen and water respectively [35,36]. For determination of the Gibbs free energy one has to include zero-point energy as well as entropic corrections to this value. However, these corrections are quite small in the case of oxygen intermediates [37]. When searching for potentially active lattice oxygen, the binding energy as calculated directly from the DFT energies should be sufficient. This binding energy for different oxygen species on a rutile (110) surface of Ru-Mn-O is presented in Fig. 14.

Although one may assume that the prepared materials feature only one type of the cationic position the projection of the structure to the (110) direction in fact differentiates two types of surface oxygen positions. The so called coordinatively unsaturated site (*cus)* position represents oxygen forming an apical Me-O bond where the O features two available bonds to interact in the interphase. This position is generally assumed to be active in the oxygen evolution reaction. The other conceivable surface position corresponds to oxygen which forms two equatorial Me-O bonds with the remaining electronic density forming one bond to interact in the interphase. This position is usually denoted as

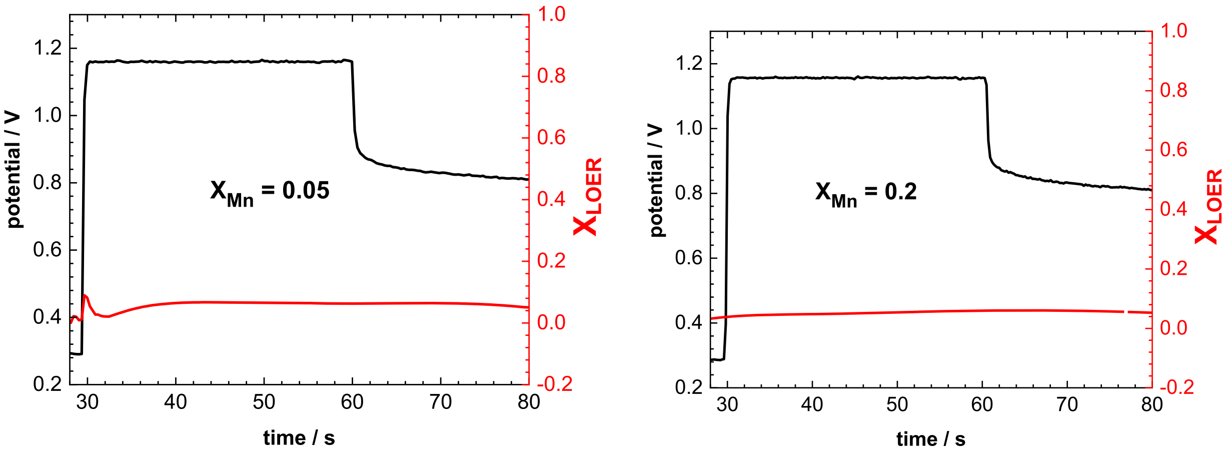

Fig. 13. Contribution of the lattice oxygen evolution reaction (LOER) to the oxygen evolution at 1.2 V vs Ag/AgCl in 0.1 M $HClO_4$ for $Ru_{0.95}Mn_{0.05}O_2$ (left) and $Ru_{0.80}Mn_{0.20}O_2$ (right) catalysts. The presented data were extracted from potentiostatic OER experiments in $H_2^{18}O$ labelled water. The fraction of the LOER is based on DEMS detection of the isotopic distribution of the produced oxygen and is presented along with the course of potential.

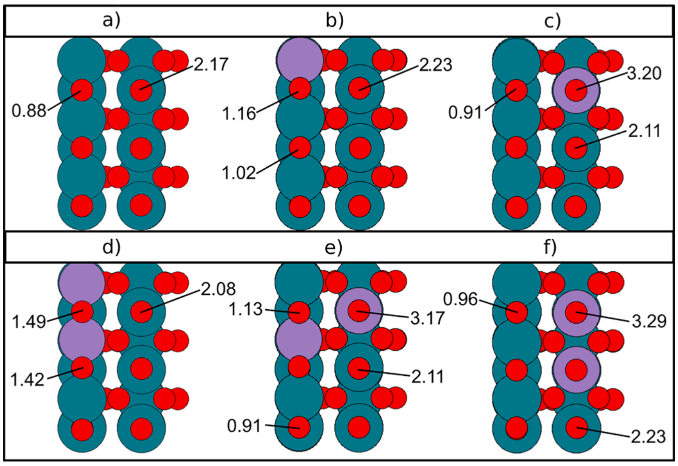

Fig. 14. DFT binding energies (in eV) of different surface oxygen species for rutile $Ru_{1-x}Mn_xO_2$ (110) across different surface configurations. **a**: Plain RuO_2. **b**: A single Mn atom in *bridge* position. **c**: A single Mn atom in *cus* position. **d**: Two Mn atoms in the *bridge*. **e**: One Mn atom in the *bridge* and one in the *cus* position. **f**: Two Mn atoms in the *cus* position. Teal atoms are ruthenium, fuchsia atoms are manganese and red atoms are oxygen. A volcano plot for this system can be found in the electronic supplementary material at https://nano.ku.dk/english/research/theoretical-electrocatalysis/katladb/rumno/.

bridging and is generally deemed as inactive in OER.

This general assignment is based on comparison of oxygen adsorption energies in *cus* and *bridge* positions. Fig. 14a shows the oxygen binding energies for the case of pure RuO_2. As is illustrated, the binding energy of oxygen in the *cus* position is significantly weaker than that for the one in the *bridge* position. One way to rationalize the activity of the *cus* site is to think of it as the weakest adsorbate in the surface, and therefore the most likely to leave the surface. The observed reactivity trend for RuO_2 suggests relatively low tendency of RuO_2 to employ the LOER mechanism in the oxygen evolution process since adsorption of oxygen into any conceivable position is unlikely to lead to a situation when the oxygen would remain (temporarily) immobilized at the electrode surface. The surface, excluding the active *cus* sites, is too stable.

The OER reactivity trends observed for pure RuO_2 are essentially replicated on Ru-Mn-O surfaces regardless of the specific arrangement the Mn may attain in the catalyst's surface (see Fig. 14). The binding of the oxygen in the *bridging* position is generally significantly stronger than in the *cus* position regardless of whether the *cus* site is occupied with Ru or Mn. Only for the case of Mn pairs in *bridge* positions is the neighboring Ru-Mn bridge site weakened (see Fig. 14d). These sites, however, are still not expected to be active at low overpotentials. It needs to be maintained that *cus* sites still represent the primary site for oxygen evolution at these conditions. The binding of oxygen adsorbates on manganese *cus* sites is significantly weaker than that of the ruthenium *cus* sites. Determining the activity of these sites via a volcano plot [38] finds that both the ruthenium and the manganese *cus* sites are indeed very active OER sites when taking into account that the proton might migrate to the bridge site for OH and OOH reaction intermediates [39]. This behavior could help to explain the observed experimental trend that OER activity increases with manganese content. The volcano plot is available in the electronic supplementary material.

In summary, the oxygen binding trends for all theoretically treated structural arrangements for Ru-Mn-O phases agrees with experimental observation of suppressed tendency of these materials to employ LOER in oxygen evolution as well as the tendency to increase activity with increasing Mn content. The weak contribution observed in labelled water experiments for materials featuring low Mn content (see Fig. 13) then can be attributed most likely to low dimensionality sites which are more frequently present at the surface of materials with finer particle sizes (see above).

It needs to be noted that although these DFT calculations support the experimental observation of suppressed LOER in oxygen evolution for materials selective of OER in presence of chlorides, they provide only limited insight into the nature of the active sites responsible for chlorine evolution (and LOER). This fact most likely just visualizes the blind spot of the simple model applied in this work, as we do not take into account low dimensionality sites (crystal edges and vertices) as well as to defects which might be present in the structure. The behavior of the Ru-Mn-O phases is in principle similar to that of the Ru-Ti-O phases despite their natural tendency for chlorine evolution.

4. Conclusions

The behavior observed for single phase nanoparticulate Ru-Mn-O oxides clearly outlines that in contrast to early theoretical predictions the selectivity of Ru based oxides in parallel oxygen and chlorine evolution can be controlled by material design. The selectivity of various Ru based oxides may be controlled not only by local structure as reported previously for Zn [4] and Ti [5] modified Ru oxides but also by chemical composition. In this light a modification of Ru oxides by incorporation of Mn leads to two effects – i) systematic increase in OER activity with an increase of the Mn content and ii) systematic shift of the selectivity towards OER in presence of chlorides. While the former trend may be in part attributed to the particle size effect independent of the chemical composition the role of the Mn present in the structure clearly stands out as the main driver of the observed trend in selectivity in parallel OER and CER. The RRDE and DEMS data clearly show that the OER and CER processes are not competing at Ru-Mn-O surfaces and the oxygen evolution process seems to be virtually unaffected on materials featuring Mn. The observed trend can be ascribed to a suppression of the lattice oxygen activation during OER on Ru-Mn-O surfaces. The DFT analysis further confirms that this LOER suppression is an intrinsic property of the R-Mn-O phase underscoring the control of the oxygen evolving mechanism in the selectivity control of the Ru based anodic materials intended for use in sea water electrolysis.

CRediT authorship contribution statement

Catalina Astudillo: Investigation, Writing – original draft. **Kateřina Minhová Macounová:** Formal analysis, Investigation, Project administration. **Adrian Malthe Frandsen:** Formal analysis, Investigation, Software. **Roman Nebel:** Investigation. **Jan Rossmeisl:** Conceptualization, Supervision, Writing – review & editing. **Petr Krtil:** Conceptualization, Formal analysis, Supervision, Writing – review & editing.

Declaration of Competing Interest

The authors declare that they have no known competing financial interests or personal relationships that could have appeared to influence the work reported in this paper.

Data availability

Data will be made available on request.

Acknowledgment

This work was supported by the Grant Agency of the Czech Republic under contract 21–03037S. The authors also acknowledge the assistance received through the research infrastructure NanoEnviCZ supported by the Ministry of Education, Youth and Sports of the Czech Republic under contract LM2018124. AMF and JR acknowledge support from the Danish National Research foundation DNRF149 and research grant 9455 from VILLUM FONDEN.

Supplementary materials

Supplementary material associated with this article can be found, in the online version, at doi:10.1016/j.electacta.2023.143295.

References

[1] W. Tong, M. Forster, F. Dionigi, S. Dresp, R.S. Erami, P. Strasser, A.J. Cowan, P. Farràs, Electrolysis of low-grade and saline surface water, Nature Energy 5 (2020) 367–377, https://doi.org/10.1038/s41560-020-0550-8.

[2] R. Balaji, B.S. Kannan, J. Lakshmi, N. Senthil, S. Vasudevan, G. Sozhan, A. K. Shukla, S. Ravichandran, An alternative approach to selective sea water oxidation for hydrogen production, Electrochem. Commun. 11 (2009) 1700.

[3] P. Farras, P. Strasser, A.J. Cowan, Water electrolysis – direct from the sea or not to be? Joule 5 (2021) 1921.

[4] V. Petrykin, K. Macounová, O.A. Shlyakhtin, P. Krtil, Tailoring selectivity for electrocatalytic oxygen evolution on ruthenium oxides by Zn substitution, Angew. Chem. Int. Ed. 49 (2010) 4813.

[5] Kateřina Minhová Macounová, Rebecca Katharina Pittkowski, Roman Nebel, Andrea Zitolo, Petr Krtil, Selectivity of Ru-rich Ru-Ti-O oxide surfaces in parallel oxygen and chlorine evolution reactions, Electrochim. Acta 420 (2022), 140878.

[6] W. Lee, T. Lee, S. Kim, S. Bae, J. Yoon, K. Cho, Descriptive role of Pt/PtOx ratio on the selective chlorine evolution reaction under polarity reversal as studied by Scanning Electrochemical Microscopy, ACS Appl. Mater. Interfaces 13 (2021) 34093.

[7] C.E. Finke, S.T. Omelchenko, J.T. Jasper, M.F. Lichterman, C.G. Ried, N.S. Lewis, M.R. Hoffmann, Enhancing the activity of oxygen evolution and chlorine evolution electrocatalysis by atomic layer deposition of TiO_2, Energy Env. Sci. 12 (2019) 358.

[8] Y. Liu, C. Li, C. Tan, Z. Pei, T. Yang, S. Zhang, Q. Huang, Y. Wang, Z. Zhou, X. Liao, J. Dong, H. Tan, W. Yan, H. Yin, Z.Q. Liu, J. Huang, S. Zhao, Electrosynthesis of chlorine from seawater-like solution through single atom catalysts, Nat. Commun. 14 (2023) 1.

[9] B. Hammer, L. Hansen, J. Nørskov, Improved adsorption energetics within density-functional theory using revised Perdew-Burke-Ernzerhof functionals, Phys. Rev. B 59 (1999) 7413.

[10] H. Hansen, I.C. Man, F. Studt, F. Abild-Pedersen, T. Bligaard, J. Rossmeisl, Electrochemical chlorine evolution at rutile oxide (110) surfaces, Phys. Chem. Chem. Phys. 12 (2010) 283.

[11] C. Malmgren, M. Hummelgård, J. Bäckström, A. Cornell, H. Olin, Nanoscale characterization of crystallinity in DSA® coating, J. Physics Conf. Series 100 (2008), 052026.

[12] R.K.B. Karlsson, H. Hansen, T. Bligaard, A. Cornell, L.G.M. Pettersson, Ti atoms in Ru0.3Ti0.7O2 mixed oxides form active and selective sites for electrochemical chlorine evolution, Electrochim. Acta 146 (2014) 733.

[13] K. Exner, J. Anton, T. Jacob, H. Over, Controlling selectivity in the chlorine evolution reaction over RuO2-based catalysts, Angew. Chem. Int. Ed. 53 (2014) 11032.

[14] P. Adiga, W. Nunn, C. Wong, A.K. Manjeshwar, S. Nair, B. Jalan, K.A. Stoerzinger, Breaking OER and CER scaling relations via strain and its relaxation in RuO_2 (101), Mat. Today Energy 28 (2022), 101087.

[15] D.F. Abbott, V. Petrykin, M. Okube, Z. Bastl, P. Krtil, Selective chlorine evolution catalysts based on Mg-doped nanoparticulate ruthenium dioxide, J. Electrochem. Soc. 162 (2015) H23.

[16] V. Petrykin, Z. Bastl, J. Franc, K. Macounova, M. Makarova, S. Mukerjee, N. Ramaswamy, I. Spirovova, P. Krtil, Local structure of nanocrystalline Ru1-x NixO2-δ dioxide and its implications for electrocatalytic behavior-an XPS and XAS study, J. Phys. Chem. C 113 (2009) 21657.

[17] R.K.B. Karlsson, A. Cornell, L.G.M. Pettersson, The electrocatalytic properties of doped TiO2, Electrochim. Acta 180 (2015) 514.

[18] J.G. Vos, Z. Liu, F.D. Speck, N. Perini, W. Fu, S. Cherevko, M.T.M. Koper, Selectivity trends between oxygen evolution and chlorine evolution on iridium-based double perovskites in acidic media, ACS Catal. 9 (2) (2019) 8561.

[19] J.G. Vos, T.A. Wezendonk, A.W. Jeremiasse, M.T.M. Koper, MnOx/IrOx as selective oxygen evolution electrocatalyst in acidic chloride solution, J. Am. Chem. Soc. 140 (2018) 1027.

[20] C.E. Frey, P. Kurz, Water oxidation catalysis by synthetic manganese oxides with different structural motifs: a comparative study, Chem. Eur. J. 21 (2015) 14958.

[21] N. Jiang, H. Meng, The durability of different elements doped manganese dioxide – coated anodes for oxygen evolution in sea water electrolysis, Surf. Coat. Technol. 206 (2012) 4362.

[22] K. Fujimura, T. Matsui, K. Izumiya, N. Kumagai, E. Akiyama, H. Habazaki, A. Kawashima, K. Asami, K. Hashimoto, Oxygen evolution on manganese–molybdenum oxide anodes in seawater electrolysis, Mater. Sci. Eng. A 267 (1999) 254.

[23] J.G. Vos, M.T.M. Koper, Measurement of competition between oxygen evolution and chlorine evolution using rotating ring-disk electrode voltammetry, J. Electroanal. Chem. 819 (2018) 260.

[24] M. Thomassen, B. Børresen, G. Hagen, R. Tunold, Chlorine reduction on platinum and ruthenium: the effect of oxide coverage, Electrochim. Acta 50 (2005) 1157.

[25] W.Q. Zaman, Z. Wang, W. Sun, Z. Zhou, M. Tariq, L. Cao, X.Q. Gong, J. Yang, Ni–Co codoping breaks the limitation of single-metal-doped IrO2 with higher oxygen evolution reaction performance and less iridium, ACS Energy Lett. 2 (2017) 2786.

[26] J. Enkovaara, C. Rostgaard, J.J. Mortensen, J. Chen, M. Dułak, L. Ferrighi, J. Gavnholt, C. Glinsvad, V. Haikola, H.A. Hansen, Electronic structure calculations with GPAW: a real-space implementation of the projector augmented-wave method, J. Phys. Condens. Matter 22 (2010), 253202.

[27] J.J. Mortensen, L.B. Hansen, K.W. Jacobsen, Real-space grid implementation of the projector augmented wave method, Phys. Rev. B 71 (2005), 035109.

[28] A.H. Larsen, J.J. Mortensen, J. Blomqvist, I.E. Castelli, R. Christensen, M. Dułak, J. Friis, M.N. Groves, B. Hammer, C. Hargus, The atomic simulation environment—A python library for working with atoms, J. Phys. Condens. Matter 29 (2017), 273002.

[29] J. Song, C. Wei, Z.F. Huang, C. Liu, L. Zeng, X. Wang, Z.J. Xu, A review on fundamentals for designing oxygen evolution electrocatalysts, Chem. Soc. Rev. 49 (2020) 2196.

[30] N. Bendtsen Halck, V. Petrykin, P. Krtil, J. Rossmeisl, Beyond the volcano limitations in electrocatalysis–oxygen evolution reaction, Phys. Chem. Chem. Phys. 16 (2014) 13682.

[31] T. Binninger, R. Mohamed, K. Waltar, E. Fabbri, P. Levecque, R. Kötz, T.J. Schmidt, Thermodynamic explanation of the universal correlation between oxygen evolution activity and corrosion of oxide catalysts, Sci. Rep. 5 (2015) 12167.

[32] E. Fabbri, T.J. Schmidt, Oxygen evolution reaction - the enigma in water electrolysis, ACS Catal. 8 (2018) 9765.

[33] M. Wohlfahrt-Mehrens, J. Heitbaum, Oxygen evolution on Ru and RuO_2 electrodes studied using isotope labelling and on-line mass spectrometry, J. Electroanal. Chem. 237 (1987) 251.

[34] K.A. Stoerzinger, O. Diaz-Morales, M. Kolb, R.R. Rao, R. Frydendal, L. Qiao, X. R. Wang, N.B. Halck, J. Rossmeisl, H.A. Hansen, T. Vegge, I.E. Stephens, M.T. M. Koper, Y. Shao Horn, Orientation-dependent oxygen evolution on RuO_2 without lattice exchange, ACS Energy Lett. 2 (2017) 876.

[35] J. Rossmeisl, Z.W. Qu, H. Zhu, G.J. Kroes, J.K. Nørskov, Electrolysis of water on oxide surfaces, J. Electroanal. Chem. 607 (2) (2007) 839.

[36] J.K. Nørskov, J. Rossmeisl, A. Logadottir, L. Lindqvist, J.R. Kitchin, T. Bligaard, H. Jónsson, Origin of the overpotential for oxygen reduction at a fuel-cell cathode, The J. Phys. Chem. B 108 (2004) 17886.
[37] J. Rossmeisl, A. Logadottir, J.K. Nørskov, Electrolysis of water on (oxidized) metal surfaces, Chem. Phys. 319 (2005) 178.
[38] I.C. Man, H.Y. Su, F. Calle-Vallejo, H.A. Hansen, J.I. Martínez, N.G. Inoglu, J. Kitchin, T.F. Jaramillo, J.K. Nørskov, J. Rossmeisl, Universality in oxygen evolution electrocatalysis on oxide surfaces, ChemCatChem 3 (2011) 1159.
[39] S. Divanis, A.M. Frandsen, T. Kutlusoy, J. Rossmeisl, Lifting the discrepancy between experimental results and the theoretical predictions for the catalytic activity of RuO_2 (110) towards oxygen evolution reaction, Phys. Chem. Chem. Phys. 23 (2021) 19141.

4.3 Discussion of computational LOER identification

The challenge with computational approaches to LOER tendency identification is that the exact origin of evolved "lattice oxygen" is unknown. The DEMS quantification of MvK is done during OER in isotope labeled water, $H_2{}^{18}O$, and thus it measures whether evolved oxygen comes from the sample (evolved as $^{16}O^{18}O$), or the electrolyte (evolved as $^{18}O_2$). In this regards, the oxygen could be more correctly labelled as "trackable", as there is no guarantee that it is even from the lattice. While this makes it difficult to model, it also highlights the importance of theory in relation to the understanding of the behaviour.

A Sabatier style analysis cannot tell the difference between LOER and OER active sites, as it is difficult to know which surface sites are populated by oxygen at the moment before being put into experimental conditions. The pure rutile RuO_2 (110) surface only has two (three if we are generous) different kinds of exposed oxygen: CUS, bridge (and sublattice). With CUS oxygen being easily evolvable, and bridge oxygen being strongly bound, it makes sense to identify one as lattice oxygen and the other as coming from the electrolyte. There is however no clear cutoff between what would be part of a real sample, and what would be present as a function reaction conditions (i.e. from the electrolyte). Imagine now a bridge site with binding energetics similar to that of the pure RuO_2 CUS site. Both of these active sites would be plotted identically on the Sabatier volcano, and they would be expected to behave similarly. Does this imply that both sites are empty from preparation? Even though this is an extreme example, these are the questions that arise when dopants are introduced in the structure. The surface becomes heterogeneous, resulting in distributions of oxygen binding energies, and weakened oxygen species. The computational screening approach introduced in this chapter therefore works mainly by the prediction of oxygen vacancy stabilization, which has been shown to correlate with LOER tendency in specifically perovskites [36, 62]. Additionally, the LOER tendency can be seen as linked to the weakening of oxygen species in the sample.

A conceptualization of LOER as due to distributions of weakened oxygen species can explain the experimental relation between surface defects / material morphology and LOER tendency [60]. When surface deformation or defects are high, the pristine crystal structure is disturbed, creating the distributions of weakened oxygen species that can be evolved as LOER. This would explain why initial studies found significant LOER tendency in RuO_2 [35], whereas newer experiments on well characterized and even oriented nanocrystals found the opposite [64, 65]. In this way, the messier the sample, the higher the LOER tendency.

5 What determines the binding energy of intermediates on oxides?

As discussed in section 3.2, ΔG_2 is a good bond strength descriptor for the Sabatier-style analysis of OER. Unfortunately, despite its efficacy, it does not convey any design principles for the control of binding energies along the OER reaction pathway. Ideally, the bond strength descriptor would be directly correlated to a controllable parameter, such that it provides a variational design principle for catalysts. Due to this, there has been substantial interest in understanding the physical origin of adsorbate binding energies [66].

5.1 Historical perspective

Between 1995 and 1997 Jens Nørskov and Bjørk Hammer wrote a series of publications outlining their Hammer-Nørskov d-band model of adsorbate binding on noble- and transition metals [67, 68, 69, 70, 71]. Based on DFT calculations, the model states that the oxygen binding energy is linearly dependent on the energy difference between the d-band of the metal and the Fermi level of the material. In an article from 2006 Hammer showcased the descriptive power of the model by applying it to a system of MgO-supported Pd thin film [72].

For oxides, a corresponding well-defined model has proven elusive [66]. In 2005 Pacchioni et al. studied systems of metal supported Mg-oxide films computationally [73, 74]. It was found that adsorbates with a high electron affinity (Au, Ag) become charged when the oxide has metal support. This is in contrast to Pd, which remains unchanged from adsorption on pure MgO. The effect was attributed to the outermost s-orbitals of Ag/Au being just below the Fermi level of the metal support (Mo), incentivizing electron tunneling through the insulating oxide. The 5s orbitals of Pd was found to be just above the metal support Fermi level, explaining the difference in charging. The effect was shown to correlate with the change in work function of the Mo support upon oxide deposition. Frondelius et al. did a similar study with oxide films (MgO and Al_2O_3) on a range of different transition metal supports. They investigated Au atoms, Au clusters, and NO_2 binding, finding that when the oxide is supported, the binding energies increase [75]. They additionally noted that low work function is generally associated with high adsorption energies.

In 2011 Suntivich et al. demonstrated correlation between σ^*-orbital occupation and ORR activity for perovskite oxides in low-temperature aqueous environments [76]. Later the same year, Lee et al. demonstrated that oxygen surface exchange in perovskites are strongly correlated to the oxygen p-band center (as relative to the Fermi level) [77]. This has since been shown to also hold true for hydrogen adsorption on oxygen in oxides [78], and just in general for ligand p-bands in inorganic compounds [79]. At the end of 2011 Suntivich et al. published another article, showcasing how electron occupancy of e_g-symmetry d-orbitals for B-site metals in perovskites serves as a good descriptor for the Sabatier bond strength [80]. This idea was further expanded upon by Calle-Vallejo et al. in 2013 [81]. They identified the number of outer electrons in transition metal (oxides) as a great descriptor for adsorption processes, producing linear trends in binding energy.

Finally, recent results of Garcés-Pineda et al. identify electronic "push and pull" effects in Fe-Ni-Zn spinel oxides between the Zn/Fe and Ni, allowing for some degree of tuning the overpotential by substituting Zn with Ni and vice versa [82]. Resulting from this, they produce a volcano plot dependent on chemical composition.

5.2 Activating TiO_2

Understanding the exact electronic descriptors of adsorbate binding on oxides could provide new avenues of catalyst design. It could for example allow for the activation of stable otherwise inactive oxides. Stable and abundant oxides like TiO_2 are ideal for the harsh conditions of acidic OER. Despite the inactivity of TiO_2 [83], studies have pointed towards Ti as the active site on DSAs for chlorine evolution [58, 84]. This showcases that it should be possible to engineer TiO_2 into being active.

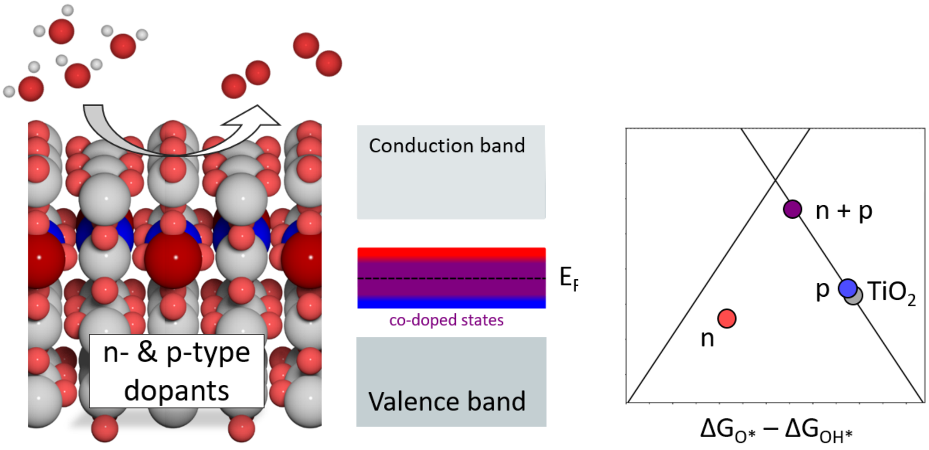

Reproduced from Ref. [85] with permission from the Royal Society of Chemistry.

5.3 Article 4: Synergistic effect of p-type and n-type dopants in semiconductors for efficient electrocatalytic water splitting

There are many studies doping TiO_2 in an attempt to enhance the electrochemical activity [86, 87, 88], and while increased activity is observed, the resulting catalysts are still nowhere good enough for commercial use. Despite this, substitutional codoping studies of TiO_2 with simultaneous n- and p-type dopants seem beholden to other fields like photocatalysis [89, 90, 91].

In the present computational and experimental study, co-substitution is applied to electrocatalysis, specifically TiO_2 and perovskite $SrTiO_3$. Using vanadium as n-type dopant and rhodium as p-type dopant, DFT analysis finds that TiO_2 is greatly activated by codoping. For both TiO_2 and $SrTiO_3$ the overpotential of the co-doped system lies in between that of solely n- or p-doped structures on the OER volcano plot. For $SrTiO_3$, the solely n-doped system is more active than the co-doped case. Additional A-site substitution with Ba, reactivates the co-doped perovskite to match the n-doped case.

Expanding the analysis to include more n-type (V, Nb, Ta, Mo, W) and p-type (Rh, Mn, Pd, Ru) dopants finds that the activation of TiO_2 is a general trend during codoping. Additionally, the volcano positions of intermediates can be somewhat tuned by adding additional dopants.

The locality of the dopant effects are investigated by varying dopant distance to the active site, resulting in a linear correlation between the inverse distance to binding site and the binding energy of the adsorbate.

For experimental verification, (co-)substituted nanoparticles were prepared by the spray-freeze freeze-drying approach. The synthesized materials were of the anatase polymorph as determined by XRD. Ultraviolet-visible (UV-vis) spectroscopy shows significant difference in the electronic structures between the pure anatase TiO_2 and the doped species. The spectra of co-doped species look similar to conductors, thus reproducing the theorized conductivity trend observed in calculation. As for the catalytic activity, only co-doped structures show increased OER activity, with Mn/Co exhibiting the highest activity.

Synergistic effect of p-type and n-type dopants in semiconductors for efficient electrocatalytic water splitting

Tugce Kutlusoy, Spyridon Divanis, Rebecca Pittkowski, Riccardo Marina,
Adrian M. Frandsen, Kateřina Minhová Macounová, Roman Nebel, Dongni Zhao, Stijn
F. L. Mertens, Harry Hoster, Petr Krtil and Jan Rossmeisl

Article reproduced from [85] with permission from the Royal Society of Chemistry.

Article and supplementary material available at DOI:

https://doi.org/10.1039/D2SC04585K

Chemical Science

ROYAL SOCIETY OF CHEMISTRY

EDGE ARTICLE

View Article Online
View Journal | View Issue

Check for updates

Cite this: *Chem. Sci.*, 2022, **13**, 13879

All publication charges for this article have been paid for by the Royal Society of Chemistry

Synergistic effect of p-type and n-type dopants in semiconductors for efficient electrocatalytic water splitting†

Tugce Kutlusoy,‡[a] Spyridon Divanis, ‡[a] Rebecca Pittkowski, [ab] Riccardo Marina,[c] Adrian M. Frandsen, [a] Katerina Minhova-Macounova, [b] Roman Nebel,[b] Dongni Zhao,[d] Stijn F. L. Mertens,[d] Harry Hoster, [de] Petr Krtil [b] and Jan Rossmeisl *[a]

Received 17th August 2022
Accepted 4th October 2022

DOI: 10.1039/d2sc04585k

rsc.li/chemical-science

The main challenge for acidic water electrolysis is the lack of active and stable oxygen evolution catalysts based on abundant materials, which are globally scalable. Iridium oxide is the only material which is active and stable. However, Ir is extremely rare. While both active materials and stable materials exist, those that are active are usually not stable and *vice versa*. In this work, we present a new design strategy for activating stable materials originally deemed unsuitable due to a semiconducting nature and wide band gap energy. These stable semiconductors cannot change oxidation state under the relevant reaction conditions. Based on DFT calculations, we find that adding an n-type dopant facilitates oxygen binding on semiconductor surfaces. The binding is, however, strong and prevents further binding or desorption of oxygen. By combining both n-type and p-type dopants, the reactivity can be tuned so that oxygen can be adsorbed and desorbed under reaction conditions. The tuning results from the electrostatic interactions between the dopants as well as between the dopants and the binding site. This concept is experimentally verified on TiO_2 by co-substituting with different pairs of n- and p-type dopants. Our findings suggest that the co-substitution approach can be used to activate stable materials, with no intrinsic oxygen evolution activity, to design new catalysts for acid water electrolysis.

Introduction

Large-scale exploration of renewable energy is vital for new sustainable energy concepts, meeting the requirement to remove the dependence on fossil fuels. Renewable energy, based on wind or solar, is affordable but suffers from their intrinsic intermittent nature and inconvenient regional distribution. These inherent disadvantages need to be mitigated by the design of novel energy storage concepts based on chemical bonds.[1]

Molecular hydrogen seems to be one of the primary candidates for a new energy storage system and energy vector.[2] The only H_2 production process fully compatible with carbon neutrality and sustainability requirements is water electrolysis, which converts electricity into chemical energy by splitting H_2O into oxygen and hydrogen. Despite significant efforts devoted to its optimization, water electrolysis still needs to be fundamentally improved in terms of efficiency and durability.[1,2]

Water electrolysis can be performed both in alkaline as well as in acid environments.[3–7] Regardless of pH, the efficiency of the overall process is controlled by the sluggish kinetics of the oxygen evolution reaction (OER) at the anode.[8]

Water electrolysis in acid media would in many cases be favored over that in alkaline media, because of more facile kinetics of the cathodic hydrogen evolution, high electrolyte conductivity, and high voltage efficiencies at high current densities.[9] Despite being technologically promising, the use of acid water electrolyzers is limited by a lack of affordable, active, and sufficiently stable OER catalysts.[10]

The catalysts showing the best trade-off between durability and performance in oxygen evolution in acid media are oxides

---

[a] *Center of High Entropy Alloy Catalysis, Department of Chemistry, University of Copenhagen, Universitetsparken 5, København Ø, 2100, Copenhagen, Denmark. E-mail: jan.rossmeisl@chem.ku.dk*

[b] *J. Heyrovsky Institute of Physical Chemistry, Academy of Sciences of the Czech Republic, Dolejskova 3, Prague 18223, Czech Republic*

[c] *New Application Research, Research and Development Division, Industrie De Nora S.p.A., 20134 Milan, Italy*

[d] *Department of Chemistry, Energy Lancaster and Materials Science Institute, Lancaster University, Lancaster LA1 4YB, UK*

[e] *Fakultät für Ingenieurwissenschaften, Lehrstuhl Energietechnik, Universität Duisburg-Essen, Lotharstra. 1, 47048 Duisburg, Germany*

† Electronic supplementary information (ESI) available. See DOI: **https://doi.org/10.1039/d2sc04585k**

‡ Both authors contributed equally to this manuscript.

based on Ir or Ru.[7,11] The low abundance and high price of these materials make the acid water electrolysis process practically unscalable.[12,13]

This fact stresses the importance of developing novel OER catalysts that are active, stable, and scalable for acid media oxygen evolution.[14] The most straightforward improvement of feasibility can be achieved by an improvement of the stability while reducing or replacing the noble metal content in the catalysts.[15,16]

One can summarize the OER process as a sequence of four consecutive one-electron/proton transfer steps, which require the formation of three surface confined intermediates.[17,18] The individual reaction steps are:

$$H_2O + * \rightarrow HO* + H^+ + e^- \tag{1}$$

$$HO* \rightarrow O* + H^+ + e^- \tag{2}$$

$$H_2O + O* \rightarrow HOO* + H^+ + e^- \tag{3}$$

$$HOO* \rightarrow * + O_2 + H^+ + e^- \tag{4}$$

In an ideal catalyst all reaction intermediates, HO*, O*, and, HOO*, bind on the surface in such a way that all reaction steps (1)–(4) take place at the equilibrium potential of 1.23 V (*i.e.*, each reaction step is driven by the energy of 1.23 eV).

The main factor limiting the process optimization of water oxidation is the scaling relation between the first [HO*] and the third intermediate [HOO*].[19–21] As both intermediates bind identically to the surface, a constant difference in adsorption energies of 3.2 eV is obtained, regardless of catalyst material. This situation greatly deviates from the ideal case where the difference in HO* and HOO* adsorption energies should equal 2.46 eV.[19,20] The validity of the scaling relation has been shown also experimentally.[22,23]

To avoid the feasibility restrictions of the state-of-the-art OER catalysts based on Ir and Ru discussed above, we propose an alternative approach: activating semiconducting materials like, *e.g.*, TiO_2, to form potent OER catalysts of high stability. The stability of many semiconducting oxides is inherently related to their wide bandgap, which, in turn, leads to low catalytic activity. The poor performance of TiO_2, chosen as a model semiconductor, in electrochemical water oxidation is well established.[24–29] Doping TiO_2 to increase its OER activity is also a well-established technique.[28–33]

This work demonstrates the activation of TiO_2 for OER catalysis by subsituting Ti-atoms with both n- and p-type dopants.[34–36] Such co-substitution has never been – to the best of our knowledge – applied in electrocatalysis. Here, we present a theoretical approach outlining a systematic way to improve the catalytic activity of semiconductors through co-substitution. The co-substitution approach optimizes the trade-off between stability and activity by preserving the intrinsic stability of the semiconducting material while increasing its activity because of the electronic states created by the dopants. The theoretical predictions are experimentally verified on model catalysts based on co-substituted TiO_2.

Results and discussion

Co-substitution approach

For semiconducting oxides, any computational approach needs to avoid finite-size effects leading to computational artefacts[20]. With the elimination of the finite size effect, it is possible to computationally assess activity trends of heavily substituted semiconductors, *e.g.* TiO_2, and position these materials on the theoretical OER activity volcano to draw a comparison with other materials. The mechanism of TiO_2 activation *via* co-substitution is shown on the rutile polymorph to maintain structural similarity with the state-of-the-art OER catalysts in acid media (RuO_2, IrO_2).

The poor conductivity of TiO_2 can be improved by n-type substitution (*i.e.*, by adding donors of electrons), which can directly provide electrons to the conduction band (CB) or create states in the bandgap close to the CB edge. The effect of the n-type dopants can be demonstrated on a model system, where TiO_2 is substituted with V. Extending the analysis to p-type substituted TiO_2 (*i.e.*, introducing acceptors of electrons *e.g.*, Rh) one finds a different type of behavior. p-Type dopants increase the probability of forming a hole in the valence band (VB). In other words, p-type dopants deplete the electron density of the VB forcing the Fermi level to move close to the electronic states created by the p-type dopants. The effect of substitution on the TiO_2 electronic structure is schematically depicted in Fig. 1, which shows the projected density of states (pDOS) of the TiO_2 rutile structure substituted with n-type (V) and p-type dopant (Rh), as well as the co-substituted structure (V + Rh). Both substituting and co-substituting the TiO_2 with Rh and V create states in the bandgap, which due to their occupancy may interact with the reactant water molecules. These newly created states may eventually (in the case of co-substitution) form a new, rather narrow, electronic band that crosses the Fermi level. In this way, the electronic structure of the co-substituted TiO_2 resembles that of a conductor. The behavior of the Fermi level, which varies according to the type of dopant introduced, is following literature.[37]

Creating these pseudo-conductor states in the bandgap of a stable, essentially semiconducting, material such as TiO_2 has a fundamental impact on the catalytic behavior of these materials. The substitution/co-substitution approach allows, along with conductivity optimization, tuning of the surface reactivity. Most n-type dopants can easily provide an electron to the binding site. Combining n- and p-type dopants leads to a situation when it becomes increasingly difficult for electrons to leave the dopant complex and participate in the surface binding. Therefore, the co-substitution strategy may be able to make stable semiconducting oxides active for OER catalysis (see Fig. 2).

The OER free energy diagrams presented in Fig. 3a identify the oxidation of HO* to O* as the potential determining step (PDS) for pristine TiO_2 (eqn (2)). This places the rutile polymorph of TiO_2 on the weak binding branch of the OER activity volcano (see Fig. 3b, grey). The n-type dopants change the PDS from the HO* → O* oxidation to O* → HOO*. This shifts the n-

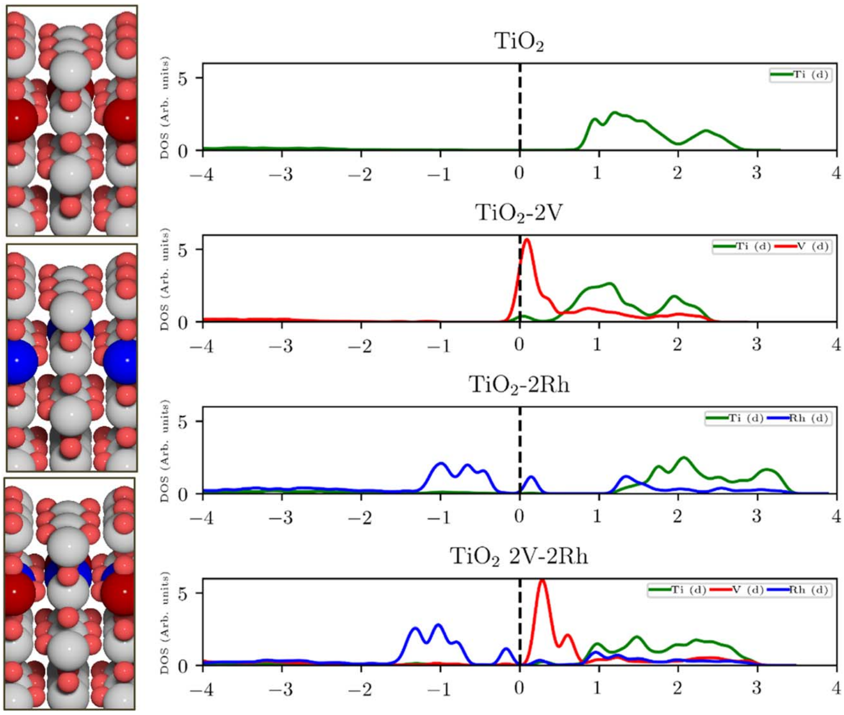

Fig. 1 Projected density of states (pDOS) of pristine and substituted TiO$_2$ and corresponding atomic structures of rutile-type TiO$_2$ (110) with V (red), Rh (blue) (from top to bottom: n-substituted, p-substituted, co-substituted). pDOS from top to bottom: pristine TiO$_2$; V-substituted TiO$_2$: the V d-states intersect with the Fermi level. The majority of the states is located at energies above the Fermi level; Rh-substituted TiO$_2$: the Rh d-states are located mostly around the Fermi level and also at higher energies above the Fermi level; and V–Rh co-substituted TiO$_2$. The dopants' d-states populate the bandgap and are placed around the Fermi level.

substituted TiO$_2$ from the weak binding branch to the strong binding branch of the activity volcano (Fig. 3b, red data point). Hence, n-type substitution makes the rutile structure highly reactive resulting in too strong oxygen adsorption. This causes an accumulation of chemisorbed oxygen intermediates eventually blocking the surface. After blocking the surface, the activity of the n-type substituted rutile does not differ from that of pristine TiO$_2$ (see Fig. 3b).

DFT analysis of the effect of p-type dopants on the theoretically assessed OER activity places the p-substituted TiO$_2$ on the weak binding side of the volcano and the predicted activity shows only a marginal improvement over that of pristine TiO$_2$. Therefore, in conclusion, the substitution of TiO$_2$ with a single type of dopant does not improve its OER activity since (i) the n-type substitution causes primarily an accumulation of strongly chemisorbed oxygen on the surface and (ii) the activity of the p-type substituted materials does not significantly change the activity of the original material.

After examining the effect of both p-type and n-type substitution on the OER activity of the TiO$_2$ surface, one may naturally consider simultaneous co-substitution of n- and p-type elements. The OER-related catalytic activity of the co-

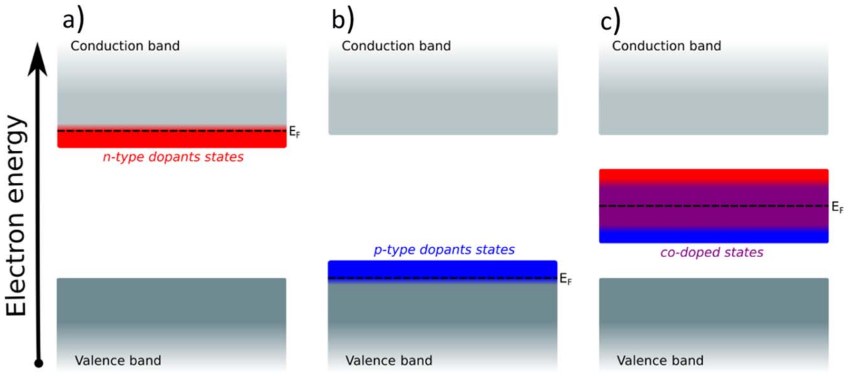

Fig. 2 (a) Insertion of an n-type dopant in a semiconductor, (b) insertion of a p-type dopant in a semiconductor, (c) simultaneous insertion of an n-type and a p-type dopant in a semiconductor and the creation of the compensated electron states.

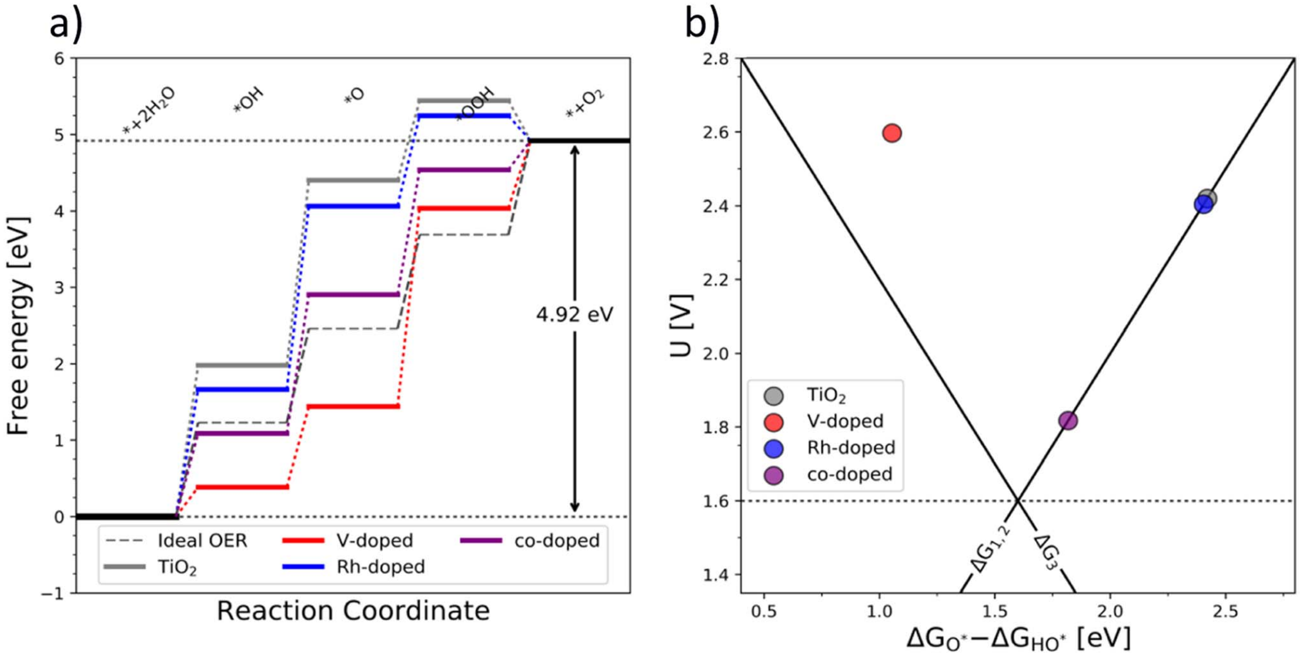

Fig. 3 (a) Free energy diagram of the pure (grey), single substituted (blue – Rh and red – V), and co-substituted (purple) TiO_2 and (b) the corresponding activity volcano depicting the increased catalytic performance of the co-substituted structure.

substituted TiO_2 is represented in Fig. 3 by the purple-colored data. The theoretical activity of co-substituted TiO_2 significantly differs from those of pristine as well as n- and p-type substituted TiO_2. The theoretical prediction places the co-substituted TiO_2 on the weak branch of the volcano; however, the theoretical overpotential is greatly reduced, mainly due to an optimized binding of the O* intermediate (Fig. 3a).

Coulombic effect

The improved binding of OER intermediates at the co-substituted TiO_2 surface retains a local character that is dependent on the relative position of the dopants in the structure. To investigate this effect, we performed a series of calculations for different local arrangements of both dopants in the unit cell by varying the relative distance of the dopants as well as their distance to the binding site. Based on the relative position of both Rh and V, the resulting catalysts may reside on either branch of the theoretical volcano (see ESI, Fig. S1†).

A phenomenological explanation of this effect is the varying electrostatic interaction which changes with the distance of the dopant to the adsorbate. To further investigate this phenomenon, we conducted calculations with a single V atom in the TiO_2 structure, when the distance between the dopant and the adsorbed intermediate was gradually increased. We selected HO* as the model intermediate since it is bound on the surface *via* a single bond. In this way, the use of a single dopant does not introduce finite-size effects. The corresponding atomic structure representations are given in the ESI, Fig. S2.† By varying the distance of dopants to the adsorbed intermediate, the binding energy of the intermediate changes, which has previously been shown for TiO_2 substituted with molybdenum.[38] In particular, we find that a linear correlation exists between the HO* binding energy and the reciprocal distance between the dopant and the binding site. The HO* binding energy shows the same variation with the reciprocal distance of the vanadium atom and binding titanium atom, as if V delivers an electron to HO*, see Fig. 4a. The generality of the coulombic effect between the dopant and the binding intermediate can be shown by extending the analysis to $SrTiO_3$, see ESI Fig. S3,† where the same type of dependence of the HO* binding energy on the reciprocal distance $1/r$ is obtained. The interaction between V^+ and HO^- is thus a simple coulombic term; the closer the dopant is to the binding site the stronger the binding due to the attraction between the negative and positive charges (see Fig. 4b).

Extending this approach to the co-substituted model, one finds the reactivity of the binding site to depend on the distance to both dopants, the relative distance of dopants, and the dielectric constant of the semiconductor. It is more complicated to show the coulombic interaction directly for the co-substituted case, as it will depend on the partial charge and the dopants' and adsorbate positions, respectively. The complexity of the model is likely to increase with an increasing number of dopants. This does not neglect the role of the nature of the dopant in binding energy control, as this determines the position of the states in the bandgap. It means, however, that for a given set of dopants, semiconductors, and intermediates the variations in binding energies are governed by electrostatics. A more detailed discussion of the coulombic effect further showing the generality of the concept irrespective of the dopant is given in the ESI, see Fig. S1–S10† for both substituted and co-substituted TiO_2.

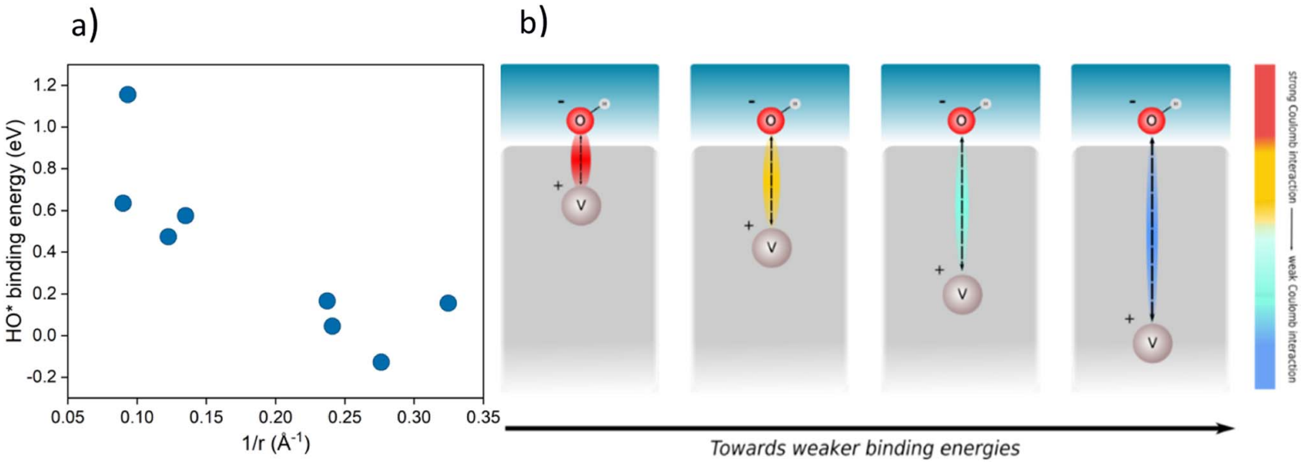

Fig. 4 (a) Binding energy of HO* against 1/*r*, where *r* is the distance of the dopant (V) from the intermediate in a TiO_2 structure for various placements in the structure (cus and bridge sites, the corresponding structures are given in ESI, Fig. S2†) (b) schematic representation of the effect of the distance between the intermediate (HO*) and the dopant (V) on the binding energy of the intermediate.

The generality of the co-substitution concept can be further demonstrated by extending it to another semiconducting system of significant stability – $SrTiO_3$ perovskite. The chosen perovskite structure shows (in its non-substituted state) a band structure similar to that of TiO_2. It also shows outstanding chemical stability but its OER-related electrocatalytic activity is rather low, in part also due to its wide bandgap.[39,40] As in the case of TiO_2, Rh and V were used as the p-type and n-type dopant, respectively. The results of the thermodynamic analysis of the OER catalysis on pristine and substituted $SrTiO_3$ structures are summarized in Fig. 5.

The results presented in Fig. 5 essentially reproduce the trends predicted for the substituted and co-substituted TiO_2. The only difference in the behavior of $SrTiO_3$ is that n-type substitution alone improves the OER activity more than the co-substituted $SrTiO_3$. This observation shows that the partially oxidized $SrTiO_3$ corresponds to the most stable phase in the overall OER reaction sequence. The co-substituted structure lies energetically in between the p- and the n-type substituted $SrTiO_3$ as in the case of TiO_2 (Fig. 5). The theoretical activity of the co-substituted $SrTiO_3$ is much lower than that of co-substituted TiO_2. This unfavorable trend can, however, be reverted by partial substitution of Sr with Ba in the A-site of the perovskite structure, which activates the co-substituted perovskite in the OER process (Fig. 6). Schematic representation of

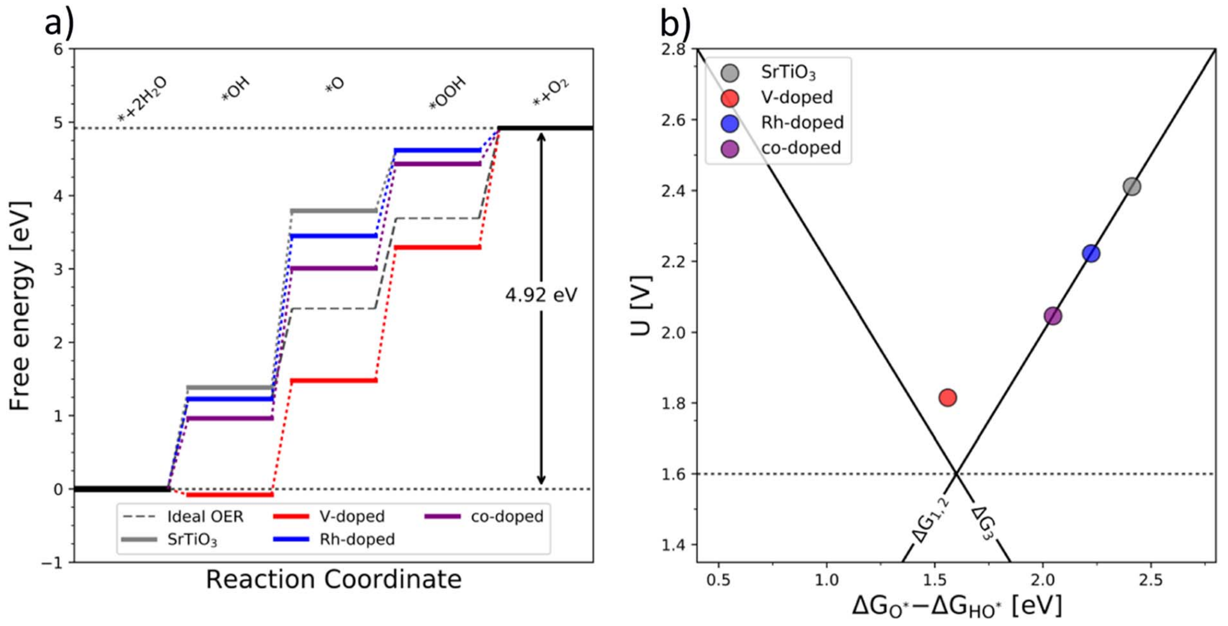

Fig. 5 (a) Free energy diagram of the pure (grey), substituted (blue and red), and co-substituted (purple) $SrTiO_3$. As in the case of TiO_2, the energy level of the intermediates corresponding to the co-substituted structure are in between the p- and n-states (b) the corresponding activity volcano.

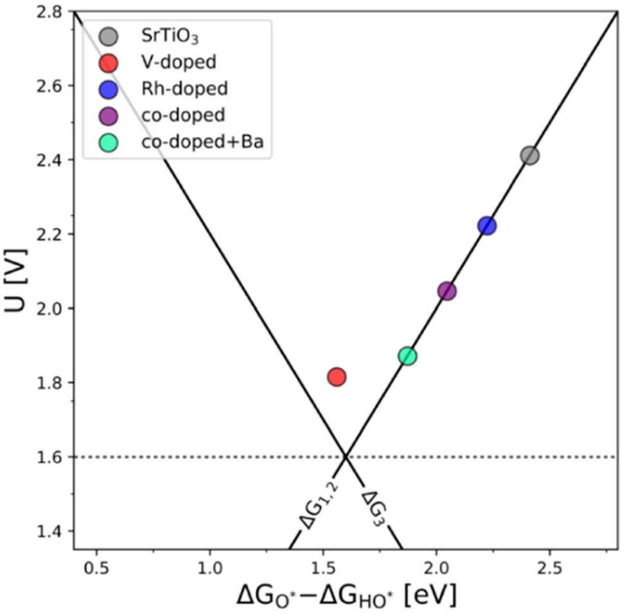

Fig. 6 The OER activity volcano of V-substituted, Rh-substituted, and V–Rh co-substituted $SrTiO_3$ with the addition of the V–Rh co-substituted $Sr_{0.84}Ba_{0.16}TiO_3$ structure, which in terms of activity it resembles the one of the co-substituted TiO_2.

the co-substituted perovskite structures $SrTiO_3$ and $Ba_{0.16}Sr_{0.84}TiO_3$ are shown in the ESI, Fig. S11.†

An improvement of the OER activity of perovskite-based catalysts connected with control of the redox state of the B-site cation in the perovskite structure has previously been reported.[3] This, however, does not explain the observed effect, since the Ba s-valence orbitals are not catalytically active. A possible explanation could be that alteration in the overall band structure occurs due to the Ba s-orbitals pushing the electronic states of both dopants to a more favorable position to facilitate the adsorption of OER intermediates.

To further test the generality of the co-substitution concept, we have broadened the initial screening of n- and p-type dopants of TiO_2 and $SrTiO_3$ to include V, Nb, Ta, Mo, and W, as n-type dopants, and Rh, Mn, Pd, and Ru as p-type dopants. Extending the co-substitution hypothesis, we have chosen the following additional pairs of p and n-type dopants: all n-type dopants (V, Nb, Ta, Mo, W) are paired with Rh, Mn, Pd, Ru. All combinations of p- and n-type dopants lead to electronic structures, which in their OER activity surpass the OER activity of pristine TiO_2. (See Fig. S12 in the ESI†).

Importantly, the calculated bandgap energies of TiO_2 and $SrTiO_3$ are significantly underestimated compared to experimental values, which is a well-known problem of DFT.[41] This may directly affect the calculated binding energies of the OER intermediates. *U*-correction partially compensates for the deviation of calculations from experiments,[37,42] but this approach also has its drawbacks. The *U*-value used for each dopant is different, thus comparing the activity of different systems is not straightforward. In addition, the binding energy of the intermediates scales with the value of *U*-correction. The details of *U*-corrected bandgap energies are given in the ESI, Fig. S13–S15.† The absolute binding energies may be affected by systematic errors in the simulations and the inherent uncertainty of the position of individual combinations of n- and p-type dopants. However, the effect of the co-substitution will apply even if the absolute values change. Hence, the computational screening approach presented here allows for narrowing the selection of prospective dopants.

An ultimate step in the co-substitution optimization of OER activity of semiconductors can be seen in further substitution of the already co-substituted structures $Ti(RhV)O_2$ and $Ba_{0.16}Sr_{0.84}Ti(RhV)O_3$, with both n-type and p-type dopants. The results of this computational approach are summarized in Fig. 7, showing the position of these materials on the theoretical volcano. For both rutile and perovskite structures, introducing several extra dopants can further increase the OER activity of the co-substituted structures. This can be traced back to variations in the band structure as a result of adding the extra dopant. The Rh and V co-substitution states dominate however the behavior, which places all structures on the weak binding side of the OER volcano.

It may be concluded that the activity improvement reflected in Fig. 7 results from the joint effect of the compensated states and the additional d-states provided by the extra dopant to the active part of the system's band structure. A representative example of the pDOS for such a system is shown in the ESI, Fig. S16,† for the case of Mn, V, and Fe dopants introduced in the TiO_2 structure.

While the theoretical analysis suggests that co-substituted TiO_2 has the potential to disrupt the OER catalyst design, the viability of the concept needs to be experimentally verified. While the theoretical screening of prospective co-substituted systems is relatively affordable, the actual synthesis of the theoretically predicted systems is less straightforward. To prove the theoretical concept, a system is required that reflects the main features of the theoretical concept yet maintains a sufficient synthetic facility. Also, the theoretically conceived co-substituted materials represent metastable phases and, thus, the experimental proof of concept must rely on a low-temperature synthetic approach,[43,44] favoring TiO_2-based systems over $SrTiO_3$-based materials.[45]

Experimental confirmation of the predicted superior OER activity of the co-substituted TiO_2 materials is still relatively complicated. It needs to be noted that rutile, which is the basis of the theoretical analysis (it represents the thermodynamically stable titania polymorph), is difficult to prepare at low temperatures. The absence of convenient low-temperature synthesis also complicates the possible stabilization of large amounts of substituting cations in its structure, since the theoretically predicted chemical compositions are likely to remain stable only if the thermal treatment does not exceed 500 °C. These synthetic approaches, however, yield the thermodynamically metastable anatase titania polymorph.[45,46] This fact should not present a fundamental problem since anatase is also an n-type semiconductor and features a similar bandgap and similar band edge energies as the rutile polymorph.[47,48] To confirm that the co-substitution approach is transferable from

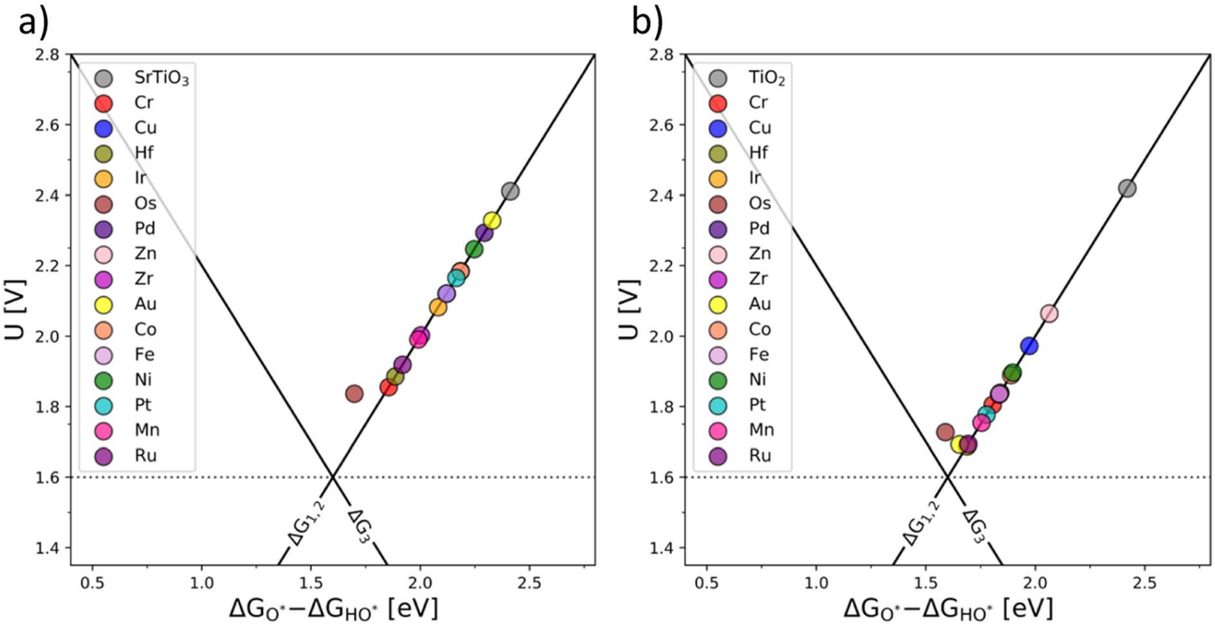

Fig. 7 OER activity volcanoes for $Sr_{0.16}Ba_{0.84}Ti(RhV)O_3$ (a) and $Ti(RhV)O_2$ (b) substituted with extra transition metal dopants (additional d-states).

the rutile model system and can be extended to the anatase polymorph, the adsorption characteristics of co-substituted anatase structures were computed (see ESI, Fig. S17†). It is shown that the same trends are observed for both major titania polymorphs (rutile and anatase) for both band structures and OER activity trends. Hence, the co-substitution approach can be generalized.

Single-substituted and co-substituted TiO_2 nanoparticles were prepared using the spray-freeze freeze-dry approach.[49,50] The substitution levels achieved in all prepared TiO_2 materials were equal to a substitution of 20% of cationic positions, either with one dopant (Cr or Mn) or two dopants (both n- and p-type substitution) in equal amounts. All synthesized titanium oxide materials were nanocrystalline and conform to the anatase structure (see Fig. 8a). Substitution of an element in the anatase structure did not cause any significant variation in the lattice parameters, the characteristic particle size, and the coherent domain sizes. Details of the structural characterization of the obtained materials are given in the ESI (see Fig. S18–S21 and Table S1).† Although the XRD-based structure of the prepared materials conforms to that of the anatase TiO_2 polymorph, the same cannot be said of their electronic structure as can be inferred from measured UV-vis spectra (see Fig. 8b). The UV-vis spectrum of pure anatase is typical for a wide bandgap semiconductor characterized by a clearly defined band gap of more than 3 eV. This type of behavior is not replicated in the substituted or co-substituted materials. The pronounced onset of the absorption in the visible region is already evident in the materials substituted with a single element (Mn, Cr in Fig. 8b). For materials subject to simultaneous n- and p-type substitution, one observes a continuous absorption extending over a rather broad interval of energies, spanning from circa 2.0 to 2.5 eV. This broad absorption band is further complemented by a resolved localized absorption band located at *ca.* 1 eV, characteristic namely for materials substituted with Co. This type of behavior is generally compatible with the conductivity behavior predicted in the DFT calculations. It needs to be noted that the co-substituted TiO_2 materials do not retain the behavior characteristic of the pure TiO_2, namely, they do not show characteristic photo-electrochemical activity.

The OER activity of the substituted TiO_2 materials was assessed in acid media and compared with that of the benchmark TiO_2 sample (see Fig. 9).[51] Details of the electrochemical characterization are given in the Experimental section. The linear sweep voltammograms of the co-substituted TiO_2 samples are presented in Fig. 9a. For better comparison, the potential necessary to drive a current density of 50 $\mu A\ cm^{-2}$ is taken as an estimate of the oxygen evolution activity (Fig. 9b). The estimated overpotentials show that the behavior of materials substituted with a single cation and that of the n- and p- co-substituted materials significantly differs, despite the similarity in UV-vis spectra. While the co-substituted materials clearly outperform the pure TiO_2 benchmark sample, the activity of the materials substituted with a single cation remains comparable with that of the benchmark, *i.e.*, non-substituted TiO_2. It can be concluded that only co-substitution has a pronounced effect on the OER activity of the TiO_2 electrodes (see Fig. 9b). Although the observed behavior is essentially in line with the DFT-based theoretical prediction presented above, the actual OER activity seems to also be affected by the chemical nature of the dopants.

The Mn/Co co-substituted structure apparently exhibits the highest activity (*i.e.*, the lowest overpotential) among all the co-substituted structures as shown in Fig. 9b. On the other hand, the large variability of the activity observed in different experiments suggests that the synthesized materials may change their activity under operando conditions in acid media. This could

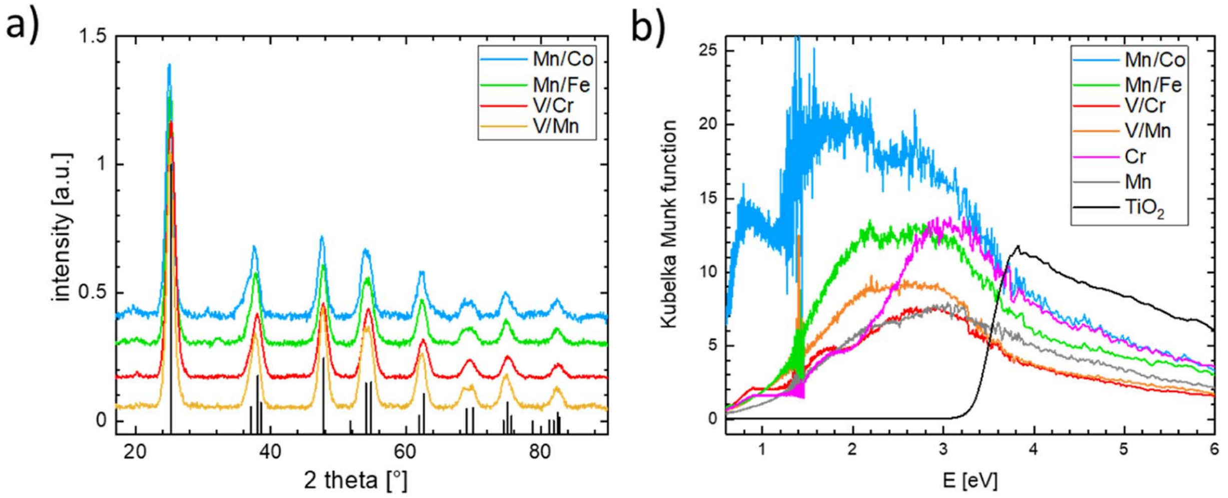

Fig. 8 (a) X-ray diffraction patterns of the synthesized n and p co-doped TiO_2 nanoparticles, the reference pattern for TiO_2 in anatase structure is included as the black line pattern and (b) UV-vis spectra of all synthesized doped TiO_2 nanoparticles including the pristine TiO_2 anatase reference.

particularly be the case for materials containing Mn and Co since oxides based on these elements are relatively good catalysts for OER,[52–56] hence the observed enhanced activity may be attributed to a local level phase separation. Such a phase separation could, however, also cause material instability when the observed anodic current might be attributed to Mn or Co oxide leaching rather than to actual water oxidation. On the other hand, the second-best performance is exhibited by the V/Cr co-substituted structure, and since the oxides of V and Cr do not form good OER catalysts in themselves,[19,57,58] one can argue that the compensation effect is responsible for their increased catalytic activity.

This uncertainty can be resolved by separately following the actual oxygen formation during anodic polarization of the prepared materials and the chemical stability of the catalysts during oxygen evolution. The oxygen formation can be followed using online mass spectrometric detection by Differential Electrochemical Mass Spectrometry (DEMS), as depicted in Fig. 10.

The data presented in Fig. 10 conclusively show that the anodic current observed at potentials positive to 1.8 V *vs.* RHE is connected with the formation of oxygen. The formation of oxygen varies on fresh electrodes but becomes fairly reproducible during repetitive polarization experiments. Although the signal of the produced oxygen generally tracks the observed anodic current (see Fig. 10c), it cannot be used to prove if the oxygen evolution proceeds quantitatively. Anodic dissolution of the electrode materials cannot be deduced from DEMS data, so the possibility of parasitic catalyst corrosion requires a separate online ICP-OES experiment, summarized in Fig. 11 and 12.

Based on these data, the biggest change in the composition of the electrode is triggered by the first contact of the electrode materials with the electrolyte solution, which results in an enrichment of the electrolyte solution with all metal components of the prepared catalyst. A comparison of the behavior of two chosen representatives of co-substituted materials Ti–Mn–Co and Ti–Mn–V phases, however, clearly outlines a qualitatively different stability behavior of the Co and Mn-containing

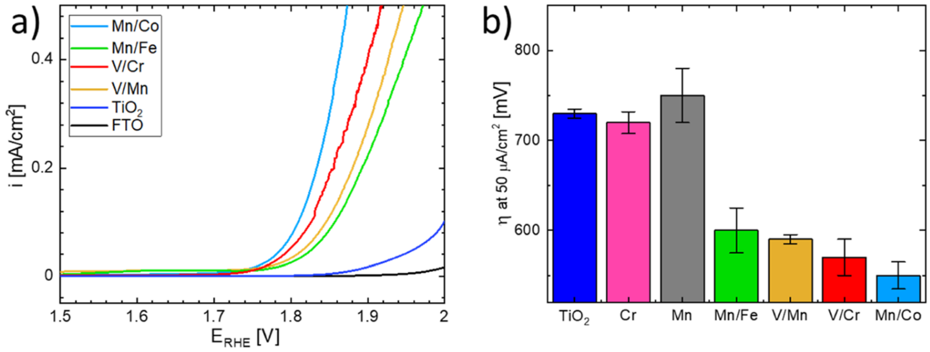

Fig. 9 (a) Linear sweep voltammograms of the synthesized co-substituted TiO_2 nanoparticles and the TiO_2 benchmark material. Voltammograms were recorded in 0.1 M $HClO_4$ with a scan rate of 5 mV s^{-1} using FTO as a current collector and (b) overpotential η necessary to drive a current density of 50 µA cm^{-2} on the co-substituted TiO_2 nanoparticles, single dopant TiO_2 nanoparticles, and the TiO_2 benchmark sample. The values included are the mean averages of three individual measurements. The assignment of individual samples is given in the figure legend.

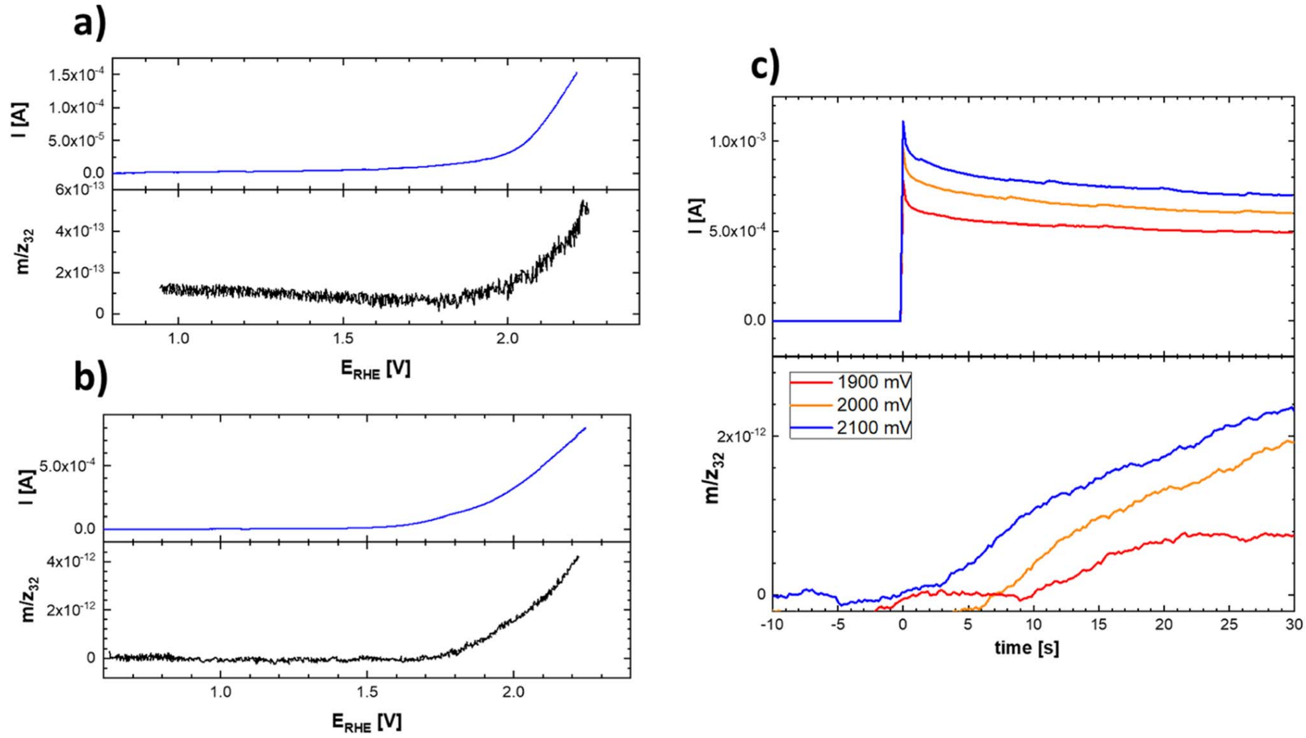

Fig. 10 Linear scan voltammograms (top) and corresponding potential course of the mass spectrometric signal (bottom) of the evolved oxygen on Ti–Co–Mn (a) and Ti–Mn–V (b) in 0.1 M $HClO_4$. Experimental conditions were identical as those indicated in Fig. 9 and (c) chronoamperometric curves and corresponding time course reflecting the oxygen evolution on Ti–Mn–V based catalyst in 0.1 M $HClO_4$ at different potentials. The actual potentials (*vs.* RHE) are indicated in the figure legend.

phases. Although the dissolution rate upon contact with sulphuric acid-based electrolyte is essentially the same for both systems, dissolution over time is more pronounced for the system containing Co than for that featuring V. The leaching of the catalysts' components into electrolyte solution starting upon contact is practically finished within the first 200 seconds in the case of material containing V, while the solution enrichment with metal cations in the case of the material containing Co still proceeds at an appreciable rate after 700 s. Regardless of the overall chemical composition, the ICP-OES data clearly shows that even Ti, generally considered to be stable in acid media, is not stable in the prepared catalysts. Its dissolution rate, however, remains about 3–5 times lower than that of the other catalyst components – Mn and Co. The contact of the catalyst with the electrolyte solution triggers a temporary potential fluctuation (rather small in the case of the Ti–Mn–V

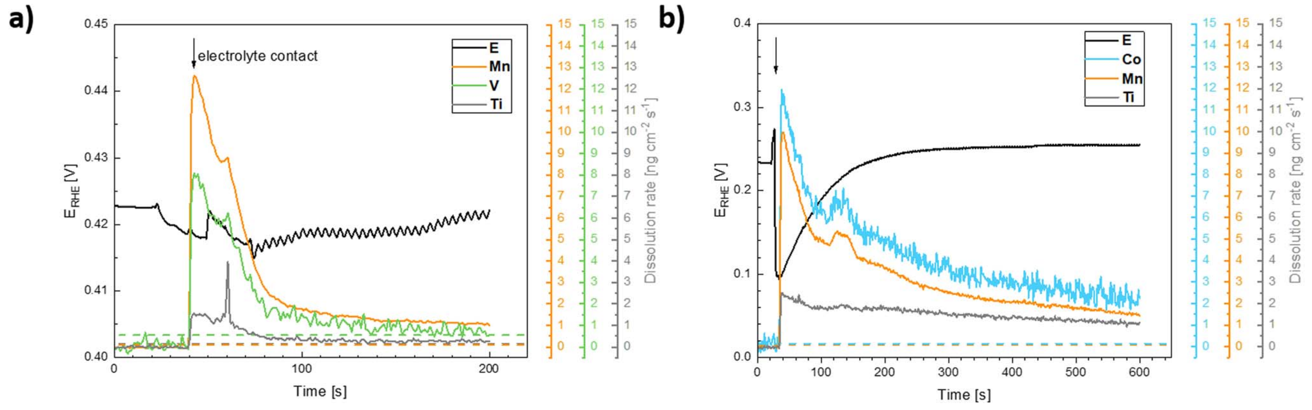

Fig. 11 Evolution of the electrode potential (*E* (V) *vs.* RHE, left axis) and ICP-OES signals of the dissolution of the catalysts components following exposure of (a) the Ti–Mn–V and (b) the Ti–Mn–Co to 0.05 M H_2SO_4 electrolyte solution. The ICP-OES signals were converted to dissolution rates.

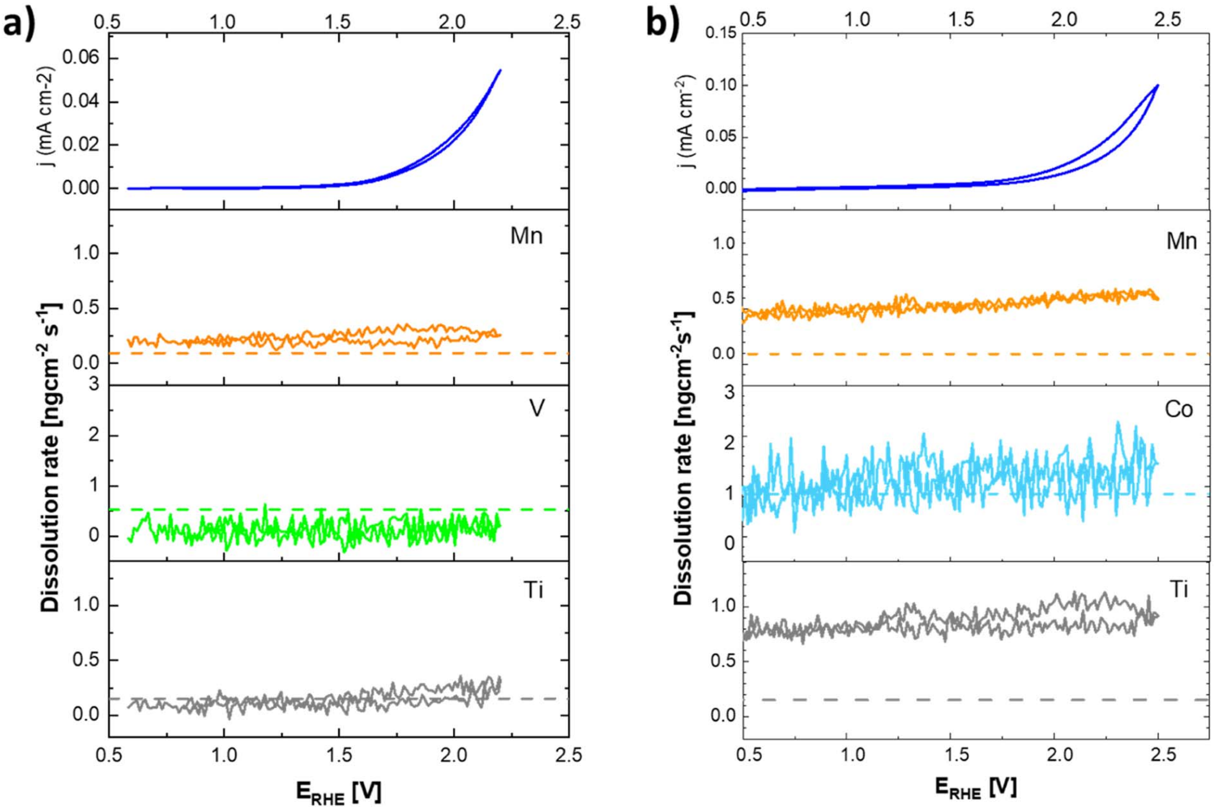

Fig. 12 Cyclic voltammogram (top) and ICP-OES signals of the dissolution of the catalysts components during cyclic polarization of (a) the Ti–Mn–V and (b) the Ti–Mn–Co catalyst in 0.05 M H_2SO_4. Dashed lines indicate the ICP-OES detection limits.

system) but the potential stabilises within *ca.* 5 minutes. It needs to be noted that the leaching of the Mn and Co is more pronounced than that of V.

The anodic polarization of the catalyst to potentials relevant to oxygen evolution reaction triggers additional changes in the chemical composition of the sample (see Fig. 12). In the case of catalysts in the Ti–Mn–V system, the anodic polarization in 0.05 M sulphuric acid does not lead to any appreciable transition metal leaching at potentials below 1.8 V *vs.* RHE (see Fig. 12).

At potentials above 1.8 V, Ti and Mn levels in solution increase above the detection limit. No leaching of V is, however, observed under these conditions. Interestingly, the rate of dissolution of the unstable component of the catalyst (Mn) is proportional to that of the stable Ti. Further, the dissolution rate of the Ti and Mn is not a simple function of the electrode potential, as a notable hysteresis between the anodic and cathodic scans of the voltammogram occurs. The microscopic state of the surface and how this state is approached therefore plays a role, similar as was observed during charging/discharging of $LiMnO_2$.[59]

In the case of catalysts in the system Ti–Mn–Co (see Fig. 12b) we observed generally the same trends, as the anodic polarization to the potential of oxygen evolution does not trigger any appreciable additional catalysts dissolution. A constant, minor dissolution of Mn, Ti, as well as Co is however observed. This dissolution signal is, however, significantly smaller than the initial dissolution of the material upon contact with the electrolyte.

The formation of dissolved Ti-containing species is somewhat surprising given the expected stability of Ti oxides in acid media. The observed behavior, when the same rate of dissolution is observed for the reactive transition metals (Mn, Co) as for the apparently stable Ti, suggests that the conditions of the oxygen evolution process promote a formation of Ti peroxo-complexes, which are known to be fairly soluble under the conditions of the experiment.[60] The destabilization through formation of Ti peroxo-complexes confirms that through the co-substitution approach Ti is indeed activated as a binding site for the oxygen intermediates in the catalytic cycle of the oxygen evolution process.

In summary, our data show that the anodic current recorded during the catalyst testing originates from the oxygen evolution process. Although the prepared materials are intrinsically unstable as shown by ICP-OES under OCP conditions, the data obtained at anodic polarization suggest that the materials stabilize themselves rather fast after exposure to the electrolyte solution, which may point to passivating behavior.[59] The observed instability of the prepared substituted and co-substituted TiO_2 nanoparticles can be explained by the random distribution of dopants in the particles. Dopants placed on the particle surface lead to leaching and loss of the dopants which in turn decreases the OER activity. Choosing a synthetic strategy that confines the dopants to the bulk[39] as an alternative could be an approach to increasing the stability of these materials.

Computational methods

The grid-based projector augmented wave (GPAW)[61,62] package along with the atomic simulation environment (ASE)[63] interface, was used for the density functional theory (DFT) calculations. The exchange and correlation energy of the electrons was expressed within the concept of the generalized gradient approximation (GGA) by implementing the RPBE[64] functional. The grid spacing was selected to be $h = 20$ Å while the atomic positions were relaxed until the total forces were lower than 0.05 eV Å^{-1}. A $4 \times 4 \times 1$ Monkhorst–Pack[65] *k*-point sampling for the 1×3 replicated TiO_2 rutile (110) surface was used, with the last two layers (out of four) of the super cell being constrained. The cubic configuration of the perovskite unit cell was used as the initial structure for the $SrTiO_3$. A $10 \times 10 \times 10$ *k*-point mesh with a plane wave energy cut-off of 900 eV and the RPBE functional were used to optimize the bulk structures. For optimizing the (100) $SrTiO_3$ surface the same parameters as in the case of rutile were used for a direct comparison between the two structures.

Experimental details

All materials were prepared by spray-freeze freeze-dry synthesis. A total metal concentration of 8 mM was maintained in all experiments. Titanium(IV) bis(ammonium lactato)dihydroxide (TBALD) solution (50 wt% in H_2O, Sigma Aldrich) was used as the source of titanium. 40 mM concentrated stock solutions of TBALD in Milli-Q quality deionized water were prepared. As the source of transition metal dopants, vanadium(V) oxide (>98%), chromium(III) nitrate nonahydrate (99%), manganese(II) acetate tetrahydrate (>99%), cobalt(II) acetate tetrahydrate (>98%), and iron(II) acetate (>95%) were all purchased from Sigma Aldrich and used as received. The precursor solutions for each experiment were prepared by dissolving the corresponding metal salts in Milli-Q quality deionized water and adding the respective amount of TBALD stock solution as the titanium source. The ratio of the initial metal precursors was adjusted to achieve the desired nominal composition; a total amount of 20 at% dopants to titanium. For co-substitution experiments, the dopants were added in a 1 : 1 ratio. The solutions were stirred for 30 minutes before the spray-freezing step. The ice precursors were prepared by spraying 100 mL of precursor solution into *ca.* 2 L of liquid nitrogen. The obtained ice precursor was freeze-dried using a FreeZone Triad Freeze Dry System 7400030 (Labconco) at reduced pressure (1 Pa) according to the following temperature protocol: the temperature was kept constant at −30 °C while the cooling chamber was evacuated, followed by a gradual increase of the temperature [−30 °C (2 h), −25 °C (5 h), −20 °C (4 h), −15 °C (6 h), +30 °C (4 h)]. The obtained foam-like precursor was carefully removed from the freeze-dryer and annealed at 500 °C for 2 h in a muffle furnace.

The crystallinity and phase purity of the synthesized materials were analyzed by powder X-ray diffraction (XRD). The diffraction patterns were recorded using a Rigaku Miniflex 600 powder X-ray diffractometer with Cu K_α radiation operating at 30 kV and 10 mA. Le Bail fits were performed to determine the unit cell parameter with the Profex 3.13.0 software package[66] based on the BGMN program.[67]

The morphology and particle size of all prepared samples were analyzed by scanning electron microscopy (SEM) using a Hitachi S4800 scanning electron microscope equipped with a Nanotrace EDX detector (Thermo Electron). The average sample composition was determined by energy-dispersive X-ray spectroscopy (EDX) measured at an accelerating voltage of 25 keV. The bandgap of the synthesized samples was determined by UV-vis diffuse reflectance spectroscopy (DRS) (PerkinElmer LAMBDA 950).

The oxygen evolution activity of the prepared materials was assessed for all materials. The TiO_2 electrodes were prepared by drop-casting on fluorine-doped tin oxide (FTO) glass (TEC 15, Dyesol, 15 Ω per sq). The catalysts suspensions were prepared by dispersing 10 mg of catalyst in a solution of 1 mL H_2O, 4 mL iPrOH, and 20 μL 5% Nafion 117 solution (Sigma Aldrich). The electrode layer was deposited by dropping 10 μL increments of the catalyst suspension onto the FTO substrate until a total catalyst loading of 100 μg cm^{-2} was reached. The deposited catalyst layer was dried in between each drop-casting step. The electrochemical experiments were performed in a three-electrode setup using the respective substituted TiO_2/FTO working electrode in combination with a platinum mesh as the counter electrode and a saturated calomel electrode (SCE) as the reference electrode. For potential control, an AUTOLAB (PGSTAT 30) potentiostat was used in all experiments. Voltammograms were recorded at a polarization rate of 5 mV s^{-1} in 0.1 M $HClO_4$ in a potential range of 1.3 to 2.0 V *vs.* RHE. Linear polarization curves were measured after collecting CVs at a scan rate of 50 mV s^{-1} to achieve a constant double layer charge.

All potentials were recalculated and reported in the reversible hydrogen electrode (RHE) scale. Electrochemical impedance spectroscopy measurements were recorded in the range from 15 kHz to 1 Hz with an amplitude of 10 mV to estimate the ohmic drop of the solution. All voltammograms were corrected for uncompensated solution resistance. The reported current densities are based on the geometric surface area of the electrodes used. All electrochemical measurements were repeated at least three times to ensure reproducibility. DEMS experiments were carried out in a home-made Kel-F single compartment cell in a three-electrode set-up using a Pt-auxiliary and an Ag/AgCl reference electrode.[68] All DEMS experiments were controlled using a PAR 263A potentiostat. The DEMS experimental setup comprises a PrismaPlusTM QMQ220 quadrupole mass spectrometer (Pfeiffer) connected to a HiPace 80 (PMP03941) turbomolecular drag pumping station (Pfeiffer). ICP-OES measurements were performed using an Agilent 5100 dual-view instrument fitted with a Seaspray nebulizer, double-pass cyclonic spray chamber, and 2.8 mm wide bore torch for high total dissolved solids applications, using a flow-through electrochemical cell of our own design as detailed elsewhere.[59]

Conclusions

Simultaneous substitution of wide bandgap semiconductors with both n- and p-type dopants affects both the electronic structure as well as the catalytic behavior of semiconducting oxides. This co-substitution significantly improves the OER activity of these materials. TiO_2 and $SrTiO_3$, known for their stability under acidic and alkaline conditions and their poor performance in OER catalysis, were chosen as model systems to outline the co-substitution effect computationally. The inclusion of both n-type and p-type dopants in these structures causes a compensation effect between the electronic states of the dopants, resulting in an alteration of the band structure, which consequently lowers the overpotential of OER. According to the pDOS, the dopants form a new band that aligns the Fermi level at an energetic position favorable for water oxidation. The calculations further reveal a sensitivity of the binding energies of the intermediates to the relative position of the dopants. Combining this local structure sensitivity with the Sabatier principle can be used to optimize the chemical composition of the co-substituted catalysts. The theoretical predictions were confirmed experimentally on the substituted and co-substituted TiO_2 – anatase. The formation of the pseudo-conductor band is reflected in the significant coloration of the substituted anatase. While a similar change in the electronic structure can be seen for a single-substituted system, only n- and p-type co-substituted materials show an actual significant improvement of the catalytic activity in oxygen-evolving reactions.

Data availability

Theoretical structures and scripts necessary for reproducing the results obtained herein, as well as experimental data, have been made freely accessible at KatlaDB – Theoretical Catalysis Database – and can be accessed *via* **https://nano.ku.dk/english/research/theoretical-electrocatalysis/katladb/codoping**-TiO_2.

Author contributions

CRediT (contributors roles taxonomy) was used for standardized author contributor role description. T. K., S. D.: data curation, formal analysis, investigation, methodology, software, visualization, writing – original draft. R. P.: data curation, formal analysis, investigation, methodology, visualization, validation, supervision, writing – original draft, writing – review & editing. R. M., A. M. F., K. M.-M., R. N.; D. Z.: data curation, formal analysis, visualization, writing – review & editing. S. F. L. M., H. H.: resources, supervision, methodology, funding acquisition, writing – review & editing. P. K., J. R.: project administration, conceptualization, resources, supervision, methodology, funding acquisition, writing – review & editing.

Conflicts of interest

There are no conflicts to declare.

Acknowledgements

T. K., S. D., R. M., and R. P. gratefully acknowledge the support Marie Sklodowska Curie Innovative Training Network Elcorel (Contract No. 722614). The project was further supported by the Czech Science Foundation within project No. 21-03037S. We acknowledge support from the Danish National Research foundation *via* grant DNRF-149. D. Z. and S. F. L. M. acknowledge support from The Faraday Institution (NEXGENNA project) and Materials Science Institute internal funds.

References

1 H. Ibrahim, A. Ilinca and J. Perron, *Renewable Sustainable Energy Rev.*, 2008, **12**, 1221.
2 M. Carmo, D. L. Fritz, J. Mergel and D. Stolten, *Int. J. Hydrogen Energy*, 2013, **38**, 4901.
3 J. Suntivich, K. J. May, H. a Gasteiger, J. B. Goodenough and Y. Shao-Horn, *Science*, 2011, **334**, 1383.
4 A. Grimaud, K. J. May, C. E. Carlton, Y.-L. Lee, M. Risch, W. T. Hong, J. Zhou and Y. Shao-Horn, *Nat. Commun.*, 2013, **4**, 2439.
5 R. Frydendal, E. A. Paoli, I. Chorkendorff, J. Rossmeisl and I. E. L. Stephens, *Adv. Energy Mater.*, 2015, **5**, 1500991.
6 C. C. L. McCrory, S. Jung, J. C. Peters and T. F. Jaramillo, *J. Am. Chem. Soc.*, 2013, **135**, 16977.
7 Y. Lee, J. Suntivich, K. J. May, E. E. Perry and Y. Shao-Horn, *J. Phys. Chem. Lett.*, 2012, **3**, 399.
8 M. Schalenbach, G. Tjarks, M. Carmo, W. Lueke, M. Mueller and D. Stolten, *J. Electrochem. Soc.*, 2016, **163**, F3197.
9 G. Matute, J. M. Yusta and L. C. Correas, *Int. J. Hydrogen Energy*, 2019, **44**, 17431.
10 K. E. Ayers, E. B. Anderson, C. Capuano, B. Carter, L. Dalton, G. Hanlon, J. Manco and M. Niedzwiecki, *ECS Trans.*, 2019, **33**, 3.
11 K. A. Stoerzinger, L. Qiao, M. D. Biegalski and Y. Shao-Horn, *J. Phys. Chem. Lett.*, 2014, **5**, 1636.
12 F.-W. Wellmer, P. Buchholz, J. Gutzmer, C. Hagelüken, P. Herzig, R. Littke and R. K. Thauer, *Raw Materials for Future Energy Supply*, Springer International, Cham, Switzerland, 2019.
13 M. Bernt, A. Siebel and H. A. Gasteiger, *J. Electrochem. Soc.*, 2018, **165**, F305.
14 Z. Wang, Y.-R. Zheng, I. Chorkendorff and J. K. Nørskov, *ACS Energy Lett.*, 2020, **5**, 2905.
15 R. K. Pittkowski, D. F. Abbott, R. Nebel, S. Divanis, E. Fabbri, I. E. Castelli, T. J. Schmidt, J. Rossmeisl and P. Krtil, *Electrochim. Acta*, 2021, **366**, 137327.
16 A. Grimaud, A. Demortière, M. Saubanère, W. Dachraoui, M. Duchamp, M.-L. Doublet and J.-M. Tarascon, *Nat. Energy*, 2016, **2**, 16189.
17 J. K. Nørskov, J. Rossmeisl, A. Logadottir, L. Lindqvist, J. R. Kitchin, T. Bligaard and H. Jónsson, *J. Phys. Chem. B*, 2004, **108**, 17886.
18 J. Rossmeisl, Z.-W. Qu, H. Zhu, G.-J. Kroes and J. K. Nørskov, *J. Electroanal. Chem.*, 2007, **607**, 83.

19 I. C. Man, H.-Y. Y. Su, F. Calle-Vallejo, H. A. Hansen, J. I. J. I. Martínez, N. G. Inoglu, J. Kitchin, T. F. Jaramillo, J. K. Nørskov and J. Rossmeisl, *ChemCatChem*, 2011, **3**, 1159.

20 S. Divanis, T. Kutlusoy, I. M. Ingmer Boye, I. C. Man and J. Rossmeisl, *Chem. Sci.*, 2020, **11**, 2943.

21 L. G. V. Briquet, M. Sarwar, J. Mugo, G. Jones and F. Calle-Vallejo, *ChemCatChem*, 2017, **9**, 1261.

22 D.-Y. Kuo, H. Paik, J. Kloppenburg, B. Faeth, K. M. Shen, D. G. Schlom, G. Hautier and J. Suntivich, *J. Am. Chem. Soc.*, 2018, **140**, 17597.

23 D.-Y. Kuo, J. K. Kawasaki, J. N. Nelson, J. Kloppenburg, G. Hautier, K. M. Shen, D. G. Schlom and J. Suntivich, *J. Am. Chem. Soc.*, 2017, **139**, 3473.

24 R. K. B. Karlsson, A. Cornell and L. G. M. Pettersson, *Electrochim. Acta*, 2015, **180**, 514.

25 M. García-Mota, A. Vojvodic, H. Metiu, I. C. Man, H.-Y. Su, J. Rossmeisl and J. K. Nørskov, *ChemCatChem*, 2011, **3**, 1607.

26 A. Fujishima and K. Honda, *Nature*, 1972, **238**, 37.

27 Á. Valdés, Z.-W. Qu, G.-J. Kroes, J. Rossmeisl and J. K. Nørskov, *J. Phys. Chem. C*, 2008, **112**, 9872.

28 N. Roy, Y. Sohn, K. T. Leung and D. Pradhan, *J. Phys. Chem. C*, 2014, **118**, 29499.

29 D. M. Jang, I. H. Kwak, E. L. Kwon, C. S. Jung, H. S. Im, K. Park and J. Park, *J. Phys. Chem. C*, 2015, **119**, 1921.

30 T. Umebayashi, T. Yamaki, H. Itoh and K. Asai, *J. Phys. Chem. Solids*, 2002, **63**, 1909.

31 L. C. Seitz, D. Nordlund, A. Gallo and T. F. Jaramillo, *Electrochim. Acta*, 2016, **193**, 240.

32 M. García-Mota, A. Vojvodic, F. Abild-Pedersen and J. K. Nørskov, *J. Phys. Chem. C*, 2013, **117**, 460.

33 Y. Wang, R. Zhang, J. Li, L. Li and S. Lin, *Nanoscale Res. Lett.*, 2014, **9**, 46.

34 Z. Yuan, J. Jia and L. Zhang, *Mater. Chem. Phys.*, 2002, **73**, 323.

35 S. S. Srinivasan, J. Wade, E. K. Stefanakos and Y. Goswami, *J. Alloys Compd.*, 2006, **424**, 322.

36 H. Luo, T. Takata, Y. Lee, J. Zhao, K. Domen and Y. Yan, *Chem. Mater.*, 2004, **16**, 846.

37 I. E. Castelli, I.-C. Man, S.-G. Soriga, V. Parvulescu, N. B. Halck and J. Rossmeisl, *J. Phys. Chem. C*, 2017, **121**, 18608.

38 X. Huang, J. Wang, H. B. Tao, H. Tian and H. Xu, *Chem. Sci.*, 2019, **10**, 3340.

39 A. R. Akbashev, L. Zhang, J. T. Mefford, J. Park, B. Butz, H. Luftman, W. C. Chueh and A. Vojvodic, *Energy Environ. Sci.*, 2018, **11**, 1762.

40 M. Cui, T. Liu, Q. Li, J. Yang and Y. Jia, *ACS Sustainable Chem. Eng.*, 2019, 7, 15346.

41 J. P. Perdew, *Int. J. Quantum Chem.*, 1985, **28**, 497.

42 V. Tripkovic, H. A. Hansen, J. M. Garcia-Lastra and T. Vegge, *J. Phys. Chem. C*, 2018, **122**, 1135.

43 M. S. Whittingham, *Curr. Opin. Solid State Mater. Sci.*, 1996, **1**, 227.

44 J. Gopalakrishnan, *Chem. Mater.*, 1995, **7**, 1265.

45 N. Satoh, T. Nakashima and K. Yamamoto, *Sci. Rep.*, 2013, **3**, 1959.

46 D. P. Macwan, P. N. Dave and S. Chaturvedi, *J. Mater. Sci.*, 2011, **46**, 3669.

47 L. Kavan, M. Grätzel, S. E. Gilbert, C. Klemenz and H. J. Scheel, *J. Am. Chem. Soc.*, 1996, **118**, 6716.

48 D. O. Scanlon, C. W. Dunnill, J. Buckeridge, S. A. Shevlin, A. J. Logsdail, S. M. Woodley, C. R. A. Catlow, M. J. Powell, R. G. Palgrave, I. P. Parkin, G. W. Watson, T. W. Keal, P. Sherwood, A. Walsh and A. A. Sokol, *Nat. Mater.*, 2013, **12**, 798.

49 V. Petrykin, K. Macounova, O. A. Shlyakhtin and P. Krtil, *Angew. Chem., Int. Ed.*, 2010, **49**, 4813.

50 K. Minhová Macounová, M. Klusáčková, R. Nebel, M. Zukalova, M. Klementova, I. E. Castelli, M. D. Spo, J. Rossmeisl, L. Kavan and P. Krtil, *J. Phys. Chem. C*, 2017, **121**, 6024.

51 M. Klusáčková, R. Nebel, K. Minhová Macounová, M. Klementová and P. Krtil, *Electrochim. Acta*, 2019, **297**, 215.

52 M. Huynh, D. K. Bediako and D. G. Nocera, *J. Am. Chem. Soc.*, 2014, **136**, 6002.

53 V. Tripkovic, H. A. Hansen and T. Vegge, *ChemSusChem*, 2018, **11**, 629.

54 E. B. Castro, C. A. Gervasi and J. R. Vilche, *J. Appl. Electrochem.*, 1998, **28**, 835.

55 A. Moysiadou, S. Lee, C.-S. Hsu, H. M. Chen and X. Hu, *J. Am. Chem. Soc.*, 2020, **142**, 11901.

56 M. Bajdich, M. García-Mota, A. Vojvodic, J. K. Nørskov and A. T. Bell, *J. Am. Chem. Soc.*, 2013, **135**, 13521.

57 S. P. Babu and A. Falch, *ChemCatChem*, 2022, e202200364.

58 X. Zheng, M. Qin, S. Ma, Y. Chen, H. Ning, R. Yang, S. Mao and Y. Wang, *Adv. Sci.*, 2022, **9**, 2104636.

59 S. Nikman, D. Zhao, V. Gonzalez-Perez, H. E. Hoster and S. F. L. Mertens, *Electrochim. Acta*, 2021, **386**, 138373.

60 K. Mühlenbach, K. Müller and G. Schwarzenbach, *Inorg. Chem.*, 1970, **9**, 2381.

61 J. J. Mortensen, L. B. Hansen and K. W. Jacobsen, *Phys. Rev. B: Condens. Matter Mater. Phys.*, 2005, **71**, 35109.

62 J. Enkovaara, C. Rostgaard, J. J. Mortensen, J. Chen, M. Dułak, L. Ferrighi, J. Gavnholt, C. Glinsvad, V. Haikola, H. A. Hansen, H. H. Kristoffersen, M. Kuisma, A. H. Larsen, L. Lehtovaara, M. Ljungberg, O. Lopez-Acevedo, P. G. Moses, J. Ojanen, T. Olsen, V. Petzold, N. A. Romero, J. Stausholm-Møller, M. Strange, G. A. Tritsaris, M. Vanin, M. Walter, B. Hammer, H. Häkkinen, G. K. H. Madsen, R. M. Nieminen, J. K. Nørskov, M. Puska, T. T. Rantala, J. Schiøtz, K. S. Thygesen and K. W. Jacobsen, *J. Phys.: Condens. Matter*, 2010, **22**, 253202.

63 A. Hjorth Larsen, J. Jørgen Mortensen, J. Blomqvist, I. E. Castelli, R. Christensen, M. Dułak, J. Friis, M. N. Groves, B. Hammer, C. Hargus, E. D. Hermes, P. C. Jennings, P. Bjerre Jensen, J. Kermode, J. R. Kitchin, E. Leonhard Kolsbjerg, J. Kubal, K. Kaasbjerg, S. Lysgaard, J. Bergmann Maronsson, T. Maxson, T. Olsen, L. Pastewka, A. Peterson, C. Rostgaard, J. Schiøtz, O. Schütt, M. Strange, K. S. Thygesen, T. Vegge, L. Vilhelmsen, M. Walter, Z. Zeng and K. W. Jacobsen, *J. Phys.: Condens. Matter*, 2017, **29**, 273002.

64 B. Hammer, L. B. Hansen and J. K. N\orskov, *Phys. Rev. B: Condens. Matter Mater. Phys.*, 1999, **59**, 7413.

65 H. J. Monkhorst and J. D. Pack, *Phys. Rev. B: Solid State*, 1976, **13**, 5188.

66 N. Doebelin and R. Kleeberg, *J. Appl. Crystallogr.*, 2015, **48**, 1573.

67 J. Bergmann, P. Friedel and R. Kleeberg, *CPD Newsl. Comm. Powder Diffr. Int. Union Crystallogr.*, 1998, **20**, 5.

68 J. Jirkovský, H. Hoffmannová, M. Klementová and P. Krtil, *J. Electrochem. Soc.*, 2006, **153**, E111.

5.4 $Ru_xTi_{1-x}O_2$ semi-conductor conductor transition

One promising avenue for activation of TiO_2 is the alloying with Ru-oxides. As mentioned previously, this alloy (and derivatives) has already shown results for the DSAs used for chlorine evolution [58]. Much in line with doping approaches, alloying hopes to stabilize the active ruthenium dioxide, and/or activate the stable titanium dioxide. Simultaneously, this would reduce the required amount of ruthenium. This chapter presents a small study on the composition space between the extremes of $Ru_xTi_{1-x}O_2$, with a particular focus on understanding the transition from semi-conductor to conductor upon introduction of ruthenium.

The system of study is presented in fig. 9. The rutile (110) slab structures where generated at varying x and relaxed by DFT. In an attempt to avoid finite size effects [39], the smallest amount of Ru atoms introduced to the structures was 2 atoms, corresponding to $x = 2/24 \approx 0.083$. Ten structures for each type of active site (Ru, Ti) at each studied value of x were randomly generated. Each structure was relaxed as is, as well as with OER intermediates, HO^*, H^b + O^*, O^*, HOO^* and H^b + OO^*. Here b designates a bridge site to include the ruthenium pathway intermediates [45]. Non-active site ruthenium atoms in the top layer are always accompanied with an oxygen adsorbate, as Ru is expected to be oxidized at OER active potentials.

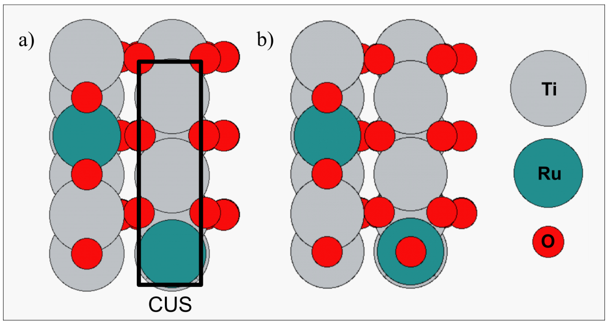

Figure 9: The rutile (110) $Ru_xTi_{1-x}O_2$ surface slab of study. **a)** Example slab with CUS sites highlighted. **b)** Example slab with an oxygen adsorbate on a ruthenium active site.

The binding energies for the OER adsorbates are presented in fig. 10. First take a look at OH binding, fig. 10a and notice how it is found to be almost binary. Either the structure is pure TiO_2, in which case the binding energy is approximately 2.0 eV, or the structure includes ruthenium, in which case binding on Ti has a mean of $\approx$1.3 eV and binding on Ru has a mean of $\approx$0.9 eV. This binding energy on Ru matches that of pure RuO_2. Notice that Ti site binding has quite a spread in binding energies, which decreases as the structure goes deep into the conductive regime. A similar trend is replicated for OOH adsorption (fig. 10d). For O+H^b adsorption with hydrogen at the bridge (fig. 10b), the trend is similar, but with a couple of key differences. Firstly, the adsorption is generally weaker on Ti than that of single site OH. Secondly, ruthenium active sites seem to have a distinct transition regime from $x = 0$ to $x = 0.25$, with weakening of the adsorbate binding. These general trends are replicated for oxygen binding (fig. 10c). Oxygen binding on Ti does however have a very large spread in the deep semi-conducting regime. This volatility in the binding energy could be predicated upon the doubly sensitive nature of the oxygen double bond, or potentially finite size effects [39].

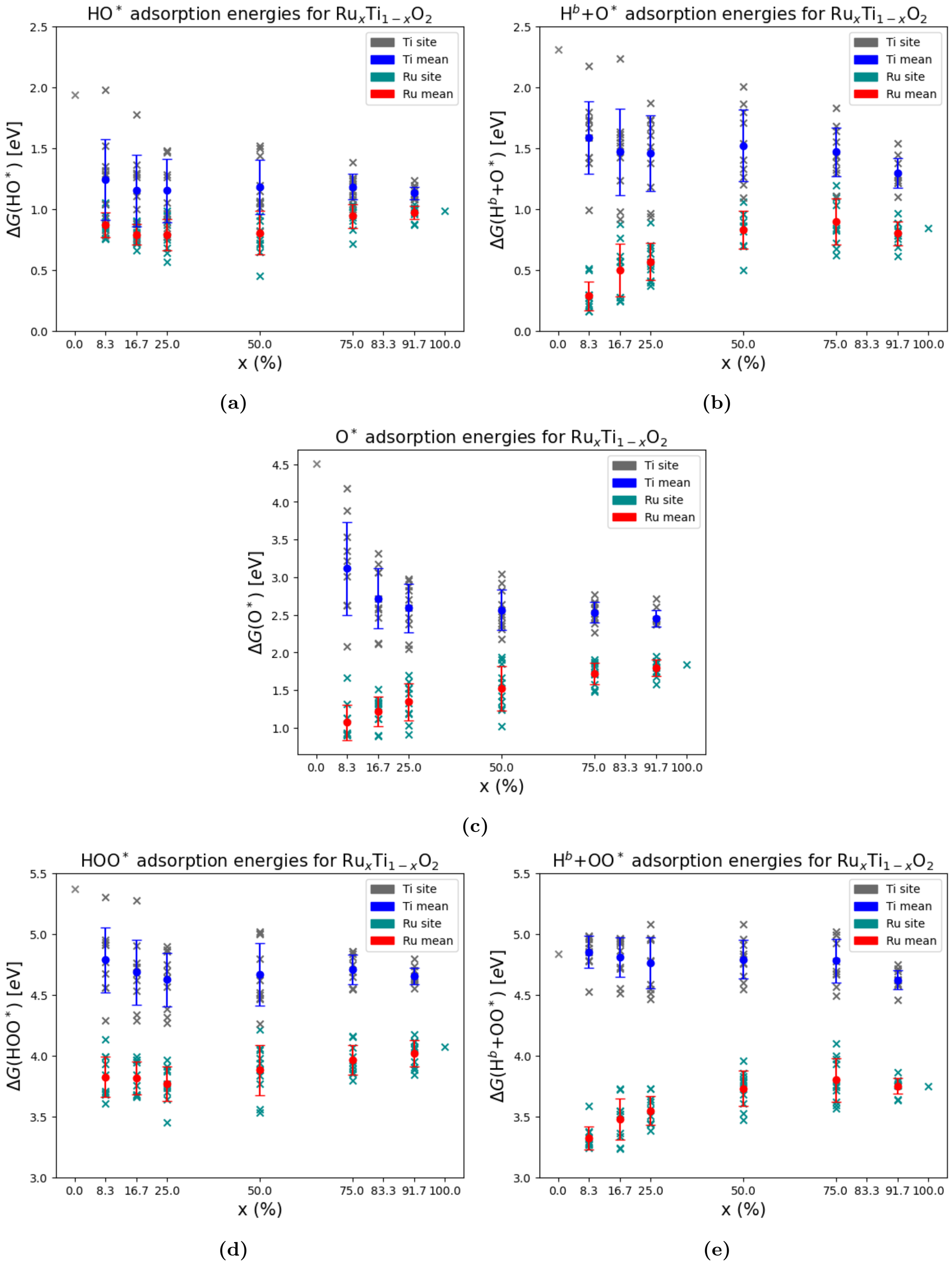

(a) **(b)**

(c)

(d) **(e)**

Figure 10: Gibbs free energies of binding $\Delta G(A)$ (in eV) for OER reaction intermediates (A) on rutile (110) Ru$_x$Ti$_{1-x}$O$_2$ at varying x. **a)** HO*. **b)** H^b + O*. **c)** O*. **d)** HOO*. **e)** H^b + OO*. Binding energies are plotted for both Ru and Ti as active sites.

Finally, for OO+H^b adsorption with hydrogen at the bridge (fig. 10e), the transition regime for ruthenium is replicated. However, this adsorbate shows a unique trait among the investigated intermediates. The binding energy on Ti does not shift towards stronger binding upon introduction of Ru in the structure. The binding energy is less that of OOH on pure Ti, and is somewhat constant throughout the entire composition space. This behaviour hints at pure TiO_2 preferring this intermediate over OOH, whereas Ru containing slabs hold no particular preference.

The transition regime observed on ruthenium sites for intermediates O+H^b and OO+H^b could be related to the relative frequency of different proton-acceptor bridge sites. However, the transition regime is also present for oxygen adsorption. It could therefore be speculated that it is related to the double-binding oxygen species present in each of these intermediates.

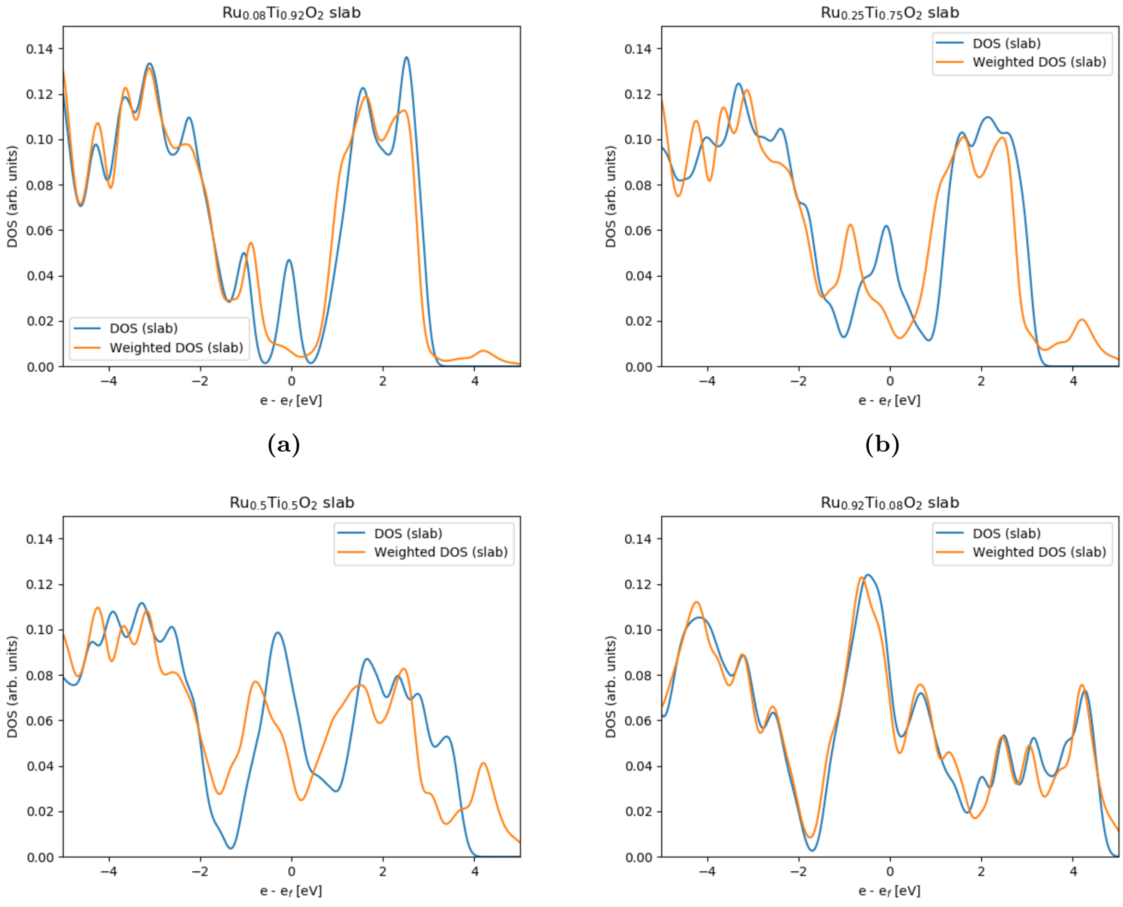

(a) **(b)**

(c) **(d)**

Figure 11: Examples of density of states for slabs at each end of the $\mathrm{Ru}_x\mathrm{Ti}_1 - x\mathrm{O}_2$ spectrum. **a)** $x = 0.08$. **b)** $x = 0.25$. **c)** $x = 0.50$. **d)** $x = 0.92$. DOS is plotted in blue. As reference, a weighted average of the pure RuO_2 and TiO_2 is presented in orange. Additionally, the x-axis is shifted by the Fermi level, e_f, such that zero represents this value.

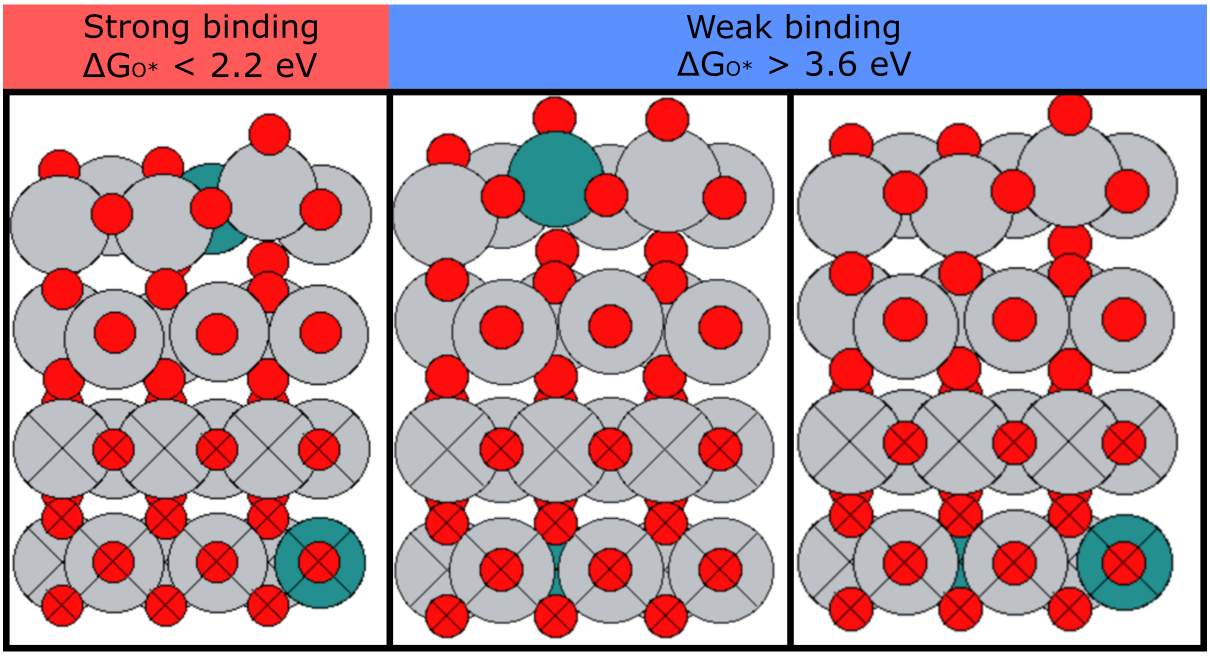

Figure 12: Structures identified with Ti oxygen binding energies at the extremes. Here the strong binding slab has a binding energy below 2.2 eV, and the weak binding slabs have binding energies above 3.6 eV.

One could be tempted to explain the wide spread of binding energies from changes in the density of states. The DOS, however, is found to be mainly related to the composition, and can therefore not explain the differences in binding energies for a specific choice of x. Examples of DOS spectra are presented in fig. 11. The DOS are compared to that of a weighted average between the DOS of pure RuO_2 and pure TiO_2. In the case of the deep semi-conducting regime (small x, fig. 11a), the weighted DOS does not represent that of the actual DOS in the band gap. Here the actual band gap resembles that of a doped semi-conductor, with states introduced by ruthenium. While this is just a single example of DOS for this composition, the small variations seen in DOS across the structures were not found to correlate with the value of binding energies. As x increases, the weighted DOS begins fitting better and better to the actual DOS, gaining close resemblance somewhere between $x = 0.25$ (fig. 11b) and $x = 0.50$ (fig. 11c). This could be indicative of the semi-conductor conductor transition regime ending, and would line up well with the associated changes seen for binding on Ru. Finally in the deep conducting region (fig. 11d), the weighted DOS resembles the DOS very closely, and there is no doubt about the conductivity of the material.

A closer look at the extreme examples of binding energies for oxygen binding at $x = 0.08$ is presented in fig. 12. From these structural pictures it is a little easier to determine the origin of the wide binding spread. In case of the strong binding example, the Ti active site has a neighbouring Ru atom in the bridge, which can serve as an electron donor to the active site. In the case of both weak binding sites, there are no clear electron donating ruthenium atoms. In the first case, the neighbouring Ru CUS site is oxidized by an oxygen adsorbate. The second ruthenium in this structure, as well as both ruthenium in the second weak binding structure, are found in the bottom layer. It can be speculated that the three layers of semi-conducting TiO_2 between the adsorbate and the

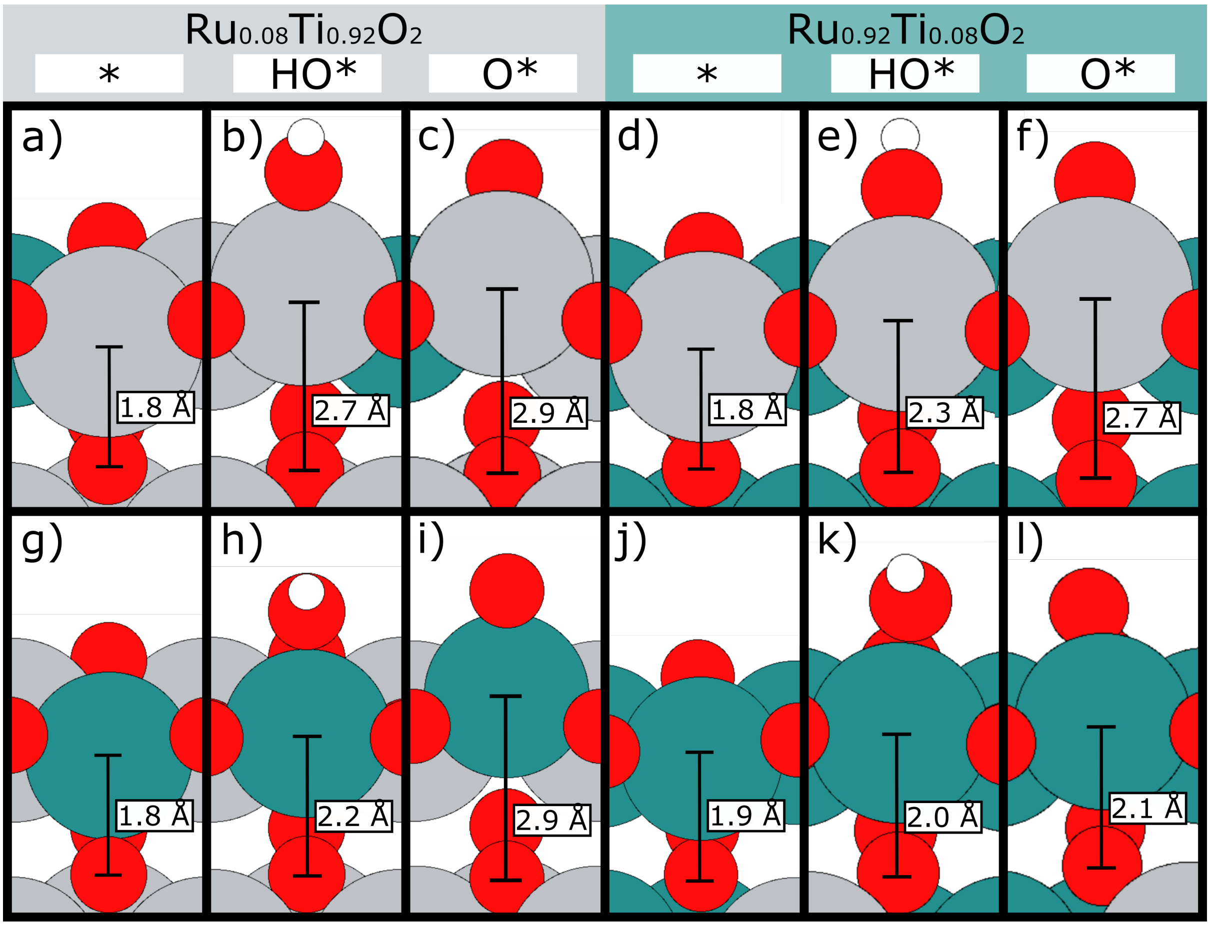

Figure 13: Bond distance from active site CUS atom to sublattice oxygen directly beneath for no adsorbate, hydroxide adsorption and oxygen adsorption. **a-c)** Ti active site for $x = 0.08$. **d-f)** Ti active site for $x = 0.92$. **g-i)** Ru active site for $x = 0.08$. **j-l)** Ru active site for $x = 0.92$. Despite being singular examples, the trends displayed are indicative of the entire data set.

bottom layer constitutes an insulating layer, disallowing electron tunneling to the active site. This echoes the coloumbic effect observed for dopants in the presented article 4 [85] (section 5.3). Another possibility is that computational artefacts arise due to the artificial nature of the constrained bottom layers. This could influence the degree to which Ru dopants can contribute electrons to surface layer binding.

A sharp reader might have noticed a peculiarity regarding the binding sites in fig. 12. That is, there seems to be surface deformation associated with the adsorption of intermediates. This is not a behaviour that is isolated to the binding energy extremes, but rather a general trend. A wider selection of examples of this behaviour is presented in fig. 13. This bond elongation trend is observed for both Ru and Ti in the case of the semi-conducting regime (figs. 13a to 13c and 13g to 13i), but mainly Ti in the conducting regime (figs. 13d to 13f). The amount of deformation also seems related to the number of bonds formed to the active site, with one bond usually elongating by around 0.5 Å, and two by around 1 Å. The only exceptions to this rule are OH binding on Ti at $x = 0.08$ (fig. 13b), which goes the full 1 Å by only a single bond, and the ruthenium active site in the conductive regime (figs. 13j to 13l).

A way to rationalize the behaviour is to view it as a (forced) coordination change due to the bonding of the adsorbate. This is somewhat contrary to a more traditional understanding of intermediate binding, which is usually thought of as happening by change of oxidation state. By changing coordination, the active site can provide electrons for the binding while minimizing additional oxidation. This is particularly relevant for TiO_2 which does not usually move beyond oxidation state $+4$. CUS site cations are under-coordinated by two-thirds of an oxygen bond. This in turn implies that any surface intermediate binding to the surface with one or more bonds over-coordinates the active site by at least one third of a bond. This increases to four thirds of a bond in case of a double-bonding intermediate. For the case of the single bonds to the surface presented in figs. 13e and 13h, the one third of over-coordination can be thought of as taken from the active site's bond to the subjacent oxygen during recoordination. This can be somewhat related to the distance of the deformation, with one third of a bond recoordinating matching 0.5 Å of deformation. If the entire two thirds are recoordinated, the structure has completely broken the bond, matching the 1 Å deformation. The only example this conceptualization does not match is fig. 13b, where it cannot explain the full bond severance upon OH adsorption.

The recoordination seems to occur when it is difficult to supply the electrons necessary for adsorbate binding. This would explain why it is seen when binding to Ti, and for Ru as a guest atom in TiO_2. On a more personal note, I enjoy how the idea of recoordination during the catalytic cycle makes the surface feel more alive under reaction conditions.

5.5 Binding energy engineering: Ti in high entropy oxides

As has just been outlined, the behaviour of Ti is quite odd due to its semi-conducting nature, wide spread of possible binding energies and recoordination tendency. In fact, the wide spread of binding energies on Ti can be reproduced in multiple other oxide systems, as has been studied by my coworkers Georgios Stavroglou, Katrine Louise Svane and Henrik Høgh Kristoffersen. With their permission I will share some of their findings here.

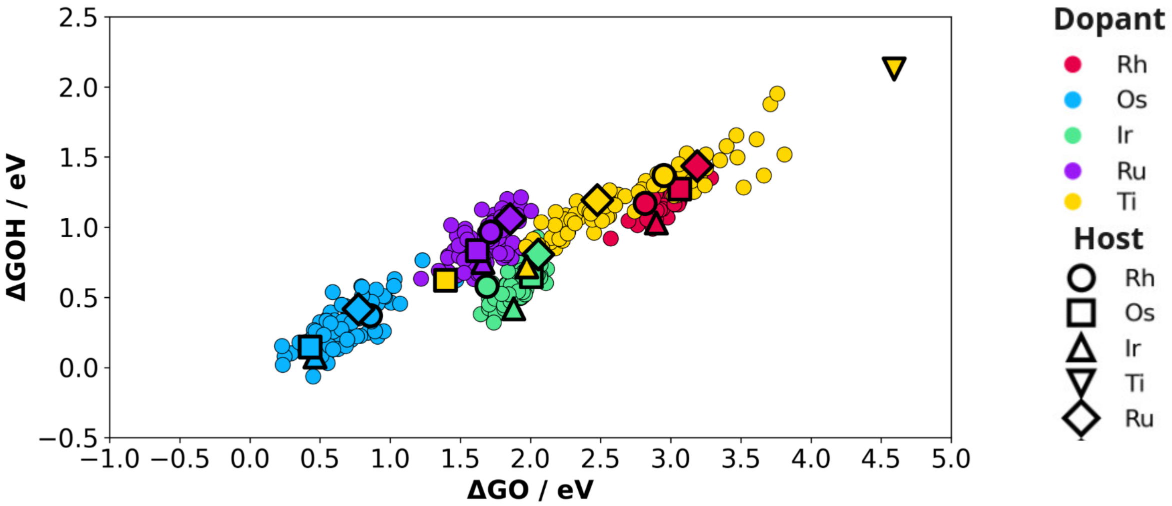

Figure 14: O-OH scaling relation for the Host-Guest system (**thick black outline**) as well as the (Rh,Os,Ir,Ru,Ti) High Entropy Oxide system (thin outline, circular points). The points are colored according to the (dopant) active site. This figure is produced by, and included with the permission of, Georgios Stavroglou.

The first system is a Host-Guest system, in which a "guest" element is introduced as active site in an otherwise pure host oxide. The second system is a near equimolar high-entropy oxide (HEO) system. Both systems are constructed from the same oxides as matching Svane's earlier work [92], that is Rh, Os, Ir, Ru and Ti. Plotting the O-OH scaling relation for these two systems yields fig. 14. The main thing to note here, is how the wide range of binding energies for Ti is essentially reproduced here. Oxygen binding energies can vary from approximately 2.0 eV to 4.0 eV (excluding host-guest outliers). This is more than twice the spread of most of the conducting active sites. A similar behaviour is illustrated for OH binding. It is therefore possible for Ti sites to be highly active, as is also illustrated by Svane in her work on HEOs [92].

Remember now from section 5.1 that binding energies have been shown to correlate to distance from oxygen p-band center to the Fermi level ([77]), as well as number of outer electrons [81]. Based on this, we hypothesize that the Fermi level relative to some stable state can serve as a descriptor for bond strength. How do we quantify the Fermi level in a way that makes it possible to compare materials? In much the same way as was done with oxygen p-bands, by reporting it relative to a band center. Inspired by Kristoffersen and Metiu [93], we choose as sharp and deep a band as possible. To be able to compare between different materials, the band has to be present in all cases. Thus it has to be an oxygen, as only oxygen is present in all oxides. Additionally, it has to be part of the treated states in DFT and not the frozen core. The oxygen $2s$ band is chosen as the reference "core" band, as it is a relatively sharp, deep, and in most cases non-interactive, state, shared by all oxides. The Fermi level (E_f) can then be quantified as:

$$E_f = e_f - e_{2s} \tag{50}$$

where e_f is the Fermi level as determined by DFT and e_{2s} is the oxygen $2s$ band center. A graphical illustration of this principle is illustrated in fig. 15. In the case of a semi-conducting oxide with a band gap, the value of e_f is determined as the midpoint of the band gap.

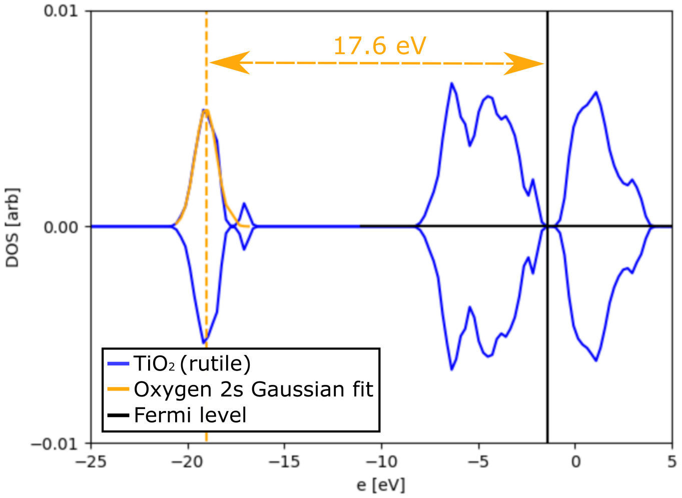

Figure 15: Visual representation of the energy difference between 2s band center of oxygen and the Fermi level for the case of rutile TiO_2.

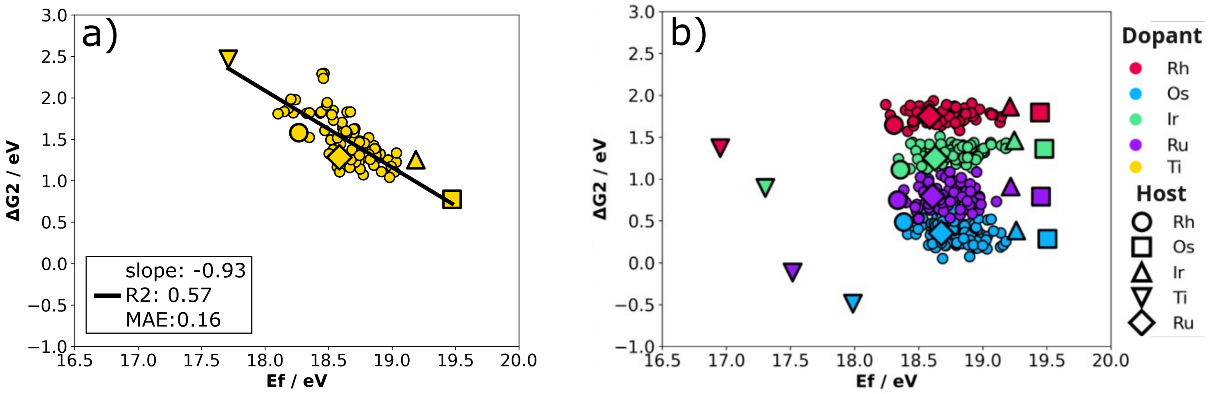

Figure 16: Dependency of ΔG_2 on Fermi level for binding on **a)** Ti and **b)** Rh, Os, Ir, Ru, Ti. The semi-conduting Ti shows correlation to the Fermi level, whereas the conducting atoms do not. This figure is produced by, and included with the permission of, Georgios Stavroglou.

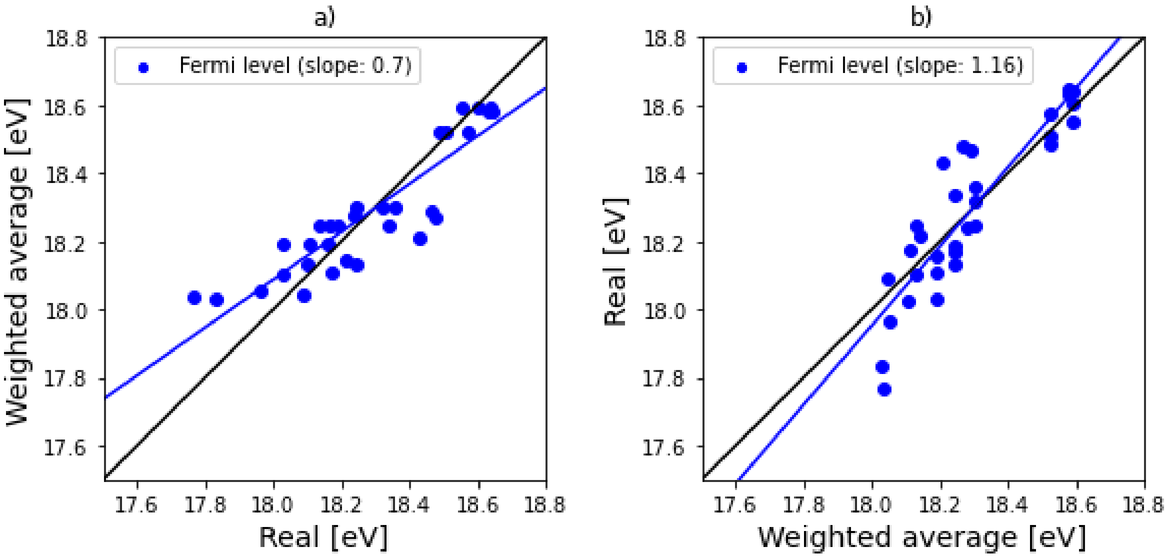

Figure 17: Model of actual Fermi level as a weighted average of a slab's constituents for a rutile HEO system of (Ti,Sn,Mn,Pt,Mo,Nb).

Applying this approach to the Host-Guest/HEO systems and plotting the results against the OER activity descriptor ΔG_2 yields fig. 16. A striking difference is found between the Ti active sites (fig. 16a) and any of the conducting elements (fig. 16b). Binding on Ti is found to be clearly correlated to E_f, while for conducting elements, no such correlation is found. Importantly, the Ti sites cross the top of the OER volcano assuming scaling relations ($1.5\ eV < \Delta G_2 < 1.7\ eV$ for $\eta < 0.5\ eV$). It therefore seems that if one has control over the Fermi level, one could choose the optimal binding energy specifically for Ti active sites. This would be the case for $E_f \approx 18.6\ eV$. Calculating the Fermi level for a wide variety of rutile polymorphs produces table 1.

Rutile oxide	TiO_2	SnO_2	CrO_2	PdO_2	MnO_2	VO_2	RhO_2
E_f [eV]	17.60	17.69	17.72	17.78	17.82	18.39	18.39

Rutile oxide	RuO_2	PtO_2	MoO_2	IrO_2	NbO_2	OsO_2
E_f [eV]	18.71	18.73	19.15	19.34	19.45	19.58

Table 1: Table of Fermi levels, calculated as the distance from oxygen 2s band center to the Fermi level (calculated by VASP).

A simple model for the prediction of the Fermi level in a high-entropy oxide would be a weighted average of the constituent oxides. Using HEO structures constructed from some of the cheaper tabulated oxides (Ti,Sn,Mn,Pt,Mo,Nb), such a model is plotted in fig. 17. Here it becomes apparent that this simple model is a decent first estimation of the Fermi level.

That the Fermi level controls the binding energy of OER intermediates on Ti, while simultaneously being somewhat predictable, is highly significant for the rational design of OER catalyst materials. As long as the primary active site is Ti, it should allow for designing catalysts with a mix of cheap elements averaging the optimal Fermi level.

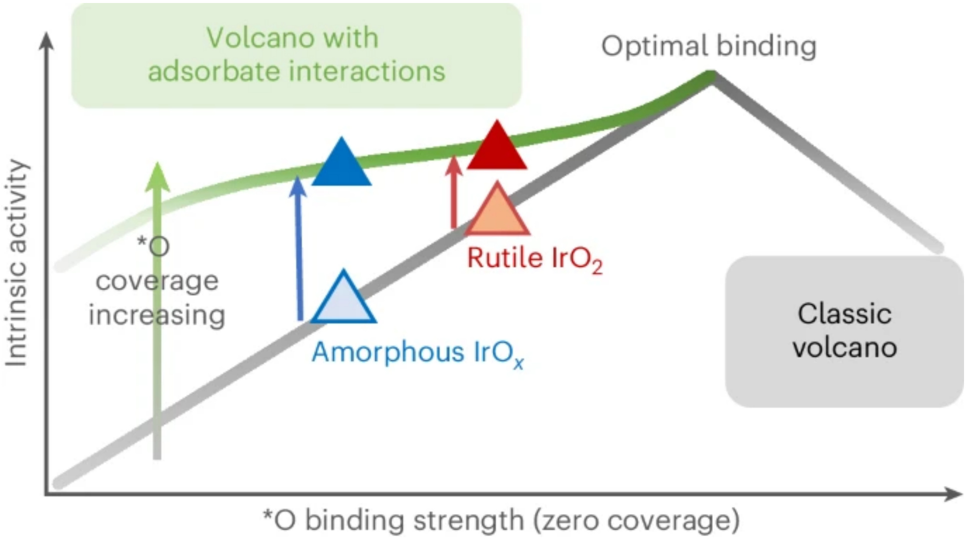

This figure is reproduced from the following attached article [94].

6 Article 5: Unravelling the effects of active site density and energetics on the water oxidation activity of iridium oxides

This paper explores the significance of adsorbate-adsorbate interactions and active site density in the reaction mechanism and energetics of amorphous and rutile iridium oxide. The amorphous IrO$_x$ was synthesized by electrodeposition on fluorine-doped tin-oxide, and the rutile IrO$_2$ was synthesized by thermal annealing of the resulting film. The materials were characterized by XRD, SEM, X-ray Photoelectron spectroscopy (XPS), ex situ X-ray Absorption Near-Edge Structure (XANES) and Extended X-ray Absorption Fine-Structure (EXAFS). XPS and XANES find that Ir in the amorphous film is a combination of oxidation states +3 and +4, whereas Ir in the rutile IrO$_2$ samples is mainly in oxidation state +4. Additionally, EXAFS find that IrO$_x$ is dominated by short-range ordered [IrO$_6$], whereas IrO$_2$ has a longer-range ordered structure. Electrochemically, cyclic voltammetry (CV) finds IrO$_x$ to be more active, to have higher current densities and to have two additional redox peaks as compared to IrO$_2$. Time-of-Flight secondary-ion mass spectrometry is applied to determine whether the increased current densities are due to porosity of the IrO$_x$ or proton penetration in the bulk. It is found that protons penetrate far deeper into the amorphous oxide compared to the rutile.

The redox chemistry of the materials is studied using time-resolved operando UV-vis spectroscopy, where both samples are found to undergo three similar redox transitions between 0.6 V and 1.5 V. The saturated redox transition density of IrOx is found to be more than six times that of IrO$_2$, explaining the higher current densities. Coverage data of the different redox species is determined and fitted to Frumkin isotherms, yielding the interaction energy for the redox species. The great fit of the Frumkin isotherm indicates the importance of adsorbate-adsorbate interactions in the systems.

To verify the nature of the redox transition associated surface species, DFT is used to explore surface states. Employing the CHE the most stable surface intermediates at varying potentials are determined. For disordered IrO$_x$ a hollandite model system is used due to its more open structure. The interaction energy between adsorbates, as well as the potential of half coverage, is determined by calculation of surface states at varying coverage. This allows for the plotting of Frumkin isotherms to compare with the experimental results. From this, it is found that redox transition 1 is likely the adsorption of OH onto CUS sites, redox transition 2 is likely the deprotonation of bridge sites, and redox transition 3 is likely the deprotonation of OH on CUS. While OH-OH interaction is well described by these results, oxygen-oxygen interactions are significantly weaker than the real systems.

The lifetime of the redox states is investigated in open circuit by time-resolved UV-vis spectroscopy. It is determined that there is a fast and a slow decay process, with fast being mainly decay of CUS site oxygen, and slow being decay of deprotonated bridge sites. The fast decay is expected to be due to reaction with water, mediated by another active oxygen species acting as proton acceptor. This decay mechanism is validated by electrochemical mass spectrometry.

Finally, the relationship between CUS bound oxygen states and reaction rate in the samples is explored. It is found that while IrO_2 has a higher turnover frequency per site at a given coverage of CUS bound oxygen, the amorphous sample populates with CUS bound oxygen at lower potentials. Thus despite the rutile structure being intrinsically more active per site, at a similar potential the amorphous sample is more active. This is rationalized by more adsorbate-adsorbate interactions, as predicated by a generally greater amount active sites. These revelations lead to a modified volcano plot dependent on the strength of these adsorbate-adsorbate interactions.

Unravelling the effects of active site density and energetics on the water oxidation activity of iridium oxides

Caiwu Liang, Reshma R. Rao, Katrine L. Svane, Joseph H. L. Hadden, Benjamin Moss, Soren B. Scott, Michael Sachs, James Murawski, Adrian Malthe Frandsen, D. Jason Riley, Mary P. Ryan, Jan Rossmeisl, James R. Durrant, Ifan E. L. Stephens

Article and supplementary material available at DOI:

https://doi.org/10.1038/s41929-024-01168-7 nature catalysis

Article

https://doi.org/10.1038/s41929-024-01168-7

Unravelling the effects of active site density and energetics on the water oxidation activity of iridium oxides

Received: 19 February 2023

Accepted: 23 April 2024

Caiwu Liang[1,2], **Reshma R. Rao**[1,2] ✉, **Katrine L. Svane**[3], **Joseph H. L. Hadden**[1], **Benjamin Moss**[2], **Soren B. Scott**[1], **Michael Sachs**[4], **James Murawski**[1], **Adrian Malthe Frandsen**[3], **D. Jason Riley**[1], **Mary P. Ryan**[1], **Jan Rossmeisl**[3] ✉, **James R. Durrant**[2] ✉ & **Ifan E. L. Stephens**[1] ✉

Understanding what controls the reaction rate on iridium-based catalysts is central to designing better electrocatalysts for the water oxidation reaction in proton exchange membrane electrolysers. Here we quantify the densities of redox-active centres and probe their binding strengths on amorphous IrO_x and rutile IrO_2 using operando time-resolved optical spectroscopy. We establish a quantitative experimental correlation between the intrinsic reaction rate and the active-state energetics. We find that adsorbed oxygen species, *O, formed at water oxidation potentials, exhibit repulsive adsorbate–adsorbate interactions. Increasing their coverage weakens their binding, thereby promoting O–O bond formation, which is the rate-determining step. These analyses suggest that although amorphous IrO_x exhibits a higher geometric current density, the intrinsic reaction rates per active state on IrO_x and IrO_2 are comparable at given potentials. Finally, we present a modified volcano plot that elucidates how the intrinsic water oxidation kinetics can be increased by optimizing both the binding energy and the interaction strength between the catalytically active states.

Water electrolysis via proton exchange membrane electrolysers is a key technology for converting renewable energy into green hydrogen[1,2]. However, the highly acidic and oxidizing conditions at the anode have thus far limited the choice of catalysts for the kinetically sluggish water oxidation reaction to oxides of iridium[3]. Iridium is one of the scarcest elements on the planet, with a production potential of <9 t yr^{-1} (ref. 4). Consequently, one of the key challenges for the terawatt-scale uptake of proton exchange membrane electrolysers is to minimise the iridium loading at the anode[4–8].

A number of iridium-based oxides have been studied, ranging from crystalline rutile oxides, amorphous oxides and alloyed oxides[9–12] to perovskites[13,14]. The catalytic activity is usually compared by normalizing the current density to the geometric area or the mass of iridium. Amorphous IrO_x is more active but less stable than crystalline rutile IrO_2, and shows a 220 mV reduction in overpotential as well as an approximately two orders of magnitude lower lifetime at 1 mA cm$^{-2}_{geo}$ (ref. 8). Recent studies on highly active $IrNiO_x$ (refs. 10,11), Li–IrO_x (ref. 9) and $SrIrO_x$ (refs. 8,13,15) have demonstrated that the surface of these materials is converted to an amorphous phase on exposure to oxygen evolution reaction (OER) potentials. Amorphous IrO_x is easier to oxidize and undergoes greater Ir–O bond shortening with increased potential compared with crystalline IrO_2 (refs. 9,10,16,17). These differences in coordination environment of the iridium centre have been suggested to influence the binding energetics of key OER intermediates, possibly

---

[1]Department of Materials, Imperial College London, London, UK. [2]Department of Chemistry, Centre for Processable Electronics, Imperial College London, London, UK. [3]Department of Chemistry, University of Copenhagen, Copenhagen, Denmark. [4]PULSE Institute, Stanford University, Menlo Park, CA, USA. ✉e-mail: reshma.rao@imperial.ac.uk; jan.rossmeisl@chem.ku.dk; j.durrant@imperial.ac.uk; i.stephens@imperial.ac.uk

resulting in the differences in activity observed[11,16,18–21]. However, the detailed mechanistic origins of the differences in activity between amorphous IrO_x and rutile IrO_2 remain poorly understood.

Studies as far back as the 1950s have suggested that water oxidation on metal oxides can proceed via sequential steps of proton-coupled electron transfer to form an O_2 molecule[22,23]. More recently, density functional theory (DFT) models have suggested that the potential-determining step for the OER on iridium oxide is the reaction of adsorbed oxygen (*O) with water to form a peroxo intermediate (*OOH): $^*O + H_2O \rightarrow {}^*OOH + H^+ + e^-$ (that is, O–O bond formation), where e^- is an electron[24,25]. Recent work by Nong et al., combining X-ray absorption spectroscopy (XAS) and DFT, has also implied that this step is the rate-determining step (RDS)[26]. Crucially however, Nong and co-workers suggest that the activation energy of the RDS decreases linearly with *O coverage, attributed to long-range interactions between *O species. Our recent work using operando optical spectroscopy agrees with this conclusion: an increase in OER kinetics correlates with the density of accumulated oxidized species (*O) on amorphous IrO_x. Conversely, using an immobilized molecular iridium catalyst, where these cooperative interactions are absent, the water oxidation kinetics were independent of *O coverage[27–29]. Although the importance of adsorbate–adsorbate interactions has been raised by Nong et al., it remains unclear how adsorbate–adsorbate interactions influence the trend in activity from one catalyst to another. This lack of quantitative understanding is derived from the difficulties in theoretically and experimentally determining electroadsorption isotherms and turnover frequencies on catalysts, with the exception of single crystals[30].

Here we use operando optical spectroscopy to compare the water oxidation energetics and kinetics of amorphous IrO_x versus crystalline rutile IrO_2. We quantitatively determine the density of redox-active centres as a function of the potential and quantify the interaction between adsorbate species by experimentally determining the electroadsorption isotherms for both amorphous IrO_x and rutile IrO_2. The location of redox-active centres is spatially resolved using isotope labelling and time-of-flight secondary-ion mass spectrometry (ToF-SIMS). The structure and local environment of the catalysts is probed using XAS. Finally, time-resolved optical spectroscopy is used to determine the intrinsic turnover frequency (TOF) values as a function of the potential. These results are corroborated with DFT calculations. By experimentally probing the potential-dependent density of active states, adsorbate–adsorbate interactions and TOF data, this study elucidates the key roles played by the electronic structure of the active site in governing the binding energy at zero coverage, in addition to the adsorbate–adsorbate interactions in controlling the weakening of the binding energy with increasing coverage, both of which control the kinetics of water oxidation. Taken together these effects reveal mechanistic origins of the differences in activity between amorphous IrO_x and rutile IrO_2 for water oxidation and provide rational design strategies for the discovery of water oxidation catalysts.

Results

Iridium local structure and its influence on proton penetration

In this study, hydrous, amorphous iridium oxide films (IrO_x, possibly hydroxylated in the as-prepared form) were prepared via electrodeposition on fluorine-doped tin oxide (FTO) glass substrates using a well-established procedure[27,31] (see Methods for synthesis). Rutile IrO_2 films were obtained via thermal annealing of the electrodeposited IrO_x films at 550 °C for 8 h, as confirmed via X-ray diffraction (see Supplementary Note 1 and Supplementary Fig. 1c for details). Scanning electron microscopy (SEM) images show that amorphous films consist of nanoparticles 100–200 nm in size, whereas rutile IrO_2 has a larger particle size due to the growth of crystals during annealing (Supplementary Fig. 1a,b). However, in the as-deposited state, IrO_x shows a combination of Ir^{3+} and Ir^{4+} redox states, whereas IrO_2 is dominated by Ir^{4+}, as determined using X-ray photoelectron spectroscopy (XPS) (Supplementary Fig. 1d), consistent with previous work[19,32]. This is further supported by ex situ XANES (X-ray absorption near-edge structure) measurements at the iridium L_3 edge. The average oxidation state is determined by the position of the white line edge, which primarily corresponds to a transition from occupied $2p$ to empty $5d$ states[10]. As shown in Supplementary Fig. 2, the d-band holes for amorphous IrO_x and rutile IrO_2 are at ~4.4 and 5.0, corresponding to average oxidation states of around 3.4 and 4.0, respectively (see Methods for XANES measurements and analysis). The fitted EXAFS (extended X-ray absorption fine structure) results (Fig. 1c, Supplementary Fig. 3 and Supplementary Table 1) show that both samples have a characteristic Ir–O interatomic distance of ~2.0 Å, with comparable first-shell coordination numbers of 5.8 (±0.5) and 6.0 (±0.7) for amorphous IrO_x and rutile IrO_2, respectively. However, rutile IrO_2 shows a stronger signal from $Ir–Ir_1$ and $Ir–Ir_2$ (an interatomic distance between 2.5 and 4 Å) whereas these signals are very weak in amorphous IrO_x. Thus, these data suggest that short-range ordered $[IrO_6]$ units are dominant for amorphous IrO_x whereas a longer-range ordered structure is present in rutile IrO_2, as shown schematically in Fig. 1a,b.

Compared with IrO_2, the cyclic voltammograms of IrO_x show higher redox current densities of around one order of magnitude, when normalized to the geometric area. IrO_x also shows a higher activity than IrO_2, as reflected in the overpotential required to achieve 0.5 mA cm^{-2}_{geo} (~210 mV and 330 mV for IrO_x and IrO_2, respectively; Fig. 1d). IrO_x shows two distinct broad redox peaks at around 0.8 and 1.2 V versus the reversible hydrogen electrode (RHE). By contrast, no distinct redox peak can be observed for IrO_2. The redox features and catalytic activity of both samples are relatively stable for 20 cycles and 2.5 h of operation (further results on the stability of the redox features, activity and morphology/structure can be found in Supplementary Note 2).

To determine whether the increased current density on amorphous IrO_x is only a consequence of a higher permeability of electrolyte within the porous structure (resulting in a higher density of catalytically active sites) or is also a result of higher proton penetration through the bulk of the oxide (resulting in the participation of subsurface iridium sites), a combination of ToF-SIMS and deuterium isotope labelling was used. The film was impregnated and covered with paraffin wax, using an adapted method from Hadden and colleagues[33]. This method minimizes the effects of varying porosity on the ion incorporation (see Fig. 1e and Supplementary Note 3 for details)—and thus focuses on the effect of surface exchange and bulk participation. However, we acknowledge that it may not completely eliminate the effects of extremely small pores within this hydrous oxide. Samples were cycled in 0.1 M $DClO_4$ (99.8% D) from 0.66 to 1.50 V_{RHE}. The depth of proton penetration during water oxidation was assessed by comparing the deuterium signal intensity between the the cycled samples and those exposed only to the electrolyte but without electrochemical cycling. Figure 1f shows that amorphous IrO_x cycled in $DClO_4$ has a higher D/H ratio than the sample without cycling, for the first 100 s of ion sputtering, corresponding to a distance of around 20 nm. This signal then drops to the same level after 100 s (see Supplementary Figs. 7–10 and Supplementary Table 2 for details). By contrast, no obvious difference in D/H ratio can be observed before and after cycling for rutile IrO_2. These results indicate that protons penetrate far deeper into amorphous IrO_x than rutile IrO_2 under rounds of cyclic voltammetry (CV), thus offering more iridium sites for redox reactions and possibly for water oxidation. We conjecture that the short-range ordered structure in amorphous IrO_x is more flexible and hence allows more protons to access than the long-range ordered—and hence presumably more rigid—structure in rutile IrO_2. This is also consistent with the observation from atom probe tomography, by Mayrhofer, Cherevko, Gault, Kasian and co-workers[34,35], which indicates that hydrous IrO_x undergoes a greater degree of oxygen exchange with the electrolyte during OER than rutile IrO_2 where exchange is limited to within 2.5 nm of the surface.

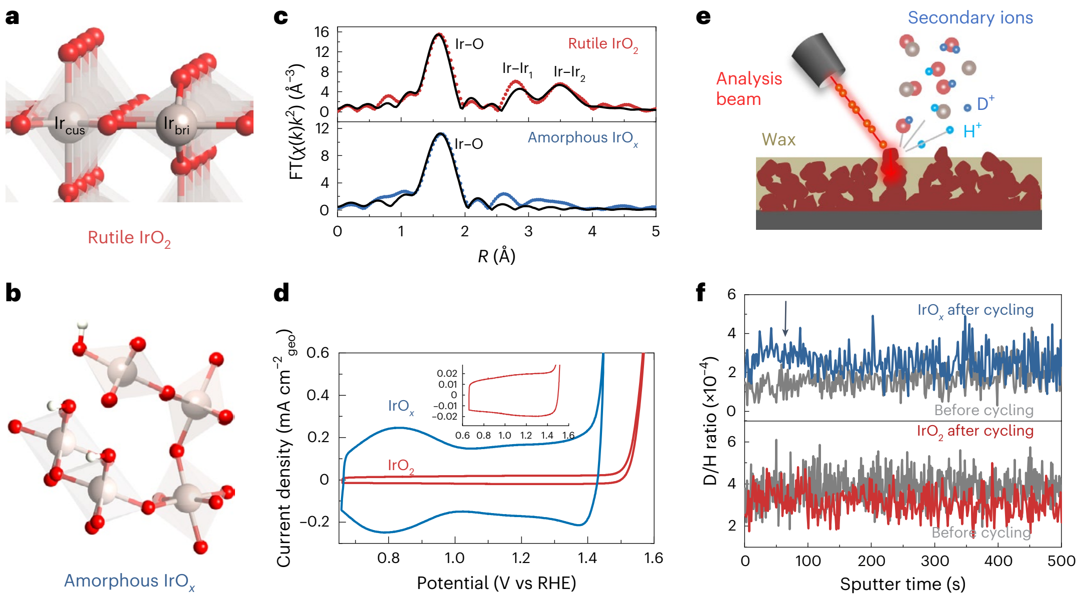

Fig. 1 | Structure, composition and electrochemical behaviour of amorphous IrO$_x$ and rutile IrO$_2$. a,**b**, Possible crystal structures of rutile IrO$_2$ (**a**) and amorphous IrO$_x$ (**b**). Grey, red and white spheres represent iridium, oxygen and hydrogen atoms, respectively. Ir$_{cus}$ denotes a coordinatively unsaturated iridium site and Ir$_{bri}$ denotes an iridium site bound to the bridging oxygen. **c**, Ex situ k^2-weighted Fourier transform (FT) of EXAFS spectra collected at the iridium L$_3$ edge of amorphous IrO$_x$ and rutile IrO$_2$, showing the iridium coordination environment. Experimental data (solid lines) and fits (dotted lines) are shown. R, interatomic distance. **d**, Cyclic voltammograms of amorphous IrO$_x$ and rutile IrO$_2$ with the same iridium loading obtained at a scan rate of 10 mV s^{-1} in 0.1 M $HClO_4$ electrolyte (curves are iR-corrected (i, current; R, resistance)). Cyclic voltammograms are obtained after five cycles. The inset shows an expansion of the cyclic voltammogram of rutile IrO$_2$. **e**, Schematic showing procedures for using ToF-SIMS to detect proton penetration in iridium oxides. Dark red polygons denote iridium oxides and the dark yellow rectangle represents the wax-covered surface. Light blue and dark blue spheres denote protons (H$^+$) and deuterium ions (D$^+$), respectively. **f**, Comparison of the D/H ratio change with ToF-SIMS sputter time in amorphous IrO$_x$ and rutile IrO$_2$ before and after electrochemical cycling in deuterated $HClO_4$ solution. The downward arrow points to the region where a higher deuterium signal was observed compared to the background.

Identification of redox transitions on IrO$_x$ and IrO$_2$

Next, we probe the redox chemistry of both materials using time-resolved operando ultraviolet-visible (UV–visible) spectroscopy and stepped potential spectroelectrochemistry (see Supplementary Note 4 for details). Figure 2a,b shows the change in the UV–visible absorption spectra (versus 0.66 V$_{RHE}$) when the potential is increased in 20 mV steps, reflecting the change in the surface speciation of the iridium oxides as a function of the potential. On increasing the potential, amorphous IrO$_x$ shows broad absorption bands at 600, 800 and 500 nm in the potential ranges of ~0.66–1.00 V$_{RHE}$, ~1.10–1.32 V$_{RHE}$ and >1.32 V$_{RHE}$, respectively (Fig. 2a). We note that these absorption spectra are highly reversible with the potential and are reproducible over several cycles, showing almost identical absorption spectra during both the forward and reverse scans. (Supplementary Figs. 12 and 13). The absorption spectra of IrO$_2$ show an increasing pattern similar to IrO$_x$, with a slight shift of the dominant absorption band to higher wavelength in the low potential regime (Fig. 2b). However, the intensity of the optical absorption is around six times lower in the case of IrO$_2$, consistent with this more crystalline and rigid structure having a lower density of redox-active iridium centres, as discussed above.

In optical spectroscopy, a change in absorbance between two potentials indicates a redox transition from one state to another. For each transition, we expect a distinct spectral shape for the change in absorbance[27,28,36–38]. To discern these transitions, we analyse the change in absorbance at each potential by subtracting the spectra at adjacent potentials in intervals of 20 mV and normalize these differences to their maximum values. This process defines our differential spectra, as shown in Fig. 2c. We note that all differential spectra are positive in the measured wavelength window, which is a result of a continuous increase in absorption with the increasing applied potential (Fig. 2a). This differs from typical molecular systems, which often display isosbestic points in absorption and thus both positive and negative regions in their differential spectra. However, this behaviour is not unique to our study and has been similarly observed in various metal oxide OER catalysts[37–39]. This is most likely because the widths of the observed spectral features are greater than the measured spectral range, in contrast to molecular systems which typically show narrower spectral features. From Fig. 2c, three distinct differential absorption spectral features can be obtained: a converging spectral shape with a peak at ~600 nm between 0.66 and 0.90 V$_{RHE}$, a peak at ~800 nm between 1.1 and 1.3 V$_{RHE}$, and a peak at ~500 nm at potentials >1.4 V$_{RHE}$. In other potential regions, a continuously changing spectral shape was observed, implying a combination of more than one redox transition process occurring. These constant differential spectra (as shown in Fig. 2d) correspond to the change in absorbance from one redox state to another (that is, state$_A$ → state$_B$, state$_B$ → state$_C$ and state$_C$ → state$_D$), and thus are denoted, respectively, as redox transition 1, redox transition 2 and redox transition 3, in accordance with our previous work (see Supplementary Note 5 for a detailed discussion)[27,28]. Three distinct spectral components are also observed for IrO$_2$, analogous to the three redox transitions observed for IrO$_x$ (see the detailed discussion in Supplementary Note 5 and Supplementary Fig. 14), with similar (but anodically shifted, see below) potential dependencies. For IrO$_2$, the peak position of redox transition 1 is shifted to 700 nm, and thus exhibits greater spectral overlap with redox transition 2; however, our deconvolution analyses clearly indicate that these two components can still be clearly resolved and their potential dependencies determined (Supplementary Figs. 16–18). These results show that, although IrO$_x$ and IrO$_2$ have substantially different CVs, they undergo the same redox transition processes, with both generating three similar redox transitions in the applied potential range. This is in agreement with a recent study that observed comparable changes in iridium 4f XPS spectra and oxygen K-edge XAS spectra with potential on both amorphous IrO$_x$ and crystalline IrO$_2$ (ref. 40).

https://doi.org/10.1038/s41929-024-01168-7

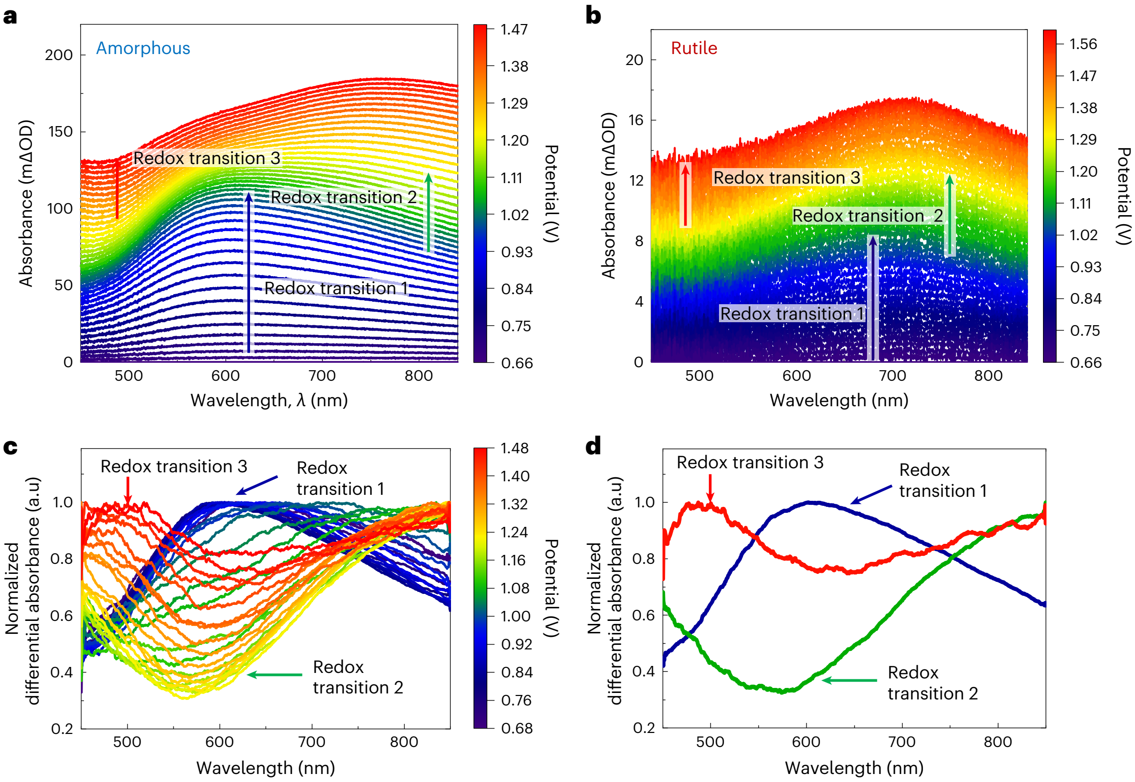

Fig. 2 | Redox transition features as function of the potential in amorphous IrO_x and rutile IrO_2. **a**, Differential absorption spectra of amorphous IrO_x during a linear sweep scan from 0.66 to 1.48 V_{RHE} in 0.1 M $HClO_4$ at a scan rate of 1 mV s^{-1} (*iR*-corrected). Absorbance changes were recorded after five CV cycles, at every 1 mV (see Supplementary Fig. 11 for the full spectra) and shown every 20 mV. The changes in absorbance are calculated with respect to the absorbance at 0.66 V_{RHE}. **b**, Differential absorption spectra of rutile IrO_2 during a linear sweep scan from 0.66 to 1.60 V_{RHE} in 0.1 M $HClO_4$ at a scan rate of 1 mV s^{-1} (*iR*-corrected). **c**, Differential analysis of absorption spectra for amorphous IrO_x at every 20 mV. The differential absorption spectra are obtained by subtracting adjacent spectra and normalizing the maximum absorbance to unity, representing a change in absorbance that corresponds to a potential change of 20 mV. **d**, Extracted spectra for individual redox transitions in amorphous IrO_x. The absorption spectra for redox transition 1 (blue), 2 (green) and 3 (red) in amorphous IrO_x are extracted from the potential regime where the shapes of the spectra in **c** are invariant, corresponding to differential spectra between 0.84 and 0.82 V_{RHE}, 1.18 and 1.16 V_{RHE}, and 1.46 and 1.44 V_{RHE}, respectively.

Quantification of redox transitions on IrO_x and IrO_2

To analyse the contribution of each redox transition to the observed spectra as function of the potential, we deconvoluted the absorption spectra through a linear combination fitting process. Specifically, we fitted the measured absorption spectra at each potential to a linear sum of the component spectra corresponding to different redox transitions. The fitting process, applied individually to the spectra at each potential, does not require assumptions about the potential dependence of various redox-state densities. It solely requires input of the spectral components, identified experimentally in Fig. 2d (see Supplementary Note 5 for the detailed fitting process and discussion). The deconvoluted absorbance intensities were converted to an area density of redox transitions using a potential step measurement in a single-redox transition regime, correlating the charge passed with the absorbance intensity according to the Lambert–Beer law (that is, the absorbance of an individual redox transition is considered to be linearly proportional to its density) (see Supplementary Figs. 19 and 20 for details). The densities of the redox transitions, obtained directly from deconvolutions, show typical sigmoid shapes with increasing potential (top panel of Fig. 3a), with similar densities of redox-active states participating in all three redox transition processes. The saturated density of redox transitions in IrO_x (~3.5×10^{16} cm^{-2}) is more than six times higher than that for IrO_2 (~5.5×10^{15} cm^{-2}) (top panel of Fig. 3b), which we attribute to the higher proton penetration in addition to the higher porosity within the structure. Assuming that the saturating densities of redox transitions observed in our spectroelectrochemical analyses indicate full coverage, the coverage θ of each redox state at a given potential is defined as $\theta = D/D_{max}$, where D is the density of states and D_{max} is the maximum saturating density. Therefore, θ is a unitless value. Notably, the state generated from redox transition 3 does not saturate within the observed potential regime, and therefore the maximum density was assumed to be the same as redox transition 1 as both redox transitions occur on the same coordinatively unsaturated (CUS) site (see 'DFT calculations' in the Methods below).

The resulting coverage (θ) versus potential (U) data, that is, the electroadsorption isotherms, can be modelled using the Frumkin isotherm with coefficient of determination R^2 values as high as 0.99, as opposed to a simple Langmuir isotherm (dashed line in Fig. 3a (top panel); see Supplementary Note 6 and Supplementary Figs. 23 and 24 for details of the fitting). These excellent fits indicate the existence of lateral interactions between the redox states, as assumed in the Frumkin model. Similar Frumkin-type behaviour and the corresponding interaction has also been observed in the redox transitions of an amorphous cobalt oxide by Risch and co-workers[39]. Mathematically, in a Frumkin electroadsorption model, the redox transition free energy ΔG^o_{redox} is a function of the redox-state coverage, that is, $\Delta G^o_{redox(\theta)} = \Delta G^o_{redox(\theta=0)} + r\theta$, where r (in electronvolts) is the interaction energy of the adsorbates at full coverage and θ is the coverage of the adsorbates ($0 < \theta < 1$). Analysing the θ–U data, we can obtain the value for the adsorbate–adsorbate interaction energy r. The fitted interaction energy r and the half-coverage potential $U_{(\theta=1/2)}$ for both amorphous and rutile iridium oxides are labelled in Fig. 3a,b. Interestingly, we found that the adsorbate–adsorbate interaction energy r values fitted from redox transition 3 on amorphous IrO_x and rutile IrO_2 are similar,

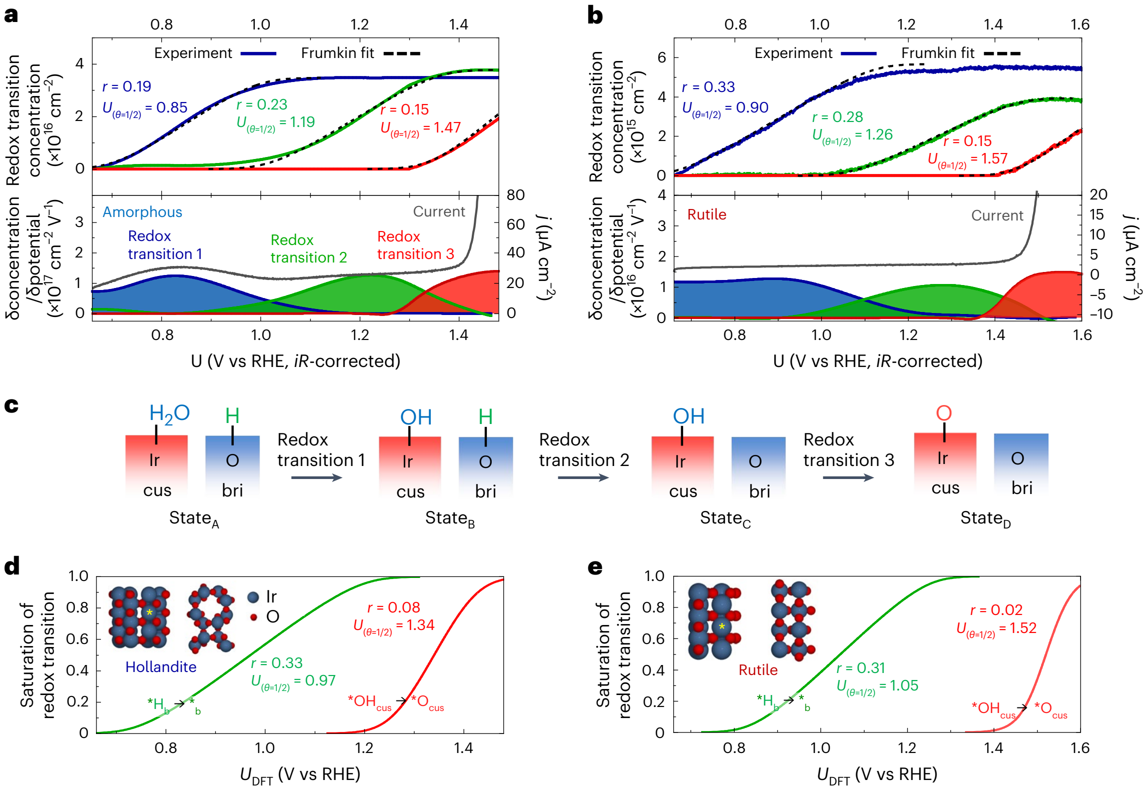

Fig. 3 | Redox transition densities as a function of potential in amorphous IrO_x and rutile IrO_2. **a**,**b**, Densities of redox transitions for amorphous IrO_x (**a**) and rutile IrO_2 (**b**) that have occurred as a function of the potential (solid lines), and the corresponding Frumkin isotherm fitting results (dashed lines). The bottom panels show the derivatives of these redox transition densities with respect to the potential U, represented as redox transition waves. These redox waves are co-plotted with the linear scan voltammetry curves (grey line, right y axis) as a comparison between optically and electrochemically determined redox transitions. j, current density. **c**, Schematic showing the proposed physical origin of the redox transitions and the redox states involved in these transitions on the basis of DFT calculations. **d**,**e**, DFT calculations for the saturation of $OH_{cus} + {}^*H_b \rightarrow {}^*OH_{cus} + H^+ + e^-$ and ${}^*OH_{cus} \rightarrow {}^*O_{cus} + H^+ + e^-$ transitions as a function of the potential U on hollandite iridium oxide (**d**) and rutile IrO_2 (**e**). The inset in **d** and **e** shows the hollandite IrO_2 (001) and rutile IrO_2 (110) surface structure, respectively. The coordinatively unsaturated iridium site is marked by the yellow asterisk.

both at about 0.15 eV, indicating that the interaction strength between the adsorbates involved in this redox transition are similar despite the changes in the iridium coordination environment between the amorphous and crystalline iridium oxides. However, for surfaces with a substantially different surface structure and/or density of CUS sites, this interaction strength may differ.

The transient rate of potential-associated redox transitions is determined by the derivative of the density of redox transitions over the potential (Fig. 3a,b, bottom panels). The peak positions for redox transitions on the amorphous and crystalline iridium oxides, obtained from a deconvolution analysis of the optical signal, were found to be at about 0.82 and 0.90 V_{RHE} for redox transition 1, 1.22 and 1.26 V_{RHE} for redox transition 2 and 1.47 and 1.57 V_{RHE} for redox transition 3 (Supplementary Table 3 and Fig. 3a,b). These optically determined redox transition waves match well with the less-well-resolved redox transitions observed in the linear sweep voltammetry curves for amorphous IrO_x. In addition, the predicted linear sweep voltammetry curves from the redox transitions are comparable to the experimentally observed curve, in terms of both curve shape and amplitude for both the amorphous and crystalline iridium oxides (grey line in the bottom panel of Fig. 3a,b and in Supplementary Fig. 21). The positions of redox transition 1 and redox transition 2 are also in agreement with the redox peak positions on amorphous IrO_x and perovskite $SrIrO_x$ determined by Geiger et al. (both are at around 0.8 and 1.2 V)[8]. Notably, the redox current for redox transition 3, corresponding to the optical data at OER-relevant potentials, is masked by the OER current measured electrochemically in the cyclic voltammogram. A redox peak at a similar potential (1.63 V_{RHE}) has also been observed by Kuo et al. on an IrO_2(110) surface[30]. It is clear that amorphous IrO_x undergoes the redox transition 3 process (~1.3 V_{RHE}) at a potential approximately 100 mV lower than rutile IrO_2 (~1.4 V_{RHE}; see Supplementary Fig. 22 for a direct comparison of the absorbance signals). This suggests that the differences in coordination between the iridium centres in amorphous and crystalline iridium oxides result in stronger binding of the oxygenated intermediates in IrO_x compared with IrO_2.

The UV–visible absorbance changes in Fig. 2 can be assigned to changes in intervalence charge transfer within the iridium d orbitals, which correlates to the oxidation of iridium and the change of surface adsorbates coordinated to the iridium centre[41–43]. Previous operando XAS studies have indicated that the first and second redox transitions in similar amorphous IrO_x may correspond to the Ir^{3+}/Ir^{4+} and Ir^{4+}/Ir^{5+} transitions[44–46], although a consensus on the exact oxidation state, especially during the OER, still has not been reached[27]. In particular, in OER potential regions where redox transition 3 occurs, previous operando XAS or XPS studies have suggested the formation of Ir^{4+} (ref. 47), $Ir^{4.x+}$ (ref. 48) or Ir^{5+} species[10,49,50]. Recent findings have suggested the formation of electrophilic oxygen species (O^{1-}) at OER-relevant potential regions[20,21,26]. Whereas the precise iridium oxidation state on the surface remains under debate, the aforementioned literature suggest that the redox transitions involve adsorbed oxygenated species. To verify the nature of these surface adsorbates, we first use DFT calculations (see the computational methods in Methods and Supplementary Note 7). We then use the behaviour of these adsorbates to represent the redox transition process, which is intrinsically linked to changes in the iridium oxidation state. We model the rutile IrO_2(110)

surface, which consists of rows of iridium atoms coordinated by bridging oxygens separated by rows of CUS sites (inset of Fig. 3e; see details in Supplementary Fig. 25). The adsorption of *H, $*H_2O$, *OH and *O on the CUS site and *H on the bridging oxygen ($*H_b$) was considered at full coverage. The calculations were performed at constant charge, and the computational hydrogen electrode[51] was used to determine the most stable surface adsorbate structure at a given potential (Supplementary Fig. 26). The interaction between the adsorbates was explored by calculating the free energy of the stepwise transition between the most stable adsorbates in a unit cell with three CUS sites, that is, at different coverages of the species. For selected surfaces the OER was modelled, two different reaction pathways were considered as described in previous work[52] (Supplementary Fig. 27). On the basis of these energies, the redox transition potential at half coverage $U_{(\theta=1/2)}$ and the interaction energy r were calculated and are plotted as adsorption isotherms in Fig. 3e. The calculated energies at half coverage for *OH (1.05 $V_{DFT\text{-}RHE}$) and *O (1.52 $V_{DFT\text{-}RHE}$) on the CUS site of rutile IrO_2 match well with experimental half-wave redox potentials for redox transition 2 (1.26 V_{RHE}) and redox transition 3 (1.57 V_{RHE}), considering the accuracy of DFT calculations[53,54] (Supplementary Table 5). Our calculations are also in agreement with previous work, which attributed the redox transitions at around 1.20 V_{RHE} and 1.63 V_{RHE} on $IrO_2(110)$ surfaces in 0.1 M $HClO_4$ to *OH and *O adsorption on the CUS site, respectively[30]. Redox transition 1 was considered to be *H desorbing from the CUS site or $*H_2O$ dissociating to form *OH on the CUS site, but the calculated potential values for both transitions (<0.19 $V_{DFT\text{-}RHE}$) do not match closely with the experimental result of 0.90 V_{RHE}, even if the possibility of an intermediate structure with some CUS sites covered by $*H_2O$ is considered (see Supplementary Fig. 26 for details). This is to be expected as the rutile surface is at the limit of stability at this potential, and the number of possible surface structures thus becomes large. Given that the saturated densities of redox transitions 1 and 2 are relatively close (with a deviation of between 3 and 30%), we anticipate that all iridium CUS sites will participate in the first redox transition with the transfer of a single electron, similar to the other two redox transitions. The differences in the total saturated densities of redox transitions 1 and 2 can be attributed to the polycrystalline nature of the sample where surface facets with an unequal number of bridge and CUS sites may be exposed. Therefore, opting for the simplest possible assignment for redox transition 1, we attribute these redox transitions to:

$$\text{redox transition 1}: \ {}^*H_2O_{cus} + {}^*H_b \rightarrow {}^*OH_{cus} + {}^*H_b + H^+ + e^- \tag{1}$$

$$\text{redox transition 2}: \ {}^*OH_{cus} + {}^*H_b \rightarrow {}^*OH_{cus} + {}^*{}_b + H^+ + e^- \tag{2}$$

$$\text{redox transition 3}: \ {}^*OH_{cus} \rightarrow {}^*O_{cus} + H^+ + e^-. \tag{3}$$

where $*_b$ represents the bridge oxygen adsoption site. The schematic in Fig. 3c shows the redox transitions and the redox states involved. The coverage of these redox states at CUS and bridge sites can be obtained using the fitted Frumkin isotherm and this DFT assignment (Supplementary Fig. 29). For amorphous IrO_x, the disordered surface structure cannot be modelled via periodic DFT calculations. Instead, as a representative of a more open IrO_x structure with a larger separation between the adsorbates, the (001) surface of hollandite IrO_2 is modelled, and calculations are carried out for the transitions $OH_{cus} + {}^*H_b \rightarrow {}^*OH_{cus} + {}^*b + H^+ + e^-$ and ${}^*OH_{cus} \rightarrow {}^*O_{cus} + H^+ + e^-$ (Fig. 3d)[18]. The energy values of redox transitions 2 (0.97 $V_{DFT\text{-}RHE}$) and 3 (1.34 $V_{DFT\text{-}RHE}$) on hollandite IrO_x are lower than on rutile IrO_2 (Supplementary Fig. 28), in agreement with our experimental observations.

Our DFT calculations also capture the interaction strength between *OH adsorbates on both the rutile and hollandite surfaces, showing that the calculated redox potential increases from 0.89 $V_{DFT\text{-}RHE}$ at one-third coverage to 1.20 $V_{DFT\text{-}RHE}$ at full coverage of *OH for the rutile structure, and from 0.80 to 1.13 $V_{DFT\text{-}RHE}$ for the hollandite structure (see Supplementary Note 8 for details of interaction parameter calculations). However, the interaction of *O cannot be fully captured using this model. The calculated interaction energies of *O are only about 0.02 and 0.08 eV for rutile and hollandite IrO_2, respectively, which are considerably lower than the experimentally observed value of 0.15 eV. This observation is in agreement with recent work suggesting that the repulsive interactions for *O species can only be captured by including solvent effects in the DFT model as the *O interactions may propagate through the water layer[26]. Therefore, we hypothesize that these interactions between *O species are mediated by the electrolyte, as also suggested by the measurements of Hu et al. on well-defined single crystal $RuO_2(110)$, where only surface ruthenium sites are active[55]. The above experimental and theoretical results indicate the key role of repulsive interactions between the adsorbates, which give rise to the Frumkin electroadsorption isotherm (Fig. 3a,b) and change the free energy of elementary steps in the OER as a function of coverage.

Correlating accumulated $*O_{cus}$ active states with the OER

Next, we investigated the lifetime of these accumulated redox states and their correlation with the water oxidation reaction on IrO_x. We measured the decay kinetics of the accumulated states when the potential was released from an oxygen-evolving potential to an open-circuit potential using time-resolved UV–visible absorption spectroscopy (see Supplementary Note 9 for details of the decay kinetics measurements)[28,37,56]. This experiment is shown in Fig. 4a, where two spectrally distinct decay phases were observed during open-circuit decay—a fast decay component (initial 1 s) with a dominant absorption decay peak at around 500 nm, and a slow decay component (100–200 s) with the maximum signal at around 800 nm (see Supplementary Note 9 and Supplementary Fig. 33 for detailed deconvolution of the decay data). The differential absorption spectra for these two phases are in excellent agreement with the differential absorption spectra of redox transition 3 and redox transition 2, respectively (Fig. 4b), indicating that the fast decay of absorbance arises primarily from the decay of $state_D$ to $state_C$ (that is, the decay of $*O_{cus}$), whereas the slow decay arises mainly from the decay of $state_C$ to $state_B$ (that is, the decay of bridge oxygen O_{bri}). Further comparison of the optical signal decay in different potential regimes shows that $state_B$ ($*OH_{cus}$) and $state_C$ (O_{bri}) remain stable even after the applied potential is switched off, indicating that these states are very stable once generated and will not be the catalytically relevant species (Supplementary Fig. 34). Conversely, the $*O_{cus}$ species decays rapidly once the applied potential is removed, indicating the reactivity of $*O_{cus}$ for forming molecular oxygen. Based on the established DFT calculations on $IrO_2(110)$[26,57,58], which suggest that the formation of *OOH from *O is the RDS, we interpret the fast decay process as described in Fig. 4c: a site in the active state ($*O_{cus}$) proceeds along the reaction path via nucleophilic attack from a water molecule, forming the O–O bond and followed by the release of oxygen. Here, the charge is balanced by other active states through accepting a proton and becoming reduced to regenerate $*OH_{cus}$ on the surface (as no charge is passed through the external circuit during open-circuit conditions). To validate this decay mechanism, we measured oxygen using highly sensitive on-chip electrochemical mass spectrometry (EC-MS). This technique enables the in situ measurement of gas products during electrochemistry with a resolution down to subpicomole per second sensitivity[59,60]. The net amount of O_2 produced during open-circuit decay from 1.46 to 1.40 V_{RHE}, detected using EC-MS, is ~0.87 nmol cm^{-2}. This amount of oxygen is in good agreement with the O_2 release expected from decay of the accumulated $*O_{cus}$ from 1.46 to 1.40 V_{RHE} (0.70–0.96 nmol cm^{-2}) (see supplementary Note 10 and Supplementary Fig. 37 for details). This analysis confirms that the decay of $*O_{cus}$ is coupled with O_2 release, with four $*O_{cus}$ atoms being consumed per molecule of O_2 generated. As a result, where τ is the time constant of this active-state decay, it implies an intrinsic rate for the RDS of $1/4\tau$ for O_2 released per second.

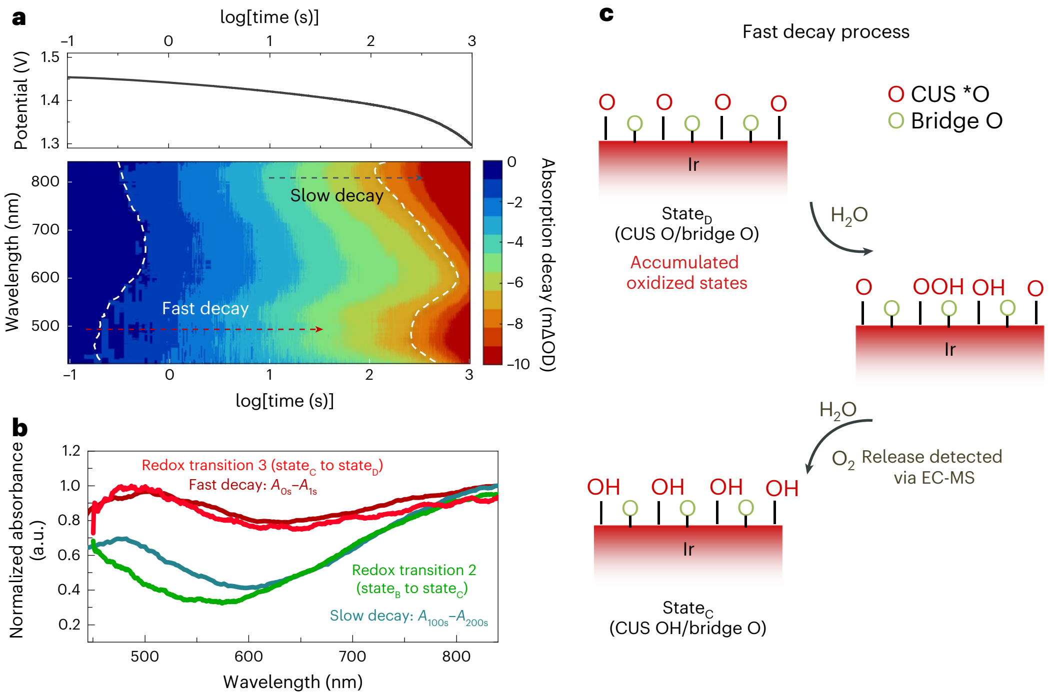

Fig. 4 | Active states for iridium oxides and their water oxidation mechanism. **a**, Change in potential (versus RHE) during open-circuit decay (top) and the change in absorbance (*A*) as a function of time after beginning decay under open-circuit conditions (bottom). The changes in absorbance are calculated with respect to absorption immediately before turning to the open-circuit potential. The colour scale represents the decrease in absorbance compared with that before open-circuit decay. The white dashed lines denote the same levels of decay in absorption. At the initial time (1 s), the absorption decay is at a maximum at wavelengths of ~500 and ~800 nm, whereas after 100 s, the absorption decay is dominant at ~800 nm. **b**, Comparison of the differential spectra obtained from the decay and redox transitions during linear sweep voltammetry. Spectra from the initial 1 s after the decay (dark red) and from 100–200 s after the decay (dark green) were obtained from Supplementary Fig. 33c. The spectral shape of redox transition 3 (light red) and redox transition 2 (light green) are from Fig. 2d. All spectra are normalized to their maximum absorbance for comparison. **c**, Proposed mechanism for the OER, involving the nucleophilic attack of water on the accumulated $*O_{cus}$ species to form molecular oxygen, corresponding to the fast decay phase in **a**, that is, the decay of state$_D$ to state$_C$.

By varying the applied potential and probing the decay when the cell is switched to open circuit, we are able to control the density of $*O_{cus}$ and investigate its effect on the intrinsic rate of the RDS (a detailed measurement of τ and calculation of the intrinsic rate can be found in Supplementary Note 9 and Supplementary Figs. 35 and 36).

Determining the intrinsic water oxidation kinetics

Having confirmed that the optically detected accumulated $*O_{cus}$ are reactive towards O–O coupling and O_2 release, we explored how these active states control the reaction rate on amorphous IrO_x and rutile IrO_2. We used two methods to estimate the intrinsic rate of the RDS as a function of the potential (and thus as a function of the $*O_{cus}$ coverage). First, we normalized the O_2 generation rate (obtained from the current) to the density of $*O_{cus}$, the active states from which the RDS (that is, O–O bond formation) proceeds. Such an RDS on IrO_2 has also been supported by other literature reports[25,26,57,58] Second, we accessed the $*O_{cus}$ decay rate resulting from O–O bond formation using the previously described potential-decay measurement. The above two analyses yield the intrinsic rate of the RDS, which are described using TOF (O_2 per $*O_{cus}$ per s) and TOF$_{decay}$, respectively.

Figure 5a shows the active-state $*O_{cus}$ coverage and the intrinsic rate of the RDS for amorphous IrO_x and rutile IrO_2. We find that whereas rutile IrO_2 has fewer active states at a given potential, it has a similar intrinsic rate of the RDS as measured by the O_2 evolution rate and a slightly lower intrinsic rate of the RDS as measured via the open-circuit decay within the studied potential regime. At more positive potentials (thus higher current densities), the coverage of $*O_{cus}$ cannot be measured due to the impact of severe bubble formation on the optical signal. We thus extrapolated the activity per $*O_{cus}$ in the higher potential range using the measured current density at the higher potential and an estimated coverage of $*O_{cus}$ from our Frumkin isotherm fitting results (Supplementary Fig. 39). We note that the TOF values obtained via both methods are in good agreement with those on mass-selected iridium oxide particles (which are presumably an amorphous/native oxide formed via the electrochemical oxidation of metallic iridium nanoparticles)[61] (Supplementary Fig. 40). This notion is in agreement with recent work using the noise level from an electrochemical scanning tunnelling microscope to probe catalytic activity locally, which showed that the OER rates are similar on a film of amorphous IrO_x, with negligible surface sensitivity[62]. To further explore the view that most, if not all, redox-active sites are also active for the OER, we evaluated the TOF per redox-active centre by normalizing the current to the total integrated charge in the first redox transition for films of varying thicknesses (see Supplementary Note 11 and Supplementary Fig. 41 for a detailed discussion). We find that the TOF is independent of the thickness, which is consistent with the notion that the sites that are redox-active are also OER-active in the hydrated amorphous oxide materials, and the observed redox transition states are thus less likely to be related to Faradaic processes of bulk sites that do not participate directly in the OER. Dau and co-workers came to similar conclusions with thickness-independent TOF values on hydrous amorphous cobalt catalysts[63–65].

Given that the coverage of the adsorbates in the Frumkin isotherm plays a key role in the binding energetics of the adsorbates and thus controls the reactivity of the states, we next compare the TOF (O_2 per $*O_{cus}$ per s) and the TOF$_{decay}$ for amorphous IrO_x and rutile IrO_2 as a function of the $*O_{cus}$ coverage (Fig. 5b). We note that for both iridium oxides, the logarithm of the TOF increases roughly linearly with the $*O_{cus}$ coverage in the observed range of coverage. This result is similar to the observation in a recent study by Nong et al.[26] where they found that

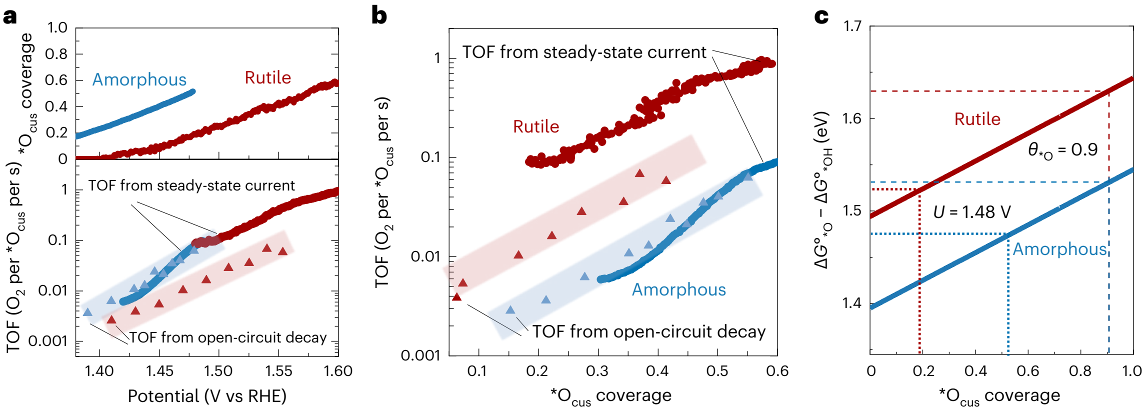

Fig. 5 | Intrinsic rate of the RDS for amorphous IrO_x and rutile IrO_2. **a**, Coverage of $^*O_{cus}$ as a function of the potential for amorphous and rutile iridium oxides (top), and the corresponding TOF per active state of amorphous IrO_x and rutile IrO_2 at the same potential (bottom). **b**, Intrinsic reaction rate per active state of IrO_x and IrO_2 as a function of the coverage of $^*O_{cus}$. The red and blue shaded regions in **a** and **b** are guides for the eye. **c**, Experimentally determined $\Delta G^\circ_{*O} - \Delta G^\circ_{*OH}$ values at different coverages of $^*O_{cus}$. The $\Delta G^\circ_{*O} - \Delta G^\circ_{*OH}$ values are calculated following the Frumkin electroadsorption isotherm $\Delta G^\circ_{*O} - \Delta G^\circ_{*OH} = \Delta G^\circ_{*O} - \Delta G^\circ_{*OH}\ (\theta_{*O} = 0) + r\theta_{*O}$, where $\Delta G^\circ_{*O} - \Delta G^\circ_{*OH}\ (\theta_{*O} = 0)$ represents the binding energy of $^*O_{cus}$ assuming zero coverage, and r (in electronvolts) is the interaction energy of the adsorbates. The values of $\Delta G^\circ_{*O} - \Delta G^\circ_{*OH}\ (\theta_{*O} = 0)$ and r were determined by fitting the electroadsorption isotherms in Fig. 3a,b. The dotted lines indicate the $\Delta G^\circ_{*O} - \Delta G^\circ_{*OH}$ values at the same potential of 1.48 V_{RHE} ($^*O_{cus}$ coverage values for IrO_x and IrO_2 are ~0.51 and ~0.19, respectively, as determined in Fig. 5a), whereas the dashed lines indicate $\Delta G^\circ_{*O} - \Delta G^\circ_{*OH}$ at a constant $^*O_{cus}$ coverage of 0.9 for each of the iridium oxides (see Supplementary Note 6 for details).

the log(current) increases linearly with the total charge, and suggested from DFT that the activation energy of the RDS decreases linearly with the increase in $^*O_{cus}$ coverage because of the long-range interactions between the *O species. Combining experimental and DFT calculation results, they suggested a chemical RDS for the OER on iridium oxides. Here, by experimentally tracking the intrinsic rate of the RDS as a function of the $^*O_{cus}$ coverage, we observe similar results. We also note that the slope values of log(TOF_{decay}) versus $^*O_{cus}$ coverage in Fig. 5b are similar for amorphous IrO_x and rutile IrO_2, which is consistent with our observation that they have similar adsorbate–adsorbate interaction energies r. The repulsive interaction observed here between oxo species causes a destabilization of the adsorbed $^*O_{cus}$ species (that is, $\Delta G^\circ_{*O} - \Delta G^\circ_{*OH}$ becomes larger), thus reducing the free energy of the RDS (O–O bond formation from $^*O_{cus}$). This suggests that the concentration of active species not only increases the reaction rate, by providing more sites where the reaction can occur, but also increases the rate by increasing the driving force or decreasing the reaction barrier caused by the change in chemical potential of these active species.

From Fig. 5b, it is also apparent that, at the same $^*O_{cus}$ coverage, the intrinsic activity of the RDS on rutile IrO_2 is around one order of magnitude higher (as measured by TOF (O_2 per $^*O_{cus}$ per s)) and factor of five higher (as measured by TOF_{decay}) than on amorphous IrO_x. We rationalize this difference in activity to the potential-dependent binding energetics of $^*O_{cus}$. From the experimentally observed energetics of $^*O_{cus}$, the values of $\Delta G^\circ_{*O} - \Delta G^\circ_{*OH}$ at $^*O_{cus}$ ($\theta_{*O} = 0$) for rutile IrO_2 is around 0.1 eV larger than that of amorphous IrO_x (that is, an extra 0.1 V is required to form $^*O_{cus}$ on rutile IrO_2), and the values for both increase with $^*O_{cus}$ coverage at a slope of roughly 0.15 eV per coverage increment due to the similar Frumkin interaction strengths (Fig. 5c). As a result, at a constant coverage of $^*O_{cus}$, compared with amorphous IrO_x, rutile IrO_2 binds oxygen more weakly, which facilitates O–O bond formation from $^*O_{cus}$ in the RDS, leading to a higher intrinsic activity per active state. On the other hand, at a constant potential, for example, at 1.48 V_{RHE}, this binding energy difference decreases to around 0.05 eV because amorphous IrO_x has a higher coverage of $^*O_{cus}$ at this potential, thus weakening the $^*O_{cus}$ binding more greatly. Therefore, the intrinsic activity at a constant potential is similar, and the order of magnitude greater geometric-area-normalized current density observed for amorphous IrO_x is mainly because it has a higher density of active states, as shown in Fig. 3a,b.

Design principles for highly active OER catalysts

The potential (and coverage) dependence of the intrinsic water oxidation kinetics determined herein show the importance of the adsorbate–adsorbate interactions in controlling the OER kinetics. The conventional approach for catalyst design has focused on developing catalysts with optimal binding energetics ($\Delta G^\circ_{*O} - \Delta G^\circ_{*OH}$) that correspond to ~1.6 eV (refs. 24,25,58). This implicitly assumes that this value is independent of the coverage. Here we have clearly experimentally demonstrated the weakening of the *O binding energy with increasing coverage. This indicates that optimal binding energetics can also be obtained on surface sites that are strongly binding at low coverage ($\Delta G^\circ_{*O} - \Delta G^\circ_{*OH} < 1.6$ eV at $\theta_{*O} \approx 0$) but have strong repulsive interactions, which weaken the *O binding energies at high coverage, thereby enabling these sites to achieve the optimal $\Delta G^\circ_{*O} - \Delta G^\circ_{*OH}$ values under reaction conditions that correspond to higher coverage.

To include the influence of adsorbate–adsorbate interactions on $\Delta G^\circ_{*O} - \Delta G^\circ_{*OH}$ values, and thus the intrinsic activity per state, we construct a new three-dimensional volcano plot. This volcano plot can be seen as a deconvolution of the previous descriptor $\Delta G^\circ_{*O} - \Delta G^\circ_{*OH}$ into two components: the binding energetics on a surface with zero *O coverage ($\Delta G^\circ_{*O} - \Delta G^\circ_{*OH}\ (\theta_{*O} = 0)$), and the interaction strength between *O species, following a Frumkin-isotherm-related equation ($\Delta G^\circ_{*O} - \Delta G^\circ_{*OH} = \Delta G^\circ_{*O} - \Delta G^\circ_{*OH}\ (\theta_{*O} = 0) + r\theta_{*O}$). The relative activity per state is represented by the thermodynamic overpotential of the OER on the active state, and is calculated from the absolute difference between the $\Delta G^\circ_{*O} - \Delta G^\circ_{*OH}$ value of the catalysts and the predicted optimal value of 1.60 eV (that is, relative activity = $-|\Delta G^\circ_{*O} - \Delta G^\circ_{*OH} - 1.6\ \text{eV}|$), as reported in the studies of Rossmeisl, Nørskov and colleagues[24,25]. We first construct this plot assuming a near-saturated coverage, $\theta_{*O} = 0.9$. As shown in Fig. 6a, the optimal activity of the states can be achieved either via optimal *O binding at low coverage without any *O interaction (that is, $\Delta G^\circ_{*O} - \Delta G^\circ_{*OH} \approx 1.6$ eV at $\theta_{*O} \approx 0$, $r = 0$ eV), which is the top of a conventional volcano plot, or via a stronger than optimal *O binding and strong interaction (for example, $\Delta G^\circ_{*O} - \Delta G^\circ_{*OH} = 1.0$ eV at $\theta_{*O} \approx 0$, $r \approx 0.7$ eV). In the latter case, although each state binds *O much more strongly than optimal at zero coverage, the strong interaction strength results in weaker binding and optimum $\Delta G^\circ_{*O} - \Delta G^\circ_{*OH}$ at high coverage.

We note that the applied potentials to achieve the same coverage are different for catalysts with different $\Delta G^\circ_{*O} - \Delta G^\circ_{*OH}\ (\theta_{*O} = 0)$ and r values. To include both potential and coverage effects, we construct a

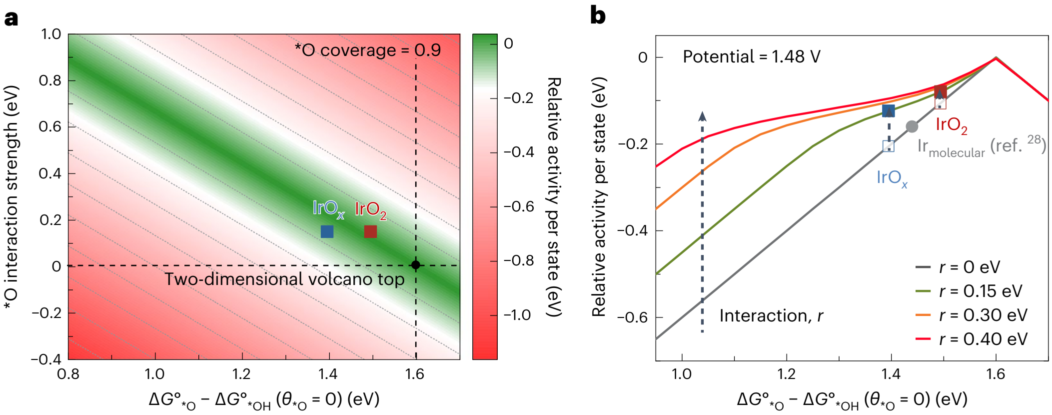

Fig. 6 | Effects of the *O interaction strength and *O binding energetics on the intrinsic activity per active state. a, Contour plot of relative activity as a function of the free energy of *O relative to *OH at an *O coverage of zero. The corresponding positions for amorphous IrO$_x$ and rutile IrO$_2$ on the plot at a near-saturated coverage ($\theta_{*O} = 0.9$) have been denoted. The relative activity is evaluated via the thermodynamic overpotential, which is calculated as the absolute difference between the energetic $\Delta G°_{*O} - \Delta G°_{*OH}$ and the theoretical optimal value of 1.6 eV (that is, relative activity = $-|\Delta G°_{*O} - \Delta G°_{*OH}$ ($\theta_{*O} = 0.9$) − 1.6 eV|); the smaller the difference, the higher the value, and the higher the activity is expected to be[24,25,58]. **b**, Relative activity per active state at a potential of 1.48 V_{RHE} and the corresponding positions for amorphous IrO$_x$ and rutile IrO$_2$ as well as a previously reported molecular iridium catalyst (assuming a mid-wave potential at ~1.44 V_{RHE} given that no interaction (that is, $r = 0$) is observed)[28]. The coverage of active states was obtained by numerically solving the Frumkin isotherm equation for given values of r and $\Delta G°_{*O} - \Delta G°_{*OH}$ ($\theta_{*O} = 0$).

volcano plot at a fixed overpotential of 250 mV (Fig. 6b and Supplementary Fig. 42). The steep part of the left side of the volcano (for example, when $\Delta G°_{*O} - \Delta G°_{*OH}$ ($\theta_{*O} = 0$) < 1.28 eV in the curve of $r = 0.15$ eV) is where the *O coverage is saturated, whereas the less steep part represents where $\Delta G°_{*O} - \Delta G°_{*OH}$ (θ_{*O}) is changing due to the Frumkin repulsion term. The Frumkin repulsion term has a higher impact on increasing the activity for a material with a stronger *O binding energy, for a given interaction strength. This is evident from our data on amorphous and rutile iridium oxide catalysts, where the adsorbate–adsorbate interaction increases the relative activity of the two materials by different degrees, although they have a similar interaction parameter (~0.15 eV). This is because the stronger binding strength of *O on the IrO$_x$ surface results in a higher coverage for IrO$_x$ compared with IrO$_2$ at this potential (Fig. 5a, top panel), and a consequently higher repulsion between adsorbates. However, both show a higher activity than the molecular iridium catalyst analysed previously, which has no adsorbate–adsorbate interaction[28]. This observation is consistent with our previous suggestion that, although the studied molecular iridium catalyst showed faster kinetics than amorphous IrO$_x$ at low overpotentials, it is less active than amorphous IrO$_x$ at higher overpotentials due to a lack of cooperative interactions between active states[28]. Similar analyses at overpotentials of 200 and 280 mV are also given in Supplementary Fig. 43. These results indicate that the potential can alter the coverage of *O species, which in turn can weaken the binding energies for catalysts that bind oxygen too strongly in a conventional volcano plot, hence improving the OER activity. This analysis elucidates the fundamental origin of the activity discrepancies between different iridium-based catalysts, including amorphous and crystalline iridium oxides.

Conclusions

In conclusion, our work combines experimental and theoretical techniques to re-evaluate the design principles for water oxidation catalysts by unravelling the role of active sites in terms of their density, ordering and interactions between them on the reaction rate. Here we have resolved the formation of the redox centres in amorphous IrO$_x$ and crystalline IrO$_2$ as a function of the potential, using time-resolved UV–visible spectroelectrochemistry and as a function of depth using ToF-SIMS combined with deuterium labelling. We also used DFT to provide a molecular-level interpretation of our results. From DFT, we assign the third spectral redox wave (redox transition 3) to the change of *OH to *O on the Ir$_{cus}$ site in both catalysts; in addition, the experimentally obtained O_2 evolution kinetics show an exponential dependence on the coverage of the species *O, corroborating predictions from earlier DFT-based models that O–O bond formation controls the reaction rate[24–26].

Our potential-decay results reveal that the intrinsic kinetics of O_2 evolution, that is, the reactivity of active *O states for O–O bond formation, are comparable, or slightly faster, on amorphous IrO$_x$ compared with crystalline IrO$_2$ at a given potential in the studied potential regime; however, the greater penetration and hence density of sites per unit geometric area of redox centres in amorphous IrO$_x$, as measured using both optical spectroscopy and ToF-SIMS, account for the substantially higher geometric current density observed in this catalyst compared with crystalline IrO$_2$. Amorphous IrO$_x$ binds more strongly to *O than to crystalline IrO$_2$ at low coverage; nonetheless, under the same potential for the reaction conditions, the coverage of *O is much higher than that of crystalline IrO$_2$, leading to greater weakening of *O as a result of repulsive adsorbate–adsorbate interactions. These two opposing effects lead to comparable intrinsic reaction rates on the two types of iridium oxide under study. On the basis of these insights, we may expect that nanocrystalline iridium-based catalysts, which exhibit the high stability[8,32] and intrinsic rate of rutile IrO$_2$ but with the high site density of amorphous IrO$_x$, will provide an optimal performance for O_2 evolution.

Beyond iridium oxides, our work highlights the role of adsorbate–adsorbate interactions on water oxidation catalysis; they are particularly important for catalysts on the strong binding side of the oxygen evolution volcano, such as with non-precious metal oxide MnO$_x$ (ref. 25). Our work leads to a more accurate description of water oxidation kinetics than conventional models that are based solely on the binding energetics at zero coverage; moreover, it provides an additional, unexplored lever to aid the discovery of more active catalysts.

Methods

Synthesis of amorphous IrO$_x$ and crystalline IrO$_2$

Amorphous IrO$_x$ was prepared using an electrodeposition method analogous to previous reports[27,31]. Typically, a solution with an iridium source was prepared by dissolving $IrCl_3$ hydrate (0.2 mmol; Fluorochem) and oxalic acid dihydrate (1 mmol; Sigma Aldrich) in water (30 ml). The pH was adjusted to 10 with K_2CO_3 (5 mmol; Sigma Aldrich,

≥99.0%). The volume of the solution was then increased to 50 ml by adding more water (20 ml). The solution was left to rest for four days at 35 °C and then stored in a refrigerator at 4 °C. The electrodeposition of IrO_x was conducted with a typical three-electrode set-up using this solution. A clean FTO glass substrate was used as the working electrode, and a platinum mesh and Ag/AgCl were used as the counter and reference electrodes, respectively. Polyimide tape was attached to the FTO surface to limit the conductive surface to ~1 × 1 cm. The electrodeposition was carried out by applying an anodic current density of 35 μA cm^{-2} for 1,000 s. The mass loading of the obtained IrO_x was around 80 μg cm^{-2}. For ToF-SIMS and XPS measurements, IrO_x was deposited on a titanium substrate for a longer deposition time of 12,000 s to obtain a thicker layer sample. SEM images were obtained from the sample deposited on both titanium substrates and FTO substrates. Rutile IrO_2 is obtained via thermal annealing of the IrO_x sample in the atmosphere at 550 °C for 8 h, at a heating rate of 10 °C min^{-1}. Thus, rutile IrO_2 sample has the same iridium mass loading as the amorphous IrO_x sample.

Characterization of materials

SEM images were obtained using a LEO 1525 scanning electron microscope (FESEM, 5 kV). X-ray diffraction measurements were carried out to determine the phase composition of each catalyst, and were obtained using a Bruker-Axs diffractometer equipped with a PSD LinxEye detector. The X-ray diffraction patterns were collected in the range of $10 \le 2\theta \le 70$ with a step size of 0.05°. XPS spectra were obtained using a Thermo Scientific K-Alpha spectrometer equipped with an aluminium Kα X-ray source (1,486.6 eV) coupled with a 180° double-focusing hemispherical analyser with a 2 s detector at an operating pressure of 1×10^{-8} mbar and a flood gun to minimize charging effects from photoemission. The iridium L_3-edge XAS data were collected using the B18 beamline at Diamond Light Source, United Kingdom. The beamline has an energy range of 2.05 –35 keV for spectroscopy. The energy of the incident X-ray beam was selected using a Si(111) monochromator, with a resolving power of $\lambda/\Delta\lambda \approx 5{,}000$. The XAS measurements for amorphous IrO_x and rutile IrO_2 were performed in fluorescence. The XAS measurements for standard sample iridium powder, $IrCl_3$ and IrO_2 (Alfa Sigma) were carried out in transmission mode.

Electrochemical measurements

All electrochemical measurements were carried out in 0.1 M $HClO_4$ prepared by dilution of concentrated perchloric acid (Suprapur 70% $HClO_4$, Merck) in ultrapure water (>18.2 MΩ cm, Sartorius). The electrochemical tests were conducted using a typical three-electrode set-up with an SP-150 or an SP-300 BioLogic potentiostat. The iridium oxides deposited on the FTO substrate (1 × 1 cm) were used directly as the working electrode. A platinum mesh and an Ag/AgCl electrode (KCl-saturated) were used as the counter and reference electrodes, respectively. The reference electrode was calibrated to the RHE in the same electrolyte using saturated H_2 on a clean platinum surface. Potentials were iR-compensated by manually subtracting the product of current and resistance $i\times R_u$, for which the resistance R_u (~25 Ω) was obtained from a high-frequency intercept of the real resistance during electrochemical impedance spectroscopy.

ToF-SIMS

ToF-SIMS measurements were performed using an IONTOF ToF-SIMS V instrument, with a sputter current of 75 nA. Bismuth ions were used as the primary analysis ion and 1 keV caesium ions were used as the sputter beam. The sputter beam was set to create a crater with a length and width of 300 μm. A square analysis area, with sides of 100 μm, was then set around the centre of the crater. Data were obtained over a mass range from mass-to-charge ratios (m/z) of 0–200 for negative secondary ions. Calibration was performed using C^-, CH^-, CH_2^- CH_3^-, O^-, OH^-, F^- and $^{35}Cl^-$. The differences between the expected and observed masses after calibration were less than 50 ppm. The samples were first electrochemically cycled in deuterated 0.1 M $HClO_4$ electrolyte and then subjected to ToF-SIMS to record the deuterium signal over the sputtering time.

Operando UV–visible absorption spectroscopy

Operando UV–visible absorption spectroscopy measurements were conducted in transmission mode. A stabilized 10 mW tungsten–halogen light source (SLS201L, Thorlabs) was used with a collimating package (SLS201C, Thorlabs). The light emitted from the lamp was transmitted through the sample and collected using a 1 cm diameter liquid light guide (Edmund Optics). Light transmitted to the spectrograph was first columnated and refocused using two 5 cm planoconvex lenses (Edmund Optics) to optimally match the optical components of the spectroscope (Kymera 193i, Andor) and charge-coupled device (CCD) camera (iDus Du420A-BEX2-DD, Andor). The detector was maintained at −80 °C during the measurements to reduce the dark current and ensure a high signal-to-noise ratio. An Ivium Vertex potentiostat was used for electrochemical measurements, where data acquisition of both the electrochemical signal (that is, the potential and current) and the optical signal is facilitated using custom-built LabVIEW[66] software (see details in the Code availability statement). This custom-built software also ensures that the two signal sources match in the same time stamp. The measurements were carried out in potentiostatic mode, with a potential step and equilibration time equal to that for typical CV at a scan rate of around 1 mV s^{-1}. At each potential, 30 averages of the spectra were obtained (where each spectral acquisition takes ~30 ms), before moving to the next potential.

DFT calculations

All DFT calculations were performed using the grid-based projector augmented wave software package[67,68]. The atomic simulation environment was used to set up and control the calculations[69]. The calculations were performed with a plane-wave basis with an energy cut-off of 500 eV. The revised Perdew–Burke–Ernzerhof functional was used to describe the effects of exchange and correlation[70].

The (110) surface of rutile IrO_2 was modelled as a 3 × 1 slab with four atomic layers, of which two were fixed in the bulk geometry at the computationally optimized lattice constants ($a = 4.59$ Å and $c = 3.19$ Å, which compare well with experimental values of $a = 4.50$ Å and $c = 3.15$ Å)[71]. Twenty ångstöms of vacuum separated the periodic images of the slab, and a dipole correction was used to decouple the electrostatic interactions on either side of the slab. The Brillouin zone was sampled using 4 × 4 k-points.

The surface of amorphous IrO_2 cannot be modelled via periodic DFT calculations; however, to gain an understanding of the differences between rutile and amorphous IrO_2 we modelled the (001) surface of IrO_2 in the hollandite structure. This surface bears similarity to the rutile (110) surface; however, adsorbates are further separated (in the x direction) and the bulk is more open, as would be expected for an amorphous structure (see Supplementary Fig. 25 for a comparison of the two surfaces). This surface is modelled as a 3 × 1 slab with six atomic layers (three frozen), corresponding to 1.5 repeats of the unit cell, and sampled using 3 × 4 k-points. The calculated lattice constants are $a = 10.13$ Å and $c = 3.18$ Å, which compare well with the experimental data of hollandite-type K_xIrO_2 ($a = 10.02$ Å, $b = 3.15$ Å, $c = 10.05$ Å and $\beta = 90.11°$)[72].

Data availability

The data that support the findings of this study are available within the main text and Supplementary Information. DFT optimized structures are available from https://nano.ku.dk/english/research/theoretical-electrocatalysis/katladb/water-oxidation-activity-of-iridium-oxides/. Data are also available from the corresponding authors upon reasonable request. Source data are provided with this paper.

Code availability

Scripts used for spectroelectrochemical data analysis are openly available at https://github.com/Caiwu-L/Paper_amorphous-IrOx_vs_Rutile_IrO2. Details of the home-built spectroelectrochemistry set-up and the LabView-based software are openly available at https://opensourcespectroscopy.com/. Python scripts used to analyse the DFT data are available from https://nano.ku.dk/english/research/theoretical-electrocatalysis/katladb/water-oxidation-activity-of-iridium-oxides/.

References

1. Bernt, M. et al. Current challenges in catalyst development for PEM water electrolyzers. *Chem. Ing. Tech.* **92**, 31–39 (2020).
2. Carmo, M., Fritz, D. L., Mergel, J. & Stolten, D. A comprehensive review on PEM water electrolysis. *Int. J. Hydrogen Energy* **38**, 4901–4934 (2013).
3. Reier, T., Nong, H. N., Teschner, D., Schlögl, R. & Strasser, P. Electrocatalytic oxygen evolution reaction in acidic environments – reaction mechanisms and catalysts. *Adv. Energy Mater.* **7**, 1601275 (2017).
4. Vesborg, P. C. & Jaramillo, T. F. Addressing the terawatt challenge: scalability in the supply of chemical elements for renewable energy. *RSC Adv.* **2**, 7933–7947 (2012).
5. Wei, C. et al. Recommended practices and benchmark activity for hydrogen and oxygen electrocatalysis in water splitting and fuel cells. *Adv. Mater.* **31**, 1806296 (2019).
6. Kasian, O., Grote, J.-P., Geiger, S., Cherevko, S. & Mayrhofer, K. J. J. The common intermediates of oxygen evolution and dissolution reactions during water electrolysis on iridium. *Angew. Chem. Int. Ed.* **57**, 2488–2491 (2018).
7. Bernt, M., Siebel, A. & Gasteiger, H. A. Analysis of voltage losses in PEM water electrolyzers with low platinum group metal loadings. *J. Electrochem. Soc.* **165**, F305 (2018).
8. Geiger, S. et al. The stability number as a metric for electrocatalyst stability benchmarking. *Nat. Catal.* **1**, 508–515 (2018).
9. Gao, J. et al. Breaking long-range order in iridium oxide by alkali ion for efficient water oxidation. *J. Am. Chem. Soc.* **141**, 3014–3023 (2019).
10. Nong, H. N. et al. A unique oxygen ligand environment facilitates water oxidation in hole-doped $IrNiO_x$ core–shell electrocatalysts. *Nat. Catal.* **1**, 841–851 (2018).
11. Reier, T. et al. Molecular insight in structure and activity of highly efficient, low-Ir Ir–Ni oxide catalysts for electrochemical water splitting (OER). *J. Am. Chem. Soc.* **137**, 13031–13040 (2015).
12. Sun, W., Song, Y., Gong, X.-Q., Cao, L.-M. & Yang, J. Hollandite structure $K_{x≈0.25}IrO_2$ catalyst with highly efficient oxygen evolution reaction. *ACS Appl. Mater. Interfaces* **8**, 820–826 (2016).
13. Seitz, L. C. et al. A highly active and stable $IrO_x/SrIrO_3$ catalyst for the oxygen evolution reaction. *Science* **353**, 1011–1014 (2016).
14. Diaz-Morales, O. et al. Iridium-based double perovskites for efficient water oxidation in acid media. *Nat. Commun.* **7**, 12363 (2016).
15. Wan, G. et al. Amorphization mechanism of $SrIrO_3$ electrocatalyst: how oxygen redox initiates ionic diffusion and structural reorganization. *Sci. Adv.* **7**, eabc7323 (2021).
16. Elmaalouf, M. et al. The origin of the high electrochemical activity of pseudo-amorphous iridium oxides. *Nat. Commun.* **12**, 3935 (2021).
17. Abbott, D. F. et al. Iridium oxide for the oxygen evolution reaction: correlation between particle size, morphology, and the surface hydroxo layer from operando XAS. *Chem. Mater.* **28**, 6591–6604 (2016).
18. Willinger, E., Massué, C., Schlögl, R. & Willinger, M. G. Identifying key structural features of IrO_x water splitting catalysts. *J. Am. Chem. Soc.* **139**, 12093–12101 (2017).
19. Pfeifer, V. et al. The electronic structure of iridium oxide electrodes active in water splitting. *Phys. Chem. Chem. Phys.* **18**, 2292–2296 (2016).
20. Pfeifer, V. et al. In situ observation of reactive oxygen species forming on oxygen-evolving iridium surfaces. *Chem. Sci.* **8**, 2143–2149 (2017).
21. Pfeifer, V. et al. Reactive oxygen species in iridium-based OER catalysts. *Chem. Sci.* **7**, 6791–6795 (2016).
22. Bockris, J. M. Kinetics of activation controlled consecutive electrochemical reactions: anodic evolution of oxygen. *J. Chem. Phys.* **24**, 817–827 (1956).
23. Bockris, J. O. M. & Otagawa, T. The electrocatalysis of oxygen evolution on perovskites. *J. Electrochem. Soc.* **131**, 290 (1984).
24. Man, I. C. et al. Universality in oxygen evolution electrocatalysis on oxide surfaces. *ChemCatChem* **3**, 1159–1165 (2011).
25. Rossmeisl, J., Qu, Z. W., Zhu, H., Kroes, G. J. & Nørskov, J. K. Electrolysis of water on oxide surfaces. *J. Electroanal. Chem.* **607**, 83–89 (2007).
26. Nong, H. N. et al. Key role of chemistry versus bias in electrocatalytic oxygen evolution. *Nature* **587**, 408–413 (2020).
27. Bozal-Ginesta, C. et al. Redox-state kinetics in water-oxidation IrO_x electrocatalysts measured by operando spectroelectrochemistry. *ACS Catal.* **11**, 15013–15025 (2021).
28. Bozal-Ginesta, C. et al. Spectroelectrochemistry of water oxidation kinetics in molecular versus heterogeneous oxide iridium electrocatalysts. *J. Am. Chem. Soc.* **144**, 8454–8459 (2022).
29. Gallagher, J. Co-operating to oxidize water. *Nat. Energy* **7**, 471 (2022).
30. Kuo, D. Y. et al. Influence of surface adsorption on the oxygen evolution reaction on IrO_2(110). *J. Am. Chem. Soc.* **139**, 3473–3479 (2017).
31. Petit, M. A. & Plichon, V. Anodic electrodeposition of iridium oxide films. *J. Electroanal. Chem.* **444**, 247–252 (1998).
32. Geiger, S. et al. Activity and stability of electrochemically and thermally treated iridium for the oxygen evolution reaction. *J. Electrochem. Soc.* **163**, F3132 (2016).
33. Hadden, J. H. L., Ryan, M. P. & Riley, D. J. Is nickel hydroxide charging only skin-deep? *ACS Appl. Energy Mater.* **3**, 2803–2810 (2020).
34. Li, T. et al. Atomic-scale insights into surface species of electrocatalysts in three dimensions. *Nat. Catal.* **1**, 300–305 (2018).
35. Kasian, O. et al. Degradation of iridium oxides via oxygen evolution from the lattice: correlating atomic scale structure with reaction mechanisms. *Energy Environ. Sci.* **12**, 3548–3555 (2019).
36. Görlin, M. et al. Tracking catalyst redox states and reaction dynamics in Ni–Fe oxyhydroxide oxygen evolution reaction electrocatalysts: the role of catalyst support and electrolyte pH. *J. Am. Chem. Soc.* **139**, 2070–2082 (2017).
37. Rao, R. R. et al. Spectroelectrochemical analysis of the water oxidation mechanism on doped nickel oxides. *J. Am. Chem. Soc.* **144**, 7622–7633 (2022).
38. Francàs, L. et al. Spectroelectrochemical study of water oxidation on nickel and iron oxyhydroxide electrocatalysts. *Nat. Commun.* **10**, 5208 (2019).
39. Risch, M. et al. Water oxidation by amorphous cobalt-based oxides: in situ tracking of redox transitions and mode of catalysis. *Energy Environ. Sci.* **8**, 661–674 (2015).
40. Mom, R. V. et al. Operando structure–activity–stability relationship of iridium oxides during the oxygen evolution reaction. *ACS Catal.* **12**, 5174–5184 (2022).
41. Frame, F. A. et al. Photocatalytic water oxidation with nonsensitized IrO_2 nanocrystals under visible and UV light. *J. Am. Chem. Soc.* **133**, 7264–7267 (2011).
42. Ooka, H. et al. Legitimate intermediates of oxygen evolution on iridium oxide revealed by in situ electrochemical evanescent wave spectroscopy. *Phys. Chem. Chem. Phys.* **18**, 15199–15204 (2016).

43. Ooka, H., Takashima, T., Yamaguchi, A., Hayashi, T. & Nakamura, R. Element strategy of oxygen evolution electrocatalysis based on in situ spectroelectrochemistry. *Chem. Commun.* **53**, 7149–7161 (2017).
44. Mo, Y. et al. In situ iridium L_{III}-edge X-ray absorption and surface enhanced raman spectroscopy of electrodeposited iridium oxide films in aqueous electrolytes. *J. Phys. Chem. B* **106**, 3681–3686 (2002).
45. Minguzzi, A. et al. Easy accommodation of different oxidation states in iridium oxide nanoparticles with different hydration degree as water oxidation electrocatalysts. *ACS Catal.* **5**, 5104–5115 (2015).
46. Hüppauff, M. & Lengeler, B. Valency and structure of iridium in anodic iridium oxide films. *J. Electrochem. Soc.* **140**, 598–602 (1993).
47. Saveleva, V. A. et al. Operando evidence for a universal oxygen evolution mechanism on thermal and electrochemical iridium oxides. *J. Phys. Chem. Lett.* **9**, 3154–3160 (2018).
48. Hillman, A. R., Skopek, M. A. & Gurman, S. J. X-ray spectroscopy of electrochemically deposited iridium oxide films: detection of multiple sites through structural disorder. *Phys. Chem. Chem. Phys.* **13**, 5252–5263 (2011).
49. Diklić, N. et al. Surface Ir^{+5} formation as a universal prerequisite for O_2 evolution on Ir oxides. *ACS Catal.* **13**, 11069–11079 (2023).
50. Velasco-Vélez, J.-J. et al. Surface electron-hole rich species active in the electrocatalytic water oxidation. *J. Am. Chem. Soc.* **143**, 12524–12534 (2021).
51. Nørskov, J. K. et al. Origin of the overpotential for oxygen reduction at a fuel-cell cathode. *J. Phys. Chem. B* **108**, 17886–17892 (2004).
52. Svane, K. L. & Rossmeisl, J. Theoretical optimization of compositions of high-entropy oxides for the oxygen evolution reaction. *Angew. Chem. Int. Ed.* **61**, e202201146 (2022).
53. Hubert, M. A. et al. Acidic oxygen evolution reaction activity–stability relationships in Ru-based pyrochlores. *ACS Catal.* **10**, 12182–12196 (2020).
54. Peng, H.-J., Tang, M. T., Halldin Stenlid, J., Liu, X. & Abild-Pedersen, F. Trends in oxygenate/hydrocarbon selectivity for electrochemical $CO_{(2)}$ reduction to C_2 products. *Nat. Commun.* **13**, 1399 (2022).
55. Hu, B., Kuo, D.-Y., Paik, H., Schlom, D. G. & Suntivich, J. Enthalpy and entropy of oxygen electroadsorption on RuO_2(110) in alkaline media. *J. Chem. Phys.* **152**, 094704 (2020).
56. Gottesfeld, S., McIntyre, J., Beni, G. & Shay, J. Electrochromism in anodic iridium oxide films. *Appl. Phys. Lett.* **33**, 208–210 (1978).
57. Ping, Y., Nielsen, R. J. & Goddard, W. A. III The reaction mechanism with free energy barriers at constant potentials for the oxygen evolution reaction at the IrO_2 (110) surface. *J. Am. Chem. Soc.* **139**, 149–155 (2017).
58. Dickens, C. F., Kirk, C. & Nørskov, J. K. Insights into the electrochemical oxygen evolution reaction with ab initio calculations and microkinetic modeling: beyond the limiting potential volcano. *J. Phys. Chem. C* **123**, 18960–18977 (2019).
59. Trimarco, D. B. et al. Enabling real-time detection of electrochemical desorption phenomena with sub-monolayer sensitivity. *Electrochim. Acta* **268**, 520–530 (2018).
60. Scott, S. B. et al. The low overpotential regime of acidic water oxidation part I: the importance of O_2 detection. *Energy Environ. Sci.* **15**, 1977–1987 (2022).
61. Zheng, Y.-R. et al. Monitoring oxygen production on mass-selected iridium–tantalum oxide electrocatalysts. *Nat. Energy* **7**, 55–64 (2022).
62. Kluge, R. M., Haid, R. W. & Bandarenka, A. S. Assessment of active areas for the oxygen evolution reaction on an amorphous iridium oxide surface. *J. Catal.* **396**, 14–22 (2021).
63. Klingan, K. et al. Water oxidation by amorphous cobalt-based oxides: volume activity and proton transfer to electrolyte bases. *ChemSusChem* **7**, 1301–1310 (2014).
64. González-Flores, D. et al. Heterogeneous water oxidation: surface activity versus amorphization activation in cobalt phosphate catalysts. *Angew. Chem. Int. Ed.* **54**, 2472–2476 (2015).
65. Pasquini, C. et al. H/D isotope effects reveal factors controlling catalytic activity in Co-based oxides for water oxidation. *J. Am. Chem. Soc.* **141**, 2938–2948 (2019).
66. Bitter, R., Mohiuddin, T. & Nawrocki, M. *LabVIEW: Advanced Programming Techniques* (CRC Press, 2017).
67. Enkovaara, J. et al. Electronic structure calculations with GPAW: a real-space implementation of the projector augmented-wave method. *J. Phys. Condens. Matter* **22**, 253202 (2010).
68. Mortensen, J. J., Hansen, L. B. & Jacobsen, K. W. Real-space grid implementation of the projector augmented wave method. *Phys. Rev. B* **71**, 035109 (2005).
69. Larsen, A. H. et al. The atomic simulation environment—a Python library for working with atoms. *J. Phys. Condens. Matter* **29**, 273002 (2017).
70. Hammer, B., Hansen, L. B. & Nørskov, J. K. Improved adsorption energetics within density-functional theory using revised Perdew–Burke–Ernzerhof functionals. *Phys. Rev. B* **59**, 7413–7421 (1999).
71. Rogers, D. B., Shannon, R. D., Sleight, A. W. & Gillson, J. L. Crystal chemistry of metal dioxides with rutile-related structures. *Inorg. Chem.* **8**, 841–849 (1969).
72. Bestaoui, N., Deniard, P. & Brec, R. Structural study of a hollandite-type K_xIrO_2. *J. Solid State Chem.* **118**, 372–377 (1995).

Acknowledgements

I.E.L.S., J.R.D., R.R.R. and C.L. would like to acknowledge the funding and technical support from BP through the BP International Centre for Advanced Materials (bp-ICAM) as well as the EPSRC grant EP/W033232/1 which made this research possible. C.L. acknowledges the Imperial College London and China Scholarship Council for the IC–CSC joint scholarship. K.L.S., A.M.F. and J.R. acknowledge the Danish National Research Foundation Center for High-Entropy Alloy Catalysis (CHEAC) DNRF-149. We acknowledge Diamond Light Source for time on Beamline B18 under Proposal SP30396. This work was supported by EPSRC grant EP/W033232/. S.B.S. acknowledges an Energy for Future fellowship from the Iberdrola Foundation. I.E.L.S. and S.B.S. acknowledge funding from ERC grant under the European Union's Horizon 2020 research and innovation program (Grant no. 866402).

Author contributions

C.L., R.R.R., I.E.L.S. and J.R.D. conceived the idea. C.L., R.R.R. and B.M. performed the XAS experiments. C.L. performed the optical spectroscopy measurements; B.M. custom-built the optical spectroscopy set-up. The code for linear combination fitting of the optical spectroscopy data was developed by M.S. and adapted by C.L., who analysed the data with the help of R.R.R., J.R.D., I.E.L.S., S.B.S., B.M. and J.M. The DFT calculations were performed by K.L.S., A.M.F. and J.R., who also analysed the results. J.H.L.H. performed the ToF-SIMS experiments; M.P.R. and D.J.R. supervised the experiments and contributed to the data analysis. The manuscript was written by C.L.; all authors reviewed and edited the manuscript.

Competing interests

The authors declare no competing interests.

Additional information

Supplementary information The online version contains supplementary material available at https://doi.org/10.1038/s41929-024-01168-7.

Correspondence and requests for materials should be addressed to Reshma R. Rao, Jan Rossmeisl, James R. Durrant or Ifan E. L. Stephens.

Peer review information *Nature Catalysis* thanks Holger Dau, Rik V. Mom and the other, anonymous, reviewer(s) for their contribution to the peer review of this work.

7 Conclusions

While this thesis is primarily focused on theory, it operates at the interface of theory and experimental work. In this regard it illustrates the importance of corroborative work. Many of the conclusions and ideas would not have been possible without the interplay with experimental groups. Another key focus of this dissertation has been the role of reaction mechanisms on model accuracy, and catalytic properties. It highlights the importance of understanding the basic assumptions of any modelling approach.

7.1 Modelling OER on RuO_2

The first article presented (section 3.3) in this thesis showcased the relevance of assumed OER reaction mechanism on the theoretical prediction of activity for rutile RuO_2 (110). It was shown that employing a reaction pathway with the protons of intermediates HO^* and HOO^* migrated to the bridge site significantly decreases the expected overpotential, putting the material in line with experimental observations. This behaviour is rationalized by the strong preference of RuO_2 towards oxygen intermediates. While this approach does lift the discrepancy between theory and experiments, another perspective from literature holds that the discrepancy is due to anti-ferromagneticity of RuO_2 [52]. That RuO_2 is magnetic is not necessarily in conflict with the view presented in the article, and both things can be true simultaneously.

7.2 LOER prediction in oxides

For articles 2 (section 4.1) and 3 (section 4.2) a computational screening method is introduced to determine the intrinsic LOER activity of oxide materials. In article 2 the method is applied to $Ru_{1-x}Ni_xO_2$ and $Ru_{1-x}Ti_xO_2$, while in article 3 it is applied to $Ru_{1-x}Mn_xO_2$. For $Ru_{1-x}Ni_xO_2$ the screening identifies weakened oxygen species on Ru-Ni bridge sites, allowing evolution at elevated electrode potentials. Using a structural characterization of this system from literature [63], a model was constructed to determine the expected number of Ru-Ni bridge sites as a function of nickel content. The model is found to be in good agreement with experimental DEMS data for the system. In the case of $Ru_{1-x}Ti_xO_2$, the screening method predicts minor lattice exchange at high Ti content. Experimental evidence does however show a large contribution of lattice exchange in real systems. This discrepancy can be explained by difficult to model structural defects, as these are widely present in the Ru-Ti-oxide systems, and defects are known to correlate with LOER tendency. Lastly for the $Ru_{1-x}Mn_xO_2$ in article 3, no significant LOER tendency is predicted nor measured, indicating good agreement between experiments and theory. For this system, the Mn content is shown to somewhat control the selectivity between OER and ClER, with more Mn selecting for OER. The two reactions are shown to be noncompeting, and LOER correlated to higher ClER selectivity. The DFT calculations predict that Mn cus sites in this system are highly active towards OER, and this is corroborated by a general increase in activity with increasing Mn content. Literature has it that LOER tendency is closely related to the ability to stabilize oxygen vacancies [36, 62]. From this perspective, it makes sense that messy samples with structural defects would show high LOER tendency. Structurally messy regions would be expected to have more weakly bound oxygen species, allowing LOER activation.

7.3 Activating the semi-conducting TiO_2

Article 4 (section 5.3) introduces the concept of co-doping TiO_2 (and perovskite $SrTiO_3$) with n- and p-type dopants to achieve activation of the otherwise inactive (but stable) semi-conductors. The co-doping approach introduces states in the band gap, and aligns the Fermi level to favor water oxidation. These predictions were confirmed experimentally, where it was found that only co-doped samples showed significant improvement of activity. As follow up studies to these results, the semi-conductor conductor transition for $Ru_{1-x}Ti_xO_2$ was investigated, as well as the properties of Ti in HEOs. The semi-conductor conductor transition for binding on Ti is found to be immediate, with the binding energy being somewhat predictable from the knowledge of whether Ru is in the structure or not. In the deep semi-conducting regime, the spread on binding energies for Ti sites is found to be large. While this is potentially due to computational artefacts, it mirrors results from a HEO system of (Rh,Os,Ir,Ru,Ti), where Ti binding energies also show large spreads crossing highly active values. It is found that the binding energy of oxygen on Ti correlates well to the Fermi level (as compared to the stable oxygen 2s orbitals) of the material in the HEO system. Additionally the Fermi level of a HEO slab is found to be well predicted by a simple weighted average of constituent oxide materials. In conjunction, these insights allow for the tuning of Ti active sites by choice of composition.

7.4 Interplay between oxygen adsorbates in rutile IrO_2 and amorphous IrO_x

The fifth and final article included in this dissertation (section 6) studies the intermediates at the surface of amorphous and rutile iridium oxide during OER conditions. The redox active centers are quantified by time-resolved UV-vis spectroelectrochemistry and DFT is employed to identify the observed redox transitions. It is found that both sample types undergo three transitions before OER activation: OH adsorption on CUS sites, deprotonation of bridge sites, and finally deprotonation of CUS bound OH. Oxygen evolution show exponential dependence on coverage of oxygen adsorbates, corroborating that O-O bond formation is reaction rate determining. The activity per site is found to be similar between rutile and amorphous despite amorphous IrO_x binding oxygen stronger at low coverage. This can be rationalized by the higher coverage displayed by the amorphous iridium oxide when comparing the systems at a specific potential. This increased coverage leads to more adsorbate-adsorbate interactions, weakening the binding. This work leads to a modified volcano plot, where the strong binding side is dependent on the interaction strength between adsorbates.

8 List of abbreviations

ASE	Atomic Simulation Environment
BEEF-vdW	Bayesian Error Estimation Functional - van der Waals
ClER	Chlorine Evolution Reaction
CHE	Computational Hydrogen Electrode
CHEAC	Center for High Entropy Alloy Catalysis
DEMS	Differential Electrochemical Mass Spectrometry
DFT	Density Functional Theory
DOS	Density Of States
DSA	Dimensionally Stable Anode
GPAW	Grid-based Projector Augment Wave
LOER	Lattice Oxygen Evolution Reaction
OER	Oxygen Evolution Reaction
ORR	Oxygen Reduction Reaction
PDS	Potential Determining Step
RHE	Reversible Hydrogen Electrode
RPBE	Revised Perdew-Burke-Ernzerhof
RRDE	Rotating Ring-Disc Electrode
SCE	Saturated Calomel Electrode
SEM	Scanning Electron Microscopy
SHE	Standard Hydrogen Electrode
UV-vis	Ultraviolet-visible
VASP	Vienna Ab initio Simulation Package
XANES	X-ray Absorption Near-Edge Structure
EXAFS	Extended X-ray Absorption Fine Structure
XRD	X-ray Diffraction
XPS	X-ray Photoelectron Spectroscopy
ZPE	Zero-point Energy

9 Additional computational details

The construction of a surface slab is done by first relaxing a bulk (including lattice parameters), then cutting it along the desired direction. For the case of rutile (110) slabs in this thesis, the cut structure is then replicated to be a 1x3x4 slab. The bottom two layers are constrained as to mimic bulk. Additionally 15 Å of vacuum is introduced above and below the structure to avoid computational artefacts. Structures are relaxed until the total forces in the system are below 0.05 eV Å^{-1}. For the data presented in sections 5.4 and 5.5, a k-point mesh of 2x2x1 is used. ZPE and entropic corrections used for the OER intermediates in this thesis are presented in table 2.

	HO*	O*	HOO*
$C_{cor}(eV)$	0.35	0.05	0.40

Table 2: ZPE and entropic corrections used for the OER intermediates throughout this thesis. They mirror those of [21].

10 Link to Master's Thesis

QR-link to Master's Thesis. https://curis.ku.dk/ws/files/403981637/Adrian_Master_s_Thesis.pdf

11 References

[1] Harry B. Gray. Powering the planet with solar fuel. *Nature Chemistry*, 1(1):7, 2009.

[2] Richard E. Smalley. Future global energy prosperity: The terawatt challenge. *MRS Bulletin*, 30(6):412–417, Jun 2005.

[3] Pasquale Marcello Falcone, Michael Hiete, and Alessandro Sapio. Hydrogen economy and sustainable development goals: Review and policy insights. *Current Opinion in Green and Sustainable Chemistry*, 31:100506, 2021.

[4] Guoping Hu, Chao Chen, Hiep Thuan Lu, Yue Wu, Congmin Liu, Lefu Tao, Yuhan Men, Guangli He, and Kevin Gang Li. A Review of Technical Advances, Barriers, and Solutions in the Power to Hydrogen (P2H) Roadmap. *Engineering*, 6(12):1364–1380, 2020.

[5] Julien Durst, Christoph Simon, Frédéric Hasché, and Hubert A. Gasteiger. Hydrogen oxidation and evolution reaction kinetics on carbon supported pt, ir, rh, and pd electrocatalysts in acidic media. *Journal of The Electrochemical Society*, 162(1):F190–F203, dec 2014.

[6] Qi Feng, Xiao−Zi Yuan, Gaoyang Liu, Bing Wei, Zhen Zhang, Hui Li, and Haijiang Wang. A review of proton exchange membrane water electrolysis on degradation mechanisms and mitigation strategies. *Journal of Power Sources*, 366:33–55, 2017.

[7] Sergio Trasatti. Electrocatalysis by oxides — attempt at a unifying approach. *Journal of Electroanalytical Chemistry and Interfacial Electrochemistry*, 111(1):125–131, 1980.

[8] Rasmus Frydendal, Elisa A. Paoli, Brian P. Knudsen, Björn Wickman, Paolo Malacrida, Ifan E. L. Stephens, and Ib Chorkendorff. Benchmarking the Stability of Oxygen Evolution Reaction Catalysts: The Importance of Monitoring Mass Losses. *ChemElectroChem*, 1(12):2075–2081, 2014.

[9] Peter C. K. Vesborg and Thomas F. Jaramillo. Addressing the terawatt challenge: scalability in the supply of chemical elements for renewable energy. *RSC Adv.*, 2:7933–7947, 2012.

[10] P. Hohenberg and W. Kohn. Inhomogeneous electron gas. *Phys. Rev.*, 136:B864–B871, Nov 1964.

[11] Adrian Malthe Frandsen. Power to X- Electrocatalysis of the Oxygen Evolution Reaction at the Atomic Scale. Master's thesis, University of Copenhagen, 2021.

[12] A. H. Larsen, J. J. Mortensen, J. Blomqvist, I. E. Castelli, R. Christensen, M. Dułak, J. Friis, M. N. Groves, B Hammer, and C Hargus. The atomic simulation environment—a python library for working with atoms. *J. Phys.: Condens. Matter*, 29:273002, Jun 2017.

[13] Jens Jørgen Mortensen, Ask Hjorth Larsen, Mikael Kuisma, Aleksei V. Ivanov, Alireza Taghizadeh, Andrew Peterson, Anubhab Haldar, Asmus Ougaard Dohn, Christian Schäfer, Elvar Örn Jónsson, Eric D. Hermes, Fredrik Andreas Nilsson, Georg Kastlunger, Gianluca Levi, Hannes Jónsson, Hannu Häkkinen, Jakub

Fojt, Jiban Kangsabanik, Joachim Sødequist, Jouko Lehtomäki, Julian Heske, Jussi Enkovaara, Kirsten Trøstrup Winther, Marcin Dulak, Marko M. Melander, Martin Ovesen, Martti Louhivuori, Michael Walter, Morten Gjerding, Olga Lopez-Acevedo, Paul Erhart, Robert Warmbier, Rolf Würdemann, Sami Kaappa, Simone Latini, Tara Maria Boland, Thomas Bligaard, Thorbjørn Skovhus, Toma Susi, Tristan Maxson, Tuomas Rossi, Xi Chen, Yorick Leonard A. Schmerwitz, Jakob Schiøtz, Thomas Olsen, Karsten Wedel Jacobsen, and Kristian Sommer Thygesen. Gpaw: An open python package for electronic structure calculations. *The Journal of Chemical Physics*, 160(9):092503, Mar 2024.

[14] J. Enkovaara, C Rostgaard, J. J. Mortensen, J Chen, M. Dułak, L. Ferrighi, J Gavnholt, C Glinsvad, V Haikola, and H. A. Hansen. Electronic structure calculations with GPAW: a real-space implementation of the projector augmented-wave method. *J. Phys.: Condens. Matter*, 22:253202, Jun 2010.

[15] J. J. Mortensen, L. B. Hansen, and K. W. Jacobsen. Real-space grid implementation of the projector augmented wave method. *Phys. Rev. B*, 71:035109, Jan 2005.

[16] David Sholl and Janice A Steckel. *Density Functional Theory: A Practical Introduction.* John Wiley & Sons, Ltd, 2009.

[17] W. Kohn and L. J. Sham. Self-consistent equations including exchange and correlation effects. *Phys. Rev.*, 140:A1133–A1138, Nov 1965.

[18] B. Hammer, L. B. Hansen, and J. K. Nørskov. Improved adsorption energetics within density-functional theory using revised perdew-burke-ernzerhof functionals. *Phys. Rev. B*, 59:7413–7421, Mar 1999.

[19] Sarah A. Tolba, Kareem M. Gameel, Basant A. Ali, Hossam A. Almossalami, and Nageh K. Allam. The DFT+U: Approaches, Accuracy, and Applications. In Gang Yang, editor, *Density Functional Calculations*, chapter 1. IntechOpen, Rijeka, 2018.

[20] Alexander Bagger, Ivano E. Castelli, Martin Hangaard Hansen, and Jan Rossmeisl. *Fundamental Atomic Insight in Electrocatalysis*, pages 1–31. Springer International Publishing, 2018.

[21] J. K. Nørskov, J. Rossmeisl, A. Logadottir, L. Lindqvist, J. R. Kitchin, T. Bligaard, and H. Jónsson. Origin of the overpotential for oxygen reduction at a fuel-cell cathode. *The Journal of Physical Chemistry B*, 108(46):17886–17892, 2004.

[22] J. Rossmeisl, Z.-W. Qu, H. Zhu, G.-J. Kroes, and J.K. Nørskov. Electrolysis of water on oxide surfaces. *Journal of Electroanalytical Chemistry*, 607(1):83–89, 2007. Theoretical and Computational Electrochemistry.

[23] G. S. Karlberg, J. Rossmeisl, and J. K. Nørskov. Estimations of electric field effects on the oxygen reduction reaction based on the density functional theory. *Phys. Chem. Chem. Phys.*, 9:5158–5161, 2007.

[24] Leanne D. Chen, Makoto Urushihara, Karen Chan, and Jens K. Nørskov. Electric Field Effects in Electrochemical CO2 Reduction. *ACS Catalysis*, 6(10):7133–7139, Oct 2016.

[25] Marc Koper. Analysis of electrocatalytic reaction schemes: Distinction between rate-determining and potential-determining steps. *Journal of Solid State Electrochemistry*, 17, 02 2012.

[26] P. Sabatier. *La catalyse en chimie organique.* Paris et Liege: Librairie Polytechnique, 1920.

[27] J.K. Nørskov, T. Bligaard, A. Logadottir, S. Bahn, L.B. Hansen, M. Bollinger, H. Bengaard, B. Hammer, Z. Sljivancanin, M. Mavrikakis, Y. Xu, S. Dahl, and C.J.H. Jacobsen. Universality in Heterogeneous Catalysis. *Journal of Catalysis*, 209(2):275–278, 2002.

[28] I. Chorkendorff and J. W. Niemantsverdriet. *Concepts of Modern Catalysis and Kinetics.* John Wiley & Sons, Ltd, 2013.

[29] Heine A. Hansen, Isabela C. Man, Felix Studt, Frank Abild-Pedersen, Thomas Bligaard, and Jan Rossmeisl. Electrochemical chlorine evolution at rutile oxide (110) surfaces. *Phys. Chem. Chem. Phys.*, 12:283–290, 2010.

[30] Gregory Jerkiewicz. Standard and reversible hydrogen electrodes: Theory, design, operation, and applications. *ACS Catalysis*, 10(15):8409–8417, Aug 2020.

[31] Kai S. Exner. On the mechanistic complexity of oxygen evolution: potential-dependent switching of the mechanism at the volcano apex. *Mater. Horiz.*, 10:2086–2095, 2023.

[32] A. Hagemeyer and A. Volpe. Catalysts: Materials. In Franco Bassani, Gerald L. Liedl, and Peter Wyder, editors, *Encyclopedia of Condensed Matter Physics*, pages 158–165. Elsevier, Oxford, 2005.

[33] Niels Bendtsen Halck, Valery Petrykin, Petr Krtil, and Jan Rossmeisl. Beyond the volcano limitations in electrocatalysis – oxygen evolution reaction. *Phys. Chem. Chem. Phys.*, 16:13682–13688, 2014.

[34] Michael Busch, Niels B. Halck, Ulrike I. Kramm, Samira Siahrostami, Petr Krtil, and Jan Rossmeisl. Beyond the top of the volcano? – a unified approach to electrocatalytic oxygen reduction and oxygen evolution. *Nano Energy*, 29:126 – 135, 2016. Electrocatalysis.

[35] M. Wohlfahrt-Mehrens and J. Heitbaum. Oxygen evolution on Ru and RuO2 electrodes studied using isotope labelling and on-line mass spectrometry. *Journal of Electroanalytical Chemistry and Interfacial Electrochemistry*, 237(2):251–260, 1987.

[36] John O'M. Bockris and Takaaki Otagawa. The electrocatalysis of oxygen evolution on perovskites. *Journal of The Electrochemical Society*, 131(2):290, feb 1984.

[37] Tobias Binninger, Rhiyaad Mohamed, Kay Waltar, Emiliana Fabbri, Pieter Levecque, Rüdiger Kötz, and Thomas J. Schmidt. Thermodynamic explanation of the universal correlation between oxygen evolution activity and corrosion of oxide catalysts. *Scientific Reports*, 5(1):12167, Jul 2015.

[38] Isabela C. Man, Hai-Yan Su, Federico Calle-Vallejo, Heine A. Hansen, José I. Martínez, Nilay G. Inoglu, John Kitchin, Thomas F. Jaramillo, Jens K. Nørskov, and Jan Rossmeisl. Universality in oxygen evolution electrocatalysis on oxide surfaces. *ChemCatChem*, 3(7):1159–1165, 2011.

[39] Spyridon Divanis, Tugce Kutlusoy, Ida Marie Ingmer Boye, Isabela Costinela Man, and Jan Rossmeisl. Oxygen evolution reaction: a perspective on a decade of atomic scale simulations. *Chem. Sci.*, 11:2943–2950, 2020.

[40] Andrew R. Akbashev. Electrocatalysis Goes Nuts. *ACS Catalysis*, 12(8):4296–4301, Apr 2022.

[41] Ambarish Kulkarni, Samira Siahrostami, Anjli Patel, and Jens K. Nørskov. Understanding catalytic activity trends in the oxygen reduction reaction. *Chemical Reviews*, 118(5):2302–2312, Mar 2018.

[42] Nitish Govindarajan, Juan M. García-Lastra, Evert Jan Meijer, and Federico Calle-Vallejo. Does the breaking of adsorption-energy scaling relations guarantee enhanced electrocatalysis? *Current Opinion in Electrochemistry*, 8:110–117, 2018.

[43] Kai S. Exner. Why the breaking of the OOH versus OH scaling relation might cause decreased electrocatalytic activity. *Chem Catalysis*, 1(2):258–271, Jul 2021.

[44] Spyridon Divanis. *Catalyst Design for Efficient Water Electrolysis.* PhD thesis, University of Copenhagen, 2020.

[45] Spyridon Divanis, Adrian Malthe Frandsen, Tugce Kutlusoy, and Jan Rossmeisl. Lifting the discrepancy between experimental results and the theoretical predictions for the catalytic activity of RuO2(110) towards oxygen evolution reaction. *Phys. Chem. Chem. Phys.*, 23:19141–19145, 2021.

[46] Adam Kiejna, Georg Kresse, Jutta Rogal, Abir De Sarkar, Karsten Reuter, and Matthias Scheffler. Comparison of the full-potential and frozen-core approximation approaches to density-functional calculations of surfaces. *Phys. Rev. B*, 73:035404, Jan 2006.

[47] Ludovic G. V. Briquet, Misbah Sarwar, Jane Mugo, Glenn Jones, and Federico Calle-Vallejo. A new type of scaling relations to assess the accuracy of computational predictions of catalytic activities applied to the oxygen evolution reaction. *ChemCatChem*, 9(7):1261–1268, 2017.

[48] Reshma R. Rao, Manuel J. Kolb, Livia Giordano, Anders Filsøe Pedersen, Yu Katayama, Jonathan Hwang, Apurva Mehta, Hoydoo You, Jaclyn R. Lunger, Hua Zhou, Niels Bendtsen Halck, Tejs Vegge, Ib Chorkendorff, Ifan E. L. Stephens, and Yang Shao-Horn. Operando identification of site-dependent water oxidation activity on ruthenium dioxide single-crystal surfaces. *Nature Catalysis*, 3:516–525, 2020.

[49] Ding-Yuan Kuo, Jason K. Kawasaki, Jocienne N. Nelson, Jan Kloppenburg, Geoffroy Hautier, Kyle M. Shen, Darrell G. Schlom, and Jin Suntivich. Influence of Surface Adsorption on the Oxygen Evolution Reaction on IrO2(110). *Journal of the American Chemical Society*, 139(9):3473–3479, 2017. PMID: 28181433.

[50] Ding-Yuan Kuo, Hanjong Paik, Jan Kloppenburg, Brendan Faeth, Kyle M. Shen, Darrell G. Schlom, Geoffroy Hautier, and Jin Suntivich. Measurements of Oxygen Electroadsorption Energies and Oxygen Evolution Reaction on RuO2(110): A Discussion of the Sabatier Principle and Its Role in Electrocatalysis. *Journal of the American Chemical Society*, 140(50):17597–17605, 2018.

[51] T. Berlijn, P. C. Snijders, O. Delaire, H.-D. Zhou, T. A. Maier, H.-B. Cao, S.-X. Chi, M. Matsuda, Y. Wang, M. R. Koehler, P. R. C. Kent, and H. H. Weitering. Itinerant Antiferromagnetism in RuO_2. *Phys. Rev. Lett.*, 118:077201, Feb 2017.

[52] Qiuhua Liang, Anja Bieberle-Hütter, and Geert Brocks. Anti-Ferromagnetic RuO2: A Stable and Robust OER Catalyst over a Large Range of Surface Terminations. *The Journal of Physical Chemistry C*, 126(3):1337–1345, 2022.

[53] Giovanni Di Liberto, Gianfranco Pacchioni, Yang Shao-Horn, and Livia Giordano. Role of Water Solvation on the Key Intermediates Catalyzing Oxygen Evolution on RuO2. *The Journal of Physical Chemistry C*, 127(21):10127–10133, Jun 2023.

[54] C Malmgren, M Hummelgård, J Bäckström, A Cornell, and H Olin. Nanoscale characterization of crystallinity in DSA® coating. *Journal of Physics: Conference Series*, 100(5):052026, mar 2008.

[55] Prajwal Adiga, William Nunn, Cindy Wong, Anusha K. Manjeshwar, Sreejith Nair, Bharat Jalan, and Kelsey A. Stoerzinger. Breaking OER and CER scaling relations via strain and its relaxation in RuO2 (101). *Materials Today Energy*, 28:101087, 2022.

[56] V. Petrykin, K. Macounova, O. A. Shlyakhtin, and Petr Krtil. Tailoring the Selectivity for Electrocatalytic Oxygen Evolution on Ruthenium Oxides by Zinc Substitution. *Angewandte Chemie International Edition*, 49(28):4813–4815, 2010.

[57] Daniel F. Abbott, Valery Petrykin, Maki Okube, Zdenk Bastl, Sanjeev Mukerjee, and Petr Krtil. Selective Chlorine Evolution Catalysts Based on Mg-Doped Nanoparticulate Ruthenium Dioxide. *Journal of The Electrochemical Society*, 162(1):H23, 2015.

[58] Rasmus K.B. Karlsson, Heine A. Hansen, Thomas Bligaard, Ann Cornell, and Lars G.M. Pettersson. Ti atoms in Ru0.3Ti0.7O2 mixed oxides form active and selective sites for electrochemical chlorine evolution. *Electrochimica Acta*, 146:733–740, 2014.

[59] Kateřina Minhová Macounová, Rebecca Katharina Pittkowski, Roman Nebel, Andrea Zitolo, and Petr Krtil. Selectivity of Ru-rich Ru-Ti-O oxide surfaces in parallel oxygen and chlorine evolution reactions. *Electrochimica Acta*, 427:140878, 2022.

[60] Lars-Åke Näslund, Carlos M. Sánchez-Sánchez, Árni S. Ingason, Joakim Bäckström, Enrique Herrero, Johanna Rosen, and Susanne Holmin. The Role of TiO_2 Doping on RuO_2-Coated Electrodes for the Water Oxidation Reaction. *The Journal of Physical Chemistry C*, 117:6126–6135, 2013.

[61] Katerina Macounova, Marina Makarova, and Petr Krtil. Oxygen evolution on nanocrystalline RuO_2 and $Ru_{0.9}Ni_{0.1}O_{2-\delta}$ electrodes – DEMS approach to reaction mechanism determination. *Electrochemistry Communications*, 11:1865–1868, 2009.

[62] J. Tyler Mefford, Xi Rong, Artem M. Abakumov, William G. Hardin, Sheng Dai, Alexie M. Kolpak, Keith P. Johnston, and Keith J. Stevenson. Water electrolysis on la1$-$xsrxcoo3$-\delta$ perovskite electrocatalysts. *Nature Communications*, 7(1):11053, Mar 2016.

[63] V. Petrykin, Z. Bastl, J. Franc, K. Macounova, M. Makarova, S. Mukerjee, N. Ramaswamy, I. Spirovova, and P. Krtil. Local Structure of Nanocrystalline Ru1−xNixO2−δ Dioxide and Its Implications for Electrocatalytic Behavior—An XPS and XAS Study. *The Journal of Physical Chemistry C*, 113(52):21657–21666, 2009.

[64] Kelsey A. Stoerzinger, Oscar Diaz-Morales, Manuel Kolb, Reshma R. Rao, Rasmus Frydendal, Liang Qiao, Xiao Renshaw Wang, Niels Bendtsen Halck, Jan Rossmeisl, Heine A. Hansen, Tejs Vegge, Ifan E. L. Stephens, Marc T. M. Koper, and Yang Shao-Horn. Orientation-Dependent Oxygen Evolution on RuO2 without Lattice Exchange. *ACS Energy Letters*, 2(4):876–881, 2017.

[65] Reshma R. Rao, Manuel J. Kolb, Niels Bendtsen Halck, Anders Filsøe Pedersen, Apurva Mehta, Hoydoo You, Kelsey A. Stoerzinger, Zhenxing Feng, Heine A. Hansen, Hua Zhou, Livia Giordano, Jan Rossmeisl, Tejs Vegge, Ib Chorkendorff, Ifan E. L. Stephens, and Yang Shao-Horn. Towards identifying the active sites on ruo2(110) in catalyzing oxygen evolution. *Energy Environ. Sci.*, 10:2626–2637, 2017.

[66] Wesley T. Hong, Marcel Risch, Kelsey A. Stoerzinger, Alexis Grimaud, Jin Suntivich, and Yang Shao-Horn. Toward the rational design of non-precious transition metal oxides for oxygen electrocatalysis. *Energy Environ. Sci.*, 8:1404–1427, 2015.

[67] B. Hammer and J. K. Norskov. Why gold is the noblest of all the metals. *Nature*, 376(6537):238–240, Jul 1995.

[68] B. Hammer and J.K. Nørskov. Electronic factors determining the reactivity of metal surfaces. *Surface Science*, 343(3):211–220, 1995.

[69] B. Hammer, Y. Morikawa, and J. K. Nørskov. CO Chemisorption at Metal Surfaces and Overlayers. *Phys. Rev. Lett.*, 76:2141–2144, Mar 1996.

[70] A Ruban, B Hammer, P Stoltze, H.L Skriver, and J.K Nørskov. Surface electronic structure and reactivity of transition and noble metals. *Journal of Molecular Catalysis A: Chemical*, 115(3):421–429, 1997.

[71] B. Hammer and J. K. Nørskov. *Theory of Adsorption and Surface Reactions*, pages 285–351. Springer Netherlands, Dordrecht, 1997.

[72] B. Hammer. Special Sites at Noble and Late Transition Metal Catalysts. *Topics in Catalysis*, 37(1):3–16, Mar 2006.

[73] Gianfranco Pacchioni, Livia Giordano, and Matteo Baistrocchi. Charging of Metal Atoms on Ultrathin MgO/Mo(100) Films. *Phys. Rev. Lett.*, 94:226104, Jun 2005.

[74] Livia Giordano, Matteo Baistrocchi, and Gianfranco Pacchioni. Bonding of Pd, Ag, and Au atoms on MgO(100) surfaces and MgO/Mo(100) ultra-thin films: A comparative DFT study. *Phys. Rev. B*, 72:115403, Sep 2005.

[75] Pentti Frondelius, Anders Hellman, Karoliina Honkala, Hannu Häkkinen, and Henrik Grönbeck. Charging of atoms, clusters, and molecules on metal-supported oxides: A general and long-ranged phenomenon. *Phys. Rev. B*, 78:085426, Aug 2008.

[76] Jin Suntivich, Hubert A. Gasteiger, Naoaki Yabuuchi, Haruyuki Nakanishi, John B. Goodenough, and Yang Shao-Horn. Design principles for oxygen-reduction activity on perovskite oxide catalysts for fuel cells and metal–air batteries. *Nature Chemistry*, 3(7):546–550, Jul 2011.

[77] Yueh-Lin Lee, Jesper Kleis, Jan Rossmeisl, Yang Shao-Horn, and Dane Morgan. Prediction of solid oxide fuel cell cathode activity with first-principles descriptors. *Energy Environ. Sci.*, 4:3966–3970, 2011.

[78] Thomas M. Østergaard, Livia Giordano, Ivano E. Castelli, Filippo Maglia, Byron K. Antonopoulos, Yang Shao-Horn, and Jan Rossmeisl. Oxidation of Ethylene Carbonate on Li Metal Oxide Surfaces. *The Journal of Physical Chemistry C*, 122(19):10442–10449, May 2018.

[79] Livia Giordano, Thomas M. Østergaard, Sokseiha Muy, Yang Yu, Nenian Charles, Soo Kim, Yirui Zhang, Filippo Maglia, Roland Jung, Isaac Lund, Jan Rossmeisl, and Yang Shao-Horn. Ligand-Dependent Energetics for Dehydrogenation: Implications in Li-Ion Battery Electrolyte Stability and Selective Oxidation Catalysis of Hydrogen-Containing Molecules. *Chemistry of Materials*, 31(15):5464–5474, Aug 2019.

[80] Jin Suntivich, Kevin J. May, Hubert A. Gasteiger, John B. Goodenough, and Yang Shao-Horn. A Perovskite Oxide Optimized for Oxygen Evolution Catalysis from Molecular Orbital Principles. *Science*, 334(6061):1383–1385, 2011.

[81] Federico Calle-Vallejo, Nilay G. Inoglu, Hai-Yan Su, José I. Martínez, Isabela C. Man, Marc T. M. Koper, John R. Kitchin, and Jan Rossmeisl. Number of outer electrons as descriptor for adsorption processes on transition metals and their oxides. *Chem. Sci.*, 4:1245–1249, 2013.

[82] Felipe Andrés Garcés-Pineda, Huu Chuong Nguyën, Marta Blasco-Ahicart, Miguel García-Tecedor, Mabel de Fez Febré, Peng-Yi Tang, Jordi Arbiol, Sixto Giménez, José Ramón Galán-Mascarós, and Núria López. Push-pull electronic effects in surface-active sites enhance electrocatalytic oxygen evolution on transition metal oxides. *ChemSusChem*, 14(6):1595–1601, 2021.

[83] Rasmus K.B. Karlsson, Ann Cornell, and Lars G.M. Pettersson. The electrocatalytic properties of doped TiO2. *Electrochimica Acta*, 180:514–527, 2015.

[84] Hyun Woo Lim, Deok Ki Cho, Jae Hyun Park, Su Geun Ji, You Jin Ahn, Jin Young Kim, and Chan Woo Lee. Rational Design of Dimensionally Stable Anodes for Active Chlorine Generation. *ACS Catalysis*, 11(20):12423–12432, Oct 2021.

[85] Tugce Kutlusoy, Spyridon Divanis, Rebecca Pittkowski, Riccardo Marina, Adrian M. Frandsen, Katerina Minhova-Macounova, Roman Nebel, Dongni Zhao, Stijn F. L. Mertens, Harry Hoster, Petr Krtil, and Jan Rossmeisl. Synergistic effect of p-type and n-type dopants in semiconductors for efficient electrocatalytic water splitting. *Chem. Sci.*, 13:13879–13892, 2022.

[86] Tsutomu Umebayashi, Tetsuya Yamaki, Hisayoshi Itoh, and Keisuke Asai. Analysis of electronic structures of 3d transition metal-doped TiO2 based on band calculations. *Journal of Physics and Chemistry of Solids*, 63(10):1909–1920, 2002.

[87] Dong Myung Jang, In Hye Kwak, El Lim Kwon, Chan Su Jung, Hyung Soon Im, Kidong Park, and Jeunghee Park. Transition-Metal Doping of Oxide Nanocrystals for Enhanced Catalytic Oxygen Evolution. *The Journal of Physical Chemistry C*, 119(4):1921–1927, Jan 2015.

[88] Linsey C. Seitz, Dennis Nordlund, Alessandro Gallo, and Thomas F. Jaramillo. Tuning Composition and Activity of Cobalt Titanium Oxide Catalysts for the Oxygen Evolution Reaction. *Electrochimica Acta*, 193:240–245, 2016.

[89] Zhi hao Yuan, Jun hui Jia, and Li de Zhang. Influence of co-doping of Zn(II)+Fe(III) on the photocatalytic activity of TiO2 for phenol degradation. *Materials Chemistry and Physics*, 73(2):323–326, 2002.

[90] Hongmei Luo, Tsuyoshi Takata, Yungi Lee, Jinfeng Zhao, Kazunari Domen, and Yan. Photocatalytic Activity Enhancing for Titanium Dioxide by Co-doping with Bromine and Chlorine. *Chemistry of Materials*, 16(5):846–849, Mar 2004.

[91] Sesha S. Srinivasan, Jeremy Wade, Elias K. Stefanakos, and Yogi Goswami. Synergistic effects of sulfation and co-doping on the visible light photocatalysis of TiO2. *Journal of Alloys and Compounds*, 424(1):322–326, 2006.

[92] Katrine L. Svane and Jan Rossmeisl. Theoretical optimization of compositions of high-entropy oxides for the oxygen evolution reaction. *Angewandte Chemie International Edition*, 61(19):e202201146, 2022.

[93] Henrik H. Kristoffersen and Horia Metiu. Reconstruction of Low-Index α-V2O5 Surfaces. *The Journal of Physical Chemistry C*, 119(19):10500–10506, May 2015.

[94] Caiwu Liang, Reshma R. Rao, Katrine L. Svane, Joseph H. L. Hadden, Benjamin Moss, Soren B. Scott, Michael Sachs, James Murawski, Adrian Malthe Frandsen, D. Jason Riley, Mary P. Ryan, Jan Rossmeisl, James R. Durrant, and Ifan E. L. Stephens. Unravelling the effects of active site density and energetics on the water oxidation activity of iridium oxides. *Nature Catalysis*, 7(7):763–775, Jul 2024.